AD-A084 921 SCIENTIFIC SYSTEMS INC CAMBRIDGE MA F/G 20/4
GLOBAL STABILITY AND CONTROL ANALYSIS OF AIRCRAFT AT HIGH ANGLE--ETC(U)
JUN 78 R K MEHRA, J V CARROLL N00014-76-C-0780
UNCLASSIFIED ONR-CR215-248-2 NL

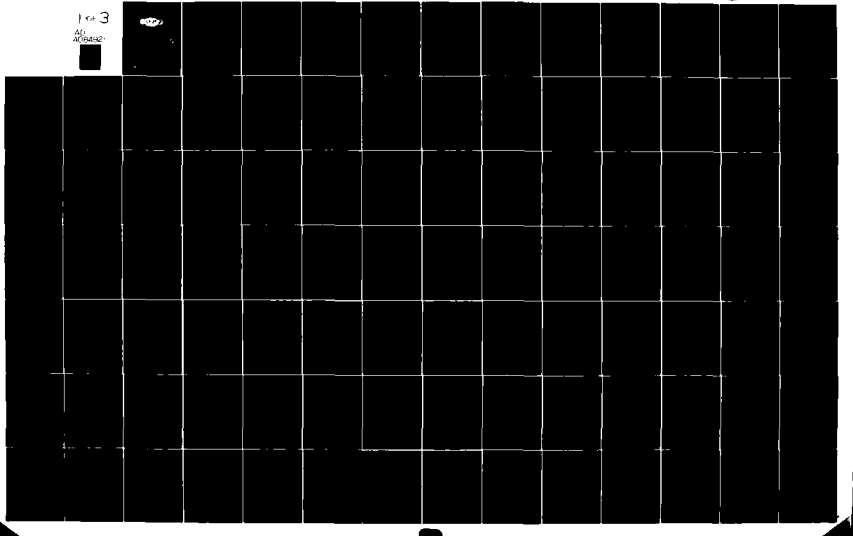

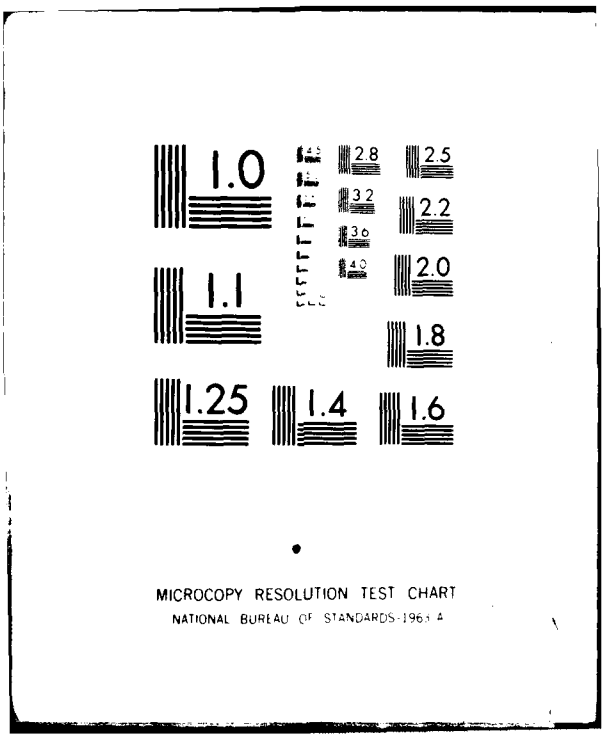
1.0
1.1
1.25
1.4
1.6
1.8
2.0
2.2
2.5
2.8
3.2
3.6
4.0
MICROCOPY RESOLUTION TEST CHART
NATIONAL BUREAU OF STANDARDS-1963-A

Report ONR-CR215-248-2

LEVEL III

13

GLOBAL STABILITY AND CONTROL ANALYSIS OF AIRCRAFT AT HIGH ANGLES-OF-ATTACK

Raman K. Mehra
James V. Carroll

Scientific Systems, Inc.
186 Alewife Brook Parkway
Cambridge, MA 02138

Contract N00014-76-C-0780

30 June 1978

Annual Technical Report for Period 1 June 77 - 31 May 78

Approved for public release; distribution unlimited.

PREPARED FOR THE
OFFICE OF NAVAL RESEARCH • 800 N. QUINCY ST. • ARLINGTON, VA. 22217

Change of Address

Organizations receiving reports on the initial distribution list should confirm correct address. This list is located at the end of the report. Any change of address or distribution should be conveyed to the Office of Naval Research, Code 211, Arlington, VA 22217.

Disposition

When this report is no longer needed, it may be transmitted to other organizations. Do not return it to the originator or the monitoring office.

Disclaimer

The findings and conclusions contained in this report are not to be construed as an official Department of Defense or Military Department position unless so designated by other official documents.

Reproduction

Reproduction in whole or in part is permitted for any purpose of the United States Government.

DISCLAIMER NOTICE

THIS DOCUMENT IS BEST QUALITY PRACTICABLE. THE COPY FURNISHED TO DTIC CONTAINED A SIGNIFICANT NUMBER OF PAGES WHICH DO NOT REPRODUCE LEGIBLY.

SECURITY CLASSIFICATION OF THIS PAGE (When Data Entered)

REPORT DOCUMENTATION PAGE

READ INSTRUCTIONS BEFORE COMPLETING FORM

1. REPORT NUMBER: ONR CR 215-248-2	2. GOVT ACCESSION NO.: AD-A084921
3. RECIPIENT'S CATALOG NUMBER	
4. TITLE (and Subtitle): Global Stability and Control Analysis of Aircraft at High Angles-of-Attack.	5. TYPE OF REPORT & PERIOD COVERED: Annual Technical Report. 1 June 1977 - 31 May 1978
	6. PERFORMING ORG. REPORT NUMBER
7. AUTHOR(s): Raman K. Mehra, James V. Carroll	8. CONTRACT OR GRANT NUMBER(s): N00014-76-C-0780
9. PERFORMING ORGANIZATION NAME AND ADDRESS: Scientific Systems, Inc. 186 Alewife Brook Parkway Cambridge, MA 02138	10. PROGRAM ELEMENT, PROJECT, TASK AREA & WORK UNIT NUMBERS
11. CONTROLLING OFFICE NAME AND ADDRESS: Office of Naval Research Vehicle and Weapons Tech. Div. (Code 211) 800 N. Quincy St., Arlington, VA 22217	12. REPORT DATE: 30 June 1978 13. NUMBER OF PAGES: 259
14. MONITORING AGENCY NAME & ADDRESS (if different from Controlling Office): 273	15. SECURITY CLASS. (of this report): Unclassified 15a. DECLASSIFICATION/DOWNGRADING SCHEDULE

16. DISTRIBUTION STATEMENT (of this Report)

Approved for public release; Distribution unlimited

17. DISTRIBUTION STATEMENT (of the abstract entered in Block 20, if different from Report)

18. SUPPLEMENTARY NOTES

19. KEY WORDS (Continue on reverse side if necessary and identify by block number)

Aircraft Stability and Control, Bifurcation Analysis, Catastrophe Theory, Atmospheric Flight Mechanics, Nonlinear Systems, High Angle-of-Attack Phenomena

20. ABSTRACT (Continue on reverse side if necessary and identify by block number)

High angle-of-attack phenomena have been of interest to aerodynamicists, aircraft designers, pilots and control system analysts ever since the advent of modern high performance aircraft. Due to the concentration of inertia along the fuselage, the modern jet fighters are highly susceptible to post-stall departures and spin. In spite of extensive design effort, modern aircraft still inadvertently enter spins which sometimes result in loss of

DD FORM 1 JAN 73 1473 EDITION OF 1 NOV 65 IS OBSOLETE S/N 0102-014-6601

393341

20. (cont.)

life and/or property. Extensive wind-tunnel testing and radio-controlled flight testing has been done over the last twenty years to gain a better understanding of the dynamic instabilities at high angles-of-attack. A basic problem has existed in interpreting these data and in making predictions of aircraft dynamic behavior so as to achieve close agreement with flight test data.

Aircraft dynamic behavior at high angles-of-attack is highly nonlinear and in the past there has been a lack of suitable techniques for analyzing the global behavior of nonlinear systems. Under a previous project with the Office of Naval Research, Scientific Systems, Inc. has developed a new approach based on Bifurcation Analysis and Catastrophe Theory Methodology (BACTM). The approach has been applied to specific jump and limit cycle behavior such as roll-coupling, pitch up, post-stall departure, divergence, spin entry, developed erect spin, and spin prevention and recovery. The aircraft used for the study of spin motions was selected because of the completeness of the aero data in the spin flight regimes, and because it is representative of modern fighters. This model was also used for studies of non-spin, high angle-of-attack behavior.

Under this project, the full six DOF aircraft model was implemented, and used not only for the above studies, but also for several new developments in the BACTM methodology. The new developments are basically in the area of generalizing and improving the numerical techniques for computing equilibrium and bifurcation surfaces, in expanding the comprehensiveness of the physical model and environment and in the study of chaotic motions.

The work on this project has centered around the application of BACTM to study the spin characteristics of a "variable sweep" fighter aircraft. The aerodynamic data for this model roughly corresponds to experimental data for the F-111, although modifications in some of the numbers, particularly C_n, are required to make simulation results agree with flight test data. We have designated this simulation model as Aircraft F.

Spin behavior is typically a post-stall phenomenon, and is characterized by angles-of-attack much in excess of the stall value of angle-of-attack. It is also possible that spin conditions will follow a roll departure motion. A certain type of spin, the erect flat spin, has been given particular emphasis in this work effort. This spin is featured by values of α (angle-of-attack) in the 75-85 degree ranges; a vertical body rotation rate, which is also constant over time, and center of mass motion which is basically helical, with the axis parallel to local vertical; and a noticeably prominent yaw rate.

PREFACE

This investigation was conducted by Scientific Systems, Inc., Cambridge, MA from June 1, 1977 under contract N00014-76-C-0780 for the Office of Naval Research, Washington, DC. This report is the second annual technical report and includes results through May 31, 1978. The sponsoring office was the Vehicle Technology Program headed by Mr. David Siegel. Mr. Robert von Husen served as the Navy Technical Monitor for the program.

The principal investigator for the study was Dr. Raman K. Mehra. He was assisted by Dr. James V. Carroll. L. Washburn and M. Riehm typed the final report.

TABLE OF CONTENTS

LIST OF FIGURES

CHAPTER I

Introduction and Summary

1.1 Scope of Work Effort

High angle-of-attack phenomena have been of interest to aerodynamicists, aircraft designers, pilots and control system analysts ever since the advent of modern high performance aircraft. Due to the concentration of inertia along the fuselage, the modern jet fighters are highly susceptible to post-stall departures and spin. In spite of extensive design effort, modern aircraft still inadvertently enter spins which sometimes result in loss of life and/or property. Extensive wind-tunnel testing and radio-controlled flight testing has been done over the last twenty years to gain better understanding of the dynamic instabilities at high angles-of-attack. A basic problem has existed in interpreting these data and in making predictions of aircraft dynamic behavior so as to achieve close agreement with flight test data.

Aircraft dynamic behavior at high angles-of-attack is highly nonlinear and in the past there has been a lack of suitable techniques for analyzing the global behavior of nonlinear systems. Under a previous project with the Office of Naval Research, Scientific Systems, Inc. has developed a new approach based on Bifurcation Analysis and Catastrophe Theory Methodology (BACTM). The approach has been applied to specific jump and limit cycle behavior such as roll-coupling, pitch up, post-stall departure, divergence, spin entry, developed erect spin, and spin prevention and recovery. The aircraft used for the study of spin motions was selected because of the

completeness of the aero data in the spin flight regimes, and because it is representative of modern fighters. This model was also used for studies of non-spin, high angle-of-attack behavior.

Under this project, the full six DOF aircraft model was implemented, and used not only for the above studies, but also for several new developments in the BACTM methodology. The new developments are basically in the area of generalizing and improving the numerical techniques for computing equilibrium and bifurcation surfaces, in expanding the comprehensiveness of the physical model and environment and in the study of chaotic motions.

The work on this project has centered around the application of BACTM to study the spin characteristics of a "variable sweep" fighter aircraft. The aerodynamic data for this model roughly corresponds to experimental data for the F-111, although modifications in some of the numbers, particularly C_n, are required to make simulation results agree with flight test data. We have designated this simulation model as Aircraft F.

Spin behavior is typically a post-stall phenomenon, and is characterized by angles-of-attack much in excess of the stall value of angle-of-attack. It is also possible that spin conditions will follow a roll departure motion. A certain type of spin, the erect flat spin, has been given particular emphasis in this work effort. This spin is featured by values of α (angle-of-attack) in the 75-85 degree ranges; a vertical body rotation rate, which is also constant over time, and center of mass motion which is basically helical, with the axis parallel to local vertical; and a noticeably prominent yaw rate.

The study of spin behavior begins with an analysis of the types and nature of equilibrium spin conditions. Because gravity plays a role, the basic system of equations is eighth order (the six force-moment equations, plus two kinematical equations for pitch and roll angles). Gravity is not a significant factor in the so-called "roll-coupling" flight regime, studied previously (Mehra et al. (1977)). In the case of spin equilibrium conditions, the presence of a non-zero gravity term causes the roll and pitch angles to enter the basic sixth-order system.

The highly nonlinear nature of flat spin, and the extreme values of state variables which typify it, require that the aerodynamic data extend over values of α and sideslip (β) which are well beyond the ranges of readily accessible data. The data we have used here for aircraft F were available in tabular form, and do encompass the necessary ranges (Moore et al. (1971)). Spline function polynomials were used to model this aero data because these functions are continuous at all interior points including certain derivatives.* Spline functions can therefore give accurate results over all points in the region with the accuracy needed to insure efficient numerical solution of the equilibrium and bifurcation surfaces. There is also flexibility, in that numerical techniques which utilize analytical expressions for the derivatives of the aero coefficients, can effectively utilize the spline approximation. Our results have confirmed the soundness of this choice.

A final note on the simulation model. The controls chosen were the standard aerosurface controls, aileron, elevator and rudder deflections. Thrust is not used as a control explicitly. This is not an undue restriction,

*This is true up to second order derivatives when cubic or bi-cubic splines are used.

since thrust is generally maximum during high-α maneuvering or is reduced to idle during spin.

Equilibrium surfaces for spin conditions were computed with satisfactory accuracy and efficiency by means of a parametric continuation procedure based on the methods of Davidenko (1953) and Lahaye (1934). In its basic form, this procedure solves a system of nonlinear algebraic equations by varying a parameter from a value for which the unknowns are readily determined to the actual value of the basic system. In our application, the parameter is one of the aerosurface controls and the unknowns are the eight state variables. The starting point is determined by a Newton-Raphson scheme, with initial guesses for the state and control at values which correspond to expected spin situations. In aircraft F, for example, the equilibrium pitch and roll rates are about 20 deg/sec, and yaw rate is roughly 10 times as large. Velocity is about 450 feet per sec, angle-of-attack about 83 deg. Sideslip, pitch and roll equilibrium angles are 5 deg or less. It has been verified that the equilibrium angular velocity is vertical. The continuation parameter, say rudder deflection, is then extended over its range from this starting point.

The particular continuation technique employed here is principally an amalgamation of methods proposed by Klopfenstein (1961), Keller (1977), and Kubicek (1976). These methods arose out of the necessity of dealing with various singularities which typify nonlinear equilibrium surfaces. The most important of these singularities are limit points and bifurcation points. Kubicek, Keller and Klopfenstein have added an arclength parameter, making it the independent variable, to eliminate the limit point singularity. Kubicek and Klopfenstein use a purely Euclidean arclength parameter, while Keller

introduces a family of "pseudo" arclength parameters which help to allow one to solve for the slopes of all of the solution curves which pass through a bifurcation point. In this way, the bifurcation points may be isolated. Continuation proceeds on the original branch using the knowledge of its slope and "jumping" over the actual bifurcation point. Then, one returns to the bifurcation point and begins continuation along the secondary branches. In addition, Keller's scheme may be extended to function spaces, so that differential systems such as Two-Point Boundary Value Problems may also be solved. The methods of Kubicek and Keller enable the computation of the complete equilibrium or bifurcation surface with just one computer run, and are typically more "robust" than Klopfenstein's method.

The eigenvalue analysis of the equilibrium surfaces for aircraft F show regions of jump, limit cycle, hysteresis and other phenomena similar to those found for aircrafts A, B and H investigated earlier (Mehra et al. (1977)). In the case of the spin phenomena, the magnitudes of the jumps are typically smaller, though there is indication that these jumps would go from flat spin to an intermediate spin ($\alpha \approx 70°$) to steep spin ($\alpha \approx 45°$). Additionally, jumps to limit cycles or oscillatory spins are also present.

The aircraft F model has also been used to generate equilibrium surfaces in non-spin regions prior to departure. A major consideration of such non-spin regimes is that roll and pitch angles generally do not have equilibrium (steady state) values, so that these variables must be decoupled from the basic system. This is done by neglecting gravity effects. The results are similar to those obtained with previous models (e.g., aircraft H). However, since angle-of-attack data were available only to -10 degrees, roll daparture studies with aircraft F were somewhat

limited. A study of the nature of equilibrium surfaces in the "transition" region between roll departure and flat spin has also been made.

In what may prove to be a very useful result in the analysis of spin motions, it was found that equilibrium surfaces in the spin regime, which have all of the features of the standard spin equilibrium surfaces, can be generated using the lower-dimensional "non-spin" equilibrium system. In this system, gravity is assumed to be zero. It should be emphasized that the numerical results are often different, but the shape of the curves is quite similar. This approximation has been made only in the study of flat, developed spins. These spins are characterized by high α_{SPIN} values, and low spin equilibrium pitch angles (θ_{SPIN}). With this situation, gravity terms in the dynamic equation for α are small. Finally, for many of the spin conditions, changing the value of V, the velocity magnitude, by 30% had a greater effect on the equilibrium curves than did eliminating gravity.

Time history runs of spin conditions for aircraft F have been made, and results confirm the predictions of the equilibrium surfaces. Those runs which begin in the developed flat spin condition follow quite accurately the results predicted by the spin equilibrium curves. Runs which attempt to achieve flat spin from non-spin conditions were also made. It has been found that, as reported in Bihrle (1976), ensuing motion in spin regions is highly sensitive to both the initial conditions and the control sequencing. Also, we discovered that it is much easier, for the given simulation model, to achieve equilibrium spin from "trim" flight conditions (controls neutral) when the velocity magnitude is held fixed. This is

equivalent to both adjusting thrust magnitude and vectoring the thrust, to keep it aligned with the current velocity vector and keeping constant magnitude. This is an approximation, but it does obviate the need at the current time to become concerned with the role of vehicle thrust in post stall and spin entry conditions. Such a concern can be more readily dealt with when more comprehensive models such as the F-4 are implemented. Similarly, spin recovery simulations have been made, and the results again indicate that the aircraft F model is highly sensitive to the recovery control sequence. We expect to develop a systematic recovery methodology once the spin bifurcation surfaces are completed.

1.2 Previous Work

Most of the theoretical and experimental results relating to the characteristics of spin motion has been performed at the NASA/Langley Research Center. The majority of this work has been experimental in nature. Theoretical, or analytical, results have been hampered by two factors: 1) the highly nonlinear nature of the spin regime, and 2) the difficulty both of obtaining wind tunnel data which are relevant to spin motions and of effectively correlating these data with the actual aircraft's performance.

Klinar and Grantham (1959) used traditional linearized analysis techniques to study flat, steady spin behavior. However, similar efforts done previously have been limited to reliance on the limited conventional static and forced oscillation aerodynamic data. These data do not always represent adequately the highly complex flow phenomena associated with flight in these stall/spin regions. Consequently, the wind-tunnel techniques were expanded. Neihouse et al. (1957, 1960) report on the development of a rotary balance mechanism by which a model is spun freely about selected spin axes, over wide ranges of angle-of-attack. They also discovered that differences between the model results and those of the aircraft became more pronounced with current high-speed designs. The differences were felt to be due to such factors as possible aerodynamic scale effects (or Reynolds number effects) and variations in testing techniques between airplanes and free-spinning-tunnel models.

Analysis made by Scher and Anglin (1959) further determined that different kinds of spins are entered depending upon whether the aircraft

was initially in a trimmed, level flight condition or spin entry was achieved from an applied yaw rotation which simulates the spin-tunnel mode. Using BACTM on our aircraft F model (Chapter III), we obtain similar results. Their results again emphasize the importance of Reynolds number effects as well as tunnel test techniques. More recently, Bihrle (1974, 1976) corroborates the large effect of Reynolds number on spin aerodynamic characteristics. In addition, he recognizes the role of gravity in spin behavior and proposes scaling the models so that the Froude number (a dimensionless quantity relating the relative effects of aerodynamic and gravitational forces) remains unchanged. Using unpowered models, Bihrle (1976) also shows that the type of subsequent spin motion is highly sensitive to the aircraft's initial condition (attitude, control setting, attitude rates, etc.); and that spin motions which ensue are highly sensitive to the sequencing and timing of the pro-spin control actions. He also found that changes in inertias, side force coefficients, and initial roll angle do not significantly influence developed spin; but that the pitch damping coefficient and center of mass location is important.

As both Bihrle (1976) and Anglin (1977) mention, it is necessary to combine the different types of aero data in order to have a reasonable model. In most instances, rotary balance data has limitations because it is evaluated at relatively few control settings, and is very unreliable for angle-of-attack less than about 50°. In other analytic results, Anglin and Scher (1964) not only use extensively both the conventional and rotary balance data to study fairly steady developed spins

and recoveries, but also define and use a non-dimensional spin-energy factor (Eq. 3.2.48 in Chapter III of this report) to indicate the relative difficulty of spin recovery. This factor is seen to be related to the antispin yawing moment coefficient. Further, they found that the antispin rolling-moment coefficient depends both on this energy factor and upon the moment of inertia about the longitudinal axis.

Prior to, and concurrently with, the analytic efforts briefly referenced above has been an extensive program of experimental flight tests and evaluations conducted by several government agencies and the military branches. These results are generally restricted to the particular aircraft being studied, and are typically aimed at developing recovery techniques and avoiding spin entry. Rutan et al. (1970), Sallada et al. (1967), Savidge (1970), Glenzer (1970), Carlson (1970), Krings and Weber (1970) and Shaw and Shields (1970) all report on the results of spin-oriented flight test experience.

Anglin (1977) reports that much remains to be done in terms of providing an aero data base for spin regimes which will be sufficiently accurate to enable adequate simulator prediction of actual aircraft response. As we have also found (Chapter III), he describes a large region in the yaw rate - angle-of-attack plane, located between the low angle-of-attack and developed flat spin regions, in which neither the conventional aerodynamics nor the more recent rotary-balance aerodynamics alone is adequate to describe the post-stall gyrations, spin entry and oscillatory spin motions which characterize this region. Further work is needed, he concludes, on understanding the behavior in this region;

and this requires the development of an aerodynamic model which incorporates features of both the conventional and rotary aerodynamics.

Other recent research worthy of note includes work by Young (1974), who used a steepest descent optimization technique to develop control histories for spin recovery. Adams (1972) showed that several spin modes and types are possible using representative aircraft models, and Moore et al. (1971) show that use of a fixed-base simulator can give results sufficiently realistic for studying stall/spin characteristics of aircraft.

The previous work described above has supplied us with much of the insight and direction needed to adapt BACTM to spin analysis problems, and to clearly outline areas in which BACTM may be utilized to investigate these problems. In the following chapters, particularly Chapter III, it will be seen that our results are in general agreement with the above; and, further, that BACTM has added fresh insight into many of these problems and possesses the capability to enhance even more our understanding of spin phenomena.

1.3 Summary of Significant Results

The significant milestones achieved on this project are given below:

- Application of BACTM to a six DOF aircraft model, with comprehensive aero data (aircraft F).
- Development of simulation model for analyzing spin behavior.
- Study of the characteristics of spin motion, and of currently used control procedures to simulate spin entry and effect spin recovery.
- Representation of tabular aero data in analytical form by means of cubic and bi-cubic spline functions.
- Expansion and generalization of methodology for generating the equilibrium and bifurcation surfaces of BACTM. Reliance on parametric continuation methods derived from work of Davidenko (1953).
- Development of continuation methodology, based on work of Rheinboldt (1977) and Keller (1977), which can compute all branches passing through a "bifurcation point."
- Generation of equilibrium curves for aircraft F in flat spin, intermediate spin (angle-of-attack about 75°) and stall departure flight regimes.

- Time history simulation runs of the aircraft F model to verify some of the equilibrium results; and to begin an analysis of the dynamics of spin entry and recovery from developed, flat spin.
- Development of an accurate and efficient means of computing numerical derivatives, using splines.

- Demonstration that flat developed spin motions, in which angle-of-attack is high and pitch angle is low, may be approximated on a first-cut basis by assuming negligible gravity.
- Observation that changing the value of V by about 30% has a more significant impact on the shape of the equilibrium curves than does neglecting gravity.
- Observation that a developed flat spin for aircraft F is featured by an extremely tight spiral, whose diameter decreases as the (pro-spin) rudder setting gets more extreme, and which drifts slightly, due to nonsymmetric lateral aerodynamics at high α. The spin velocity, then, is almost entirely vertical, and the spin rotation produces about 0.5 g's acceleration.
- Demonstration that a high-α limit cycle condition (steep, oscillatory spin) is reached both by a stall-departure maneuver starting from trim conditions, and by a spin recovery maneuver starting from the flat spin equilibrium conditions. The limit cycle family provides the link between the high-α equilibrium states and the trim equilibrium states. The recovery from this high α limit cycle condition by a fixed change in control settings is possible, since the stability of the limit cycle varies greatly over the physical range of the aero-surface control movements.

1.4 Organization of the Report

The report is organized into two main chapters, II and III, and a supporting chapter, IV. Chapter II contains a discussion of the techniques by which BACTM was modified to enable the study of the spin behavior of aircraft; also included in this chapter is material on chaotic motion and strange attractors. Chapter III describes the use of BACTM to analyze a particular aircraft model, Aircraft F, in all high-α regimes, including spin. There is extensive discussion of Aircraft F's behavior in terms of equilibrium surfaces and time history simulations. Chapter IV briefly discusses other topics of interest, including spectral analysis of chaotic motions and a preliminary look at using BACTM to synthesize a simple command augmentation system. Conclusions and recommendations are stated in Chapter V, and a list of symbols and nomenclature is included in Appendix A.

CHAPTER II

Further Developments of Bifurcation Analysis and Catastrophe Thoery Methodology (BACTM)

This chapter describes in detail the numerical algorithms used for computing equilibrium and bifurcation surfaces for a general nonlinear dynamic model of an aircraft under stall and spin conditions. Notation for the symbols presented in this chapter is given in Appendix A.

2.1 A General Computational Procedure Based on "Continuation" Methods

Continuation methods refer to those numerical techniques which "continue" a solution line, or locus, from some point in the state-parameter space where the solution is known. That is, suppose the solution to the nonlinear algebraic system

$$\underline{f}(\underline{x},\delta) = 0 \tag{2.1.1}$$

is desired. In this equation, $\underline{f}$ and $\underline{x}$ are each vectors of dimension n (a more concise, mathematical way of saying this is $\underline{f},\underline{x} \in R^n$; which means that $\underline{f}$ and $\underline{x}$ are elements of the Euclidean n-space of real numbers, that is, they are n-dimensional). Also, δ in this equation is a scalar, and has a special role as the continuation parameter. The idea behind the continuation methods is that we somehow know all solutions $\underline{x}$ satisfying (2.1.1), for a given $\delta = \delta_0$. These methods then supply a means of explicitly varying δ from δ_0 to some desired value, δ_1, where analytic or numerical solutions are difficult to obtain. As an example, suppose we wish to know

all values of x satisfying $f(x,\delta) = x^3 + 2ax^2 + bx + \delta = 0$ at any given value for δ. It is clear that at $\delta = 0$, we have three solutions, $x = (0, -a \pm \sqrt{a^2 - b})$. This, then, is a natural starting point for continuing the solution to some nonzero value of δ. Note in this example that a and b are also parameters, but that they remain fixed in value for the entire process.

Continuation methods have been applied to several varieties of problems which are typically multi-dimensional, nonlinear and possessing no "analytic" solution, i.e., a solution which can be explicitly derived. Problems which have been solved using continuation methods include certain kinds of two-point boundary value problems and boundary layer problems (including singular perturbation problems), in addition to the algebraic problem defined by (2.1.1).

The type of problem of interest here is that of solving a system of nonlinear algebraic equations of the form (2.1.1). In our applications,

$$\delta \in \{\delta a, \delta e, \delta r\}, \tag{2.1.2}$$

the set of aerosurface controls--aileron, elevator, and rudder, respectively.

Given that some solution point $\underline{x}^0(\delta_0)$ has been found (such a solution by definition satisfies (2.1.1)), the point $\underline{x}^0$ is called <u>C^1-regular</u> if the Jacobian

$$F \triangleq \left[\frac{\partial f_i(\underline{x},\delta)}{\partial x_j}\right] \tag{2.1.3}$$

an n x n matrix, is nonsingular (invertible). Otherwise, it is a <u>singular</u>

point. The notation C^1 refers to the continuity of $\underline{f}(\underline{x})$ and all of its first derivatives.

The solution to (2.1.1) at $\underline{x}^0$ is "continued" through other solution points by varying δ over some range of values. For any regular point $(\underline{x}^0, \delta_0) \in R^n \times R^1$, the implicit function theorem ensures the existence of a unique regular solution to (2.1.1) through this point. The notation $R^n \times R^1$ means that the (n+1)-space to be considered is comprised of two particular subspaces: R^n for the state variables $\underline{x}$, and R^1 for the scalar continuation parameter. Continuation solution algorithms generally fall into one of two different conceptual classes. The first class was initially investigated and developed by Lahaye (1934, 1948), and the second approach is usually attributed to Davidenko (Rall, 1968). Davidenko's approach is often called continuation-by-differentiation, and that of Lahaye belongs to the class of iterative continuation techniques. The Davidenko approach consists in the application of some suitable discrete-variable method to solve

$$\frac{d\underline{f}}{d\delta} = F\left(\frac{d\underline{x}}{d\delta}\right) + \frac{\partial \underline{f}}{\partial \delta} = 0, \qquad \delta \in D, \ \underline{x}(\delta_0) = \underline{x}^0 \tag{2.1.4}$$

where D is the set of admissible parameters, e.g., if $\delta = \delta e$, then $D = [-25,10]$ for aircraft F. Eq. (2.1.4) says that δ is to be varied in a way that ensures (2.1.1) being always true. A problem with this approach, especially where n is large, is the necessity for evaluating at each point the matrix F and the $(n \times 1)$-vector

$$\underline{f}_\delta \triangleq \left(\frac{\partial f_i}{\partial \delta}\right) \tag{2.1.5}$$

and this is usually very costly. If we try to reduce the order of the system model to offset this difficulty, there may arise fatal accuracy problems. On the other hand, Lahaye's iterative continuation approach uses a locally convergent iterative method (of a Newton-Raphson nature) to solve (2.1.1), the original equation, at an increasing (or decreasing) sequence $\{\delta_k\}$ of parameter values in D. In its basic form the method starts at the known solution $\underline{x}^0$ and selects steps $(\delta_{k+1} - \delta_k)$ such that the last iterate at δ_k is an acceptable starting point for the iteration at δ_{k+1}. At each point, (2.1.1) is satisfied to within some $\varepsilon_k > 0$, where $\varepsilon_k \simeq \|\underline{f}^k\|$. (See Appendix A for notation.)

The recent trend has been to combine the two ideas by using a feasible, low-order method of solving (2.1.4) as a predictor and then following it with a locally convergent iterative process for (2.1.1) as a corrector. In particular, Klopfenstein (1961), Keller (1977), Rheinboldt (1977) and Kubicek (1976) have developed versions which seem particularly suited to the task at hand: the computation of equilibrium and bifurcation surfaces for high-performance aircraft operating in high-α (nonlinear) flight regimes. One of the major results described in this report is the modification and adaptation of the relevant techniques presented in the above references to two principal aspects of BACTM analysis, the computation of equilibrium surfaces and bifurcation surfaces. The utilization of these algorithms, and the refinements needed to handle certain situations, is discussed below.

More recently, we have found that other methods may be better suited to the particular application of computing bifurcation surfaces for aircraft in the spin regime. This is because of both the dimensionality of this

system (increased due to gravity coupling) and the highly nonlinear characteristics of the motions in developed spin. Briefly, these methods involve techniques which avoid the computation of the Jacobian (Ralston, 1975, Ralston and Jennrich, 1978). A derivative-free algorithm as well as one-dimensional search algorithms in the corrector phase of continuation, will also be discussed below.

Consistent with the notation employed elsewhere in this report, the equilibrium system of equations has the same form as (2.1.1), viz.:

$$\underline{f}(\underline{x},\delta) = 0 \tag{2.1.6}$$

where $\delta \in (\delta a, \delta e, \delta r)$ and the dimension and form of the state $\underline{x}$ and the function (mapping) $\underline{f}$ depend, in general, on whether one is in a spin or a non-spin *flight regime.* See Section 3.2 and Mehra, Kessel, Carroll (1977), respectively, for the distinctions. Eq. (2.1.6) is derived from the aircraft dynamic equations, which are concisely expressed as

$$\dot{\underline{x}} = f(\underline{x},\underline{\delta}) \tag{2.1.7}$$

where

$$\underline{\delta} \triangleq (\delta a, \delta e, \delta r) \tag{2.1.8}$$

(Hence, the mathematical definition of dynamic equilibrium is $\dot{\underline{x}} = 0$. For a stable equilibrium, $\frac{d^n \underline{x}}{dt^n} = 0$, for all $n > 0$)

The bifurcation system of equations has the same form, but an additional equation is added, to specify the requirement that the Jacobian matrix F be singular at a bifurcation point. This is in addition to the equilibrium requirement (2.1.6). We denote the resulting set of equations as

$$\underline{g}(\underline{y},\delta_i) = 0 \tag{2.1.9}$$

Like (2.1.6), (2.1.9) has the form of Eq. (2.1.1), and can thus be solved by the continuation methods presented here. Furthermore, (2.1.9) is related to (2.1.6) as follows:

$$\underline{y} = \begin{bmatrix} \underline{x} \\ \delta_j \end{bmatrix} \tag{2.1.10a}$$

where

$$\delta_j, \delta_i \in (\delta a, \delta e, \delta r), \quad i \neq j; \tag{2.1.10b}$$

and

$$\underline{g}(\underline{y},\delta_i) = \begin{bmatrix} \underline{f}(\underline{x},\delta_i) \\ \Delta \end{bmatrix} \tag{2.1.11a}$$

where

$$\Delta \triangleq \det(F) \tag{2.1.11b}$$

The solution of (2.1.9) yields a curve $\delta_j(\delta_i)$, δ_k fixed, in the control space called a bifurcation surface. We are at liberty to choose any two δ_i from the control set $(\delta a, \delta e, \delta r)$, but the third one, δ_k, remains fixed in value. Also, while the bifurcation surface is the particular curve δ_j vs. δ_i, solution of (2.1.9) clearly supplies values for $\underline{x}$ as well, at each point (δ_i, δ_j) on the bifurcation surface. The system (2.1.9) is essentially the equilibrium system (2.1.6) augmented by the constraint $\Delta = 0$. (This is discussed in more detail below.) The equilibrium system dimensionality is consequently increased by one in the bifurcation system, so that an extra dependent variable, $\delta_j \in (\delta a, \delta e, \delta r)$, $j \neq i$, may be added.

The bifurcation surfaces are consequently more difficult to generate for two reasons:

i) the size of the system is (n+1), where n is the size of the equilibrium system. For the non-spin system considered here, n = 5, and for the spin system, n = 8.*

ii) a much worse problem than (i) is posed by the presence of the constraint on Δ, the determinant of the Jacobian of $\underline{f}$. Even in the n = 5 case, it is wholly impractical to expand Δ analytically, so that evaluating the Jacobian of $\underline{g}$, (2.1.11a), of necessity requires using a numerical differentiation algorithm on at least the $(n+1)^{th}$ row of

$$G \triangleq \underline{g}_{\underline{y}} = \left[\frac{\partial g_i}{\partial y_j}\right] \qquad (2.1.12)$$

Except for extra core and extra care, problem (i) above is relatively straightforward to surmount. The second problem, on the other hand, requires extreme caution and precision, in addition to more complicated algorithms. Consequently, when using continuation-based methods requiring the first derivative, the core and run-time costs are high.

We shall now discuss in more detail a particular predictor-corrector continuation algorithm developed by Kubicek (1976).

2.1.1 Continuation Method of Kubicek (1976)

Kubicek's method employs the basic method of Davidenko (Rall, 1968,

*There is a dimensionality-flexibility tradeoff for the spin system, which centers around the velocity variable, V. V can be solved for explicitly in terms of the remaining 7 variables and the controls, but at some cost in flexibility and adaptation to several aircraft models. We have opted more for flexibility in this regard, and so n = 8 for spin, not 7.

Ficken, 1951, Davidenko, 1953) to solve (2.1.4), in combination with the Newton method and Adams integration formulas. This particular method has become the basis for our continuation algorithms, since it was found to be capable of solving accurately and efficiently a wide variety of nonlinear algebraic equations required by the BACTM approach to high-performance aircraft analysis.

Kubicek has introduced certain modifications to the basic continuation methods of Davidenko which make the solution of Eq. (2.1.1) more feasible on digital computers. In essence, this approach represents a subset of the methodology assembled by Keller (1977), Rheinboldt (1977), et al.; however, certain features of the Kubicek algorithm are worth detailing.

Basically, an arclength parameter is introduced to evaluate the dependence $\underline{x}(\delta)$, which is assumed to be continuously smooth in the (n+1)-dimensional space $(\underline{x},\delta)$. (This assumption is not necessary in the method of Keller, which can handle the singularities, or bifurcations points.) Quite often, $\underline{x}(\delta)$ is smooth in the augmented space R^{n+1} and singular in R^n. In such an instance, the system (2.1.4) cannot be solved, because the (n x n) Jacobian F, Eq. (2.1.3), is non-invertible, i.e., singular. This happens at limit points, Fig. 2.1. At such points, δ is no longer monotonically increasing or decreasing, and F is singular. However, a properly-selected arclength parameter will remain monotonic at limit points; this enables smooth continuation around limit points, as shown below.

By introducing the arclength parameter s, so that $(\underline{x},\delta)$ become $[\underline{x}(s),\delta(s)]$, the system (2.1.4) "inflates" to

$$F\dot{\underline{x}} + \frac{\partial \underline{f}}{\partial \delta}\dot{\delta} = 0 \qquad (2.1.13)$$

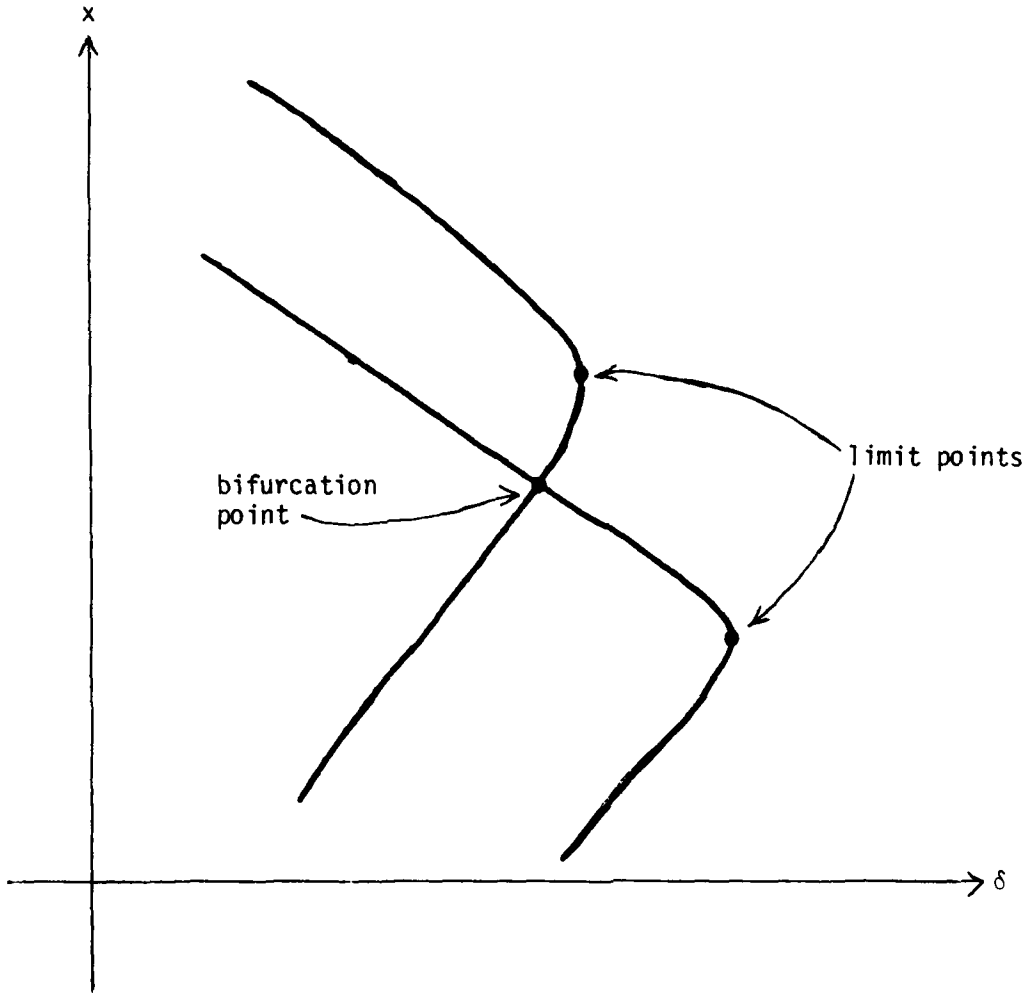

Figure 2.1

Bifurcation and Limit Points

and we choose initially a standard Euclidean arclength relationship

$$\left(\frac{dx_1}{ds}\right)^2 + \cdots + \left(\frac{dx_n}{ds}\right)^2 + \left(\frac{d\delta}{ds}\right)^2 = \dot{x}_1^2 + \ldots + \dot{x}_n^2 + \dot{\delta}^2 = 1 \qquad (2.1.14)$$

where

$$\dot{\underline{x}} \triangleq \frac{d\underline{x}}{ds}$$
$$\dot{\delta} \triangleq \frac{d\delta}{ds} \qquad (2.1.15)$$

Eq. (2.1.14) is comparable to the more complicated pseudoarclength normalizations introduced by Keller (described in the next section), which are useful in the algorithms which solve for the branches at bifurcation points*, shown in Fig. 2.1. Kubicek generalizes the solution procedure by generating a nonsingular (n x n) matrix of the form

$$\Gamma_k = \begin{bmatrix} \frac{\partial f_1}{\partial x_1}, \ldots, \frac{\partial f_1}{\partial x_{k-1}}, \frac{\partial f_1}{\partial x_{k+1}}, \ldots, \frac{\partial f_1}{\partial x_{n+1}} \\ \vdots \\ \frac{\partial f_j}{\partial x_1} \\ \vdots \\ \frac{\partial f_n}{\partial x_1}, \ldots, \frac{\partial f_n}{\partial x_{k-1}}, \frac{\partial f_n}{\partial x_{k+1}}, \ldots, \frac{\partial f_n}{\partial x_{n+1}} \end{bmatrix} \qquad (2.1.16)$$

*Singular points are points $(\underline{x},\delta)$ where the Jacobian matrix F is non-invertible, or singular. Both limit and bifurcation points are singular points.

In this definition, we have set $x_{n+1} = \delta$ for consistency. Note that Γ_k is n x n square because one column, $\partial \underline{f}/\partial x_k$, is eliminated. Since $k \in (1,n+1)$, there are n+1 possible Γ_k to analyze.

We shall not go into the full detail here (Keller, 1977, has such detail), but will mention that at least one nonsingular Γ_k does exist at a limit point, thereby allowing continuation through that point. This is a consequence of the fact that, while F is singular, it has rank n-1 at a limit point. Thus, the corank, equal to (n-rank), is 1. At a bifurcation point, the corank exceeds 1, and there is no invertible Γ_k. It is possible, therefore, to associate the corank of F at singular points with the number of equilibrium branches intersecting at that point. At a simple bifurcation point, for example, F has corank 2 and two branches intersect (Fig. 2.1). At regular points, F is nonsingular; thus corank of F is zero, but a (smooth) branch also passes through. If an x_k, $1 \leq k \leq n+1$, can be found so that its corresponding Γ_k is regular, then the system (2.1.13) can be recast as follows:

$$\dot{\underline{f}} = \Gamma_k \left(\frac{dx_j}{ds} \right)_{\substack{j \neq k \\ 1 \leq j \leq n+1}} + \left(\frac{\partial \underline{f}}{\partial x_k} \right) \dot{x}_k = 0 \qquad (2.1.17)$$

In this equation, the vector (dx_j/ds) is n-dimensional, as the $k^{\underline{th}}$ element is not used, and $x_{n+1} \triangleq \delta$. Eq. (2.1.17) can then be solved for n of the n+1 parametric derivatives:

$$\left(\frac{dx_j}{ds} \right)_{\substack{j \neq k \\ 1 \leq j \leq n+1}} = -\Gamma_k^{-1} \left(\frac{\partial \underline{f}}{\partial x_k} \right) \dot{x}_k \qquad (2.1.18)$$

or, equivalently,

$$\frac{dx_j}{ds} = \beta_j \frac{dx_k}{ds}, \quad j = 1,2,\ldots,(k-1),(k+1),\ldots,(n+1) \tag{2.1.19}$$

The final parametric derivative is determined by using (2.1.19) in Eq. (2.1.14):

$$(\dot{x}_k)^2 = \left(1 + \sum_{\substack{j=1 \\ j\neq k}}^{n+1} \beta_j{}^2\right)^{-1} \tag{2.1.20}$$

In Eq. (2.1.20), the sign ambiguity is resolved by the orientation of the arclength parameter s along the curve. This may be done somewhat arbitrarily at the solution starting point, $(\underline{x}_0,\delta_0)$, which must be supplied (or obtained from a Newton-type iteration). This solution branch will then emanate in one direction from the starting point, and can be made to emanate in the other direction by selecting the other sign.

Thus, the method of Kubicek is more "robust" than that of Klopfenstein (1961) in that the latter retains the special role of δ as the continuation parameter--Klopfenstein inverts Γ_{n+1}, which is actually F, at every point rather than the more general Γ_k. Numerical difficulties are more likely to be avoided by Kubicek's algorithm, which at each step utilizes the "best" continuation parameter x_k. The value of the subscript k is determined by means of Gaussian elimination using controlled pivoting. That is, at any point in the reduction process for inverting Γ_k, the current pivot element chosen from Γ_k, γ_{ij}, has the largest magnitude of all candidate elements. Once γ_{ij} is chosen, all remaining $i^{\underline{th}}$ row and $j^{\underline{th}}$ column elements of Γ_k are eliminated as candidate elements

for selection of subsequent pivot elements. Then, γ_{ij} is used to reduce all other elements in column j to zero by means of the so-called "elementary matrix operation"

$$\{\text{Row } \ell \text{ of } \Gamma_k\} = \rho_\ell \cdot \{\text{Row i of } \Gamma_k\} + \{\text{Row } \ell \text{ of } \Gamma_k\} \tag{2.1.21}$$

where the scalar ρ_ℓ is adjusted so that (2.1.21) produces a zero for element $\gamma_{\ell j}$, $\ell \neq i$. That is, to zero all elements of column j except the $i^{\underline{th}}$, the right side of (2.1.21) becomes

$$\rho_\ell \cdot \gamma_{ij} + \gamma_{\ell j} = 0,$$

$$\rho_\ell = -\gamma_{\ell j}/\gamma_{ij} \tag{2.1.22}$$

The process continues in this manner, one column at a time. Eq. (2.1.22) indicates the role of the pivot elements γ_{ij} in the matrix inversion process. If at any step in the process no nonzero γ_{ij} can be found, the matrix is singular.

The process just described is a Gaussian elemination procedure. The pivoting is controlled in the Kubicek algorithm by allowing each column in Γ_k to be selectively scaled. This allows the user to "bias" the selection of a particular variable from $(\underline{x},\delta)$ as the continuation parameter. Typically, of course, the desired choice is $\delta = x_{n+1}$. The scale parameter for the column associated with x_{n+1} is then some value less than 1., say 0.001, while those for the other columns may be kept at 1. This approach has been developed by Deist and Sefor (1967).

The complete procedure involves performing the elimination process (2.1.21) n times on the n-by-(n+1) array

$$\Gamma \triangleq \frac{\partial \underline{f}}{\partial(\underline{x},\delta)} = \left[F, \frac{\partial \underline{f}}{\partial \delta}\right] \tag{2.1.23}$$

In so doing, n columns are selected for Γ_k, under the selection criterion that γ_{ij} have the largest magnitude of the candidate elements. This insures that the "most nonsingular" Γ_k is selected of the (n+1) possibilities. The one unselected column in this process becomes column k. When the resulting reduced Γ matrix is deprived of this column, $\tilde{\Gamma}_k$ results. $\tilde{\Gamma}_k$ is Γ_k of (2.1.16), but operated on several times by the elementary matrix operations (2.1.21). $\tilde{\Gamma}_k$ has the property that there is exactly one nonzero element (indicated by x) in each of its n rows and columns, e.g.,

$$\tilde{\Gamma}_k = \begin{bmatrix} 0 & 0 & x & . & . & 0 & 0 \\ 0 & 0 & 0 & . & . & x & 0 \\ . & . & . & . & . & . & . \\ . & . & . & . & . & . & . \\ x & 0 & 0 & . & . & 0 & 0 \\ 0 & 0 & 0 & . & . & 0 & x \\ 0 & x & 0 & . & . & 0 & 0 \end{bmatrix} \tag{2.1.24}$$

Eq. (2.1.17) thus becomes

$$\tilde{\Gamma}_k \dot{\underline{x}} + \tilde{\underline{f}}_{x_k} \dot{x}_k = 0 \tag{2.1.25}$$

where $\tilde{\underline{f}}_{x_k}$ is the $k^{\underline{th}}$ column of the reduced Γ matrix.

Upon expansion, (2.1.25) has the form of (2.1.19), so that the β_j from the latter expression are readily extracted, and the n $\dot{x}_i = dx_i/ds$

are found from (2.1.19), $i \neq k$. Also, (2.1.20) produces $\dot{x}_k$. Given the n+1 $\dot{x}_i$ elements, the Newton step size $\Delta\underline{x}$ is obtained for the full (n+1)-dimension x. Note that $\Delta x_k = 0$ in this procedure. What the above process has effectively done is compute a Newton iteration step, based on the standard multi-dimensional Newton-Raphson formula

$$\Delta\underline{x}^{(p)} = -\Gamma^{-1}\underline{f}(\underline{x}^{(p)}), \tag{2.1.26}$$

where p is the iteration counter ($\underline{x}^{(0)}$ is given), and $\underline{x}$ includes the original $\underline{x}$, plus δ.

To summarize, we have solved (2.1.17) for the $\dot{x}_j \triangleq dx_j/ds$, $j \neq k$, $1 \leq j \leq n+1$; i.e., we have found the β_j in (2.1.19). Using Eq. (2.1.20), which represents the standard Euclidean arclength relationship utilized by Klopfenstein and Kubicek, all (n+1) quantities $(\dot{\underline{x}},\dot{\delta})$ are determined. These derivatives are then used by the Kubicek algorithm to predict the next point on the curve. This is done by using Adams-Bashforth integration formulae. The logic of Kubicek and Deist and Sefor which regards the parameter δ as interchangeable with any state element x_i at each point makes this algorithm very robust in terms of singularities and numerical roundoff difficulties. This is because the value k can change from point to point along the continuation solution. After the Adams integration step (predictor step), the new point $(\underline{x},\delta)$, where all n+1 quantities have changed, is the next starting point for the Newton iteration (corrector step) to the point again satisfying (2.1.6).

The Kubicek algorithm has been discussed in considerable detail because it plays a major role in the adaptation of BACTM to handle large

order, complex systems. However, we have implemented other methods which, although not used as much at this point, do exhibit promise in certain aspects. Ultimately, it is hoped to develop a unified, comprehensive and flexible package for BACTM which utilizes the most appropriate algorithm for the task at hand. Some of the other algorithms which are currently being developed will now be discussed.

2.1.2 Continuation Method of Davidenko (1953) and Numerical Differentiation

If Eq. (2.1.1) can be put in the form:

$$\frac{d\underline{x}}{d\delta} = \underline{M}(\underline{x},\delta) \tag{2.1.27}$$

any number of numeric integration methods will be able to solve for a complete branch of solutions once an initial solution is found. This transformation is accomplished by differentiating Eq. (2.1.1) to obtain (2.1.4) so that

$$\underline{M} = -\left(\frac{\partial \underline{f}}{\partial \underline{x}}\right)^{-1}\left(\frac{\partial \underline{f}}{\partial \delta}\right) = -F^{-1}\left(\frac{\partial \underline{f}}{\partial \delta}\right) \tag{2.1.28}$$

When this equation can be solved, either an interpolatory integration method (such as Runge-Kutta) or a predictor-corrector method (such as Euler-Newton or Adams-Bashforth) can be used to continue along a branch. This is the essence of Davidenko's method, which has subsequently been refined considerably.

The first task, then, is to solve for the partial derivative of $\underline{f}$ with respect to any x_i or δ, since these comprise elements of Γ_k. In

the past we have solved for these derivatives analytically while setting up the problem. However, this severely limits the range of problems which may be solved and, moreover, makes the process of applying the technique to a new problem extremely complicated.

As a result, we have implemented a numeric differentiation routine. This routine is based on a cubic spline fit* to the function $\underline{f}(\underline{x},\delta)$, evaluated at selected points $\underline{y} = (\underline{x},\delta)$, centered on $\underline{y}_0$, the point where the actual derivative, $\partial\underline{f}/\partial\underline{y} = \partial\underline{f}/\partial(\underline{x},\delta) \triangleq \Gamma$ is desired. To understand the process more readily, consider the scalar case: $x, f, \delta \in R'$. The goal, then, is to numerically evaluate $\partial f/\partial x$ and $\partial f/\partial\delta$ at $\underline{y}_0 = (x_0,\delta_0)$. For $\partial f/\partial x$, evaluate f at the five points

$$f((x_0 + p\varepsilon),\delta_0), \qquad p = -2,-1,0,1,2 \tag{2.1.29}$$

Note that we have $f(x_0,\delta_0)$ at $p = 0$. The increment size ε is chosen so that

$$\|f(\underline{y}_0) - f(\underline{y})\| \simeq 10^{-4} \tag{2.1.30}$$

This choice of ε allows sufficient accuracy of the fit without introducing serious numerical difficulty; ε must provide a large enough spread in Δy so that the slope obtained is representative, yet not be so large as to deteriorate precision. We then use each of the five $\underline{y}$ as knots for the spline fit. The polynomial approximation resulting from this is analytic at $\underline{y}_0$, by definition, so that evaluation of $\partial f/\partial x$ at y_0 is straightforward.

Similarly, for $\partial f/\partial\delta$ at y_0, fix x at x_0, evaluate f at the five points

$$f(x_0,(\delta_0 + p\varepsilon)) \tag{2.1.31}$$

*Curve-fitting using splines is discussed in detail in Section 3.2.1.

and make a spline fit and evaluation as before.

The extension to $\underline{x},\underline{f} \in R^n$ follows immediately. For each $\partial \underline{f}/\partial x_i$, make five evaluations of the vector $\underline{f}$ by varying x_i only, keeping $x_j = x_{j_0}$, $j \neq i$, and $\delta = \delta_0$. Each of the f_m are then spline-fitted, and this produces the set of vectors $(\partial f_m/\partial x_i)$, for each x_i, and δ.

2.1.3 Keller-Klopfenstein Continuation (Keller, 1977)

Limit points. Using the Davidenko method, all points along a solution branch can be computed as long as the n x n matrix F can be inverted. If F is singular with:

$$\dim N(F) \geq 1 \tag{2.1.32}$$

where $N(\cdot)$ denotes null space, special procedures must be used at such a point. The null space dimension here is equivalent to the corank of F. Adding a "normalization" equation and a new parameter to the system can avoid this problem in some cases. Keller (1977) uses the normalization:

$$N_3 \triangleq \theta \dot{\underline{x}}_0^T(\underline{x} - \underline{x}_0) + (1-\theta)\dot{\delta}_0(\delta - \delta_0) - (s - s_0) = 0 \tag{2.1.33}$$

where s is the arclength parameter, $0 < \theta < 1$, and $\underline{x}_0$, δ_0, and s_0 are the values at the initial point for the branch in question. The system now becomes:

$$\underline{g}(\underline{y},s) \triangleq \begin{bmatrix} \underline{f}(\underline{y}) \\ N_3(\underline{y},s) \end{bmatrix} = 0 \tag{2.1.34}$$

where:

$$\underline{y} = \begin{bmatrix} \underline{x} \\ \delta \end{bmatrix} \tag{2.1.35}$$

This system can be dealt with in the same manner as Eq. (2.1.1). The normalization N_3 is said to have better numerical properties near bifurcation points. Keller proves that, using (2.1.33) as the normalization equation, $\partial g/\partial \underline{y}$ is nonsingular if and only if:

$$F \text{ is nonsingular} \tag{2.1.36}$$

or:

$$\partial \underline{f}/\partial\delta \notin R(F), \text{ where } R(\cdot) \text{ denotes range space.} \tag{2.1.37}$$

Case (2.1.37) corresponds to a "limit point." At such a point (see Figure 2.1) two branches do not intersect, but $d\underline{x}/d\delta \to \infty$. In this case, solution of the augmented system (2.1.34) continues normally. The proof can be developed by utilizing Gaussian elimination techniques. We shall discuss this and other aspects of Keller's method in more detail in later reports.

For dealing with limit points alone, Keller's method is somewhat cumbersome, particularly in the choice of N_3 for an arclength relationship. The method of Kubicek, discussed in Section 2.1.1, is quite adequate at limit points, using the simpler normalization (2.1.14). However, the Keller approach is more comprehensive, and can handle the computation of equilibrium branches at bifurcation points. We shall now outline how this is done, saving some of the detail for later reports.

Bifurcation points. If, at some point on a branch, neither condition

(2.1.36) or (2.1.37) is satisfied, $\partial g/\partial y$ will be singular and continuation of the augmented system will also fail. This is a "bifurcation" point, where at least two branches cross. At such a point two steps must be accomplished. First, the bifurcation must be skipped over so that continuation may proceed along the same branch. Second, a point on the other branch must be found as an initial point for continuation along it.

Any predictor-corrector method can be used to skip over a bifurcation point. This simply involves choosing an initial solution and step size for a single prediction step for which the correction step will converge to a solution past the bifurcation point.

Finding the second branch at the bifurcation point is more complicated. To begin, consider a simple bifurcation point, at which two branches intersect. Here, the rank of Γ is $n - 1$. Γ is an n-by-(n+1) matrix, recall. Multiple bifurcation points have more than two branches intersecting at y^*, and the rank of Γ is less than $n - 1$. By examining the nature of the various terms in the power series expansion of $f(x,\delta)$ near such a bifurcation point, y^*, one realizes that the two branches emanating from y^* lie tangent at y^* to a plane defined by the two eigenvectors associated with the two zero eigenvalues of $\Gamma^T\Gamma$, which is a square (n+1)-by-(n+1) matrix of rank n-1. This matrix, then, has a corank of $(n+1)-(n-1) = 2$; hence, two zero eigenvalues. Once Γ is found, therefore, the plane is readily determined, and all branches can be located by a search in this plane for $f = 0$ points. This search is done along an arc of fixed radius from y^*, and sufficiently close to y^*.

To summarize, the algorithm of Keller differs from that of Kubicek in these significant areas:

(i) The pseudo-arclength normalization of Keller is more comprehensive than the purely geometric relationship (2.1.14) employed by Kubicek, and is capable of dealing with bifurcation points;

(ii) The Gaussian elimination procedure for selecting x_k as continuation parameter at each point seems to be capable of effecting numerical solutions more efficiently. Incorporating it into Keller's algorithm could well enhance its usefulness.

(iii) A final distinction which has practical, if not theoretical, significance, is the means by which one proceeds along the solution branches. Both schemes utilize predictor-corrector algorithms, with some form of Newton method as a corrector:

$$\underline{x}_{new} = \underline{x}_{old} - \Gamma_k^{-1}\underline{f} \qquad (2.1.38)$$

However, Kubicek uses the Adams-Bashforth explicit multistep method, with variable order, to integrate (2.1.19) and (2.1.20), whereas Keller suggests a modified Euler-Newton scheme, which is really a first-order Adams algorithm. There is more flexibility in the more complete Adams method.

2.1.4 Applications of the Kubicek Continuation Algorithm

The algorithm works exceptionally well as coded for solving aircraft F equilibrium surfaces, (2.1.6), both in spin and non-spin regimes. There is consequently no need to discuss the algorithm per se with regard to these surfaces. However, the computation of bifurcation surfaces of aircraft F, defined by (2.1.9), did necessitate more care in setting up the problem and, in the case of spin bifurcation surfaces, required in addition

some modification to the algorithm itself. These points will now be discussed in more detail.

2.1.4.1 Bifurcation Surfaces

Let $\underline{\bar{x}}(\delta)$ represent an equilibrium solution to (2.1.6). It is obvious that the variation of one element of $\underline{\delta}$ ($\underline{\delta} = (\delta a, \delta e, \delta r)$) will generate an equilibrium surface in the state-control space. A bifurcation point on the equilibrium surface implies a change in structural stability for control variations in the neighborhood of the bifurcation point. Points A and B are bifurcation points in Figure 2.2, and the loci of their projection onto the control subspace is what we call a bifurcation locus.

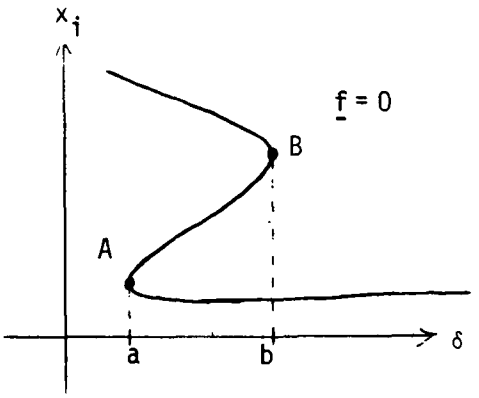

Figure 2.2
Equilibrium Surface

The set of bifurcation loci on a particular control subspace is called a bifurcation surface. The locus is generated by varying any two of the three controls, holding the third one fixed. It is obvious that the bifurcation points are a subset of the equilibrium points. The criterion for an elementary bifurcation point* is

*An elementary bifurcation point has a zero eigenvalue. More general bifurcation points such as Hopf Bifurcation points have purely imaginary eigenvalues. (See Mehra et al. (1977) for details.)

$$\Delta \triangleq \det(F) = \det\left[\frac{\partial \underline{f}}{\partial \underline{x}}\right] = 0 \tag{2.1.39}$$

(i.e., the Jacobian is singular). The difficulty at bifurcation points arises from the fact that, if

$$\underline{f}(\underline{x},\delta) = 0 \tag{2.1.6}$$

is true, then

$$F\frac{d\underline{x}}{d\delta} + \frac{\partial \underline{f}}{\partial \delta} = 0 \tag{2.1.4}$$

when δ is one of the controls selected as a parameter. (See Section 2.1.) It is seen from Fig. 2.2 that $d\underline{x}/d\delta$ is the slope of the $\underline{f} = 0$ locus for values of $\underline{x}$ and $\underline{\delta}$ on that locus. Also, points A and B are characterized by the fact that $d\underline{x}/d\delta$, the slope, is infinite. Hence, the continuation solution

$$\frac{d\underline{x}}{d\delta} = -F^{-1}\left(\frac{\partial \underline{f}}{\partial \delta}\right) \tag{2.1.40}$$

breaks down. This is equivalent to saying that the inverse of the Jacobian F does not exist, i.e., Eq. (2.1.39) holds.

Thus, unadulterated continuation methods break down at such points, as these methods solve for $\underline{x}(\delta)$ by integration of (2.1.40). Kubicek's algorithm avoids this by introducing an arclength parameter and by augmenting the Jacobian with an extra column representing the parameter, and eliminating (via Gaussian reduction) that column which leaves the most nonsingular square matrix (this amounts to interchanging the parameter δ_i with

an x_k as necessary; x_k then becomes the parameter and continuation via an equation like (2.1.40) or (2.1.18) remains valid).

To summarize, Eqs. (2.1.6), evaluated for some starting value $\bar{\underline{x}}_0$, and (2.1.40), which continues the solution from $\bar{\underline{x}}_0$, generate equilibrium surfaces. Bifurcation surfaces--represented by points a and b in the control-space in Figure 2.2 --are generated in a similar way, with the basic equilibrium system being enhanced by one dimension (representing the constraint (2.1.39)). Thus, the bifurcation system is indeed given by (2.1.9).

For equilibrium surfaces, one of the controls is selected as a parameter, leaving the other two fixed. For bifurcation surfaces, one of the controls is still a parameter, but one of the remaining two controls becomes a state variable, because of the introduction of Δ in $\underline{g}$ (see (2.1.11a)). The bifurcation surfaces then are generated by a system similar to (2.1.13), viz.:

$$\dot{\underline{g}} = \frac{d\underline{g}}{ds} = \left[\frac{\partial g_i}{\partial y_j}\right]\frac{d\underline{y}}{ds} + \left(\frac{\partial \underline{g}}{\partial \delta_i}\right)\frac{d\delta}{ds} = 0 \tag{2.1.41}$$

or, in compact form,

$$\dot{\underline{g}} = G\dot{\underline{y}} + \underline{g}_\delta \dot{\delta} = 0 \tag{2.1.42}$$

As outlined in Sec. 2.1.1, Eq. (2.1.42) is solved for the (n+1) derivatives* $\dot{\underline{y}}$ (the $(n+1)^{\underline{th}}$ element of $\underline{y}$ is δ_j, as defined in (2.1.10a)), as functions of the scalar δ. This latter derivative is then determined from the arc-length normalization relationship

*In the spin flight regime, n = 8. Thus, the equilibrium system (2.1.6) is 8th order, the bifurcation system (2.1.9) is 9th order, and the matrix Γ of Sec. 2.1.2 is a (9 x 10) array.

$$\dot{\underline{y}}^T\dot{\underline{y}} + (\dot{\delta})^2 = 1 \tag{2.1.43}$$

See Sec. 2.1.1 for details.

2.1.4.2 Non-spin bifurcation considerations

In the non-spin case, $n = 5$ (gravity effects are neglected and V is assumed constant). However, even though this system is considerably smaller than the spin system (for which $n = 8$), the Γ array is of size 6×7. Furthermore, because

$$\Delta = \det(F) \tag{2.1.11b}$$

represents the $(n+1)^{\underline{th}}$ element of $\underline{g}$ (hence row $(n+1)$ of

$$G = \left[\frac{\partial g_i}{\partial y_j}\right], \tag{2.1.12}$$

there are serious computational problems to consider.

These problems center on the computation of G and the $(n+1)$-by-$(n+2)$ array

$$\Gamma = \left[G \,\vdots\, \frac{\partial \underline{g}}{\partial \delta_i}\right], \tag{2.1.44}$$

which is often more difficult than inverting the submatrix of Γ, Γ_k. For example, the bottom row of Γ, (2.1.44), is given by

$$\Gamma_{(n+1),\cdot} = \left(\frac{\partial \Delta}{\partial(\underline{y}, \delta_i)}\right)^T \tag{2.1.45}$$

where $\underline{y}$ is defined by (2.1.10a). It is of practical necessity to compute at least this row using a numerical differentiation algorithm.

Even for $n = 5$, deriving the analytic expression for Δ is excessively laborious, not to mention all of its partials; needless to say, there is no point in speculating about the $n = 8$ (spin) case.

Thus, the last row of Γ in either the spin or the non-spin case is determined by numerical differentiation. The first column element in this row, $\gamma_{(n+1),1}$ is given by $\partial\Delta/\partial p$. As described in Sec. 2.1.2, the numerical differentiation of this term involves five evaluations of $\Delta(p)$, with all other variables fixed. For each state, and the two selected controls, this must be done; altogether seven times for each of the last row elements of Γ, in the non-spin case. Thus, 35 evaluations of Δ are needed each time an evaluation of Γ is made. There can be several evaluations of Γ made for each point on the continuation solution, due to the iterative nature of the Newton-corrector steps. Every evaluation of Δ requires full evaluation of the matrix F. It is possible to do this using numerical differentiation, but there is obviously a tremendous saving in time to be had if the terms in F can be analytically derived, as well as all other elements of Γ (F is a submatrix of Γ) for which this is feasible.

Thus, the above strategy was adopted for computing Γ, both in the spin and non-spin cases; i.e., use analytic expressions for the elements γ_{ij} as far as possible, using numerical differentiation only for the last row of Γ, (2.1.45). This modification provided the opportunity to compare the precision of the numerical differentiation results with the "exact" expressions, and the numerical adequacy of the former was verified.

Another modification made to run bifurcation solutions was to evaluate

the aerodynamic coefficients only once for every point actually accepted as a solution point, and not every time Γ, or even $\underline{f}$, is evaluated. This results in considerable time savings, as the aero data for aircraft F requires interpolation routines.

The modifications discussed above, when applied to the non-spin bifurcation system, can generate almost a solution point per CPU second on the CDC 6400, an improvement by about a factor of 50 on the unmodified system.

2.1.4.3 Spin Bifurcation Surfaces

The spin bifurcation system worsens the "curse of dimensionality." In this regard, incorporating an algebraic solution for V, which reduces the basic system dimension from 8 to 7, does not help very much computationally. This is because all of the partials involving V in Γ would have to be carried along by the chain differentiation rule. V could be specified to be constant, but it is as yet unclear whether this action would obscure transition dynamics in the post-stall departure and spin entry flight regimes.

With this background, the $n = 8$ spin system was incorporated into the BACTM bifurcation package, modified as described above for the smaller, non-spin system. Numerical difficulties were encountered immediately, which centered around the Newton-Raphson iteration algorithm.* More specifically, the problem lies with the Newton corrector step, computed by the relation

$$\Delta\underline{y}^{(k)} = (\underline{y}^{(k+1)} - \underline{y}^{(k)}) = -G^{-1}\underline{g}(\underline{y}^{(k)}), \qquad (2.1.46)$$

*These difficulties were present as well when a scaled velocity, $\eta \triangleq V/V_{scale}$ was introduced. V_{scale} was given a value which put η in the range of values of the other variables, all of which are in radian units.

where

$$\underline{y} = (p,q,r,\alpha,\beta,V,\theta,\phi,\delta_j)^T \triangleq (\underline{x},\delta_j)^T \tag{2.1.10a}$$

$$\underline{g} \triangleq \underline{g}(\underline{y},\delta_i) = \begin{pmatrix} \underline{f}(\underline{x},\delta_i) \\ \Delta \end{pmatrix} \tag{2.1.11a}$$

and

$$\Delta \triangleq \det\left(\left[\frac{\partial f_i}{\partial x_j}\right]\right) = \det\,(F) \tag{2.1.11b}$$

(In the continuation process employed by BACTM, the Newton-Raphson algorithm itself is considered a Corrector, as it refines the approximation $\underline{g} \simeq 0$ iteratively. The Prediction step is made by the Adams-Bashforth multistep method.) The algorithm above works quite well for all of the BACTM systems except the spin bifurcation system. In this case, if $\varepsilon^{(k)}$ is defined as

$$\varepsilon^{(k)} \triangleq \|\underline{g}(\underline{y}^{(k)},\delta_i)\| \tag{2.1.47}$$

where $\underline{y}^{(k)}$ is the $k^{\underline{th}}$ Newton iterate at a (predicted) point designated by (δ_i,δ_j); then, it typically happens that

$$\varepsilon^{(k+1)} > \varepsilon^{(k)} \tag{2.1.48}$$

for the spin system. Worse, this happens over a range of k values, so that the sequence $\{\Delta\underline{y}^{(k)}\}$ becomes "unstable" with respect to the iteration. If a solution $\underline{g} \simeq 0$ is found under these conditions, it invariably

is at a point far removed from the regime of interest.

By the nature of the Newton algorithm, assuming $\underline{g} \in C^1$, the class of functions continuous in all first derivatives, there exists a region R centered on $\underline{y}^{(k)}$ such that

$$\varepsilon^* < \varepsilon^{(k)} \tag{2.1.49}$$

where the stepsize producing ε^* relates to $\Delta\underline{y}^{(k)}$ by

$$\Delta\underline{y}^* = \rho^{(k)}_{\circ} \Delta\underline{y}^{(k)} \tag{2.1.50}$$

where $\rho^{(k)} \in (0,1]$ is a Euclidean metric between two points in R. Basically, this says that if one cuts back sufficiently on the step size as given by Eq. (2.1.46), then one will eventually find a step size (2.1.50) for which (2.1.49) holds, if $\underline{g}$ is "sufficiently smooth."*

The above represents an aspect of one general approach to the basic goal of ensuring a decreasing sequence $\{\varepsilon^{(k)}\}$; that is, the one-dimensional search algorithm. These methods accept the minimizing direction as computed by (2.1.46), even though it uses only first order information. Then, a scalar one-dimensional search is made along this direction for a point, $\underline{y}^*$, which is "minimizing." Several algorithms exist, and two have been implemented. The first of these merely halves $\Delta\underline{y}^{(k)}$, evaluates $\underline{g}$ at that point, compares its norm to $\varepsilon^{(k)}$, and halves the stepsize again, continuing until either $\varepsilon^* < \varepsilon^{(k)}$ or $\|\Delta\underline{y}\| < 10^{-12}$. The latter condition indicates either that $\underline{g}$ is not continuous at $\underline{y}^{(k)}$, or that the first order information at that point is inadequate. This algorithm was successful in some regions, but less so in others, even with

*This is easy to see geometrically if one constructs a scalar system from Eq. (2.1.46).

modifications such as permitting (2.1.48) up to three consecutive times.

Another one-dimensional algorithm which was implemented involves considering only the segment along the direction $\Delta\underline{y}^{(k)}$ between the points $\underline{y}^{(k)}$ and $(\underline{y}^{(k)}+\Delta\underline{y}^{(k)})$. If one defines a scalar arclength parameter σ such that $\underline{y}(\sigma = 0) = \underline{y}^{(k)}$ and $\underline{y}(\sigma = 1) = \underline{y}^{(k+1)}$, then it is possible to construct a cubic polynomial in σ using only previously computed quantities: $\underline{g}(\underline{y}^{(k)})$, $G(\underline{y}^{(k)})$ and $\underline{g}(\underline{y}^{(k+1)})$. The cubic is then assumed to approximate the function ε in this interval, and its minimum value should be close to the function minimum. This method has fared little better than the first one mentioned, but is has not been tested completely. A combination of the above two algorithms is also being considered.

Other algorithms under consideration, but as yet not implemented, include one-dimensional search and a least squares method based on stepwise regression. The latter is useful especially if G is nearly singular. If singularity problems arise, the method of stepwise regression may be employed, as it eliminates variables so that $\underline{g}$ is better parameterized. The remaining variables are those which "do the most good" in reducing ε, or $\varepsilon^2 = ||\underline{g}||^2$. Stepwise regression can deal with nonlinear formulations and bounded spaces.

Another general approach which shows great promise, but is yet to be tested, involves derivative-free algorithms. In these, the Newton approach is forsaken entirely in favor of methods which rely only on the evaluation of $\underline{g}(\underline{y})$. By the proper sequence of (n+1) such evaluations, a secant plane in n-space may be constructed. At each iteration, the use of this plane along with the "optimality criterion"--i.e., minimizing

the distance between a point in this plane and the desired point--provides information for replacing one of the (n+1) $\underline{y}$-points with a new point. Then, the new set of (n+1) points defines a new secant plane which improves the optimality criterion. In a convergent sequence, the secant plane iterates in the limit to the tangent plant which contacts the function $\underline{g}$ at $\underline{y}^*$, such that $\underline{g}(\underline{y}^*) = 0$, the desired solution. Ralston (1975) and Ralston and Jennrich (1978) discuss a specific derivative-free algorithm (D.U.D.--doesn't use derivatives) which holds some promise for our applications.

CHAPTER III

BACTM Applied to the Study of Aircraft F Stall-Spin Behavior

This chapter describes in detail the aircraft model, designated Aircraft F, which is used in this report for the study of high-α, post-stall and spin motions. Also discussed in detail are descriptions of stall and spin behavior; the nature of spin and stall; the dynamic equations which describe the above motions; the aerodynamic data for aircraft F; and BACTM results for aircraft F in spin entry. stalling maneuvers, wing rock, post-stall gyrations, developed spin motion, and spin recovery. An explanation of the spin behavior of aircraft F completes the chapter.

3.1 Nature of Aircraft Stall and Spin Behavior

In this section a brief overview will be presented to provide some insight into the physical phenomena of aircraft stall and spin. Briefly, an aircraft encounters a stall condition when loss of lift occurs due to excessive buildup of angle-of-attack (α). High performance aircraft are particularly susceptible to this phenomenon if only because their design goal is to operate near the extremes of the flight envelope in accomplishing mission objectives. Stall and spin are related because post-stall behavior can include departure into spin conditions. Since, as will be shown in this report, spin motions can be stable equilibria, it is important to understand enough about spin phenomena to be able to effect recovery control sequences which transfer the aircraft state from the domain of attraction of spin equilibrium points into the domain of

attraction of nonspin stable equilibrium points.

3.1.1 Nature and Characteristics of Spin

For most aircraft, high angle-of-attack departures from stall quite often proceed to entry into one of several spin modes. Whether a spin condition is achieved, and if so, which one, depends to a great extent on the particular aircraft configuration and control settings, as well as the flight condition. In general, the spin modes are characterized by the incidence angle (angle of attack), α. A typical classification of "erect" spin modes has five categories (Rutan, et al. (1970)):

(1) Steep - Smooth

(2) Steep - Mild Oscillation

(3) Steep - Oscillatory

(4) High-α - Highly oscillatory

(5) Flat

For certain configurations, "inverted" spin is possible, but this particular phenomenon has not been investigated in this report. Other investigators, e.g., Adams (1972) and Young (1974), classify erect spin as steep, intermediate, or flat, and oscillatory or steady. At any rate, the higher the equilibrium angle of attack is, the flatter the spin. Typical values of α during a fully developed spin, derived from a study of F-4 behavior (Adams 1972), are $\alpha \approx 80° - 85°$ for a flat spin, $\approx 72°, 73°$ for an intermediate spin, and $\approx 45° - 60°$ for a steep spin.

There are basic characteristics of spin motion common to all of the spin modes defined above:

(i) The angle of attack remains greater than the stall angle of attack (α_{STALL});

(ii) the center-of-mass follows a helical path, with the net velocity being almost totally vertical and constant sink rate;

(iii) the aircraft attitude changes at a steady rate (of magnitude ω), and the axis of rotation is almost totally vertical.

In the development of the equations for analyzing developed, or equilibrium, spin, the above characteristics will be incorporated as dynamic constraints. Other assumptions, such as constant speed (V), will be discussed later. The visual cue for a spin is excessive and continuous yaw rate.

The fully-developed, or equilibrium, spin is often achieved after only a few rotations. Once the spin is established, the trajectory is essentially vertical. In this situation, equilibrium is a result of a balance of the aerodynamic (decomposed into lift and drag), gravity and the centrifugal forces (the latter arising from the helical motion). The drag vector opposes the velocity, and so is largely vertical; hence, the lift vector tends to lie in the horizontal plane, and the radius of the helix, R, adjusts until the resultant centrifugal term, $\omega^2 R$, balances the lift term. During an established spin, the presence of non-zero sideslip, β, is quite often prominent in the generation of the coupling moments which maintain the equilibrium spin. These particular moments are usually affected by the rudder setting.

When an aircraft enters a spin from a basically straight and level flight condition, the center of gravity follows a path that initially was horizontal, but changes to a vertical spiral. Such a significant change in flight condition, caused basically by entry into a stall region, is bound to produce at least transient oscillatory behavior in p,q,r, the rotation rates about the vehicle roll, pitch and yaw axes, respectively.

Generally, such oscillations dissipate before one or two spin revolutions have occurred; however, in some instances, these oscillations may grow in amplitude. Characteristic of such oscillatory spins is the large change of aircraft attitude with respect to the horizon as roll rate p oscillates (Kerr (1956)). The oscillations may cause the motion to change from a spin to a post-stall gyration, in which rolling motion is prominent.

We have devoted the bulk of our spin analysis efforts in this report to the study of spin behavior when the aircraft is in flat spin situations. This is primarily because flat spins have tended to be the most troublesome ones, in that recovery from them is usually very difficult to achieve. This is because much of the spin equilibrium regime is stable, which requires active control for recovery. Aircraft susceptible to post-stall entry into flat spins tend to have such characteristics as lengthened fuselage forebodies, increased relative distribution of mass in the fuselage, and wings with short span. The design ideal is that the aircraft equilibrium be unstable in flat spin over as wide a control regime as possible, so that recovery from flat spin is easy.

3.1.2 Nature and Characteristics of Stall

Stall is the condition of dramatic loss of lift due to a change in the operating state of the aircraft. Stall entry is typically a longitudinal phenomenon, in that application of elevator will cause angle-of-attack to grow excessively. Lift is proportional to angle-of-attack until a value for α is reached, α_{STALL}, at which flow separation around the wings occurs. The wake becomes turbulent, lifting capacity is sharply reduced, and the aircraft is said to have stalled. Stall, then, is a major phenomenon of high-α flight. Often, pre-stall buffeting or wing rock

warn the pilot, though not always in time. Subsequent to stall, depending on the state of the aircraft, there may be post-stall departure into spin, roll departure, or autorotation; all of these are undesirable motions, particularly spin, which can be an equilibrium state, structurally stable over the available range of control values.

The pilot generally has to assume active control of the vehicle once the aircraft has stalled, and there may be extreme conditions which only an autopilot can deal with. In any event, one of the main goals of aircraft and flight control system design is to extend the operational flight regime as much as possible by avoiding stall situations, and to provide the pilot with adequate warning when he is about to encounter stall.

3.2 Spin Equations of Motion, Assumptions, Constraints

The equations of motion which adequately model spin behavior require both the full set of coupled nonlinear terms and a data base for the aerodynamic coefficients which is comprehensive enough to include regimes in which spins occur. In the equations that follow, engine thrust and gyroscopic terms are not included. The role of engine thrust in spin entry and recovery dynamics will be studied in subsequent projects. Previous work (Grafton 1966, Lusby 1961) has shown these effects to be small;* furthermore, the greatly reduced airflow along the longitudinal axis may cause serious engine damage, erratic thrust behavior, and flameouts. Finally, the variation of atmospheric density ρ with altitude h is neglected, so that dynamic pressure $\bar{q}$ is a function only of airspeed V. The basic equations, then, are:

$$\dot{\alpha} = q + \left[-\left(\frac{\bar{q}S}{mV} C_x - \frac{g}{V} \sin\theta + r \sin\beta \right) \sin\alpha + \left(\frac{\bar{q}S}{mV} C_z + \frac{g}{V} \cos\theta \cos\phi - p \sin\beta \right) \cos\alpha \right] \sec\beta \tag{3.2.1}$$

$$\dot{\beta} = -\left[\left(\frac{\bar{q}S}{mV} C_x - \frac{g}{V} \sin\theta \right) \sin\beta + r \right] \cos\alpha + \left(\frac{\bar{q}S}{mV} C_y + \frac{g}{V} \cos\theta \sin\phi \right) \cos\beta - \left[\left(\frac{\bar{q}S}{mV} C_z + \frac{g}{V} \cos\theta \cos\phi \right) \sin\beta - p \right] \sin\alpha \tag{3.2.2}$$

$$\left(\frac{\dot{V}}{V} \right) = \left(\frac{\bar{q}S}{mV} C_x - \frac{g}{V} \sin\theta \right) \cos\alpha \cos\beta + \left(\frac{\bar{q}S}{mV} C_y + \frac{g}{V} \cos\theta \sin\phi \right) \sin\beta + \left(\frac{\bar{q}S}{mV} C_z + \frac{g}{V} \cos\theta \cos\phi \right) \sin\alpha \cos\beta \tag{3.2.3}$$

*However, thrust seems to play a prominent role in spin entry dynamics. See Sec. 3.3.

$$\dot{p} = \left[-\left(\frac{I_z - I_y}{I_x} + \frac{I_{xz}^2}{I_x I_z} \right) qr + \left(1 - \frac{I_y - I_x}{I_z} \right) \frac{I_{xz}}{I_x} pq + \frac{\bar{q}Sb}{I_x} \left(C_\ell + \frac{I_{xz}}{I_z} C_n \right) \right] \Bigg/ \left[1 - \frac{I_{xz}^2}{I_x I_z} \right] \tag{3.2.4}$$

$$\dot{q} = \frac{\bar{q}S\bar{c}}{I_y} C_m + \frac{I_z - I_x}{I_y} pr + \frac{I_{xz}}{I_y} \left(r^2 - p^2 \right) \tag{3.2.5}$$

$$\dot{r} = \left[\left(\frac{I_{xz}^2}{I_x I_z} - \frac{I_y - I_x}{I_z} \right) pq - \left(1 + \frac{I_z - I_y}{I_x} \right) \frac{I_{xz}}{I_z} qr + \frac{\bar{q}Sb}{I_z} \left(\frac{I_{xz}}{I_x} C_\ell + C_n \right) \right] \Bigg/ \left[1 - \frac{I_{xz}^2}{I_x I_z} \right] \tag{3.2.6}$$

These equations are derived principally from Adams (1972), but some of the terms in the expansion of the force-moment coefficients were added from other sources (Moore, Anglin (1971) and Brady (1969)). Notation is presented in Appendix A.

The following kinematical relationships are needed to fully describe the motion:

$$\dot{\theta} = q \cos\phi - r \sin\phi \tag{3.2.7}$$

$$\dot{\phi} = p + q \tan\theta \sin\phi + r \tan\theta \cos\phi \tag{3.2.8}$$

$$\dot{\psi} = q \sin\phi \sec\theta + r \cos\phi \sec\theta \tag{3.2.9}$$

$$\dot{R} = V_x^I \cos\eta + V_y^I \sin\eta \tag{3.2.10}$$

$$\dot{R\eta} = -V_x^I \sin\eta + V_y^I \cos\eta \tag{3.2.11}$$

$$\dot{h} = V_z^I \tag{3.2.12}$$

where

$$V_x^I = V[\cos\alpha\cos\beta\cos\psi\cos\theta + \sin\alpha(\cos\psi\sin\theta\sin\phi - \sin\psi\cos\phi) + \sin\alpha\cos\beta(\cos\psi\sin\theta\cos\phi + \sin\psi\sin\phi)] \quad (3.2.13a)$$

$$V_y^I = V[\cos\alpha\cos\beta\sin\psi\cos\theta + \sin\alpha(\sin\psi\sin\theta\sin\phi + \cos\psi\cos\phi) + \sin\alpha\cos\beta(\sin\psi\sin\theta\cos\phi - \cos\psi\sin\phi)] \quad (3.2.13b)$$

$$V_z^I = V[-\cos\alpha\cos\beta\sin\theta + \sin\alpha\cos\theta\sin\phi + \sin\alpha\cos\beta\cos\theta\cos\phi] \quad (3.2.13c)$$

In Eqs. (3.2.1) to (3.2.6) the aerodynamic coefficients are expanded as follows:

$$C_x = C_x(\alpha,\beta,\underline{\delta}=0) + C_{x_{\delta e}}(\alpha,\beta)\delta e \quad (3.2.14a)$$

$$C_y = C_y(\alpha,\beta,\underline{\delta}=0) + C_{y_{\delta e}}(\alpha,\beta)\delta e + C_{y_{\delta a}}(\alpha,\beta)\delta a + C_{y_{\delta r}}(\alpha,\beta)\delta r + \left(\frac{b}{2V}\right)\left[C_{y_p}(\alpha)p + C_{y_r}(\alpha)r\right] \quad (3.2.14b)$$

$$C_z = C_z(\alpha,\beta,\underline{\delta}=0) + C_{z_{\delta e}}(\alpha,\beta)\delta e \quad (3.2.14c)$$

$$C_\ell = C_\ell(\alpha,\beta,\underline{\delta}=0) + C_{\ell_{\delta e}}(\alpha,\beta)\delta e + C_{\ell_{\delta a}}(\alpha,\beta)\delta a + C_{\ell_{\delta r}}(\alpha,\beta)\delta r + \left(\frac{b}{2V}\right)\left[C_{\ell_p}(\alpha)p + C_{\ell_r}(\alpha)r\right] \quad (3.2.14d)$$

$$C_m = C_m(\alpha,\beta,\underline{\delta}=0) + C_{m_{\delta e}}(\alpha,\beta)\delta e + \left(\frac{\bar{c}}{2V}\right)C_{m_q}(\alpha)q \quad (3.2.14e)$$

$$C_n = C_n(\alpha,\beta,\underline{\delta}=0) + C_{n_{\delta e}}(\alpha,\beta)\delta e + C_{n_{\delta a}}(\alpha,\beta)\delta a + C_{n_{\delta r}}(\alpha,\beta)\delta r$$
$$+\left(\frac{b}{2V}\right)\left[C_{n_p}(\alpha)p + C_{n_r}(\alpha)r\right] \qquad (3.2.14f)$$

The above system, Eqs. (3.2.1) - (3.2.12), allows a complete time history for general motion of the aircraft. Note that Eqs. (3.2.1) - (3.2.8) are a self-contained sub-system, not requiring information from Eqs. (3.2.9) - (3.2.12); the converse is not true.

We shall now digress a bit to discuss how the equilibrium system used by BACTM is developed from the dynamic system of equations. By "equilibrium" is meant dynamic equilibrium. That is, we are seeking all sets of points $(\underline{x},\underline{\delta})$ for which $\underline{f}(\underline{x},\underline{\delta}) = 0$. Here, the elements of the vector $\underline{f}$ consist of the right-hand terms in Eqs. (3.2.1) - (3.2.8), for one system; the elements of the vector $\underline{x}$ are $(p,q,r,\alpha,\beta,V,\theta,\phi)$, for that system; and the elements of $\underline{\delta}$ are $(\delta a,\delta e,\delta r)$. At $\underline{f} = 0$, of course, all time derivatives of $\underline{x}$ are zero, so that p,q,r, etc., have fixed values. This is dynamic equilibrium. There remains the very important issue of classifying the equilibrium points. First, some definitions: A <u>stable</u> equilibrium point is one in which motions originating at some point in the neighborhood of the equilibrium point $\bar{\underline{y}} \triangleq (\bar{\underline{x}},\bar{\underline{\delta}})$, ultimately return to $\bar{\underline{y}}$; an <u>unstable</u> equilibrium point is one in which any motion beginning at a non-equilibrium point near $\bar{\underline{y}}$ will ultimately diverge from $\bar{\underline{y}}$. All equilibria for linear systems, $\dot{\underline{x}} = F\underline{x} + G\underline{\delta}$, are either stable or unstable. For nonlinear systems, such as we are dealing with here, motions not only may either converge or diverge asymptotically, but also may develop into <u>limit cycles</u>. This is

a motion in which the time solution $\underline{x}(\underline{\delta};t)$, also referred to as an orbit or trajectory, returns at some time $(t+T)$ to its value at t, where T is fixed. Depending on its amplitude, frequency, and other issues (some of them probably subjective), a limit cycle may or may not be considered a stable motion. There are other points to emphasize, however. First, limit cycles themselves are stable or unstable, in the same sense that equilibrium points, or curves, are; that is, motions starting near a stable limit cycle ultimately end on it, and conversely for unstable limit cycles. Second, a point on a stable limit cycle is <u>not</u> an equilibrium point, because $\dot{\underline{x}} \neq 0$.

Equilibrium points are classified typically by investigating the first order term* in the power series (e.g., Taylor) expansion of $\underline{f}(\underline{x},\underline{\delta})$, evaluated at $\bar{\underline{y}}$. By the nature of nonlinear systems, then, the validity of the stability classification is restricted to those regions centered on $\bar{\underline{y}}$ where the zeroth and first order terms of the expansion of $\underline{f}$ are almost equal to $\underline{f}$ itself. (This comment has particular relevance to limit cycle motions.) Specifically, the eigenvalues of the Jacobian matrix, F or $\partial\underline{f}(\underline{x},\underline{\delta})/\partial\underline{x}$, evaluated at $\bar{\underline{y}} = (\bar{\underline{x}},\bar{\underline{\delta}})$, are used to classify the equilibrium point. For the eighth-order dynamic system (3.2.1) - (3.2.8), F is 8×8, and yields eight eigenvalues. If all of these have negative real parts (any complex eigenvalue has a conjugate mate, as all coefficients in the equation $\dot{\underline{x}} = F\underline{x}$ are real) at $\bar{\underline{y}}$, that equilibrium point is stable; if one or more has a positive real part, the equilibrium is unstable. As alluded to above, this classification, depending as it does only on linear analysis, cannot provide quantitative information about limit cycles

*It can be proven that first order analysis is sufficient for accurate classification of "nice" nonlinear functions if done in a region close to the point about which the expansion is done.

(we are developing for BACTM, however, a novel approach for quantitative analysis of limit cycles, using continuation methods. This will be described in more detail later). In a region where limit cycle behavior exists, the "governing" equilibrium branch will be unstable, typically possessing one very lightly damped complex pair of eigenvalues (i.e., real part close to zero, but positive); the others have negative real parts. Thus, when the (linear) eigenanalysis shows a lightly damped complex pair, all we can say is that limit cycle motion is expected in the region. We cannot quantify the limit cycle (e.g., amplitude, period, stable or unstable, etc.) without further analysis. The equilibrium point which indicates limit cycle motion is actually an unstable one, and this is in fact true in a "local" sense (that is, in the region about $\bar{y}$ where the linear approximation to $\underline{f}$ is valid). Motions starting near such a point diverge; however, once their amplitudes are large enough so that nonlinear influences are greater, a limit cycle may result. If this happens, the global motion is stable, and is the asymptotic limit of motions emanating near the locally unstable equilibrium point. Such a limit cycle is a stable attractor, and we have seen many examples of these (see Mehra et al., 1977). Unstable limit cycles do play an important role as well, but their quantification is considerably more difficult than that of stable limit cycles. Global bifurcations deal with the annihilation of stable limit cycles by unstable ones, as system parameters (e.g., control settings) change.

In summary, then, equilibrium points may be stable or unstable. For a certain type of unstable point, the one with one unstable complex pair

of eigenvalues, limit cycle notion may result, but not locally. Motion is locally divergent from all unstable points and locally convergent to all stable points.

We return now to the aircraft spin equilibrium system. In order to find the spin equilibrium points, two extra conditions are needed:

i) an equilibrium is specified a priori by the requirement

$$\begin{bmatrix} \dot{p} \\ \dot{q} \\ \dot{r} \\ \dot{\alpha} \\ \dot{\beta} \\ \dot{V} \end{bmatrix} = 0$$

This result is derived from the equilibrium requirement for constant angular velocity and steady helical motion.

ii) the spin characteristics are specified as dynamical constraints, to be incorporated in the system Eqs. (3.2.1) - (3.2.12). These constraints are:

$$h = h^*, \text{ a specified constant;} \tag{3.2.15}$$

this decouples the $\dot{h}$ equation and lets $\bar{q} = \bar{q}(V)$ only.

$$\underline{\omega} = \dot{\psi}\hat{\underline{z}}^I \tag{3.2.16}$$

where $\underline{\omega}$ represents the total angular velocity of the aircraft;

$$\psi(t^*) = 0 \tag{3.2.17}$$

where t* is the time at which the equilibrium solution is made. This relationship results in no loss of generality, because of the natural decoupling of ψ from the basic dynamical system, Eqs. (3.2.1) - (3.2.8). Finally,

$$\underline{V} = R\dot{\psi}\hat{\underline{T}} - \dot{h}\hat{\underline{z}}^I \tag{3.2.18}$$

where $\hat{\underline{T}}$ is the unit vector in the direction tangent to the trajectory, and $\hat{\underline{z}}^I$ is the locally vertical unit vector. This is the constraint for helical motion. It leads to the relationships

$$\begin{aligned} &\underline{V} \cdot \hat{\underline{R}} = 0 \\ &R = \frac{V_H}{|\dot{\psi}|}, \quad V_H = \sqrt{V_x^{I^2} + V_y^{I^2}} \\ &\dot{\eta} = \dot{\psi} \end{aligned} \tag{3.2.19}$$

In (3.2.19), V_H is the magnitude of the horizontal component of velocity, and $\dot{\psi}$ is the heading rate. When constraints (3.2.15) - (3.2.17) are incorporated into the full dynamic system of equations, the system reduces to a five-dimensional set of nonlinear algebraic equations for the equilibrium points in the state space. Before presenting this equilibrium system, a few consequences of incorporating the constraints will be detailed.*

The requirement $\dot{V} = 0$ allows for the direct algebraic solution of V as a function of $(\alpha,\beta,\delta,p,r,\theta,\phi)$, using Eq. (3.2.3). Specifically, V is the solution of a quadratic equation. Condition (3.2.16) results in the identities

*Later, we will show an eighth order spin equilibrium which was actually used for the numerical solutions. This system was used because it is less configuration-dependent and because the continuation algorithms developed for BACTM (Ch. II) can efficiently handle large order systems.

$$\begin{aligned}
\dot{\phi} &= 0 \\
\dot{\theta} &= 0 \\
\dot{\psi} &= \omega \\
p &= -\omega \sin\theta \\
q &= \omega \cos\theta \sin\phi \\
r &= \omega \cos\theta \cos\phi
\end{aligned} \tag{3.2.20}$$

Considering the last three of these identities, it is seen that a new state variable, ω, has been defined, replacing the set (p,q,r), for a net reduction of two in the order of the system. Also recall that the time rate of change of the Euler angles $(\dot{\psi},\dot{\theta},\dot{\phi})$ is not an orthogonal set. This is <u>not</u> true of the roll, pitch, and yaw rates (p,q,r), which are orthogonal body axis components of the total aircraft angular velocity vector, $\underline{\omega}$. As vector components, $(\dot{\psi},\dot{\theta},\dot{\phi})$ do add up to $\underline{\omega}$ also, but only in special cases may $\dot{\psi}$ be associated with yaw rate, $\dot{\theta}$ with pitch rate, and so on. This means, as (3.2.20) shows, that all Euler angle rates but $\dot{\psi}$ may be zero, yet because of projections, all of (p,q,r) are nonzero. The reader needing further amplification of this aspect of aircraft kinematics is referred to an appropriate text covering kinematics, e.g., Goldstein (1950), and in particular, Etkin (1972).

The equilibrium system of equations is:

$$\begin{aligned}
0 = \dot{\alpha} = \omega \sin\phi\cos\theta + [&-\sin\alpha(F_1 C_x - \frac{q}{V}\sin\theta + \omega \cos\theta\cos\phi\sin\beta) \\
&+ \cos\alpha(F_1 C_z + \frac{q}{V}\cos\theta\cos\phi + \omega \sin\theta\sin\beta)]\sec\beta
\end{aligned} \tag{3.2.21}$$

$$0 = \dot{\beta} = -[\sin\beta(F_1 C_x - \frac{g}{V}\sin\theta) + \omega\cos\theta\cos\phi]\cos\alpha + \cos\beta(F_1 C_y + \frac{g}{V}\cos\theta\sin\phi) - [\sin\beta(F_1 C_z + \frac{g}{V}\cos\theta\cos\phi) + \omega\sin\theta]\sin\alpha \tag{3.2.22}$$

$$0 = (\cos\theta\cos\phi\dot{\omega}) = \frac{1}{F_9}\left[-\left(F_8 - \frac{I_y - I_x}{I_z}\right)\omega^2\sin\theta\cos\theta\sin\phi - \left(1 + \frac{I_z - I_y}{I_x}\right)F_6\,\omega^2\cos^2\theta\sin\phi\cos\phi + b\,F_4(F_5 C_\ell + C_n)\right] \tag{3.2.23}$$

$$0 = (-\sin\theta\dot{\omega}) = \frac{1}{F_9}\left[-\omega^2\cos\theta\sin\phi\cos\phi\left(F_8 + \frac{I_z - I_y}{I_x}\right) + \omega^2 F_5\left(1 - \frac{I_y - I_x}{I_z}\right) - \sin\theta\cos\theta\sin\phi + b\,F_2(C_\ell + F_6 C_n)\right] \tag{3.2.24}$$

$$0 = (\cos\theta\sin\phi\dot{\omega}) = \bar{c}\,F_3\,C_m + \omega^2\left[F_7(\cos^2\theta\cos^2\phi - \sin^2\theta) - \frac{(I_z - I_x)}{I_y}\sin\theta\cos\theta\cos\phi\right] \tag{3.2.25}$$

The system of Eqs. (3.2.17) - (3.2.21) may be compactly expressed as

$$\underline{f}(\underline{x},\underline{\delta}) = 0 \tag{3.2.26}$$

where

$$\underline{x} = (\alpha,\beta,\omega,\theta,\phi) \tag{3.2.27}$$

In the above system, the following identities are introduced

$$F_1 = \frac{\rho V S}{2m} \qquad F_6 = \frac{I_{xz}}{I_z}$$

$$F_2 = \frac{\rho V^2 S}{2I_x} \qquad F_7 = \frac{I_{xz}}{I_y}$$

$$F_3 = \frac{\rho V^2 S}{2I_y} \qquad F_8 = F_5 F_6 \qquad (3.2.28)$$

$$F_4 = \frac{\rho V^2 S}{2I_z} \qquad F_9 = 1 - F_8$$

$$F_{10} = \frac{b}{2V}$$

$$F_5 = \frac{I_{xz}}{I_x} \qquad F_{11} = \frac{\bar{c}}{2V}$$

Note the presence of V in the F_i. This requires, then, the introduction of the quadratic expression for V into the system, which is usually no problem for solution procedures which are iterative in nature, given a starting point. When the system is solved for the equilibrium values $(\bar{\alpha},\bar{\beta},\bar{\omega},\bar{\theta},\bar{\phi})$, and $\bar{V}$, then other quantities, such as $\bar{R}$, may be found:

$$\bar{R} = \frac{\bar{V}}{\bar{\omega}} [\sin\bar{\alpha}(\cos\bar{\phi} - \cos\bar{\beta}\sin\bar{\phi})]$$

It is worthwhile also to monitor, at the equilibrium solution points, the following parameters, which have been found by experimenters to be useful in detecting departure into spin:

Directional Departure Parameter

$$C_{n_{\beta_{DYN}}} = C_{n_\beta}\cos\alpha - \frac{I_z}{I_x} C_{\ell_\beta}\sin\alpha \qquad (3.2.29)$$

Lateral Control Directional Parameter

$$LCDP = C_{n_\beta} - C_{\ell_\beta}\left[\frac{C_{n_{\delta a}} + K C_{m_{\delta r}}}{C_{\ell_{\delta a}} + K C_{\ell_{\delta r}}}\right] \qquad (3.2.30)$$

where $K = \frac{\delta r}{\delta a}$.

Both $C_{n_{\beta_{DYN}}}$ and LCDP should be positive for stable motion. However, they were originally intended to compensate for the dynamic, or forced oscillation, derivatives. Therefore, when more complete aero data bases are utilized, parameters such as $C_{n_{\beta_{DYN}}}$ and LCDP may lose some significance. They are, in essence, a preliminary design tool. Other derivatives such as C_{n_β} and C_{m_β} may be interesting, and it is certainly of interest to verify that

$$\bar{\alpha} > \alpha_{STALL}.$$

Because of the improved methodology developed during the project, it has become possible to use a somewhat more general set of dynamic equations for the study of spin behavior. This set is an eighth order system, and it has the advantage of flexibility and ease in terms of deriving the elements of the system Jacobian matrix analytically. This system consists of Eq. (3.2.1) - (3.2.6) as well as the kinematic relations (3.2.7) and (3.2.8), and has been coded directly. By reasonable choice of initial conditions, the solution of this set either for time history trajectories or for equilibrium surfaces will automatically incorporate the constraint relationships (3.2.15) - (3.2.17).

Additionally, a second set of velocity state variables is used when time history solutions are generated. This set uses the body-axis components of $\underline{V}$, namely (u,v,w), as state variables instead of the set (V,α,β) which is defined by Eqs. (3.2.1) - (3.2.3). The set (V,α,β) is the wind-axis velocity state and the set (u,v,w) is the body-axis velocity state,

whose dynamical relations are given by:

$$\dot{u} = -g \sin\theta + vr - wq + \frac{\bar{q}S}{m} C_x \tag{3.2.31}$$

$$\dot{v} = g \cos\theta\sin\phi + wp - ur + \frac{\bar{q}S}{m} C_y \tag{3.2.32}$$

$$\dot{w} = g \cos\theta\cos\phi + uq - vp + \frac{\bar{q}S}{m} C_z \tag{3.2.33}$$

where C_x, C_y, C_z are the total aero force coefficients along the aircraft x-, y- and z-axes. An auxiliary set of relations enables computation of variables of importance:

$$\alpha = \tan^{-1}(w/u) \tag{3.2.34}$$

$$\beta = \sin^{-1}(v/V) \tag{3.2.35}$$

$$V = \sqrt{u^2 + v^2 + w^2} \tag{3.2.36}$$

The use of the body-axis set is disadvantageous in that the aerodynamic coefficients are functions of α and β, so that (3.2.34) and (3.2.35) must be carried along. However, with this set, and with the equation for heading angle (also the yaw angle in a yaw-pitch-roll inertial-to-body Euler transformation sequence)--Eq. (3.2.9)--several kinematic and dynamic variables of interest in the force-moment equations may be generated rather easily. Also, this set is "cleaner" in form than the wind-axis set, as it avoids the transcendental terms in α and β which represent the body-to-wind axis transformation.

Some more terms which are worth monitoring in the study of stall and spin behavior include

$$\text{TURNS} = \frac{1}{2\pi}\int_{t_0}^{t_f} \dot{\psi}\, dt \tag{3.2.37}$$

$$E = \tfrac{1}{2}\, mV^2 + \tfrac{1}{2}\, \underline{\omega}\cdot\underline{I}\cdot\underline{\omega} \tag{3.2.38}$$

$$\dot{E} = mV\dot{V} + I_x p\dot{p} + I_y q\dot{q} + I_z r\dot{r} \tag{3.2.39}$$

where

$$\dot{V} = (u\dot{u} + v\dot{v} + w\dot{w})/V \tag{3.2.40}$$

if the body-axis velocity set is used

$$\omega = \sqrt{p^2 + q^2 + r^2} \tag{3.2.41}$$

$$V_{VERT} = -u\sin\theta + (v\sin\phi + w\cos\phi)\cos\theta, \tag{3.2.42}$$

positive downward,

$$V_{NORTH} = \cos\psi[u\cos\theta + (v\sin\phi + w\cos\phi)\sin\theta] - \sin\psi(v\cos\phi - w\sin\phi) \tag{3.2.43}$$

$$V_{EAST} = \sin\psi[u\cos\theta + (v\sin\phi + w\cos\phi)\sin\theta] + \cos\psi(v\cos\phi - w\sin\phi) \tag{3.2.44}$$

$$h = h_0 - \int_{t_0}^{t_f} V_{VERT}\, dt \tag{3.2.45}$$

$$x_{NORTH} = x_{NORTH_0} + \int_{t_0}^{t_f} V_{NORTH}\, dt \tag{3.2.46}$$

$$y_{EAST} = y_{EAST_0} + \int_{t_0}^{t_f} V_{EAST}\, dt \tag{3.2.47}$$

$$E_s = \tfrac{1}{2}\, I_v\dot{\psi}^2/(\bar{q}Sb) \tag{3.2.48}$$

where

$$I_v = \sin^2\theta I_x + (\sin^2\phi I_y + \cos^2\phi I_z)\cos^2\theta + I_{xz}\cos\phi\sin 2\theta \qquad (3.2.49)$$

(when $I_{xy} = I_{yz} = 0$)

$$D_{SPIN} = \left[\sum_{i=1}^{n}\left[\frac{x_i - x_{s_i}}{x_{s_i}}\right]^2\right]^{\frac{1}{2}} \qquad (3.2.50)$$

E is a scalar quantity representing total vehicle kinetic energy (assuming a purely rigid body); the first term is due to translational (center of mass) motion, and the second represents the rotational contribution. Here, $\underline{I}$ is the moment of inertia tensor, written as a square 3×3 matrix; thus, pre- and post-multiplication of $\underline{I}$ by the angular velocity vector $\underline{\omega} = (p,q,r)$ results in the scalar quantity (assuming that the off-diagonal terms of $\underline{I}$, I_{xy}, I_{xz}, and I_{yz}, are zero)

$$\tfrac{1}{2}\underline{\omega}\cdot\underline{I}\cdot\underline{\omega} = \tfrac{1}{2}I_x p^2 + \tfrac{1}{2}I_y q^2 + \tfrac{1}{2}I_z r^2 \qquad (3.2.51)$$

Note that the only sensible axis system for coordinatization of $\underline{I}$ is the body-axis system, and thus $\underline{\omega}$ is also in this system for compatibility.

$\dot{E}$ is merely the time rate of change of E, the kinetic energy. D_{SPIN} is a Euclidean metric which is an indicator of how far a given point in the state space, $\underline{x}$, is from a known (input) stable equilibrium spin location, $\underline{x}_{SPIN}$. In (3.2.50), x_i is a component of the state vector $\underline{x}$, say α, x_{s_i} is the value of that component at a known spin equilibrium condition, and n is the number of state elements in $\underline{x}$. D_{SPIN}, then, is

intended to provide some indication of how far a particular point $\underline{x} \in R^n$ is from a known spin equilibrium point, $\underline{x}_s$.

Equations (3.2.37) - (3.2.50) represent relations for quantities which are of interest in investigating spin motion, as well as the quantities defined by Eq. (3.2.29), (3.2.30) and C_{m_β}. Also, selected terms from the basic dynamic set of equations are usually of interest.

3.2.1 Aircraft F Configuration; Representing Aero Data by Spline Functions

Because of the completeness and compactness of data which is relevant to the study of spin conditions, aircraft Configuration B from Moore, Anglin (1971) will be used first in this study. We shall henceforth call this configuration aircraft F. Additionally, there are several sources of aerodynamic data for the F-4 Series of aircraft, namely, Rutan (1970), Adams (1972), Moore and Anglin (1971), Brady (1969); however, some extra effort is required to coalesce and reduce these data to the form of aircraft F, and so the F-4 Series will be investigated later. Moore, Anglin (1971) use the F-4 data, but not for the study of equilibrium spins, so no high-α data is supplied there. Data for Aircraft F are presented in Tables I and II.

Aircraft F is a variable sweep fighter aircraft whose aerodynamic data is somewhat equivalent to that of the F-111, although it must be emphasized that values were modified, especially the C_n derivatives, to allow the simulation results to readily produce "typical" spin motions.

It has been decided to model the aero data for aircraft F by using cubic and bi-cubic splines. A cubic spline is a means of representing data points by third order polynomials. The values of the four coefficients

which specify the polynomials are determined by continuity and smoothness conditions at the so-called "knots," which are typically but not necessarily the data points themselves. Thus, the cubic polynomial between any two knots differs from that between the neighboring knots, but their respective coefficients are selected so that, at their common knot, the value itself and (for cubic splines) the value of the first two derivatives match. The bi-cubic spline is conceptually similar to the cubic spline, except that it is a cubic polynomial in two variables, and not one. See Eq. (3.2.52). We have developed analytic functions in (α,β) for the coefficients by using cubic and bi-cubic splines, for the following reasons:

(i) splines assure smoothness, especially at the boundaries (knots);

(ii) The numerical algorithm employed by BACTM to generate the equilibrium surfaces requires the partial derivatives of the right hand side of Eqs. (3.2.1) - (3.2.6) with respect to the state and control variables--i.e., it is required to generate the matrix*

$$\left[\frac{\partial \underline{f}}{\partial \underline{x}}\right]$$

Since $(\alpha,\beta) \in \underline{x}$, expressions such as $\frac{\partial\left(C_{n_\beta}\right)}{\partial\alpha}$ will be required. The stability analysis in the neighborhood of the equilibrium surfaces also requires this matrix.

(iii) The data need not be supplied over uniform increments. This has the potential for saving much core on the computer, since the smoother portions of the data don't require as many points to adequately define the function.

*The coefficients are linear in the control variables δ so this aspect is straightforward, since the partials are the control stability derivatives.

TABLE I

Aircraft F:

Weight, N (lb)	222 410 (50 000)
Wing Area, m^2 (ft^2)	48.77 (525.0)
Wing span, m (ft)	19.20 (63.0)
Mean aerodynamic chord, m (ft)	2.76 (9.04)
I_x, kg-m^2 (slug-ft^2)	67 790 (50 000)
I_y, kg-m^2 (slug-ft^2)	427 348 (315 200)
I_z, kg-m^2 (slug-ft^2)	476 564 (351 500)
I_{xz}, kg-m^2 (slug-ft^2)	0 (0)
Maximum control-surface deflections:	
δ_e, deg	10, -25
δ_a, deg	±15
δ_r, deg	±30

TABLE II Aerodynamic Characteristics, Aircraft F

α, deg \ β, deg	C_Y									C_n								
	-40	-30	-20	-10	0	10	20	30	40	-40	-30	-20	-10	0	10	20	30	40
-10	0.547	0.436	0.324	0.145	0.000	-0.156	-0.320	-0.431	-0.542	-0.042	-0.042	-0.042	-0.020	0.000	0.016	0.036	0.036	0.036
-5	0.585	0.464	0.343	0.158		-0.143	-0.320	-0.441	-0.561	-0.042	-0.043	-0.044	-0.021		0.016	0.038	0.037	0.036
0	0.583	0.467	0.351	0.167		-0.126	-0.309	-0.425	-0.540	-0.039	-0.041	-0.042	-0.022		0.015	0.038	0.037	0.035
5	0.572	0.459	0.346	0.173		-0.106	-0.284	-0.397	-0.510	-0.037	-0.038	-0.039	-0.022		0.015	0.037	0.036	0.035
10	0.543	0.443	0.342	0.180		-0.102	-0.266	-0.367	-0.467	-0.035	-0.034	-0.034	-0.021		0.016	0.032	0.032	0.032
15	0.506	0.430	0.353	0.186		-0.017	-0.256	-0.339	-0.421	-0.029	-0.037	-0.024	-0.016		0.012	0.024	0.026	0.028
20	0.471	0.402	0.332	0.189		-0.084	-0.223	-0.297	-0.370	-0.005	-0.003	-0.001	-0.008		0.005	0.006	0.008	0.011
25	0.484	0.390	0.295	0.161		-0.051	-0.187	-0.282	-0.376	0.031	0.028	0.024	0.007		-0.006	-0.015	-0.010	-0.004
30	0.544	0.420	0.295	0.139		-0.017	-0.198	-0.323	-0.447	0.029	0.032	0.035	0.024		-0.021	-0.029	-0.020	-0.011
35	0.618	0.484	0.350	0.172		-0.042	-0.242	-0.377	-0.511	0.016	0.025	0.034	0.028		-0.027	-0.033	-0.025	-0.016
40	0.672	0.541	0.410	0.219		-0.097	-0.285	-0.416	-0.547	0.035	0.032	0.030	0.025		-0.021	-0.031	-0.033	-0.036
45	0.652	0.532	0.412	0.254		-0.126	-0.301	-0.422	-0.542	0.046	0.033	0.020	0.017		-0.013	-0.021	-0.034	-0.046
50	0.612	0.503	0.394	0.239		-0.127	-0.300	-0.416	-0.525	0.038	0.016	-0.005	-0.015		0.003	0.004	-0.017	-0.038
55	0.618	0.496	0.373	0.190		-0.097	-0.287	-0.410	-0.532	0.034	0.007	-0.020	-0.039		0.037	0.020	-0.007	-0.033
60	0.670	0.517	0.363	0.153		-0.051	-0.280	-0.424	-0.581	0.044	0.012	-0.020	-0.048		0.048	0.013	-0.018	-0.050
65	0.715	0.574	0.433	0.120		-0.049	-0.303	-0.444	-0.585	0.071	0.042	0.013	-0.049		0.038	-0.003	-0.032	-0.061
70	0.681	0.588	0.494	0.174		-0.075	-0.359	-0.453	-0.546	0.072	0.053	0.033	-0.023		0.021	-0.021	-0.040	-0.060
75	0.638	0.565	0.492	0.247		-0.107	-0.378	-0.451	-0.524	0.054	0.036	0.022	-0.008		0.006	-0.022	-0.038	-0.054
80	0.619	0.551	0.482	0.289		-0.143	-0.378	-0.447	-0.515	0.039	0.022	0.005	-0.012		-0.007	-0.013	-0.030	-0.047
85	0.615	0.546	0.476	0.310		-0.167	-0.370	-0.440	-0.509	0.037	0.016	-0.004	-0.014		-0.004	-0.006	-0.023	-0.040
90	0.620	0.546	0.471	0.317		-0.184	-0.355	-0.430	-0.504	0.027	0.009	-0.009	-0.015		0.008	0.002	-0.017	-0.033

α, deg \ β, deg	C_l									C_m								
	-40	-30	-20	-10	0	10	20	30	40	-40	-30	-20	-10	0	10	20	30	40
-10	-0.030	-0.017	-0.004	0.001	0.000	-0.004	0.004	0.017	0.030	0.119	0.155	0.191	0.269	0.329	0.291	0.248	0.184	0.1192
-5	-0.011	-0.003	0.006	0.003		-0.005	-0.007	-0.004	0.000	0.336	0.246	0.155	0.189	0.173	0.176	0.186	0.261	0.336
0	0.024	0.023	0.022	0.008		-0.012	-0.022	-0.024	-0.025	0.420	0.266	0.113	0.081	0.063	0.063	0.117	0.269	0.420
5	0.051	0.046	0.040	0.017		-0.021	-0.039	-0.045	-0.050	0.418	0.225	0.032	-0.031	-0.037	-0.050	0.026	0.222	0.418
10	0.076	0.060	0.044	0.020		-0.023	-0.046	-0.062	-0.078	0.418	0.160	-0.098	-0.142	-0.148	-0.162	-0.090	0.164	0.418
15	0.096	0.068	0.040	0.020		-0.024	-0.043	-0.071	-0.099	0.378	0.074	-0.229	-0.222	-0.218	-0.228	-0.215	0.081	0.378
20	0.096	0.065	0.033	0.019		-0.023	-0.038	-0.070	-0.101	0.326	0.013	-0.299	-0.307	-0.284	-0.309	-0.321	0.003	0.326
25	0.075	0.047	0.019	0.010		-0.019	-0.031	-0.059	-0.087	0.386	0.030	-0.326	-0.359	-0.401	-0.381	-0.361	0.013	0.386
30	0.065	0.039	0.012	0.007		-0.010	-0.015	-0.042	-0.068	0.491	0.083	-0.324	-0.343	-0.531	-0.437	-0.347	0.072	0.491
35	0.051	0.033	0.015	-0.000		0.000	-0.012	-0.030	-0.048	0.535	0.124	-0.287	-0.377	-0.579	-0.412	-0.337	0.099	0.535
40	0.038	0.023	0.008	-0.007		0.003	-0.017	-0.032	-0.047	0.486	0.121	-0.244	-0.493	-0.603	-0.439	-0.340	0.073	0.486
45	0.060	0.037	0.014	-0.005		-0.006	-0.023	-0.046	-0.069	0.247	0.037	-0.174	-0.115	-0.617	-0.550	-0.265	-0.009	0.247
50	0.091	0.065	0.038	0.002		-0.011	-0.030	-0.057	-0.083	0.073	-0.049	-0.170	-0.444	-0.626	-0.507	-0.091	-0.009	0.073
55	0.089	0.070	0.050	0.018		-0.019	-0.045	-0.063	-0.084	0.024	-0.113	-0.249	-0.515	-0.647	-0.410	-0.182	-0.079	0.024
60	0.087	0.070	0.052	0.028		-0.026	-0.051	-0.069	-0.086	-0.185	-0.299	-0.412	-0.638	-0.703	-0.482	-0.333	-0.259	-0.185
65	0.091	0.072	0.052	0.029		-0.028	-0.052	-0.070	-0.088	-0.494	-0.558	-0.621	-0.705	-0.805	-0.648	-0.470	-0.392	-0.494
70	0.092	0.072	0.052	0.027		-0.027	-0.053	-0.072	-0.090	-0.719	-0.773	-0.826	-0.868	-0.953	-0.812	-0.706	-0.713	-0.719
75	0.093	0.073	0.052	0.027		-0.016	-0.052	-0.073	-0.093	-0.868	-0.975	-1.082	-1.082	-1.136	-0.998	-0.999	-0.834	-0.868
80	0.095	0.072	0.049	0.027		0.000	-0.050	-0.071	-0.096	-1.000	-1.186	-1.371	-1.294	-1.328	-1.201	-1.308	-1.154	-1.000
85	0.095	0.072	0.049	0.029		-0.006	-0.061	-0.074	-0.097	-1.135	-1.351	-1.567	-1.541	-1.619	-1.493	-1.522	-1.329	-1.135
90	0.096	0.073	0.050	0.032		-0.027	-0.052	-0.075	-0.098	-1.274	-1.487	-1.700	-1.811	-1.974	-1.843	-1.672	-1.473	-1.274

TABLE II, concluded

α, deg	C_X	C_Z	$C_{X_{\delta_h}}$, per deg	$C_{Z_{\delta_h}}$, per deg	$C_{m_{\delta_t}}$, per deg	C_{m_q}, per rad	$C_{Y_{\delta_r}}$, per deg	$C_{n_{\delta_r}}$, per deg	$C_{l_{\delta_r}}$, per deg	$C_{Y_{\delta_a}}$, per deg	$C_{n_{\delta_a}}$, per deg	$C_{l_{\delta_a}}$, per deg	C_{Y_p}, per rad	C_{n_p}, per rad	C_{l_p}, per rad	C_{Y_r}, per rad	C_{n_r}, per rad	C_{l_r}, per rad
-10	-0.0090	0.8500	0.0061	-0.0127	-0.0264	-26.040	0.0035	-0.0014	0.0002	0.0005	-0.0002	-0.0008	0.030	-0.010	-0.140	0.120	-0.170	0.040
-5	-0.0250	0.4600	0.0055	-0.0156	-0.0297	-26.040	0.0034	-0.0013	0.0002	0.0005	-0.0002	-0.0008	0.060	-0.010	-0.190	0.130	-0.170	0.040
0	-0.0300	0.0800	0.0050	-0.0150	-0.0303	-26.040	0.0032	-0.0013	0.0002	0.0011	-0.0002	-0.0008	0.120	-0.010	-0.190	0.160	-0.170	0.040
5	-0.0286	-0.3200	0.0043	-0.0148	-0.0300	-24.420	0.0031	-0.0012	0.0002	0.0006	-0.0001	-0.0008	0.190	-0.010	-0.160	0.130	-0.170	0.090
10	0.0098	-0.7300	0.0035	-0.0143	-0.0305	-22.790	0.0029	-0.0013	0.0002	0.0008	-0.0001	-0.0009	0.230	-0.010	-0.180	0.010	-0.180	0.130
15	0.0451	-1.1300	0.0026	-0.0154	-0.0312	-26.230	0.0030	-0.0013	0.0001	0.0010	0.0000	-0.0008	0.240	0.000	-0.180	0.000	-0.220	0.220
20	0.0731	-1.5300	0.0017	-0.0184	-0.320	-29.670	0.0032	-0.0013	0.0001	0.0013	0.0001	-0.0008	0.230	0.010	-0.160	0.430	-0.260	0.310
25	0.0991	-1.9200	0.0008	-0.0207	-0.0346	-33.700	0.0033	-0.0013	0.0001	0.0018	0.0001	-0.0009	0.260	0.190	-0.180	1.050	-0.270	0.480
30	0.0920	-2.3300	-0.0003	-0.0241	-0.0370	-37.720	0.0032	-0.0013	0.0002	0.0014	0.0002	-0.0009	0.290	0.360	-0.260	1.200	-0.280	0.640
35	0.0708	-2.6500	-0.0012	-0.0250	-0.0361	-42.900	0.0029	-0.0012	0.0002	0.0013	0.0003	-0.0009	0.290	0.580	-0.380	0.790	-0.280	1.160
40	0.0465	-1.7470	-0.0021	-0.0220	-0.0316	-44.690	0.0025	-0.0009	0.0003	0.0027	0.0003	-0.0009	0.560	0.400	-0.550	0.230	-0.180	1.590
45	0.0397	-1.6896	-0.0035	-0.0169	-0.0247	-41.810	0.0019	-0.0007	0.0004	0.0014		-0.0009	1.230	0.260	-0.600	-0.180	-0.080	0.990
50	0.0354	-1.7054	-0.0043	-0.0144	-0.0174	-19.000	0.0019	-0.0006	0.0004	0.0007		-0.0007	1.700	0.190	-0.570	0.780	0.160	0.350
55	0.0392	-1.7492	-0.0048	-0.0120	-0.0114	2.000	0.0041	-0.0006	0.0003	0.0002		-0.0006	1.540	0.140	-0.450	2.610	0.990	0.250
60	0.0397	-1.7680	-0.0045	-0.0103	-0.0087	-7.000	0.0016		0.0001	-0.0013		-0.0005	-0.140	-0.310	-0.270	2.270	0.820	0.130
65	0.0344	-1.8142	-0.0047	-0.0093	-0.0034	-30.000	-0.0005		0.0001	-0.0035		-0.0005	-1.180	-0.470	-0.150	0.490	0.000	0.030
70	0.0358	-1.9020	-0.0052	-0.0105	-0.0040	-27.000	0.0004		0.0000	-0.0035		-0.0004	-0.090	-0.050	-0.100	-0.180	-0.110	0.000
75	0.0395	-1.9490	-0.0053	-0.0106	-0.0040	-4.000	0.0005		0.0000	-0.0027		-0.0005	0.640	-0.150	-0.100	-0.010	-0.110	0.010
80	0.0407	-1.9634	-0.0052	-0.0082	-0.0040	-3.000	-0.0000		0.0000	-0.0025		-0.0006	0.580	0.040	-0.133	0.090	-0.110	0.020
85	0.0412	-1.9690	-0.0050	-0.0071	-0.0040	-17.000	-0.0005		-0.0001	-0.0024		-0.0005	0.610	-0.040	-0.140	0.100	-0.110	0.010
90	0.0412	-1.9690	-0.0061	-0.0077	-0.0040	-24.000	-0.0008		-0.0002	-0.0024		-0.0002	0.730	-0.050	-0.150	0.160	-0.110	0.010

The general form of a bi-cubic spline is

$$S(\alpha,\beta) = \sum_{i=1}^{4} \sum_{j=1}^{4} C_{ij}[\alpha - A(\ell_\alpha)]^{i-1}[\beta - B(\ell_\beta)]^{j-1} \qquad (3.2.52)$$

where $A(\ell_\alpha)$ and $B(\ell_\beta)$ are the values for α and β, respectively, at the lower left corner of the rectangle of values for α and β which contains the input set (α,β). S is the value of the particular coefficient at the input set (α,β). Library routines (IMSL) are used to generate the C_{ij}, and to compute S and its partials.

Use of splines may appear to be introducing an overly-sophisticated approach for a data base as relatively simple as the aircraft F model, but when the more complex data bases such as that for the F-4 are added, the value of the spline approximations should be more appreciated. To assure a good spline fit, the location of the junction points, or knots, is an important factor. When this and similar considerations are efficiently dealt with, the method of splines becomes an efficient modeling tool. In our applications, the knots are placed at each data point. More background on the theory and uses of splines may be found in Ahlberg, Nilson and Walsh (1967).

Splines by their nature allow for accurate modeling of the partial derivatives of the dependent variable (aerodynamic coefficients) with respect to the independent variable(s) (α and/or β). This fact is important in the application here, because these partials are required in order to evaluate the equilibrium and bifurcation surfaces; and the accuracy of their values may often be critical to efficiently starting up the

numerical solution. Whereas curves which result from a less rigorous patching-together of polynomials may well experience severe discontinuity problems for their derivatives at the boundary points, spline-produced curves by their nature (i.e., the constraint that the second derivatives be equal at each knot which "shares" two splines) have no such problems.

The splines used to model aircraft F's aerodynamic data are "natural" cubic (or bi-cubic) splines*, and the knots are specified to be located at each data point. Of the 22 coefficients which are used by aircraft F, all but four are functions of α and are thus modeled by the one-dimensional cubic splines. C_y, C_n, C_ℓ, and C_m only are functions both of α and β and are modeled by bi-cubic splines. Cubic spline plots are shown in Figs. 3.1 to 3.6. These are plots of each of the 18 α-dependent coefficients, and their respective partials with respect to α (in degrees). The plot of the basic function is the line containing the x's, the latter representing the data points (hence, also the knots) obtained from Moore, Anglin (1971). Both the coefficients and their partials with respect to α are computed and plotted in dimensionless units. The units for α (abscissa) are degrees. The derivative with respect to α is plotted as a clean, solid line. Notice how smooth the derivative curves are. The large change in shape of most of the curves beginning in the range $\alpha \simeq 35°$ to $50°$ (.69 to .91 radians) is due principally to the loss of rudder control effectiveness for $\alpha \gtrsim 50°$. See, in particular, the plots of the lateral mode coefficients appearing in Figs. 3.3 to 3.6.

The bi-cubic spline, two-dimensional, plots of a representative function of both α and β, $C_m(\alpha,\beta)$, are presented in Figs. 3.7 and 3.8.

*A natural cubic spline is one whose second derivatives are zero at the end points.

Fig. 3.7 shows C_m and its β-derivative, C_{m_β}, both of which are in dimensionless units, plotted against sideslip angle β, in degrees. The two plots shown in Fig. 3.7 are for two different values of angle-of-attack α, 65° and 32.5° respectively. The latter value for α represents an interpolation on the data. By rotating the projection plane depicted in Fig. 3.7 by 90°, one obtains plots of $C_m(\alpha,\beta)$ and its α-derivative, C_{m_α}, versus α, shown in Fig. 3.8 . The units are as in Fig. 3.7 . The two values of β for which the Fig. 3.8 plots are made, ±25°, are the interpolation values for β.

A final note on the use of spline function approximations by BACTM. Because the spline package had already been implemented to represent the aero data, it was also decided to use splines, and the same routines, in evaluating numerical derivative, e.g., to generate elements of $[\partial \underline{f}/\partial \underline{x}]$ which are difficult to obtain analytically. This duality of function adds to the efficiency of BACTM. See Section 2.1.2 for a discussion of the numerical differentiation algorithm.

3.3 Entry into Spin; Explanation of Equilibrium Surface Plots

Experience shows that a very complete set of aerodynamics is required to represent properly the extremely complex aircraft motions which arise during stall/spin flight conditions. In this section, we shall explore the spin entry behavior of aircraft F. This model does not possess all of the desirable features for undertaking a thorough, realistic study of spin behavior. However, it has been an excellent model in providing a small yet adequate basis about which to construct the BACTM Spin Analysis system; and for providing much insight into the nature of developed spin motion in particular.

The results to be shown in this section, however, will reveal that careful study of the equilibrium surfaces generated by BACTM is required in order to understand the subtleties of nonlinear, high-α aircraft motion. Interpretation of equilibrium surfaces is a case in point. It can be rigorously demonstrated that motions originating in the vicinity of a "stable" branch (such branches are labeled with an "S" in the figures) will ultimately arrive at a point on that branch, thereby achieving a condition of dynamic equilibrium (i.e., $\dot{\underline{x}} = 0$). See Section 3.2 and Chapter II for further discussion. Chapter II contains a bibliography referencing detailed proofs. The only problem, then, for regions dominated by a stable branch is determining quantitatively the neighborhood from which all motions lead to that branch (this neighborhood is called a "domain of attraction"). Very often, a boundary to the domain of attraction is a "simple" unstable branch, e.g., one in which there is one positive real root--this

branch is designated by a "U". In Fig. 3.9 we can see an example of this situation. The point A in this figure is centered on a stable branch in the equilibrium flat spin region. This branch is bordered above and below by a U-branch. Thus, motions initiated with a control setting close to that of point A, and with initial conditions inside the two U-branches, will return to the S-branch. Units for this and subsequent figures are degrees.

Before proceeding further, we will now explain some of the details of Fig. 3.9, which is a typical plot of an equilibrium surface. The branches shown represent loci of points for which $\underline{f}(\underline{x},\underline{\delta}) = 0$, generated by holding two of the elements of $\underline{\delta}$ at given values, and varying the third (see Chapter II). The letters on these branches provide local stability information, as follows: for the n^{th} order system $\dot{\underline{x}} = \underline{f}(\underline{x},\underline{\delta})$, the local stability information is obtained from the eigenvalues of the square matrix $[\partial \underline{f}/\partial x]$, which is part of the first order (linear) term in the polynomial expansion of $\underline{f}$. This matrix is of size $n \times n$, and always yields n eigenvalues, which may either be real or in complex pairs (since $[\partial \underline{f}/\partial \underline{x}]$ has real elements). If all n of the eigenvalues have negative real parts, the equilibrium point is a stable one, designated by S. Any other situation results in an equilibrium point which is locally unstable. Several unstable cases are now outlined: if there are (n-1) eigenvalues with negative real parts, and the remaining one is positive (this one is necessarily a real eigenvalue as complex eigenvalues come in pairs), the point is designated by a U; if (n-2) have negative real parts and a complex pair has a positive real part, the point is designated by L. However, if there are (n-2) "stable" eigenvalues and two real, positive ones, then the point has two simple U's, or is designated by the symbol A, as

seen in the table at the top of Fig. 3.9. Except for the one, unique stable case (S), the table gives symbolic correspondences for all combinations of unstable eigenvalues; that is, eigenvalues with positive real parts.

To summarize to this point, when U-branches have been found near S-branches, they typically outline much of the domain of attraction to that stable branch.

As for all other (unstable) branches, there are two major points of interest with regards to aircraft F equilibrium results:

1) The stability analysis is local, and based only on first order, or linear, information. This means that at a U-branch, say the one including point E in Fig. 3.9, the motion will diverge locally; in fact, for any unstable point, any point but an S-point, the motion diverges locally. But we can say more regarding the point E case: if the motion starts on the S-branch side of the U-branch, it will ultimately come to equilibrium on the S-branch. This is a global result however, and is obtained not from the information provided by $[\partial \underline{f}/\partial \underline{x}]$ at point E, but from a more global knowledge of the equilibrium surface--that is, we know that the S-branch "attractor" exists. If the motion starts on the other side* of the U-branch, it is unclear from the equilibrium surface plot what will ultimately happen. The divergence feature applies only in a local sense and guarantees only that there will be no equilibrium near the U-branch. Globally, the motion is attracted elsewhere from the U-branch, either to a distant S-branch (not shown), or to a limit cycle, perhaps the one governed by the L-branch above point E in Fig. 3.9a; or finally, to an

*Strictly speaking, motions originating exactly on the U-branch or any other unstable branch, will remain there; however, the smallest perturbation will induce divergent behavior, which is what happens in the real world.

essentially erratic motion not characterized as either a stable equilibrium ($\dot{\underline{x}} = 0$) or a limit cycle ($\underline{x}(t+T) = \underline{x}(T)$, $0 < T < \infty$). Thus, local instability is not necessarily global instability.

2) L-branches are of particular interest, because they are very prevalent in high-α flight regimes, and particularly so in the spin entry region depicted in Fig. 3.9 (the lower branch which includes points B, C, D, E). As defined above, the L-branches define unstable equilibrium points at which $[\partial \underline{f}/\partial \underline{x}]$, the Jacobian matrix, has (n-2) "stable" eigenvalues and one unstable complex pair. Locally, then, this indicates oscillatory divergence. Globally, however, it is quite possible that this divergence is in actuality growth to a stable limit cycle (hence, the L-symbol designation). The existence and stability of limit cycles is not explicitly obtained from the equilibrium surfaces (we are currently developing an algorithm to do this analysis), but stable limit cycles in our experience are always associated with an L-branch. In a sense, then, stable limit cycles may be regarded as stable equilibria, unless amplitude variations are excessive. At any rate, there are domains of attraction to stable limit cycles, although their boundaries are not as easily computed as are those for the proper equilibrium points (S-branches). Also, there are known to exist unstable limit cycles. In analogy to the U-branches, if a motion could begin exactly on an unstable limit cycle, and be free of random disturbances, it would remain on this cycle. Typically, of course, the motion readily diverges, usually to a stable limit cycle. Unstable limit cycles are very difficult to isolate, and there exists no known algorithm of sufficient generality which can compute their location. They do exist however, and, as the continuation parameter (δr in Fig. 3.9)

changes, are capable of annihilating a stable limit cycle. This phenomenon is called a global bifurcation, and may explain the limit point below point B in Fig. 3.9a. Here, as one decreases δr from point D, the equilibrium curves tell us to expect a Hopf bifurcation (S-to-L transition on the branch) to a limit cycle. Such limit cycles are typically stable, at least when in the region close to the S branch, but again, this information cannot be obtained from Fig. 3.9. As δr decreases, however, this limit cycle is annihilated; we cannot indicate for sure exactly where (although the figure indicates approximately -21°, the limit cycle motion is not a local motion, and the limit cycle may be annihilated at a very different value, if at all), but, given that this occurs, it is quite likely that the motion will be attracted to a stable limit cycle governed by the segment of the equilibrium branch including point B. This hypothetical control sequence outlines how a relatively "clean" rolling motion at point D ($\delta a = 15°$ in this example, recall) is corrupted into buffeting and oscillatory motion which conceivably, as δr is decreased further, undergoes a jump to oscillatory, steep spin conditions (point B). From analysis of time history results, discussed in more detail later, there is a strongly stable--i.e., possessing a large domain of attraction--limit cycle in the vicinity of point B. This situation precludes transition from steep spin to the flat spin equilibrium at point A, using δr alone.

Summarizing unstable branches, then, the major point is that in a local sense all motions diverge from them; however, limit cycles typically exist about a subset of these, the L-branches, and these themselves may be stable (attractors) or unstable. When a stable limit cycle exists,

it is usually centered on the L-branch; however, the motion will never decay to the L-branch itself. In spite of this, it is often convenient to consider the stable limit cycle as an equilibrium condition, which may be disrupted as a neighboring unstable limit cycle converges upon it, under the influence of changing control parameters.

A final note on limit cycles: they are a distinctly nonlinear phenomenon, lacking many properties of the linear oscillator. In the latter, an incremental change in initial conditions results in an incrementally different, yet stable, orbit. Such a change applied in a limit cycle region will only produce a temporary perturbation, followed by decay to the original limit cycle. That is, in a given subspace, there are only a countable number of possible limit cycles, while a continuum of amplitudes is possible for the linear oscillator.

Returning to the aircraft F spin entry case, Fig. 3.9 is a representative situation (the insensitivity to δe of the equilibrium surfaces in this flight regime will be indicated later; thus, $\delta e = 0°$ is selected), in that the flat, equilibrium spin region, the upper branch in Fig. 3.9a, has a relatively small stable equilibrium region. Further, the steep and intermediate spin regions, the upper part of the lower branch, as well as most of the other non-equilibrium regions, are characterized by oscillatory behavior, with limit cycle motion quite likely. As stated above, several of the limit cycle regions exert strong attraction on neighboring motions, making transition to flat spin very difficult. At any rate, our experience with aircraft F indicates that oscillatory motions at intermediate angles of attack ($30° \lesssim \alpha \lesssim 65°$) is a general feature for any control

setting; this observation consequently adds to our desire to study in detail the behavior and stability of limit cycle motion in general, and the stall/post-stall/spin entry flight regime in particular, because of its oscillatory character. A more useful study of spin entry would involve using the F-4 model, which is more realistic and representative in this flight regime.

In addition to the above situation, Bihrle (1976) has noted (and it is verified here) that ensuing high-α motion is extremely sensitive both to control sequencing and to relatively small variations in the initial conditions. Results presented here provide the basis for the above observations and are typical of systems with bifurcations.

In the following discussion, we have concentrated on right pro-spin motions; that is, yaw rate (r) is positive, due to negative rudder (δr) deflection, and aileron (δa) is positive. For convenience, then, we shall define

$$\underline{\delta}_{SPIN} \triangleq (\delta a, \delta e, \delta r) = (15, -21, -25) \text{ degrees}$$

Because of nonlinear dynamics, this set of controls corresponds to more than one equilibrium point. However, associated with $\underline{\delta}_{SPIN}$ is a stable, developed flat spin equilibrium state for aircraft F,

$$\underline{x}_{SPIN} \triangleq (p, q, r, \alpha, \beta, V, \theta, \phi)$$
$$= (30, -4., 100., 73.5, -3., 443, -16.6, -2.29)$$

The units are degrees and feet per second. These quantities will be used for reference in the following sections.

Finally, it should be noted that many of the equilibrium surfaces presented in this chapter may not contain all of the possible equilibrium

branches for the given control region. This is not necessarily a minor detail, because some of the branches not shown may possibly represent stable attractors for certain limit cycle motions.

3.3.1 High-α Motions to Stall, Aircraft F

Fig. 3.10 shows equilibrium surfaces in the (r,α,p)-δe plane for aircraft F, centered on the trim state with neutral controls. As will be the case unless otherwise specified, velocity (V) is fixed at 600 fps, and gravity is assumed negligible (i.e., the non-spin set of dynamic equations is used). Note that there are regions ($\delta e > 0$) where five equilibrium solutions exist, and three of these are stable. As δe goes negative, pitch-up occurs, signified by the growing values in α. From $\delta e \simeq -15°$ the stable branch changes into a limit cycle branch; this signifies the onset of wing rock behavior and pre-stall buffeting. Note in particular that on the roll-rate plot, there is a region in $\delta e > 0$ for which no solutions are shown. At the boundary points to this region, α has reached its minimum value of -10°, and no aerodata were available below this value. Fig. 3.11a shows a time history plot in which V is free to vary and δe is increased from 0° to -9°, then -17°, then -20°. Note that when δe is -17° and -20°, there is evidence of large longitudinal oscillations, but little wing rock motion. Fig. 3.11b shows a different δe time sequence than 3.11a, with velocity allowed to vary, and basically similar results. If velocity is kept constant, buffeting and wing rock activity are very prominent (Fig. 3.11c) as will be shown in Sec. 3.3.3, where Figs. 3.10 and 3.11 are discussed further.

We consider now a maneuver in which both heading change and high-g pullup is accomplished by pulling the stick back sharply (high negative δe),

and then over (high aileron). The δe maneuver can be traced in Figure 3.10, and Figure 3.12 shows the δa direction from Point A in Figure 3.10. It is seen in Figure 3.12 that, for $\delta e = -11°$, beyond $\delta a = 15°$ there is a jump, or a Hopf Bifurcation, to a limit cycle with high values of (r, ι, p). The time history presented in Figure 3.13 confirms these conclusions, although the transition to post-stall divergence occurring at 30 sec. is aided by introducing negative δr as well. Note that the presence of nonzero δr causes the initiation of spin-like behavior in the post-stall motions. The DSPIN parameter, a normalized metric for $\|(\underline{x},\underline{\delta}) - (\underline{x}_{SPIN},\underline{\delta}_{SPIN})\|^2$, shows a return to spin conditions. The oscillatory nature of the developing spin is typical of aircraft F behavior in transitioning from trim to high-α flight regimes.

The equilibrium surfaces in Fig. 3.14 show the rudder effect on the type of equilibrium condition which produces aircraft behavior similar to that of the maneuver discussed above. In this instance, $\delta e = -20°$ and $\delta a = 0°$, while δr varies. The segment of the L-branch (limit cycle behavior expected) near $(p,r) = 0$, $\delta r = 0°$, actually exhibits very mild unstable growth to oscillatory behavior (very large characteristic or response time) when the corresponding time history run is made (figure not shown); but, as δr moves from 0° to negative values, the response quickens greatly, and the oscillations grow. A similar effect is noted in the trajectories of Fig. 3.13.

3.3.2 Non-Spin Equilibrium Surfaces (Aircraft F)

As above, these results were generated from the non-spin set of dynamic equations, which assume zero gravity and constant velocity (V). Except where stated otherwise, V is assumed to be 600 fps. It turns out,

at least for aircraft F, that the non-spin set can also be used in the spin regime without destroying essential features. This represents a significant result for first-cut analysis; the numerical results, however, do differ, since gravity does play a role in spin behavior. However, gravity has negligible influence on equilibrium behavior in non-spin, high-α regimes. Moreover, steady state values for θ and ϕ do not exist in the high-α regimes. Hacker and Oprisiu (1974) show that the effects of gravity in roll coupling may be taken into account by a perturbation analysis.

The projections of the equilibrium manifold on different planes in the state and control space are shown in Figures 3.10, 3.12, 3.14, 3.15 and 3.16. In each of these runs, the control is extended from $\underline{x} = 0$ over as much of its allowable range as possible, with the remaining two controls fixed at zero. The elevator case has been discussed in Section 3.3.1. As will be seen, the rudder introduces the most dramatic changes in equilibrium conditions in this region (Figures 3.14 and 3.15). In fact, the aileron behaves as an almost purely linear control over its entire range for $\delta e = \delta r = 0°$, and all equilibria are stable (Figure 3.16). Note how roll rate (p) is the only variable reasonably sensitive to δa changes; thus, there is also decoupling. But the rudder, in this as well as most other aircraft F flight regimes, exhibits far different characteristics. This is further exemplified by the time history shown in Figure 3.17. This figure shows the clear growth to a high-amplitude limit cycle as δr steps in 10° increments from 0° to -40°, with $\delta a = \delta e = 0°$. Clearly, the effect of rudder is nonlinear in this region, and there is a high degree of

coupling, as both Figure 3.15 and 3.17 show.

From Point A in Figure 3.15, $\delta r = -6.4°$, a surface is generated along the δe direction, and the results are shown in Figure 3.18.* This figure represents a parallel slice of the surface only 6.4° removed along the δr direction from the projection shown in Figure 3.10, yet it is evident how dramatic the difference is, both qualitatively and quantitatively. A third section of the equilibrium surface, for $\delta r = -25°$, is presented in Figure 3.19, and represents the projection along δe centered on Point B in Figure 3.15. Again, there is a considerable difference in the shape of the surface. Note further that inspecting the p-plot alone may cause one to suspect a possible bifurcation point; that is, the point where the branches intersect, at δe -4°. This is not the case, however, because there is no such overlap for the (α,r) curves.

From Point C in Figure 3.18, the $\delta e = 0°$ point, an orthogonal projection is generated along the third control direction, δa, and Figure 3.20 shows the results. For the $(\delta e,\delta r)$-values given, i.e., (0,-6,4°), the $\delta a = 0°$ point is a precariously stable one. Only small variations are needed to cause either a jump ($\delta a < 0$) or development of an unstable or limit cycle conditions ($\delta a > 0$).

Returning to Figure 3.16, for which $r = 0$, some other projections of the equilibrium surface are compared in Figures 3.21 and 3.22. In Figure 3.21, with the same controls as Figure 3.20, i.e., $\delta r = -6.4°$,

*In this figure, and in others where it appears, an asterisk indicates that two pairs of complex eigenvalues of $[\partial \underline{f}/\partial \underline{x}]$ have positive real parts--an LL-condition.

AD-A084 921 SCIENTIFIC SYSTEMS INC CAMBRIDGE MA F/G 20/4
GLOBAL STABILITY AND CONTROL ANALYSIS OF AIRCRAFT AT HIGH ANGLE--ETC(U)
JUN 78 R K MEHRA, J V CARROLL N00014-76-C-0780
UNCLASSIFIED ONR-CR215-248-2 NL

2 OF 3
AD A084932

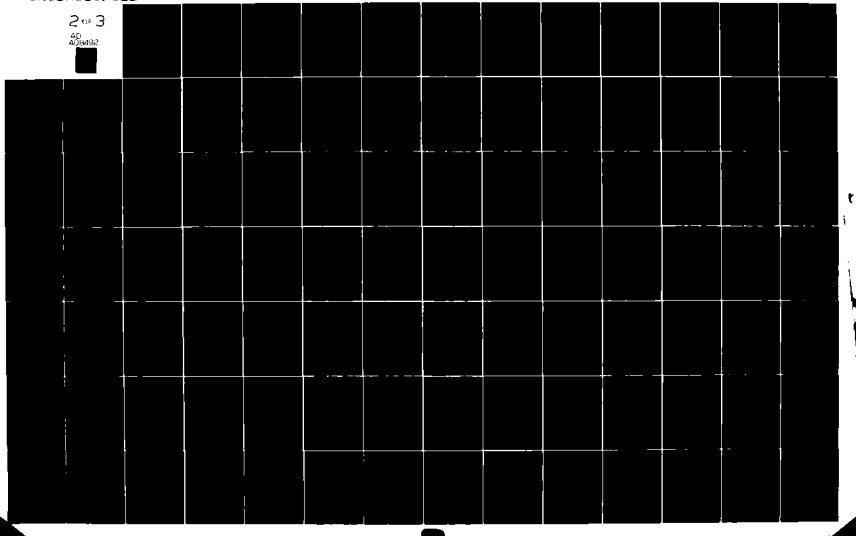

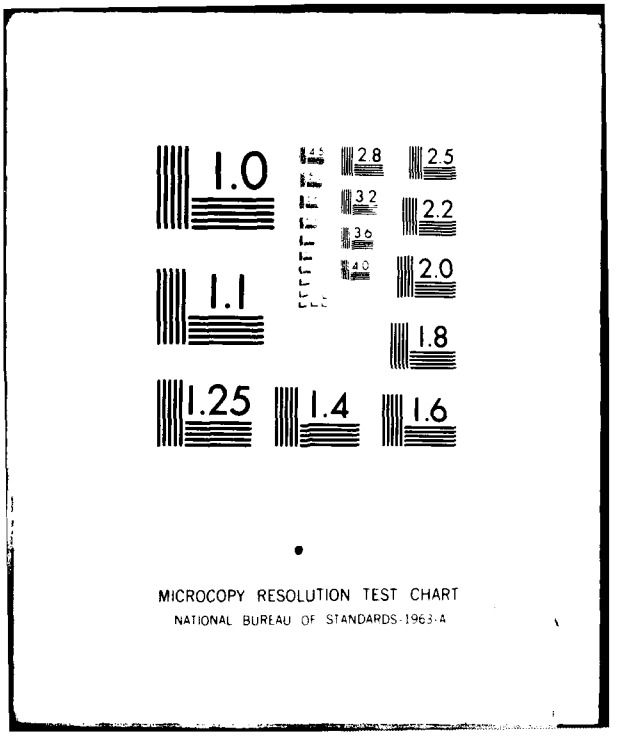
1.0
1.1
1.25
1.4
1.6
1.8
2.0
2.2
2.5
2.8
3.2
3.6
4.0
MICROCOPY RESOLUTION TEST CHART
NATIONAL BUREAU OF STANDARDS-1963-A

$\delta e = 0°$, another branch of the equilibrium surface is shown. Aileron has now lost its linear influence here, and there is significant coupling as well as sharp lack of symmetry in p. Figure 3.22, for which $\delta r = -25°$, shows very similar curves as does Figure 3.16, for which $\delta r = 0$; however, the equilibrium values have increased, and more significantly, roll rate is almost totally insensitive to δa commands. The aircraft is in an autorotational state in roll. Figure 3.23 is a case similar to Figure 3.22, i.e., $\delta r = -25°$, except that now $\delta e = 10.3°$ (pitch down). It can be seen that higher equilibrium values ensue for this δe, with somewhat less stability. (Only the r-δa plot is shown since others are quite similar).

A further effect of the rudder can be seen by comparing Figure 3.12 with Figure 3.24. In both of these figures, $\delta e = -11°$ and δa is the independent variable. For $\delta r = 13°$ in Figure 3.24, there are no stable regions on the branch and there is no symmetry. Both of these results are expected. Elevator influence on the rudder controllability may be seen by comparing Figure 3.25 ($\delta a = 15°$, $\delta e = 0°$) with Figure 3.26 ($\delta a = 15°$, $\delta e = 7.3°$) and Figure 3.27 ($\delta a = 15°$, $\delta e = -11°$). These surfaces again give evidence of the richness of nonlinearities and hysteresis-type behavior, with several different kinds of equilibria over the control regime. The aileron effect on rudder may also be noted by comparing Figure 3.25, for which $\delta e = 0°$ and $\delta a = 15°$, with Figure 3.15, for which $\delta e = 0°$ and $\delta a = 0°$. There is some change, although not to the degree shown by the elevator, revealed further by a comparison of Figure 3.26 ($\delta e = 7.3°$) with Figure 3.25 ($\delta e = 0°$) especially in α and p. To say that δr has nonlinear influence on p is an understatement, after inspecting Figure 3.26. Figure 3.27, where $\delta e = -11°$ and

$\delta a = 15°$, is most unusual because the curves close upon themselves as rudder is varied. The geometry is more evident by comparing Figure 3.27 with Figure 3.28. In the latter, $\delta r = 0°$, $\delta a = 15°$ and δe varies, so that it is "orthogonal" to Figure 3.27. The line E-E' represents the plane depicted by Figure 3.27; conversely, the line D-D' in Figure 3.27 is in the plane depicted by Figure 3.28.

The equilibrium surfaces presented in this section were shown to provide a feel for the great variety of behavior which is possible in these high-α regimes. One can begin to understand, with particular reference to the time history results shown in Fig. 3.29, and its relevant equilibrium surfaces shown in Figs. 3.24 and 3.26, that in certain regions the smallest change in starting conditions can result in widely divergent results.

3.3.3 Wing Rock Motions

Wing rock has been mentioned briefly in discussing the aircraft F time history presented in Figure 3.11, Section 3.3.1. This particular phenomenon arises as the result of developing instability of airflow over the wings, a consequence of α approaching its stall value. The main feature of wing rock is pronounced roll oscillations whose amplitude increases at least through stall, and which usually couple into yaw and pitch oscillations. The coupling effects are due to the high-α nature of the motion. In fact, the rolling effects so prominent in wing rock are the result primarily of the elevator control actions. This basic longitudinal-lateral coupling is a main feature of high-α dynamics. Figure 3.10 demonstrates this coupling of δe deflections into the lateral dynamics (p,r), and should be referred to in examining the results shown in Figure 3.11.

Figure 3.11a shows a pre-stall buffeting which has only traces of lateral oscillation. Aileron and rudder are fixed in the neutral position for Figure 3.11, and the initial state is in trim. As can be seen, velocity is allowed to vary in 3.11a and 3.11b--the aircraft is effectively in a free-fall state--and this causes damping in the more prominent longitudinal oscillations. In Figure 3.11b, the damping is enhanced by changing the elevator control sequence. Here, δa is set and held at -15° after 20 seconds. However, if a thrust schedule is introduced which maintains V constant, the δe control sequence which was used in Figure 3.11a produces very different results, as can be seen in Figure 3.11c. In this figure, the roll rate oscillations become very severe, and they induce strong pitch oscillations as well. This pronounced limit cycle behavior is predicted by Figure 3.10, which was generated assuming constant velocity.

3.3.4 Post-Stall Gyrations

It is seen from inspection of the global equilibrium surfaces (e.g., Figure 3.9), which show both spin and non-spin regimes, that there is a basic barrier between these two regimes. This is due physically, in part, to the great changes which occur in the state of the vehicle as it undergoes transition from trim to spin conditions. The velocity vector changes approximately 90°, from roughly horizontal to vertical (and down); angle-of-attack similarly undergoes very large changes. Time history runs to be shown (Section 3.3.5 and 3.4) indicate that if the initial conditions are close to either those of stable, developed flat spin or of trim--and the controls are set to values representative of these two conditions--then the ensuing motions will stay in these regions and are stable. The spin

motion shows a well-developed spiral, with constant vertical velocity, pitch, roll and angle-of-attack (for an aircraft in "flat" spin, the equilibrium pitch angle magnitude is typically no larger than about 15°; thus, the aircraft is spiraling down "on its belly" with substantial yaw rate). But as Fig. 3.9 shows, if the controls move from trim (Point D) towards spin settings (Point A), then the motions indicative of stable, developed flat spin may not result since limit cycle regimes with large domains of attraction exist around Point B. Physically, it is known that once α exceeds its stall value, the aircraft becomes subject to violent oscillatory motions indicative of the loss-of-lift condition attendant with flow separation at high-α. These motions are called post-stall gyrations, and if there is any kind of equilibrium associated with them, it is most certainly not a stable equilibrium point. Once the controls move to values where high-α nonlinearities predominate, Hopf Bifurcations are seen to occur and only limit cycle equilibria exist. And, as stated earlier, to move from a limit cycle solution to a stable equilibrium point typically requires special sequencing of control changes. At least this is the case with the aircraft F model as defined and described in this report. It is easy to sequence the controls so that aircraft F enters an inadvertent spin-like condition; however, this spin is usually not the smooth, flat spin located at Point A in Figure 3.9. The entered spin is predominantly oscillatory, and a steep or intermediate spin which corresponds to a location not on an equilibrium surface since they are all unstable in this region, but one evolving from the intermediate region of the post-stall gyration governed by limit cycle (L) branches. This region is basically located between the spin and non-spin

regions and is featured by a family of limit cycles. It is not clear whether these limit cycles should be designated as "spin motions" or high-α post-stall gyrations, as they cover a broad range of α values (see Fig. 3.9b).

A spin entry run is presented in Figure 3.29. In this run, the controls were initially at trim; then δe was set to -10° at 20 sec, δr to -29° at 40 seconds and δa to 15° at t = 45 seconds. The results are consistent with what has been discussed above. The pitch-up action, pulling back on the stick, causes stall; thereupon lateral control inputs trigger the gyrational limit cycle behavior.

A similar run is shown in Figure 3.30 . Here, the trajectory begins with trim conditions, but δa is stepped to 15° and δe to -11°, and held (rudder remains momentarily at 0°). The initial conditions correspond to the S-segment of the equilibrium surface shown in Figure 3.27. As δr is then varied in steps to 14°, this induces the oscillatory behavior shown in Figure 3.30. The mean value of α indicates that an intermediate spin has been achieved ($\bar{r}$ is also high, with $\bar{q}$ very small, proportionally). A spiral of sorts has most likely developed, as the number of turns (the plot variable TURNS) is increasing at a steady rate (small oscillations superimposed), and XNORTH and YEAST are approaching a steady-state mean value, with oscillation. Finally, a rough comparison of mean values of r and ω indicates that most of the angular motion is in yaw.

3.3.5 Spin Equilibrium Surfaces

A more complete study of spin equilibrium surfaces will be given in Sec. 3.4, so many of the relevant equilibrium surfaces will be shown there.

The figures presented in this section have the feature that they were generated using the full eighth-order spin dynamic system, in which gravity effects are included (pitch-roll coupling) and velocity is allowed to vary. Figure 3.31 shows the r and α vs. δa surfaces for a left pro-spin control setting, $\delta e = 0°$, $\delta r = 28.3°$ (the combination $\delta a < 0°$ and $\delta r > 0°$ produces negative yaw rate). The shape of these curves is seen to be quite similar to the surface generated in the right pro-spin control region (see Figure 3.34). Later, when the non-spin system is used to qenerate the spin equilibrium surfaces, it will be seen that this shape persists, although the numerical results differ. Figure 3.32 shows that the absolute variation of V is small (about 6%), so that there is justification in assuming V constant. A surface projected onto the r-axis is presented in Figure 3.33, in which δr is the independent control and $\delta a = -15°$, $\delta e = 0°$ (left pro-spin controls). Noting again the common shape vis-a-vis Figure 3.31, the δa plot, and the fact that the right pro-spin control region possesses the same type of manifold, the right and left pro-spin manifolds are presented over the δa-δr plane as shown in Figure 3.34. Manifold A represents the right pro-spin manifold (surface) and Manifold B represents the left pro-spin manifold. Non-spin equilibrium surfaces are not shown in this figure; they would be centered about the origin and would not be in contact with either spin manifold.

While aircraft F possesses symmetry to the extent displayed by the presence of two spin manifolds of similar shape, it will be noted that the left pro-spin branches presented in this section do not possess stable segments, whereas the right pro-spin branches, shown in Sec. 3.4, do. This is a reflection of the asymmetry of the aerodynamic data which is used by the model.

3.3.6 Spin Entry Time Histories

Given that a stable, developed spin equilibrium manifold exists (for right pro-spin controls), the problem of reaching this manifold from non-spin flight conditions remains to be considered. As discussed earlier, there exists a large intermediate region between the clearly-defined spin region and the non-spin region. It corresponds to the flight regime which is often categorized "post-stall gyrations." The aircraft motion in this regime sometimes appears chaotic, with large oscillations of often-irregular frequency but is mostly of a limit cycle type. We will characterize this region as a limit cycle region based on such results as presented in Figure 3.9. It effectively acts as a barrier to a sudden jump from trim to spin conditions or vice versa. The time histories presented in this section show this behavior, and they further indicate that a large segment of this intermediate, limit cycle region is characterized by motions normally designated as oscillatory spin. Furthermore, it is usually steep ($\alpha \approx 55°$) or intermediate ($\alpha \approx 70°$) in nature, based on the mean value of angle-of-attack.

Figure 3.35 presents a case in which the controls are moved from neutral to $\underline{\delta}_{SPIN}$ at $t = 2$ seconds. (The initial flight condition is trim. $\underline{\delta}_{SPIN}$ is defined at the beginning of Sec. 3.3.) If the spin manifolds were as simple, relatively, as those of the roll departure region, say, then one would expect to see entry into developed spin. This does not happen, however. There is clearly a post-stall condition, but yaw rate does not reach the required level (about 100°/sec), and generally the energy interchange maintains a somewhat chaotic

post-stall gyration. In this run, velocity was allowed to vary. If, however, V is fixed to the value corresponding to the stable segment of the equilibrium spin manifold for the control set $\underline{\delta}_{SPIN}$ (V = 443 fps), then the rerun of the above trajectory produces a more uniform transient oscillatory behavior which decays somewhat towards a mildly oscillatory spin condition (Figure 3.36). This example points out that the role of thrust in spin entry studies must receive more attention. By forcing $\dot{V} = 0$ we are effectively maintaining thrust at a level which exactly opposes aerodynamic drag. This becomes physically unrealistic, however, in simulations where α and β undergo dramatic variations, as happens here; this means that the thrust direction is fluctuating wildly, as well as thrust magnitude.

The maneuver discussed with regards to Fig. 3.12 and 3.13 may also be considered as a spin entry sequence. Fig. 3.37 shows a variation of this maneuver in which the rudder takes the place of the aileron as the lateral control during the maneuver. As previously mentioned, the rudder plays a more critical role in converting post-stall motion into spin entry and subsequent spin motion, and Fig. 3.37 shows that an oscillatory, left pro-spin is induced by maintaining δr at 10° while the elevator is stepped from 0° to -14° in 2 second intervals, 2° at a time from t = 0. It is not in this case necessary to step δe in sequences to -14° to show this effect, but we have done so here and in other instances to observe the effect of intermediate control values. However, more care is needed in general with large control changes, as unwanted jump phenomena may occur, placing the motion in a different region than desired.

The following runs present variations on the run depicted in Fig. 3.36. In these runs, the control sequencing for spin entry was made more realistic:

$\delta e = -21°$ from t = 0 sec; δr changed from 0° to -25° at t = 2 sec; and δa changed from 0° to 15° at t = 6 sec. In addition V was fixed at 443 fps for all runs and the trajectory begins from trim conditions, as does the case shown in Fig. 3.36. The run shown in Fig. 3.38 is exactly similar to the Figure 3.36 case, except for the difference in control sequencing mentioned above. Comparison shows that the final, oscillatory state is quite similar.

Following the example of Bihrle (1976), the next runs show the effect of changing the initial roll angle from a trim value to a number such as 60°. Figure 3.39 shows that, again, the only significant difference is in the transient region, which lasts about 20 seconds. If initial pitch angle is changed to -50° in addition, Figure 3.40, the ensuing motion is substantially different. Yaw rate does not achieve the same value, and neither does angle-of-attack. These results indicate that more study of the effects of changing the initial state would be desirable. As an eventual goal, methods for determining the domains of attraction of all stable equilibria (points and limit cycles) should be developed.

3.4 Developed Spin Motion

It has been mentioned earlier that the task of effecting transition from non-spin to stable, flat spin equilibrium requires passing through a highly chaotic and oscillatory intermediate region of post-stall gyrations. It is consequently much easier to study spin behavior by making time history runs whose initial conditions correspond to $(\underset{\sim}{x}_{SPIN}, \underset{\sim}{\delta}_{SPIN})$. If the trajectory begins at

$$\underline{x}_{SPIN} = (p,q,r,\alpha,\beta,V,\theta,\phi)$$
$$= (30,-4,100,73.5,-3,443,-16.6,-2.29)$$

and

$$\underline{\delta} = \underline{\delta}_{SPIN} = (\delta a,\delta e,\delta r) = (15,-21,-25)$$

(all angular terms in degrees, V in fps), the ensuing spin motion is very smooth, as indicated by Figure 3.41. This figure shows the horizontal trace of the vehicle center of mass, and the altitude variation for the initial conditions described above. These conditions are in the middle of the stable spin equilibrium branch, Point A of Figure 3.42. At t = 15 seconds, δr is changed to -29°, so that a jump occurs to the upper limit cycle branch, Point B. The only apparent result of this δr change in Figure 3.41 is a slight tightening of the spiral, although yaw rate increases more dramatically. Figure 3.43, which time-shifts the δr change to -29° at t = 0, does confirm the growth to a limit cycle condition.

From Figure 3.41 it can be observed that the equilibrium flat spin for aircraft F generates a very tight spiral which slowly drifts to the right, due to asymmetries in the aerodynamic data. Also, it can be seen that the rate of descent is constant. Additionally, although it is not shown here, the state variables remain constant for $\delta r = -25°$, and exhibit well-damped transient behavior to new steady state values when δr is changed to -29°. Virtually all of the vehicle's velocity in this condition is vertical and the aircraft's orientation with respect to the horizon is almost "flat" ($\theta = -16°$, $\phi = -3°$), with a very high yaw rate (about 100 degrees per second). The following sections discuss these and similar results in more detail.

3.4.1 Equilibrium Surfaces in the Developed Spin Region

The typical spin equilibrium curve is seen in Figure 3.42. In this figure, δr is varied while $\delta a = 15°$ and $\delta e = -21°$ and V is fixed at 443 fps. A very similar curve is shown in Figure 3.44. Here, $\delta e = 0°$ but that is the only difference from Figure 3.42. Obviously, the elevator has little effect on this particular type of spin motion. Both of these surfaces were generated using the non-spin equilibrium set, neglecting gravity.

Choosing $\delta r = -25°$, the projection along δa is shown for α in Figure 3.45. Again, $V = 443$, $\delta e = 0°$ and the non-spin set (which neglects gravity) is used. If δe is changed to $-21°$, the α vs. δa branch shown in Figure 3.46 results.

Finally, a composite of all of the relevant equilibrium points, for all relevant control states, is projected onto the $(r-\alpha)$ plane (Fig. 3.47). These variables are the most significant ones in terms of analyzing spin motion. Very noticeable is the "gap" between the non-spin and spin regions.

3.4.2 Importance of Assumptions Concerning Spin Equilibria; Comparisons

In this section the significance and validity of some of the assumptions relevant to generating the spin region equilibrium surfaces is discussed. This is done mainly by means of comparison of various effects.

One result mentioned in the last section is that, once the aircraft is in the stable flat spin condition, elevator controllability becomes negligible. This is readily seen by comparing Figure 3.42, where $\delta e = -21°$, with Figure 3.44 where $\delta e = 0°$. Figure 3.48 shows the

small effect of δe in this spin equilibrium region. Only roll rate is moderately affected as δe takes values of 0°, -11° and -21°; and angle-of-attack, surprisingly, is effectively unchanged. A possible explanation is the large value of local sideslip at the elevator locations, generated by the large steady yaw rate. Notice that $V = 600$ in this figure.

Of somewhat more importance, however, is the validity of the assumptions of fixing velocity and neglecting gravity effects in the spin region. If this assumption can be accepted as valid for initial phases of analysis of spin motion, then spin region equilibrium and bifurcation surfaces can be generated by the simpler 5 DOF non-spin system of equations. Figure 3.49 shows that, at least for aircraft F in the flat spin region, the simplifying assumption $V = \text{const}$, $g = 0$ may be used for initial spin analyses. In fact, changing the velocity is seen to produce greater differences than neglecting gravity. In this figure, $\delta a = 15°$ and $\delta e = -21°$; also, the $g \neq 0$ branch, because it was run using the full spin system, does not have associated with it a constant velocity. However, as Figure 3.32 shows, the V range is only about 20 fps. Another surprising result is the total insensitivity of angle-of-attack to these changes.

A conclusion to be drawn from this comparison is that, for flat developed spin using the aircraft F model, since pitch angle is small (about 15°) and $\alpha \simeq 90°$, the term $\cos \alpha \sin \theta$, which couples gravity into the $\dot{\alpha}$-equation, is quite small. Furthermore, gravity does not directly couple into the $\dot{p}$ and $\dot{r}$ equations, as does V (through dynamic pressure and by influencing the aerodynamic coefficients).

Another observation of practical significance is that only one consistent set of assumptions is needed in order to generate a truly global equilibrium surface, examples of which are shown in Figs. 3.9, 3.50 and 3.51. One needs only to choose a "reasonable" value for V in order to generate these figures with the easier non-spin equations. Notice that it is not possible--and we did make simulation runs to verify this--to use the spin equations, with nonzero gravity, to produce equilibrium manifolds in non-spin regions; roll and pitch angles, which must be included in this system, have no equilibrium values in most non-spin regions.

3.5 Spin Recovery and Prevention

In terms of the concepts employed by BACTM to analyze aircraft behavior, it is possible to state the goal of spin recovery as follows: spin recovery is achieved by control sequences which move the equilibrium point from a stable spin region to either an unstable spin equilibrium point or a point on a non-spin equilibrium branch, stable or unstable, from which other control actions can produce trim conditions. A jump from one stable equilibrium to another in the spin regime is undesirable.

With regard to prevention of spin situations, it will be seen that the rudder is the most sensitive aerosurface control for aircraft F, in terms of spin entry. The aileron also has considerable influence, but with this particular model, rudder influence predominates. In view of this, high-speed/large-attitude-change maneuvers which require large elevator and aileron deflections (e.g., a rolling pull-up maneuver) become very prone to spin-entry situations unless use of the rudder is carefully controlled.

The next section deals with some of the aspects of spin recovery, based on BACTM analysis using aircraft F, and the following section will cover aspects of spin prevention.

3.5.1 Spin Recovery with Aircraft F

For aircraft F, a right pro-spin control setting of $(\delta a, \delta e, \delta r)=(15°,-21°,-25°)$ designated $\underline{\delta}_{SPIN}$, represents the "spin control setting." This setting, along with the proper values of the state variables, $\underline{x}_{SPIN}$, results in a flat, equilibrium spin. See Point A in Fig. 3.42. The magnitude and sign sense of the controls $\underline{\delta}_{SPIN}$ is very representative of similar spin settings

of other aircraft; the elevator (δe) is large and negative, to provide the high α needed for stall and subsequent spin (although once in stable spin, the aircraft F equilibrium state is quite insensitive to elevator control actions--see Figure 3.48); the aileron (δa) is at its extreme setting, of opposite sign to the rudder (δr); and the large negative rudder generates the high positive yaw rate which signifies the development of spin behavior following post-stall gyrations. The aileron is of opposite sign in a spin setting because of the effect of adverse yaw due to the aileron; that is, for a positive yaw rate ($\delta r < 0$), a negative roll rate ($\delta a > 0$) induces a positive yaw moment, thereby enhancing the yaw rate. In a coordinated turn, both δa and δr have the same sign, and yaw rate (r) is predominantly sensitive only to δr. Proper sequencing of controls for spin entry is important, because hysteresis effects are especially prominent in these high-α regions. For example, the elevator is a much more effective control for spin entry when it is applied while sideslip (β) is still small in magnitude. This is consistent with the usual circumstance of spin following a stall; and the elevator typically induces stall because of its direct influence on angle-of-attack. See Fig. 3.10. Furthermore, elevator control effectiveness is practically nonexistent for high values of β.

When a significant yaw rate is added to post-stall motions, and when angle-of-attack (α) approaches values for which autorotation in yaw is possible (i.e., $C_n \approx 0$), then entry into spin will most likely result. For

aircraft F, $C_n \simeq 0$ around $\alpha = 65°$. Spin may be considered a form of autorotational yawing. This is a condition marked by a general ineffectiveness of the lateral controls. However, by using the equilibrium surfaces, recovery control sequences can be developed.

The standard method for spin recovery is to rapidly proceed to an anti-spin setting--i.e., for our example, this would involve zeroing the elevator and fixing δr and δa at their opposite extremes. This and similar techniques based on aerosurface control actions alone are not always effective, and aircraft are often equipped with special thrusters and drag parachutes for spin recovery purposes. However, it is possible to effect recovery from spin with the aircraft F model, and Fig. 3.9 indicates how this may be done.* This figure shows the equilibrium surfaces for $\delta a = 15°$, $\delta e = 0°$, $V = 600$ and $g = 0$.

From the spin state, the elevator is returned to the neutral position; this corresponds to point A in Fig. 3.9 . Then, the rudder is increased from -25° to at least 15°. This will induce two jumps, the first one to a limit cycle around point B, and the second to a limit cycle around point C on the lower branch. Then δr may be decreased to 0° (point D), as this last equilibrium branch passes through small values for α and r. These control actions must be taken over a long enough period to allow the transient motions to die out. Point D in Fig. 3.9 corresponds to point D in Fig. 3.16, which is an equilibrium surface showing the final recovery sequence: roll rate p is reduced by returning the aileron to its neutral setting. Note that it involves a control effort (change in rudder from one extreme setting to the other) which is used in practice for spin recovery. Again, the equilibrium surfaces generated by BACTM tend to confirm previous results and past

*There are other possibilities which we shall try to investigate at a later time, with more comprehensive models, such as the F-4.

experience, while at the same time pointing out alternative possibilities (which we expect to explore in more detail at a later time). A further characterization of the limit cycle behavior is required for obtaining optimal recovery procedures. This is because more information needed about the limit cycle domains of attraction in the sensitive intermediate-α region ($25° \lesssim \alpha \lesssim 65°$). Eventually, a complete calculation of the bifurcation surfaces (both Hopf and elementary) should be done for spin recovery control design.

Another possibility for a spin recovery strategy "leading with δa" is presented in Fig. 3.50. Here, δa is reduced from 15° so that a jump occurs, to a limit cycle condition around point B from point A (the latter point is the same point A in Fig. 3.9). This jump will actually increase p, the roll rate, but this is a desirable method of rolling the aircraft into the airflow, which reduces α, as can be seen. The final step, then, is to reduce δr in magnitude to its neutral setting, and Fig. 3.15 shows that this returns (r,α,p) to trim values. Similarly, time history runs confirm this. As with Fig. 3.9, Fig. 3.50 represents equilibrium conditions for $\delta e = 0°$, $V = 600$ fps and $g = 0$.

It should be recognized that excessive application of the "anti-spin" control actions, in attempting to effect spin recovery, can lead to a "reverse spin" situation if the controls are not moved towards neutral quickly enough. A common method of spin recovery is to oscillate the controls, particularly δa and δr, back and forth between their limits. The frequency of the oscillations is usually determined by visual cues available to the pilot, in conjunction with the autopilot. Fig. 3.51 shows a

spin reversal situation. At 42 seconds, the controls were changed from right pro-spin ($\delta a, \delta e, \delta r$) = (15°,-21°,-30°), to left pro-spin, (-15°,-21°,30°). It can be seen that, within 5 or 6 seconds, the yaw rate has changed sign but not magnitude, and the basic spin condition remains otherwise unaffected.

3.6 Explanation of Spin Behavior of Aircraft F

As with other aircraft analyzed in the literature for spin behavior, the main feature of aircraft F in developed spin is an extremely high angle-of-attack and persistent, steady yaw rate. The presence of these conditions simultaneously, without major fluctuation between high and low values of r and α, indicates the spin condition. Once the aircraft has been maneuvered into a stall condition, both the equilibrium surfaces and the time history simulations indicate that wild, oscillatory post-stall oscillations and gyrations result. The aircraft has entered a flight regime lacking in stable equilibrium points; if the lateral controls have been set to "pro-spin" positions just prior to or at the onset of stall, then the yawing motion will predominate the post-stall dynamics. If inertia coupling and aerodynamic forces and moments are then phased together so that the values of angle-of-attack and sideslip generate negligible yaw-moment coefficient, C_n, then the yawing motion will become autorotational. For aircraft F, this will occur when α is about 70° and β is within ±10°. In a "pro-spin" control setting, the aileron is moved in the opposite sense to the rudder, and both controls are typically at or close to their extreme values. Thus if aileron is positive, for negative roll rate, but the rudder is negative, the positive yaw rate generated by the rudder will be enhanced by the adverse aileron yaw.

The transition dynamics from trim condition to spin equilibrium for aircraft F involves limit cycle oscillations. A thorough analysis of the generation and interplay of the aerodynamic, inertial and gravitational

forces and moments is not merited for this model, since aerodynamic data were developed in order to simulate full spin motion. However, it is felt that post stall gyrations produced by the model are similar, in general, to what is actually experienced in flight tests of military aircraft.

The model limitations and open-loop nature of the simulation make complete transition from trim conditions, controls neutral, to stable, developed spin a very difficult task. The equilibrium surfaces are useful starting points, but in regions where stable branches are nonexistent, they cannot predict easily the nature of the motion to be encountered in that region. Thus, an exhaustive series of runs would be required in order to proceed completely from trim to spin. However, we have been able to show that by making two runs, one with initial conditions at $(\underset{\sim}{x}_{SPIN}, \underset{\sim}{\delta}_{SPIN})$ and the other at trim, that respective control sequences may be chosen, using the information provided by the equilibrium surfaces, so as to bring them to a common final state. Fig. 3.52 shows a trajectory which began in a spin condition. At 0.5 seconds, the rudder was changed from -25° to 25°, and δa changed from 15° initially to 7.5° (t = 20 seconds) and 0° at 30 seconds. The resulting oscillatory spin matches very closely the final condition of the trajectory shown in Fig. 3.53, which began in trim and had the following control sequence:

time (seconds)	δa	δe (degrees)	δr
0	15	-11	0
2.	15	-11	1.5
8.	15	-11	7.0
30.	15	-11	11.3
40	15	-11	14.0
50	15	-11	11.3
60.	15	0.	25.
70.	0.	0.	25.

This is an important result in that it does show that the model produces motions that proceed from trim to spin and vice versa. As the equilibrium surfaces show, there exist several attractors (both points and orbits) and their associated domains of attraction which make it very difficult to effect excursions in the state-control space. We have effectively combined two runs which take advantage of more favorable equilibrium structures in their respective starting regions and brought them to a common point. From this point, completely new control sequences must be used in order to return to either starting point. The composite equilibrium surfaces shown in Fig. 3.9 and 3.50, for $\delta e = 0°$, show that the jump form the spin condition to highly oscillatory regions is much easier than going in the reverse direction. Here, it can be seen that the jump is to a limit cycle surface in the $(\delta a, \delta r)$ plane. Once the jump occurs, elevator controllability becomes more prominent, as can be seen by comparing Fig. 3.9 with Fig. 3.54, which has $\delta e = -11°$. The elevator change does not appreciably affect the shape of the spin equilibrium branch, but greatly changes the non-spin branch.

The ease with which one can move from one point to the other along the equilibrium surfaces is influenced greatly, as mentioned above, by the structural stability properties of these surfaces in control space. Another related factor is the location of the attractors in this space and the various "domains of attraction." Based on our results, it seems that the domain of attraction for the stable segment of the spin equilibrium branch is much smaller than neighboring domains of attraction of limit cycles. This necessitates precision control sequencing, sensitively attuned to the current state, in order to achieve stable spin.

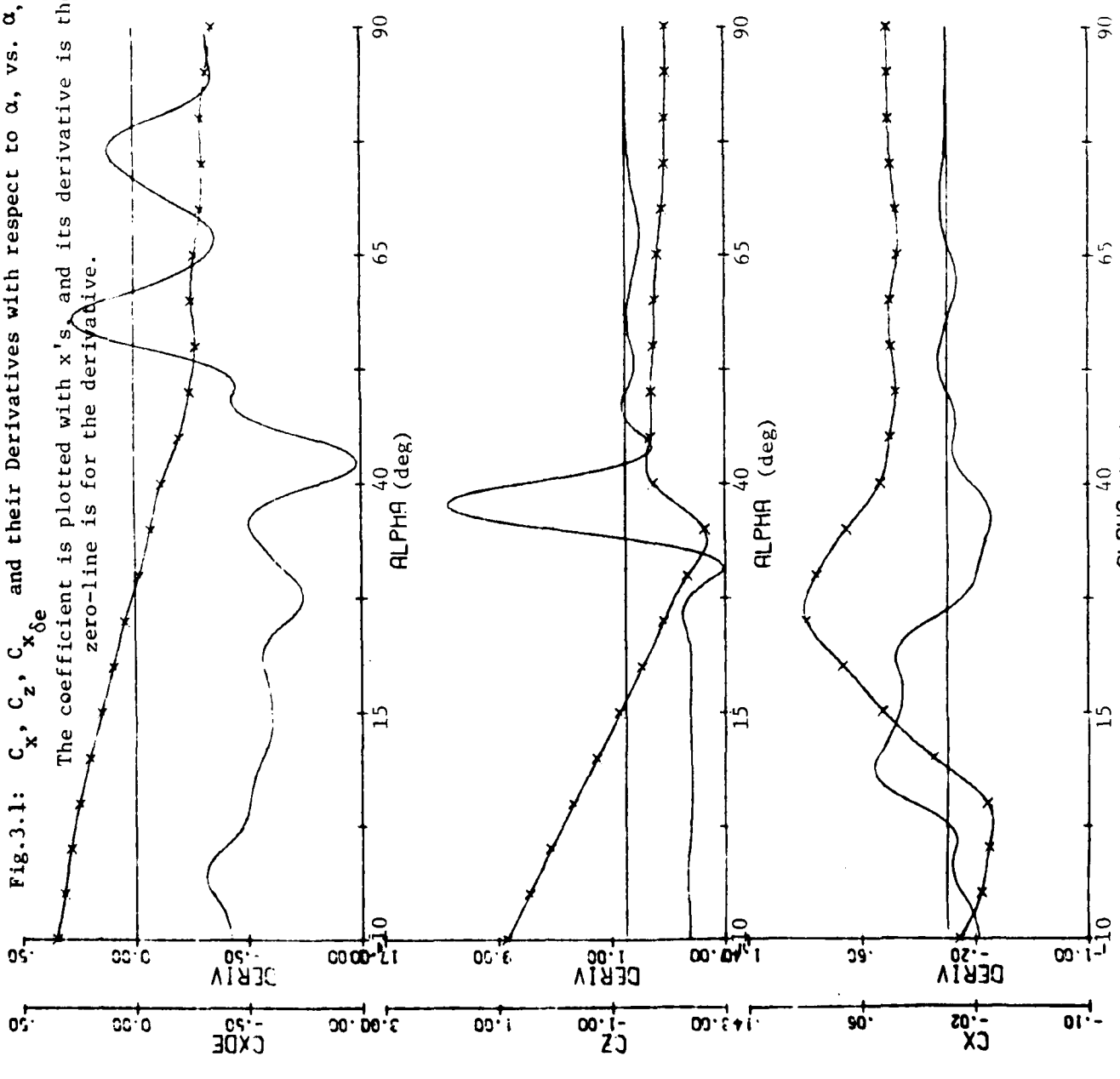

Fig.3.1: C_x, C_z, $C_{x_{\delta e}}$ and their Derivatives with respect to α, vs. α, Aircraft F.
The coefficient is plotted with x's, and its derivative is the smooth line. The zero-line is for the derivative.

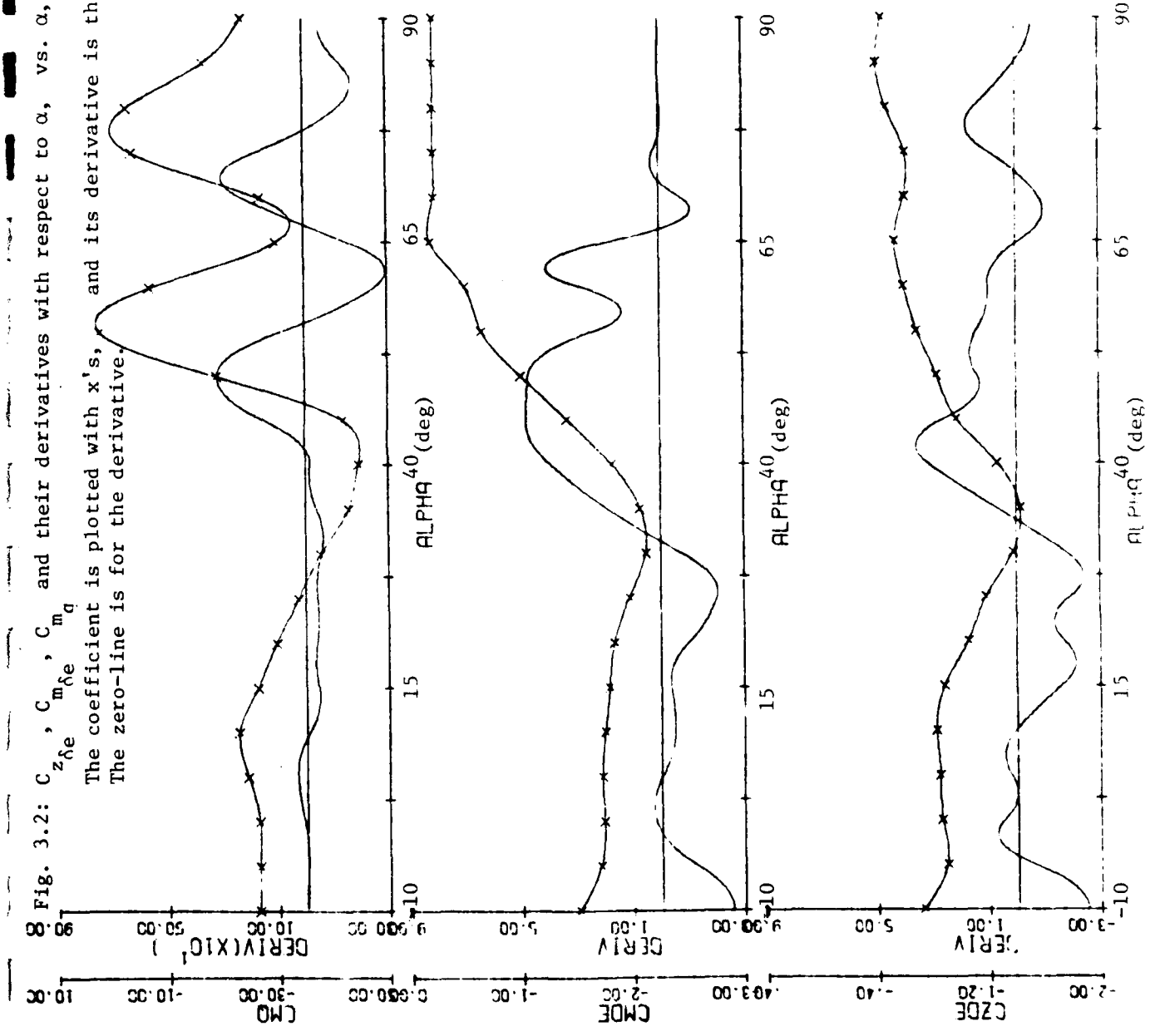

Fig. 3.2: $C_{z_{\delta e}}$, $C_{m_{\delta e}}$, C_{m_q} and their derivatives with respect to α, vs. α, Aircraft F
The coefficient is plotted with x's, and its derivative is the smooth line.
The zero-line is for the derivative.

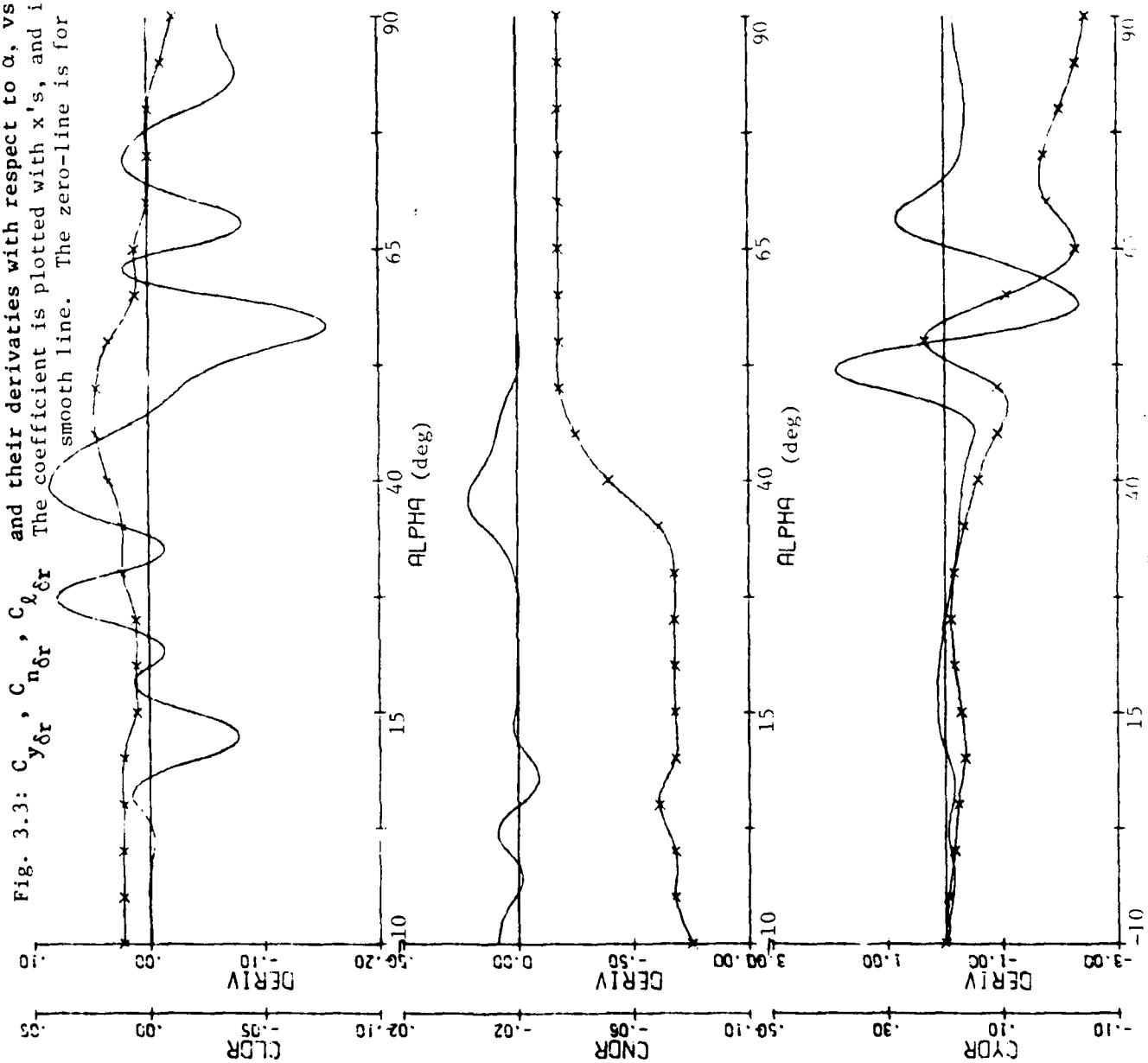

Fig. 3.3: $C_{y_{\delta r}}$, $C_{n_{\delta r}}$, $C_{l_{\delta r}}$ and their derivaties with respect to α, vs. α, Aircraft F. The coefficient is plotted with x's, and its derivative is the smooth line. The zero-line is for the derivative.

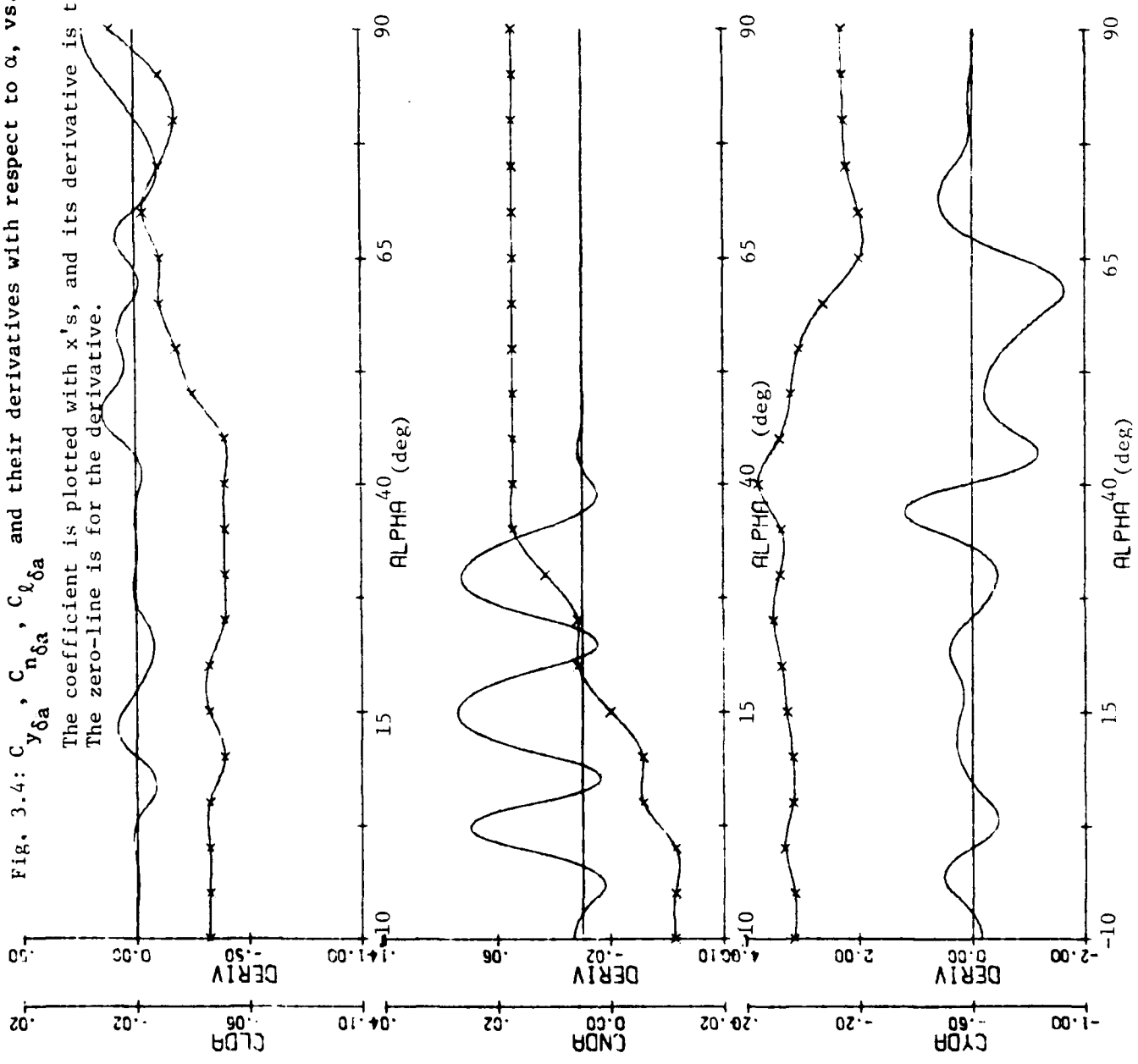

Fig. 3.4: $C_{y_{\delta a}}$, $C_{n_{\delta a}}$, $C_{\ell_{\delta a}}$ and their derivatives with respect to α, vs. α, Aircraft F.
The coefficient is plotted with x's, and its derivative is the smooth line.
The zero-line is for the derivative.

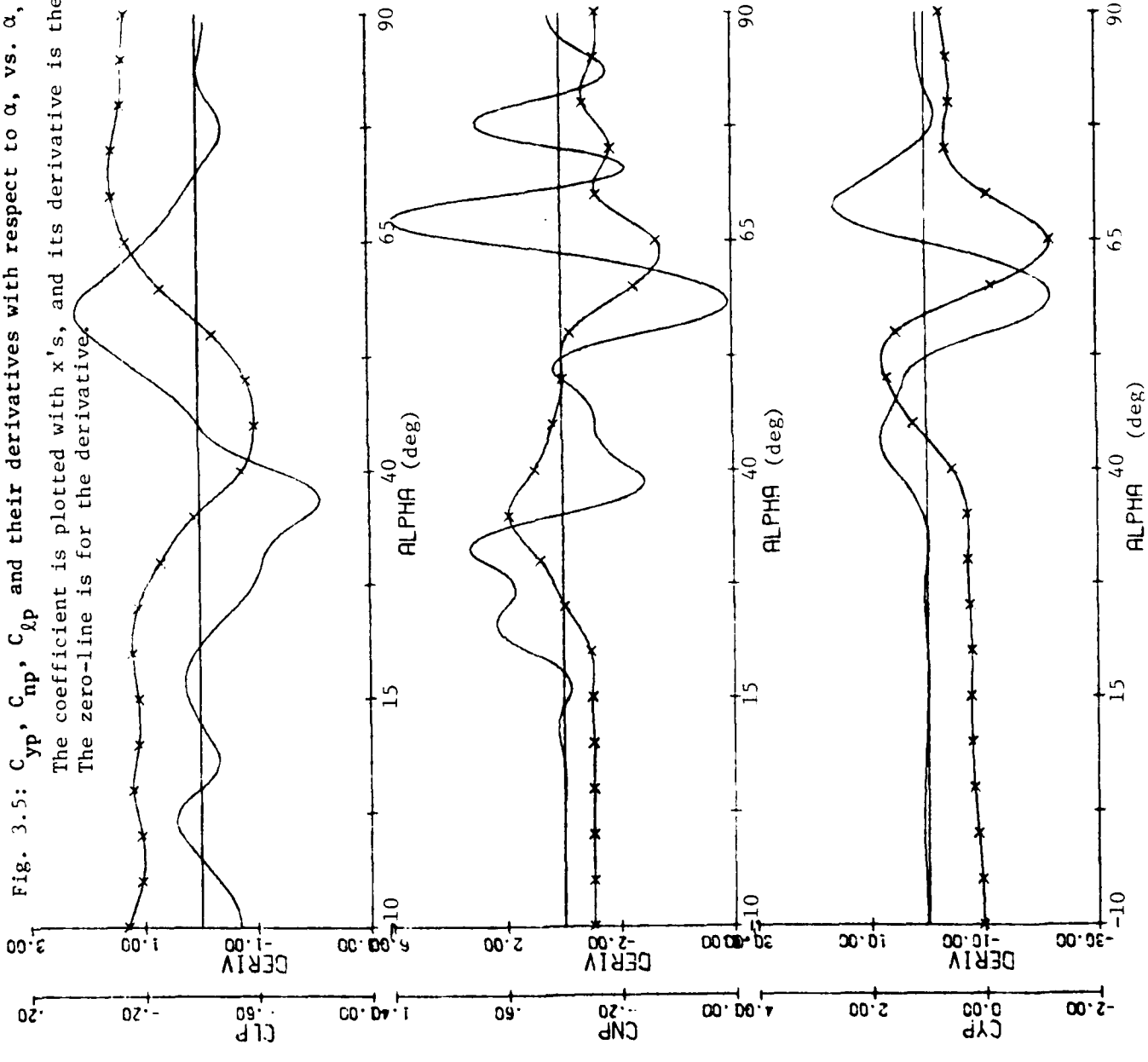

Fig. 3.5: C_{yp}, C_{np}, $C_{\ell p}$ and their derivatives with respect to α, vs. α, Aircraft F.
The coefficient is plotted with x's, and its derivative is the smooth line.
The zero-line is for the derivative.

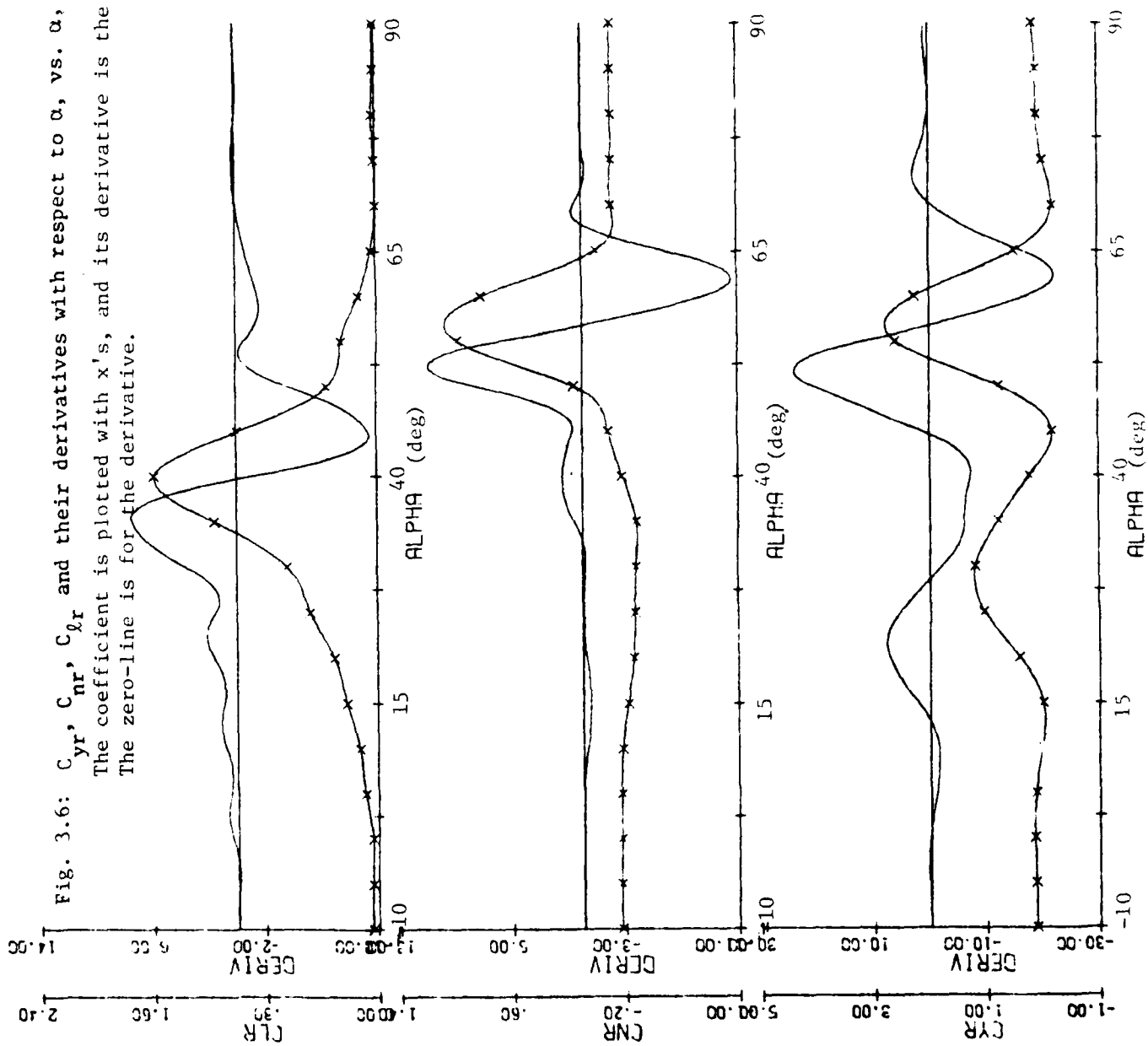

Fig. 3.6: C_{yr}, C_{nr}, $C_{\ell r}$ and their derivatives with respect to α, vs. α, Aircraft F.
The coefficient is plotted with x's, and its derivative is the smooth line.
The zero-line is for the derivative.

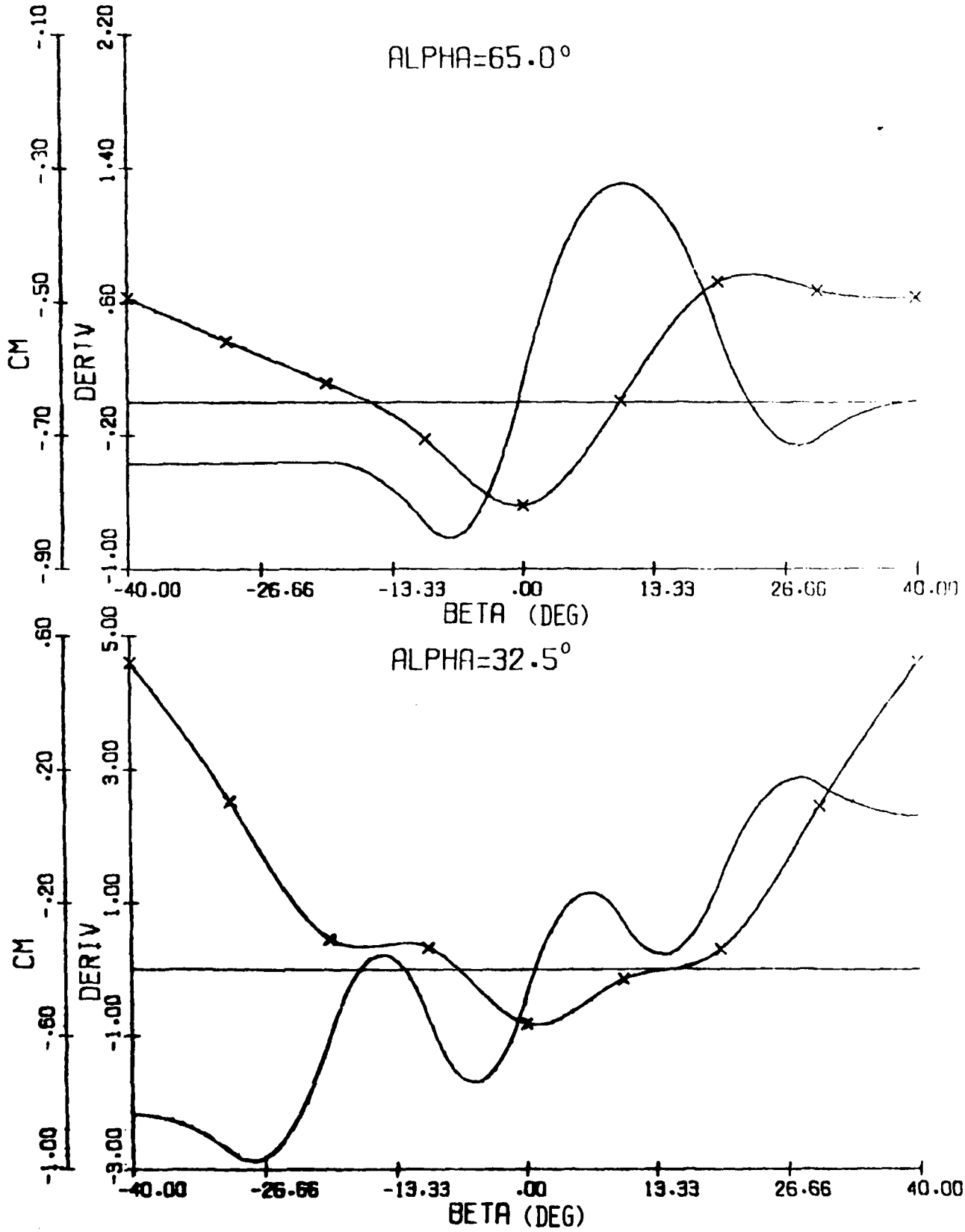

Fig. 3.7: $C_m(\alpha,\beta)$, with x's, and $\partial C_m/\partial\beta$, smooth, vs. β; $\alpha = 65°$, 32.5°

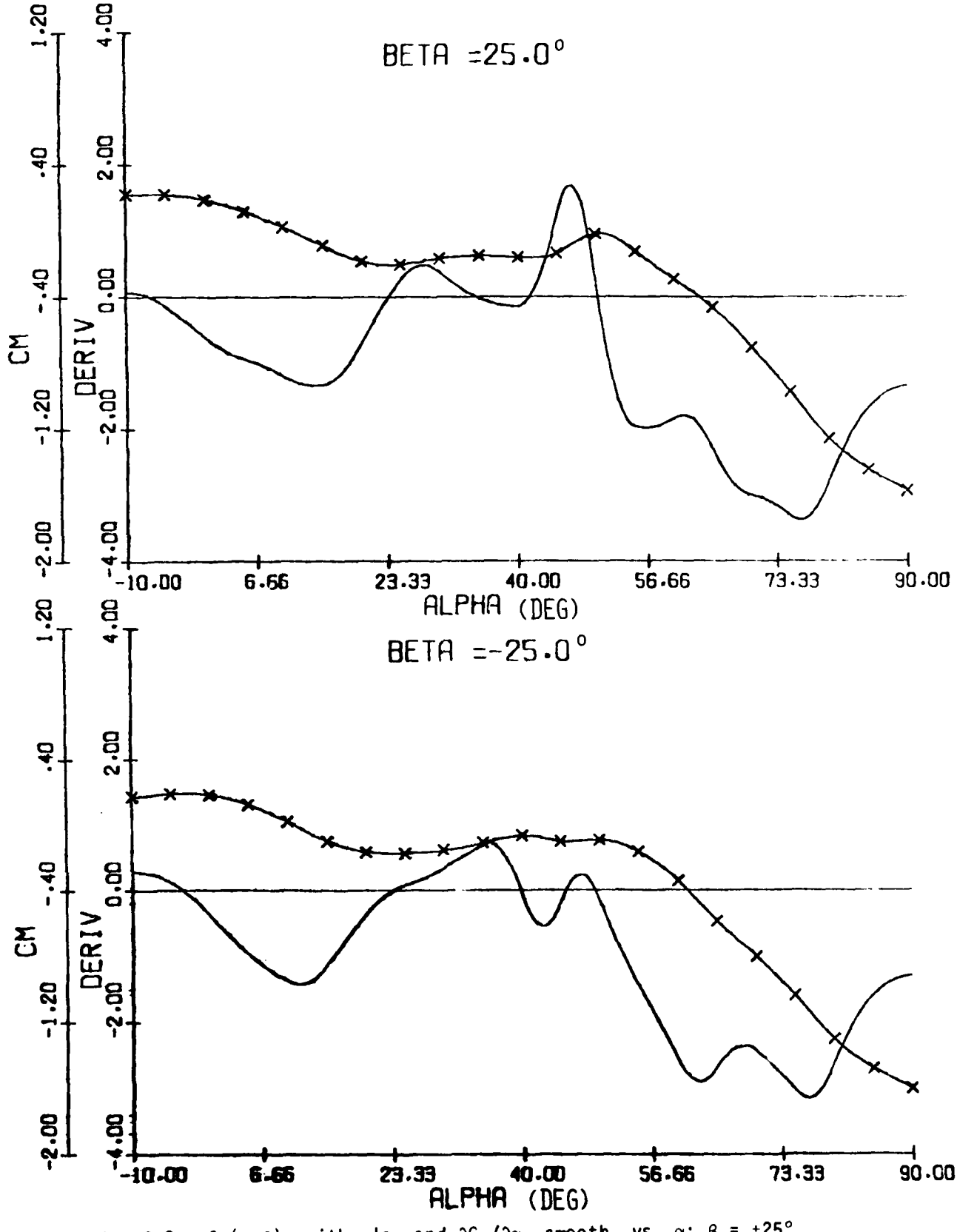

Fig. 3.8: $C_m(\alpha,\beta)$, with x's, and $\partial C_m/\partial\alpha$, smooth, vs. α; $\beta = \pm 25°$

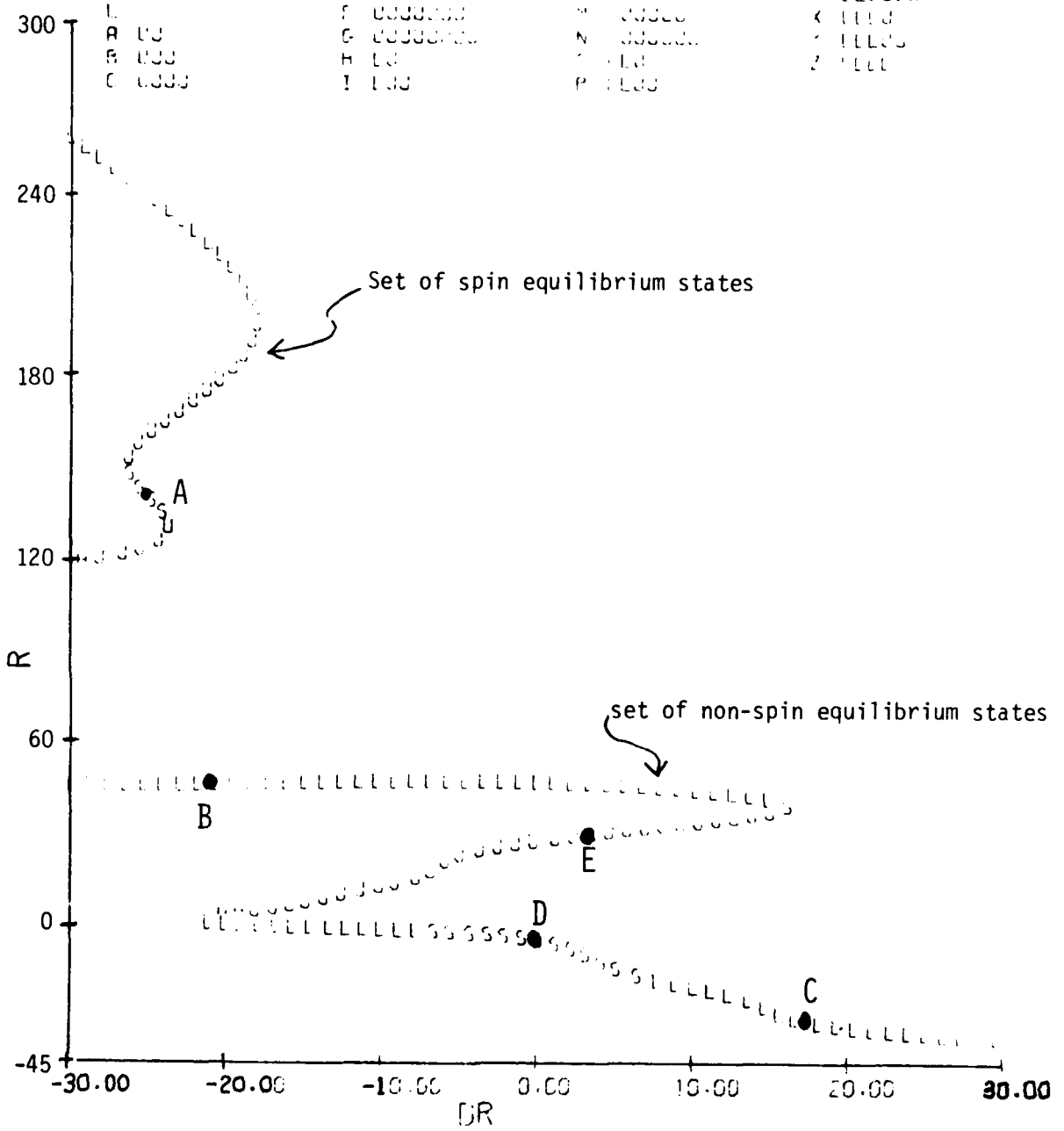

FIGURE 3.9(a)
Equilibrium Surface: r,α,p vs. δr
δa = 15°, δe = 0°, V = 600 fps, g = 0

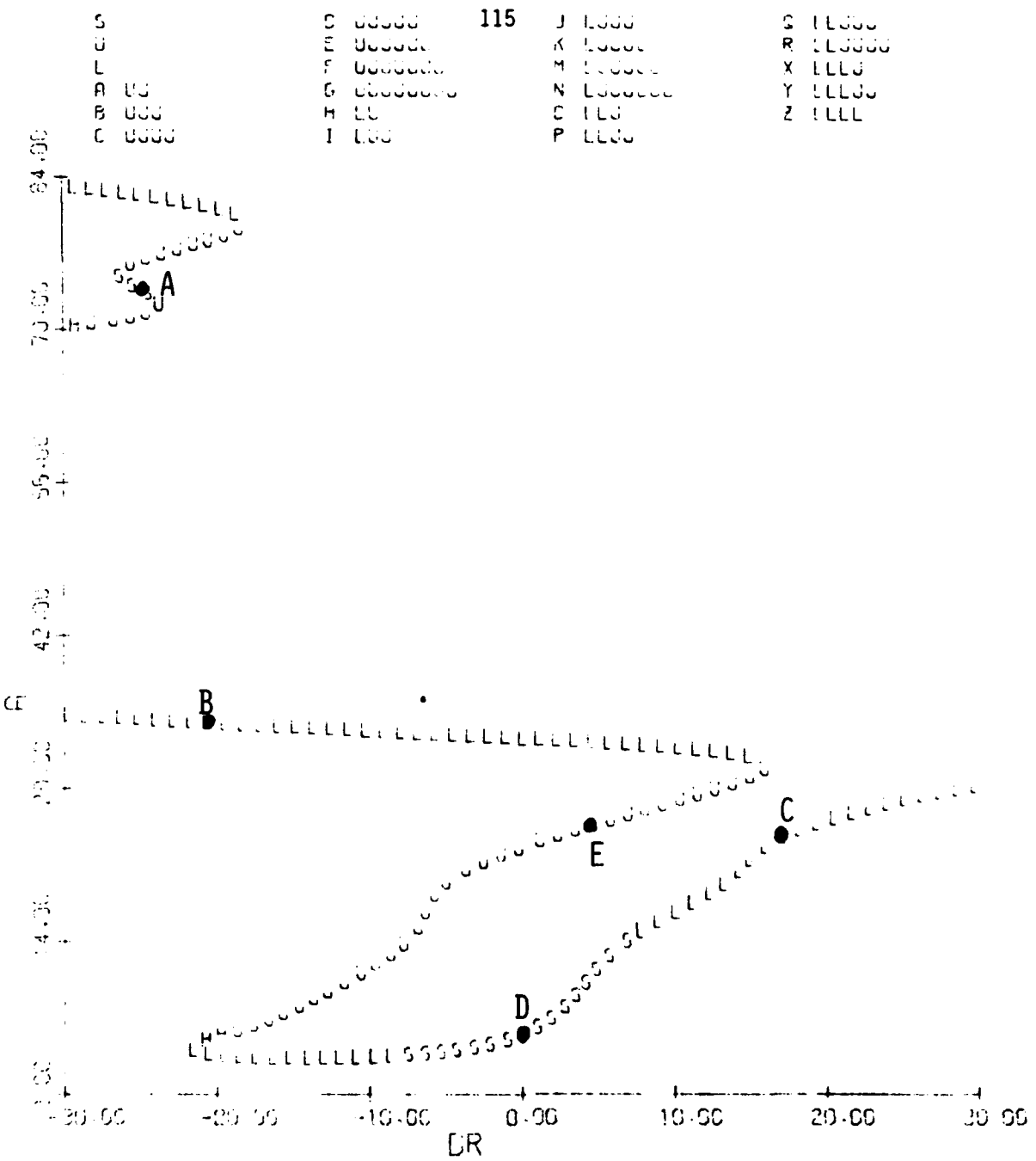

FIGURE 3.9(b) (cont.)

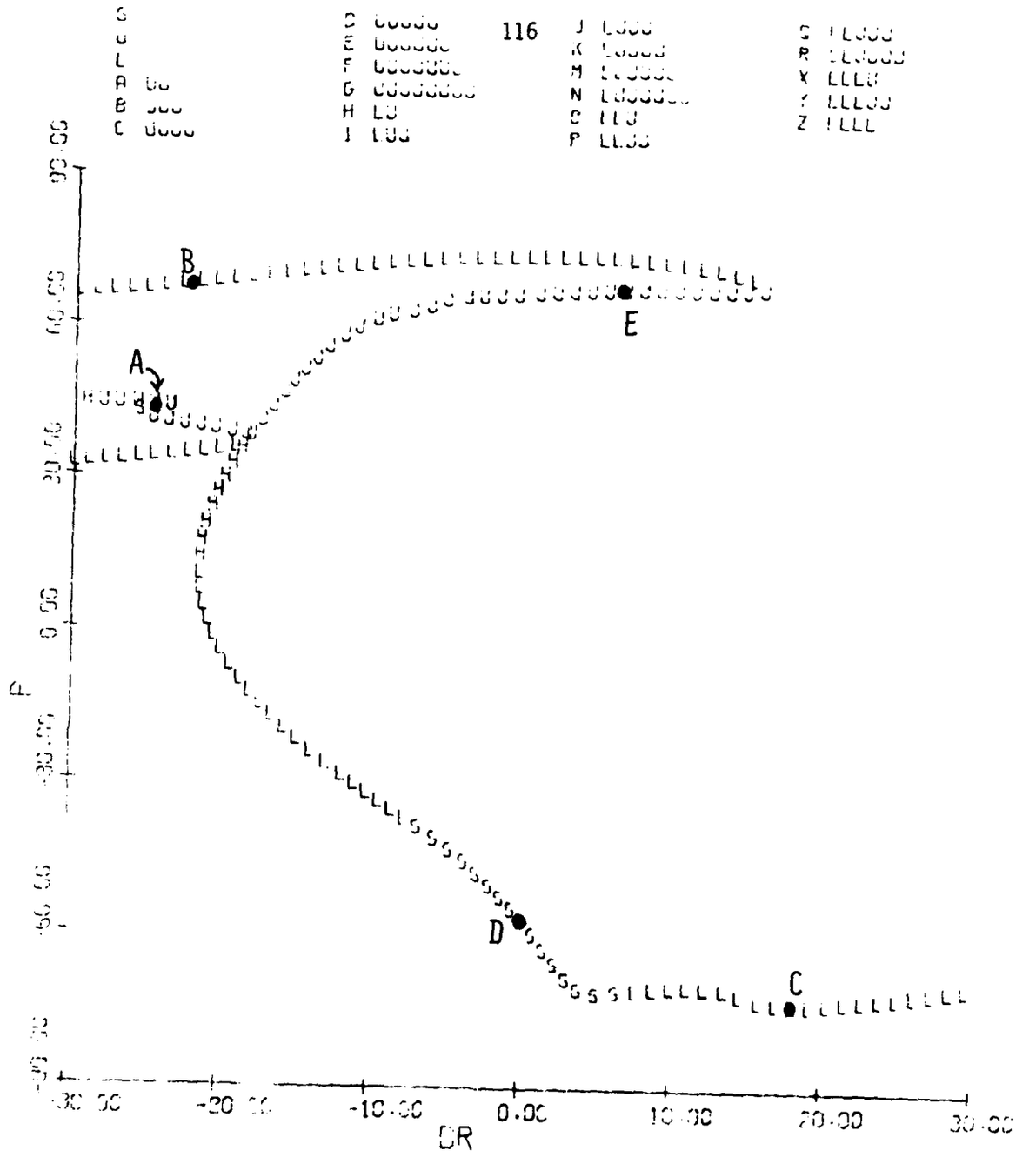

FIGURE 3.9(c) (concluded)

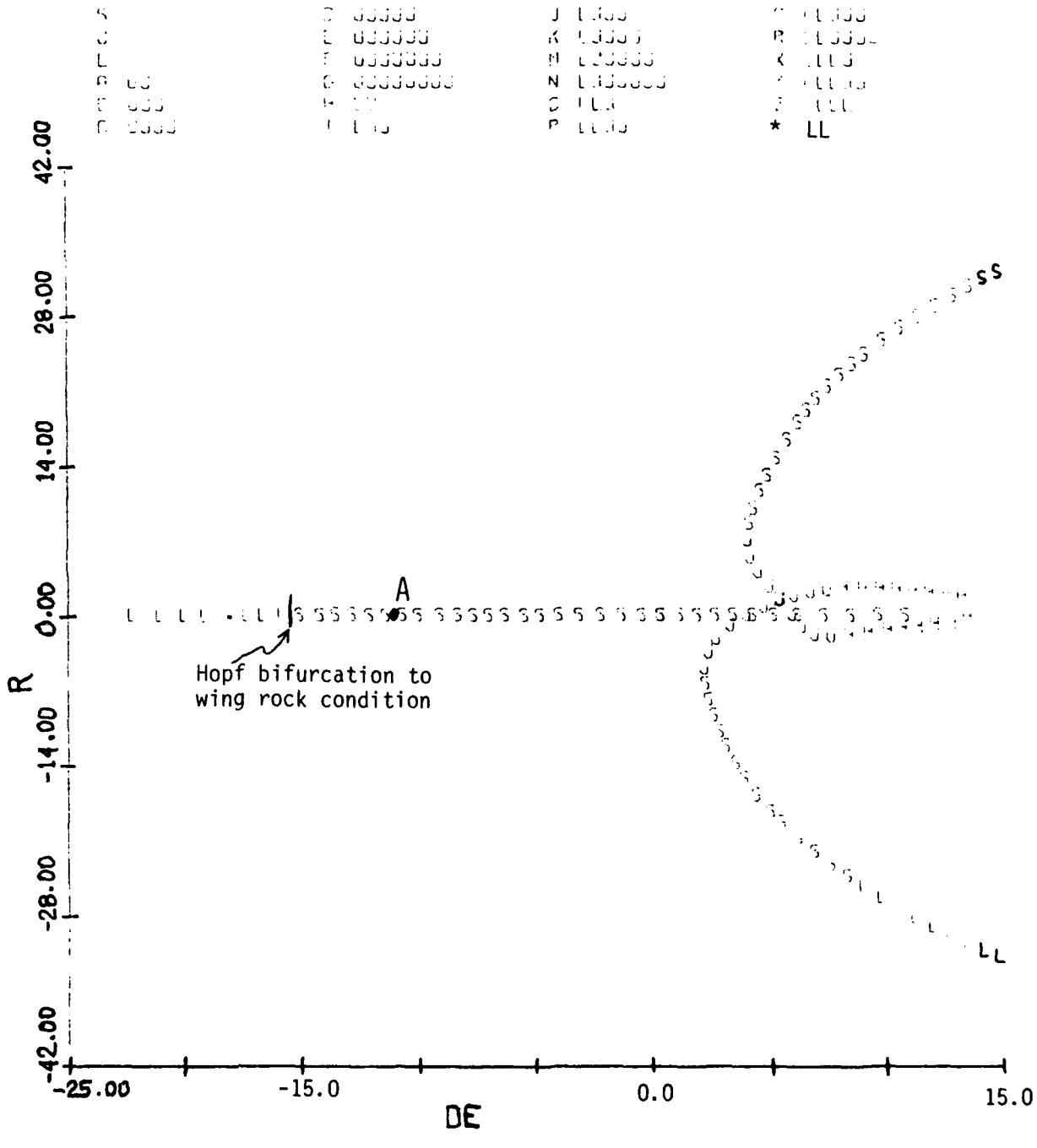

FIGURE 3.10(a)
Equilibrium Surface: r,α,p vs. δe
δa = 0°, δr = 0°, V = 600 fps, g = 0

The * refers to an LL instability

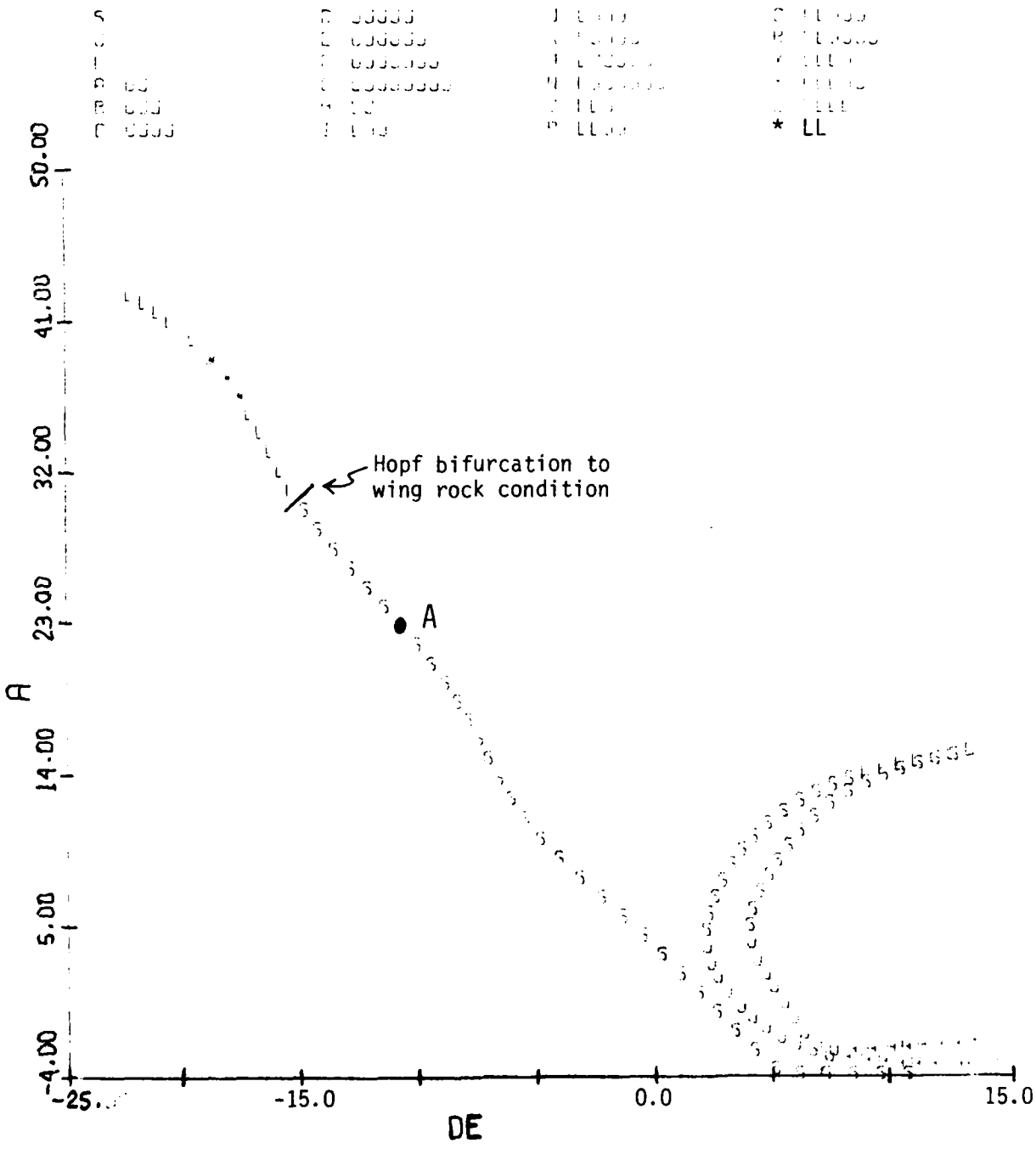

FIGURE 3.10(b) (cont.)

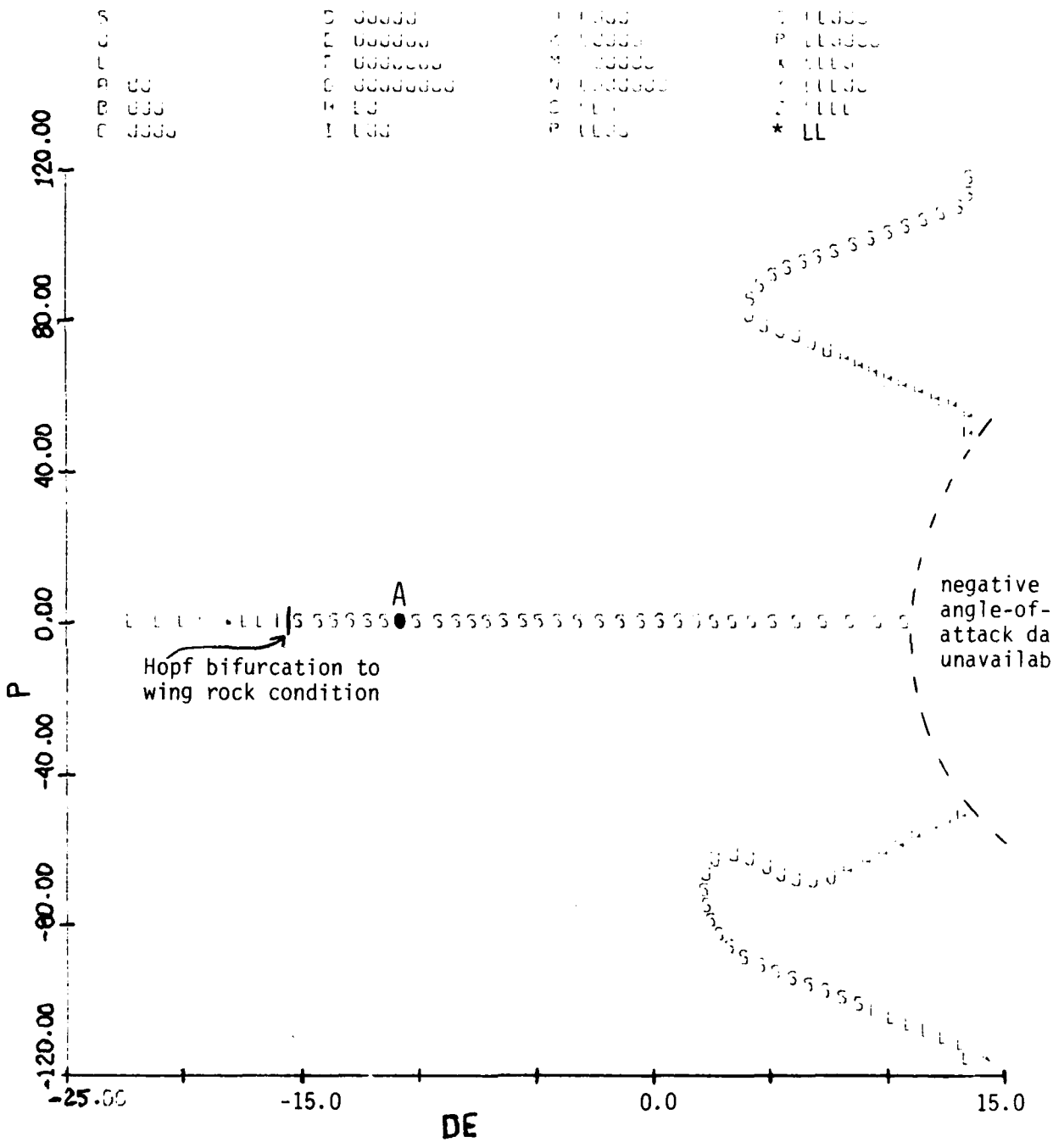

FIGURE 3.10(c) (concluded)

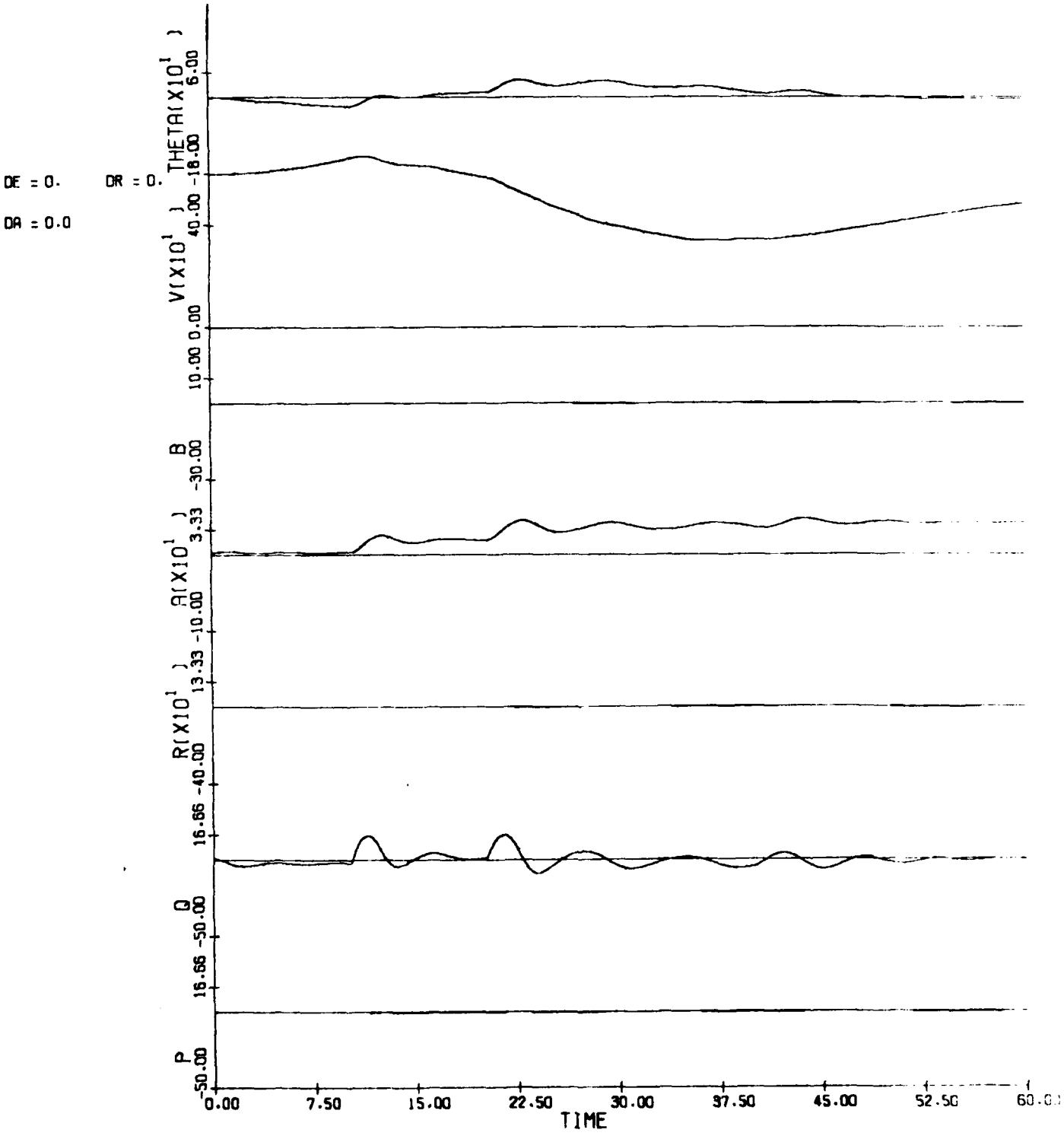

Figure 3.11(a)
Time History: Wing Rock Study; $\delta a = 0°$, $\delta r = 0°$

$$\delta e = \begin{cases} 0°, & t<10 \\ -9°, & 10 \leq t \leq 20 \\ -17°, & 20 \leq t < 40 \\ -21°, & t \geq 40 \end{cases}$$

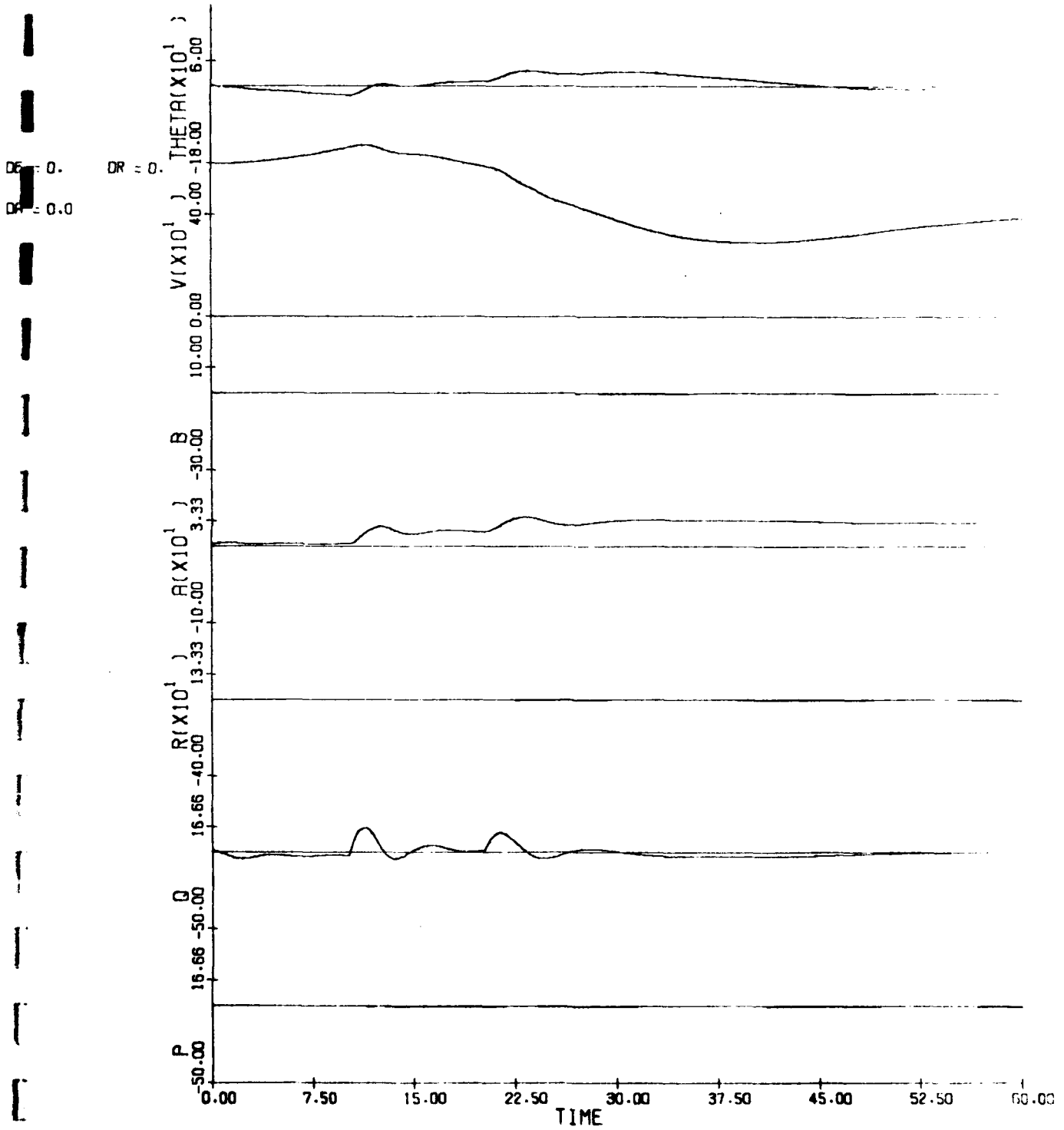

FIGURE 3.11(b) (cont.)

$$\delta e = \begin{cases} 0, & t<10 \\ -9, & 10 \leq t < 20 \\ -15, & t \geq 20 \end{cases} \qquad \delta a = \begin{cases} 0°, & t < 20 \\ -15°, & t \geq 20 \end{cases} ; \quad \delta r = 0°$$

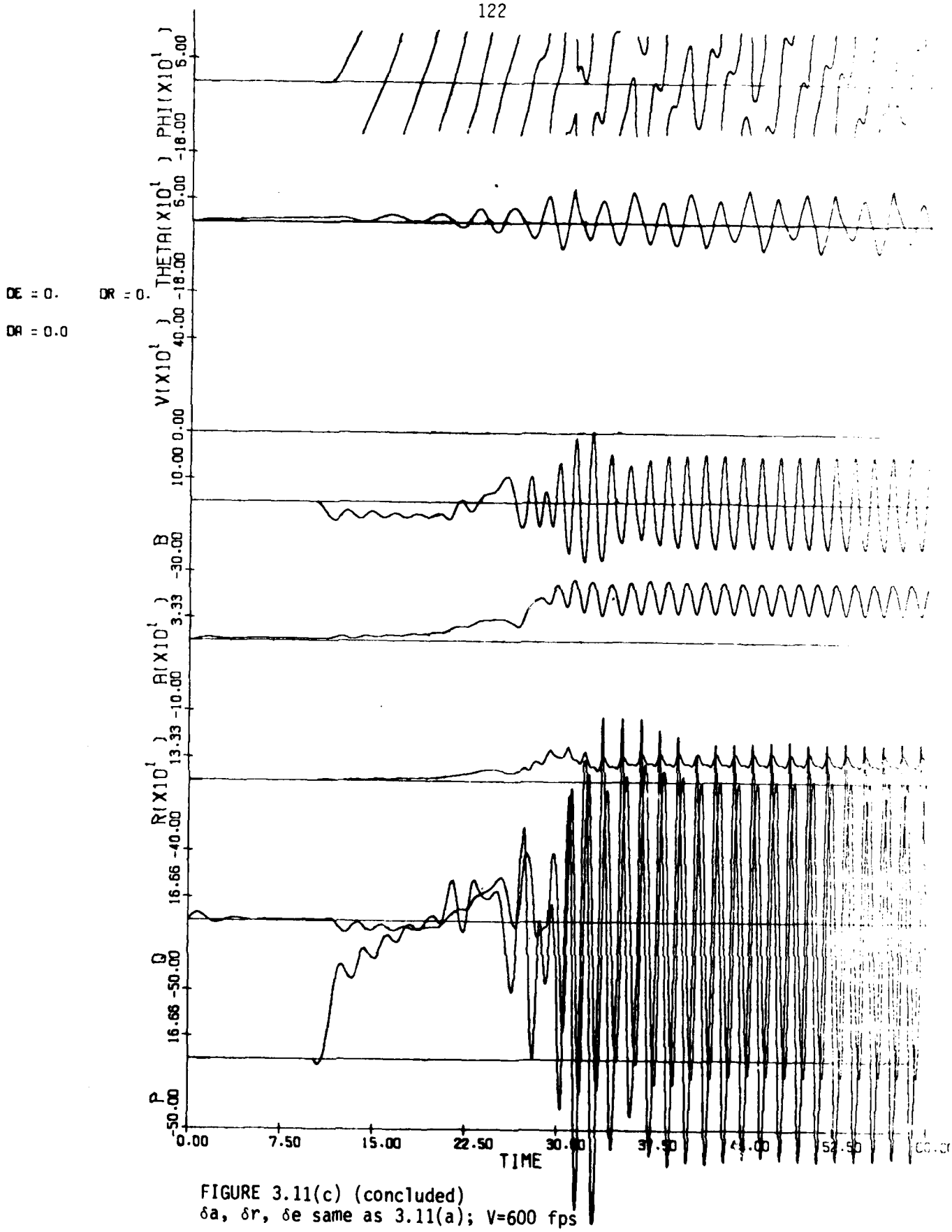

FIGURE 3.11(c) (concluded)
δa, δr, δe same as 3.11(a); V=600 fps

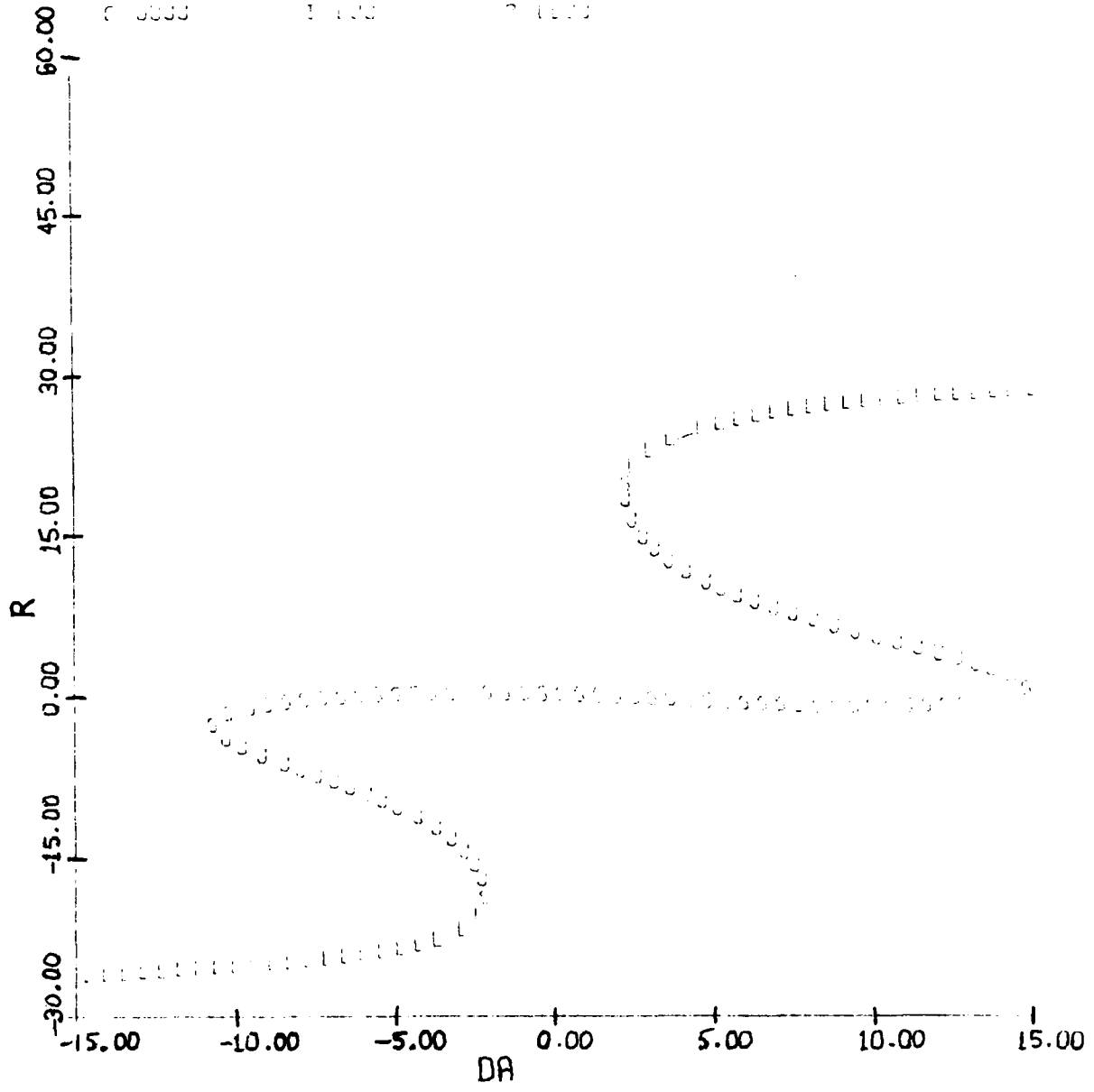

FIGURE 3.12(a)
Equilibrium Surface: r,α,p vs. δa
δe = -11°, δr = 0°, V = 600 fps, g = 0

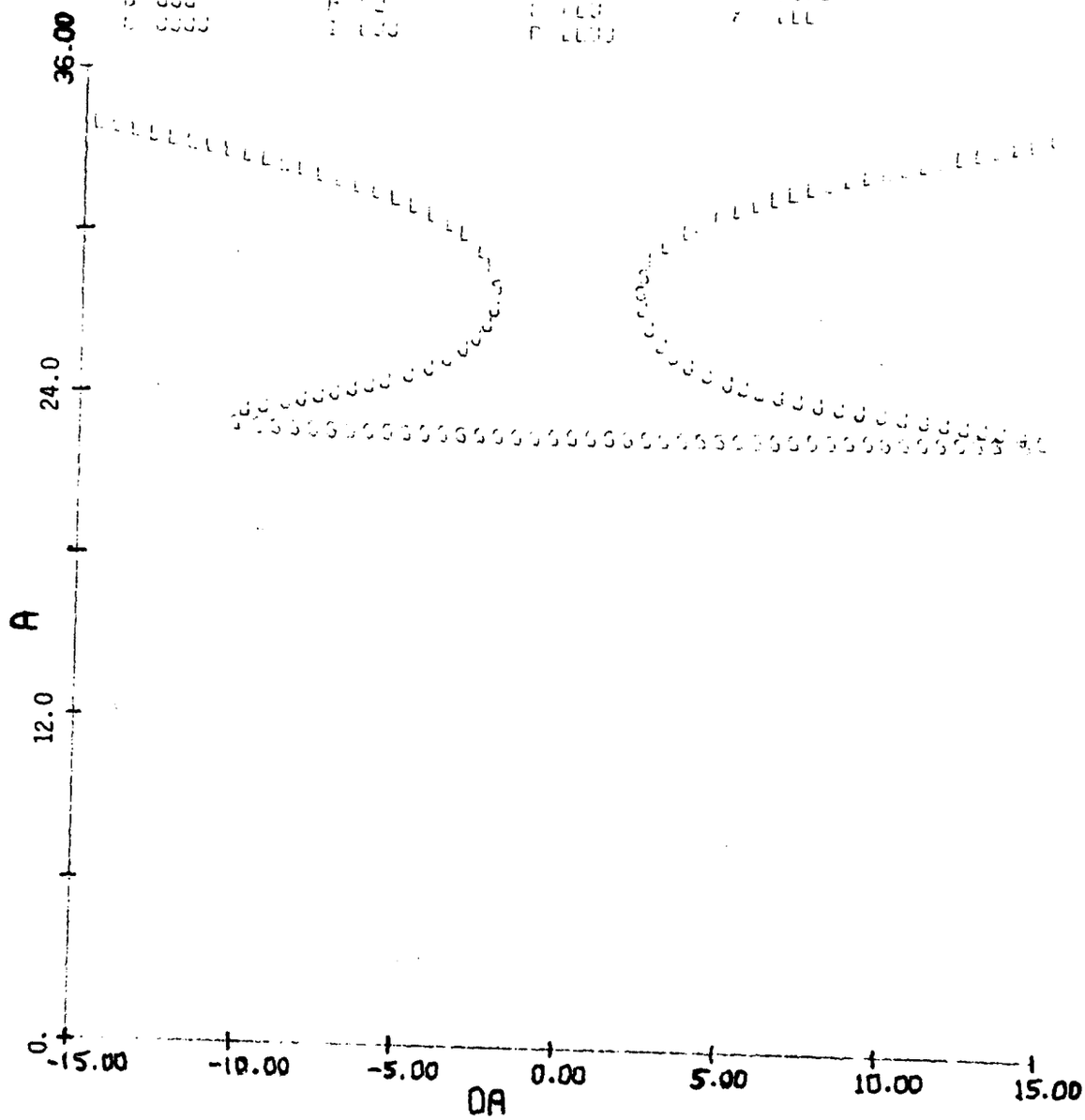

FIGURE 3.12(b) (cont.)

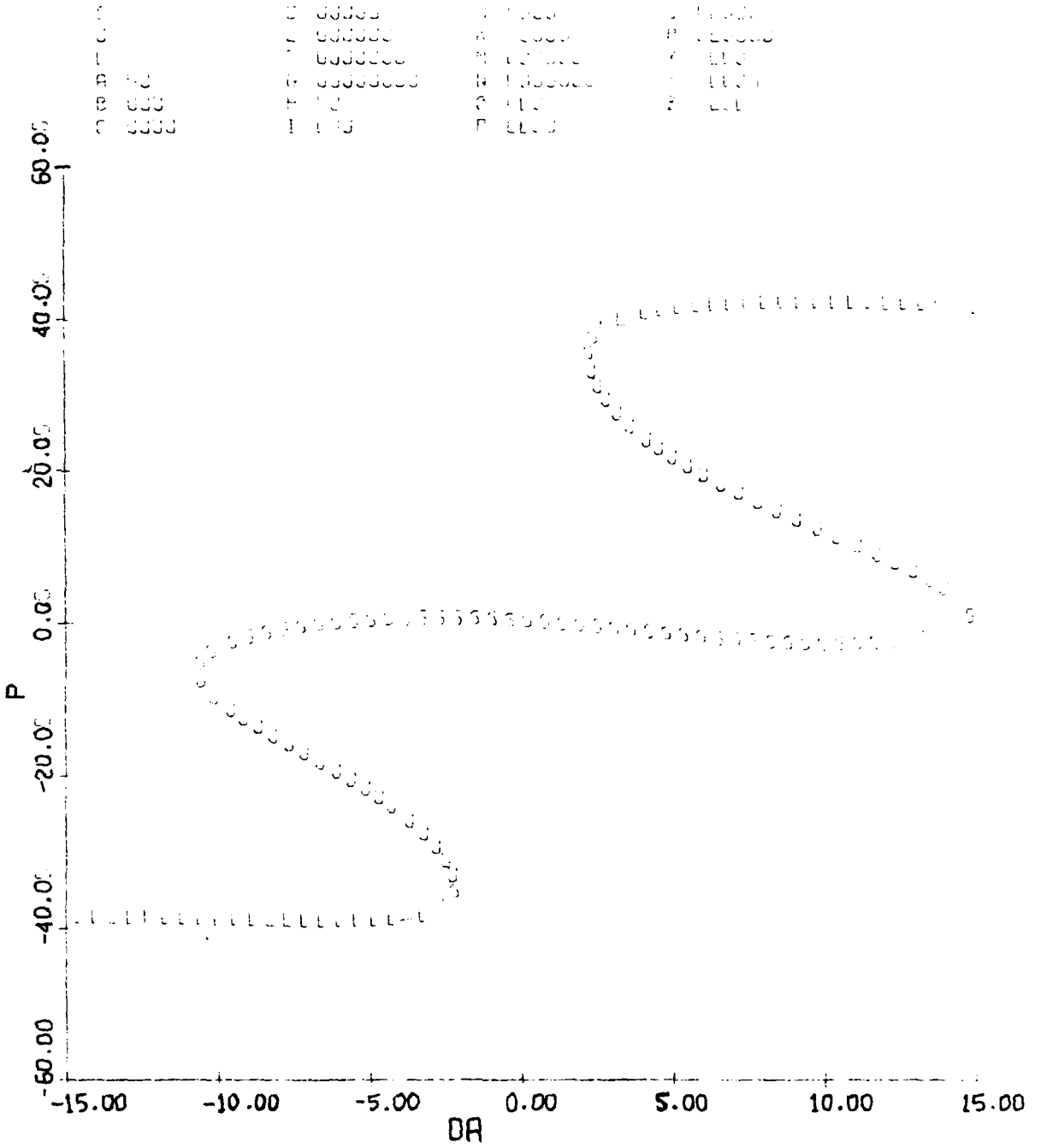

FIGURE 3.12(c) (concluded)

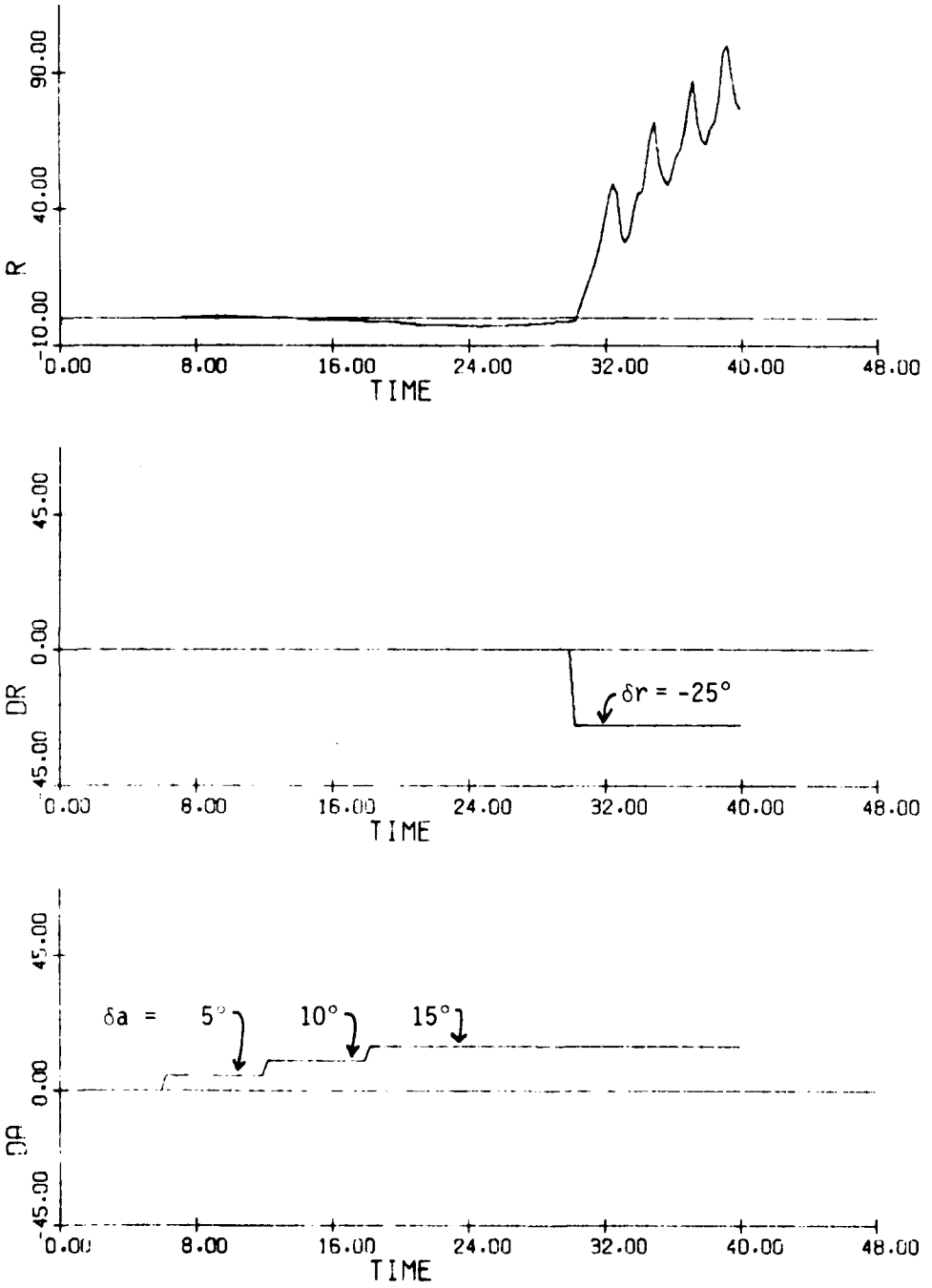

Figure 3.13(a)

Time History: Bank Maneuver; $\delta e = -11°$

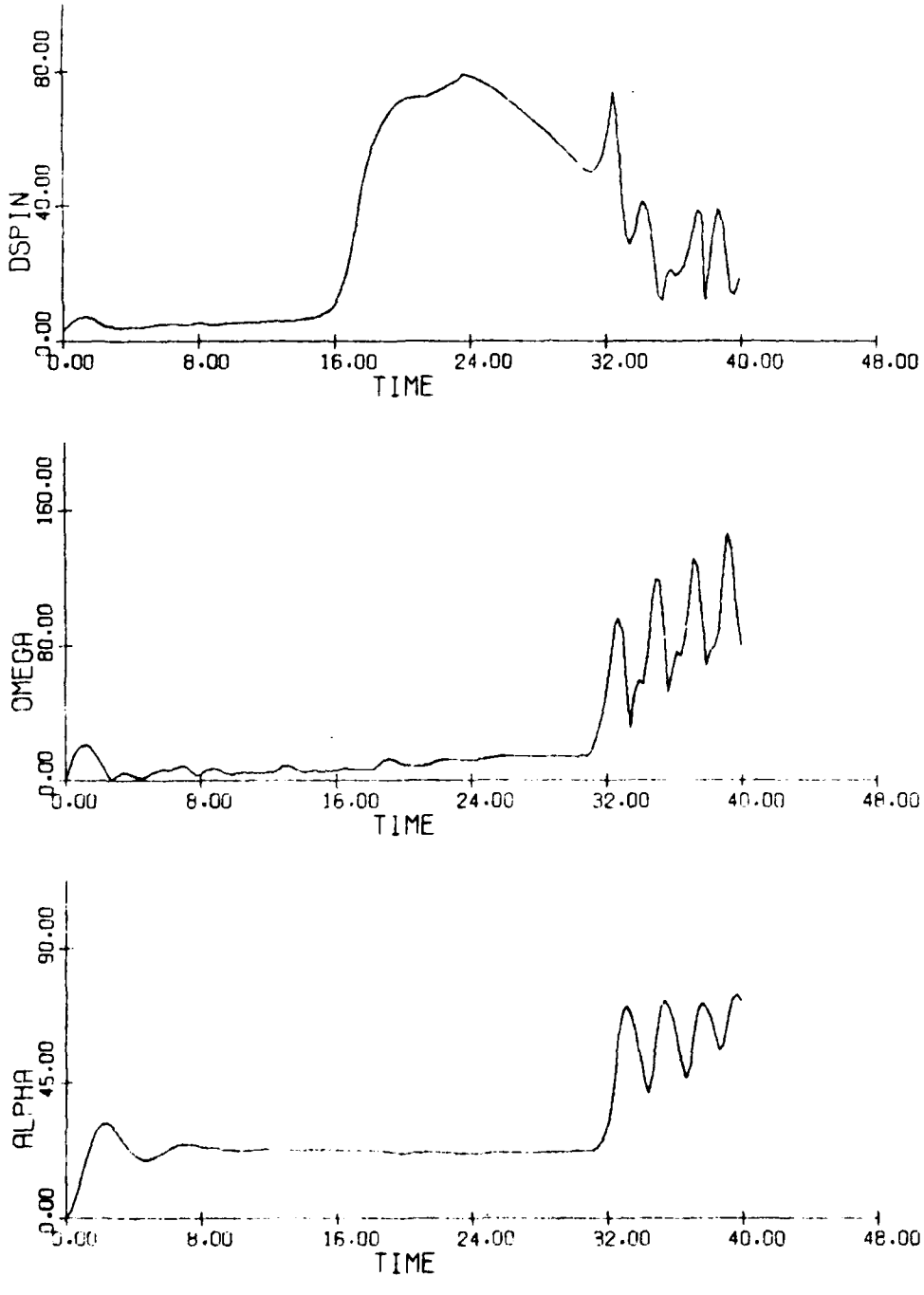

Figure 3.13(b) (concluded)

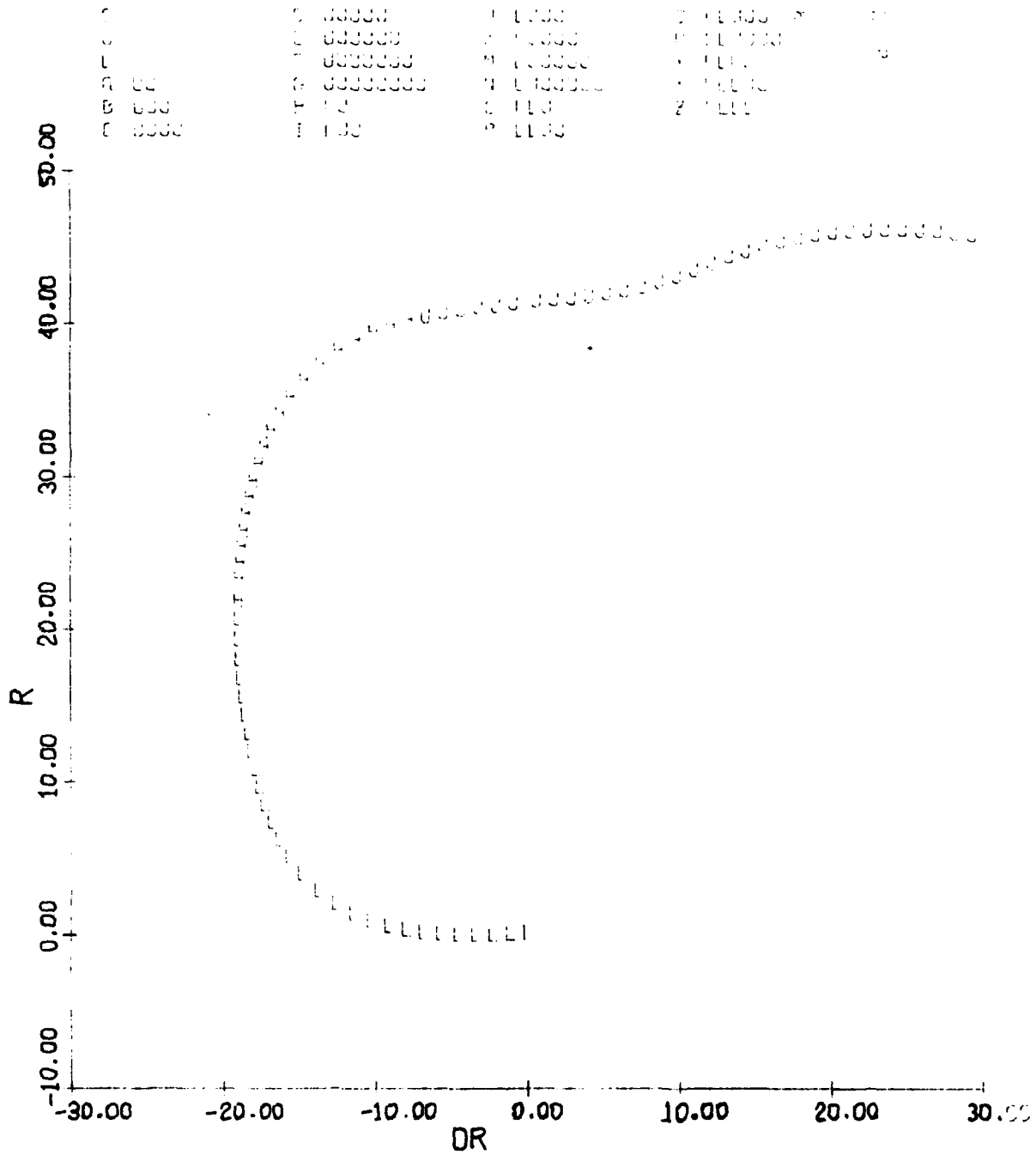

FIGURE 3.14(a)
Equilibrium Surface: r,α,p vs. δr
δa = 0°, δe = -20°, V = 600 fps, g = 0

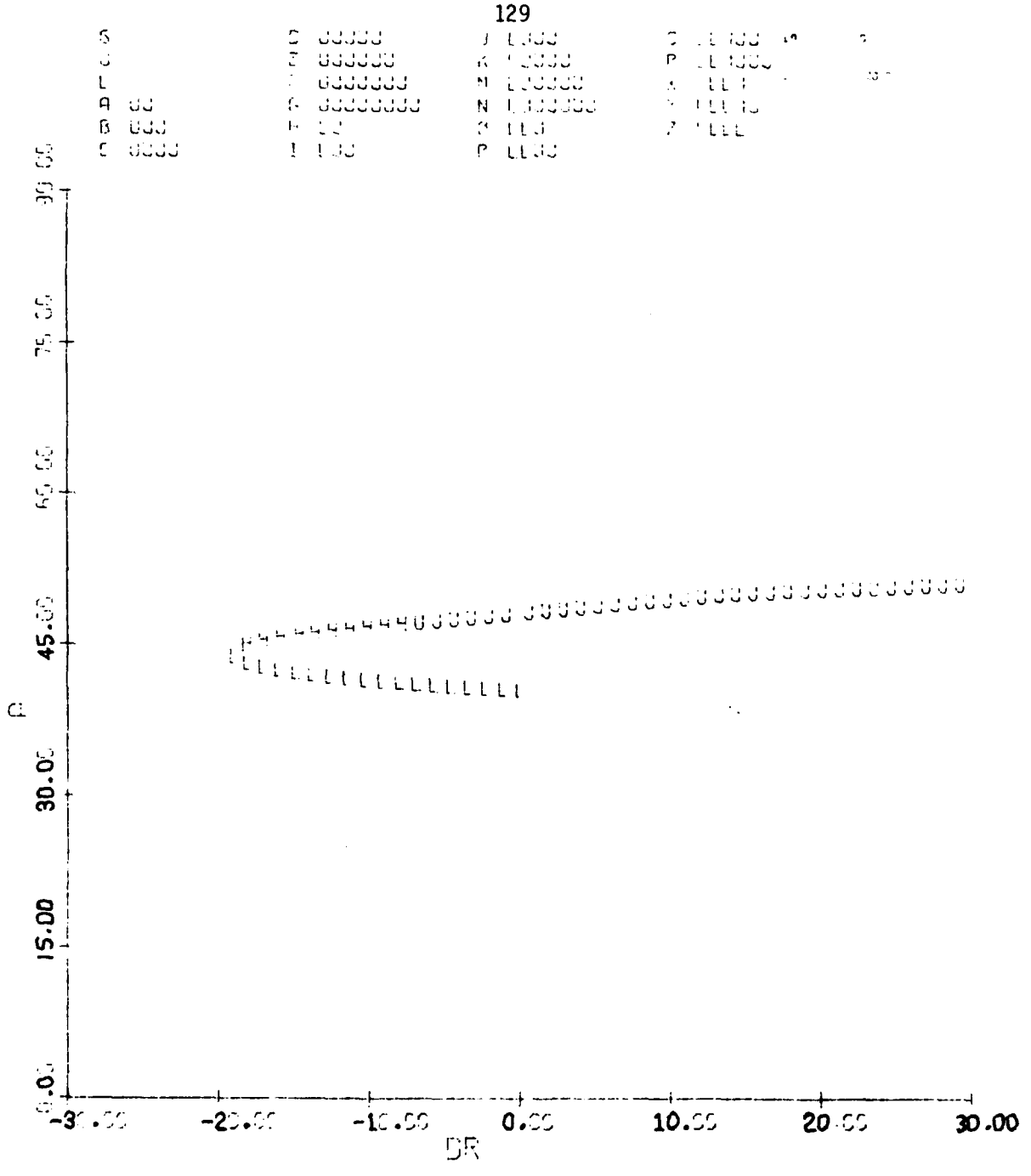

FIGURE 3.14(b) (cont.)

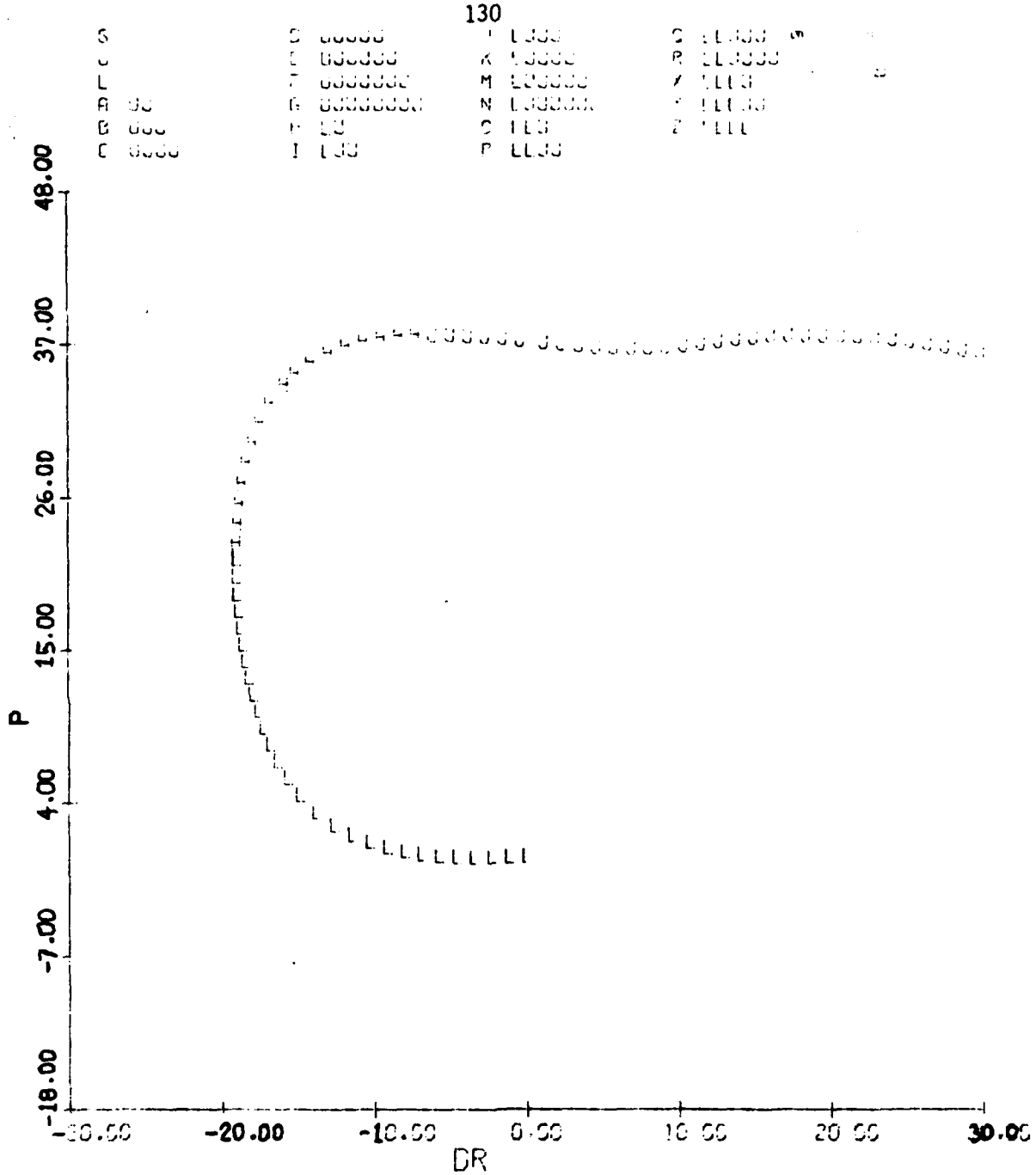

FIGURE 3.14(c) (concluded)

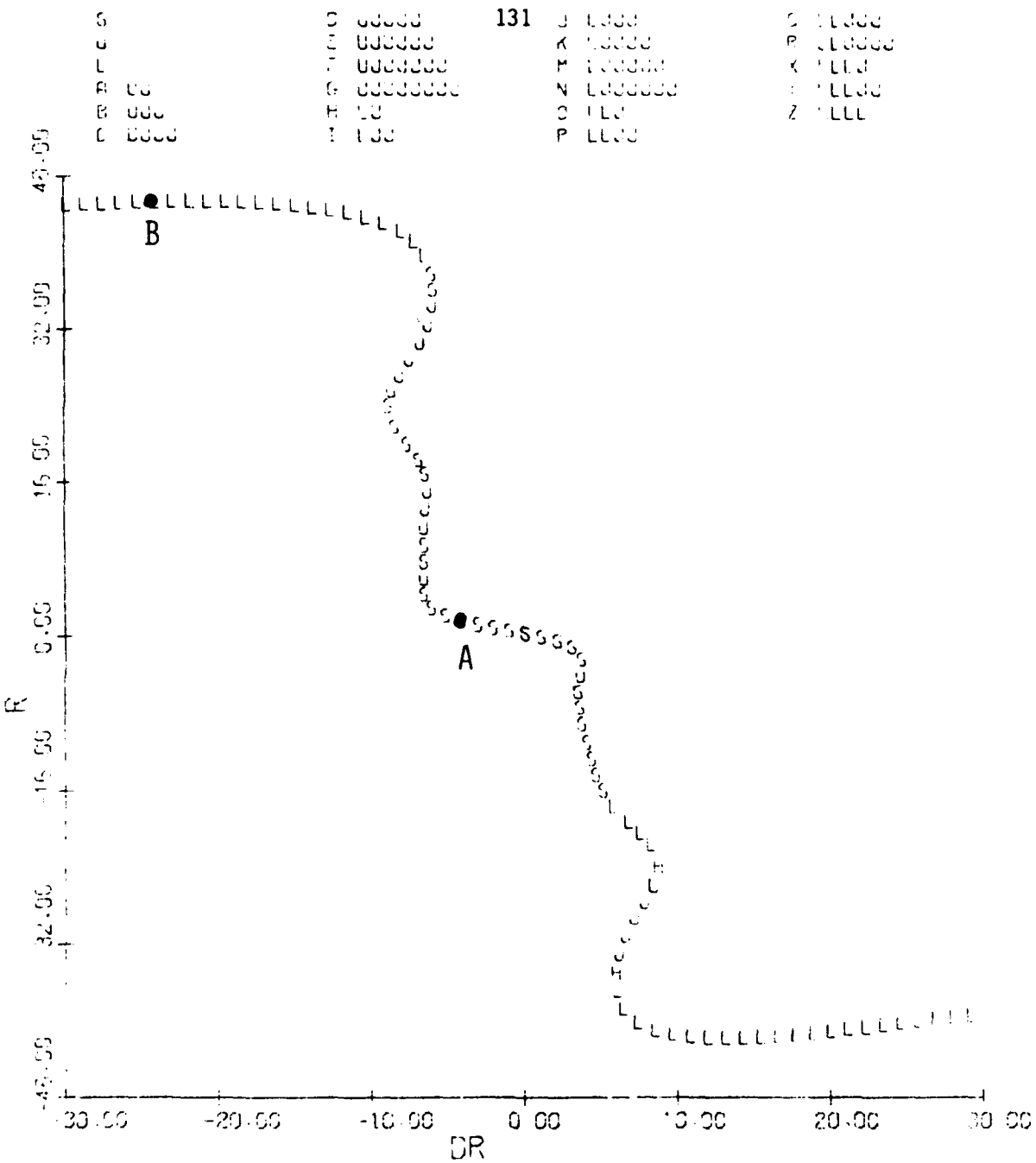

FIGURE 3.15(a)
Equilibrium Surface: r,α,p vs. δr
δa = 0°, δe = 0°, V = 600 fps, g = 0

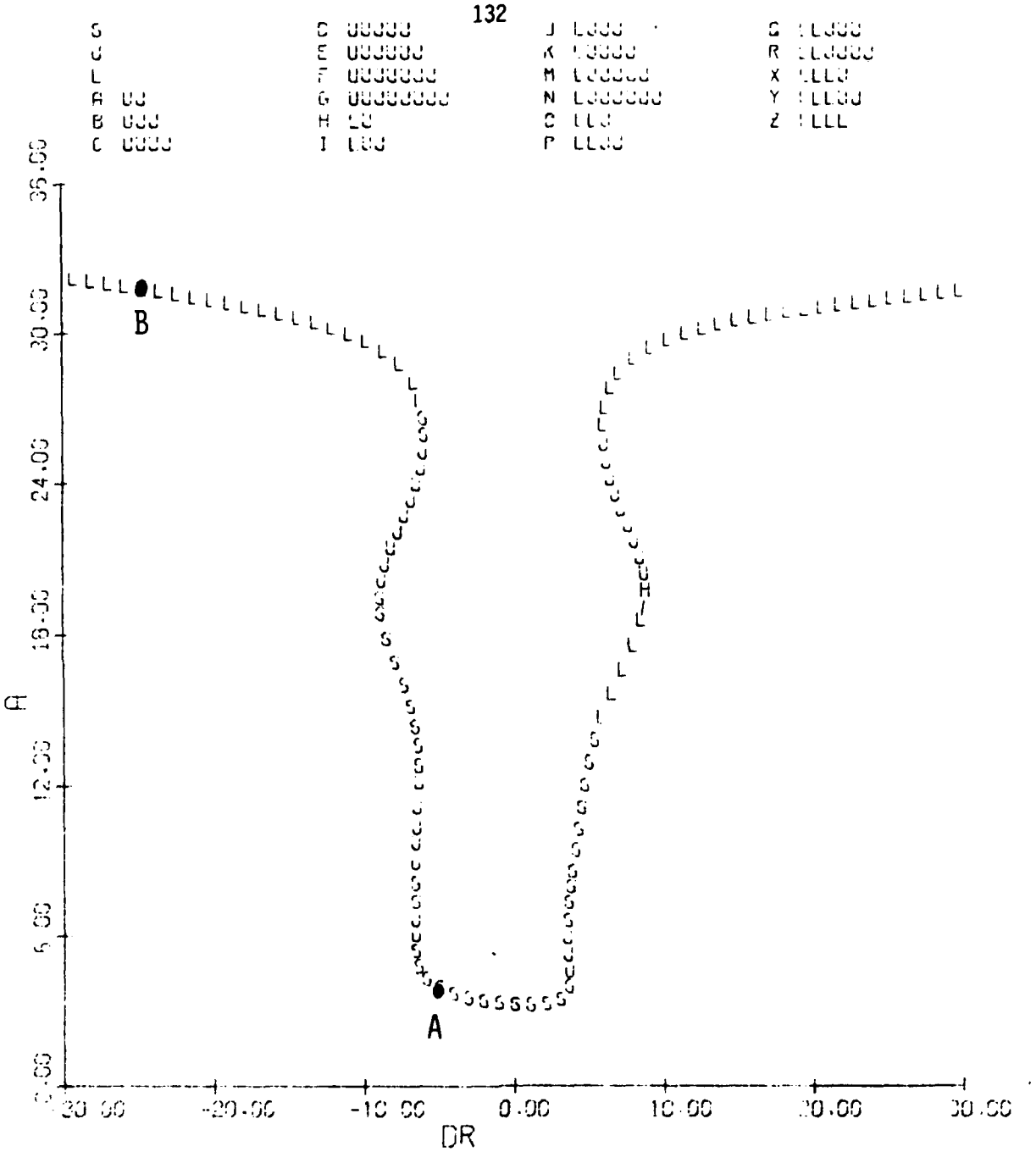

FIGURE 3.15(b) (cont.)

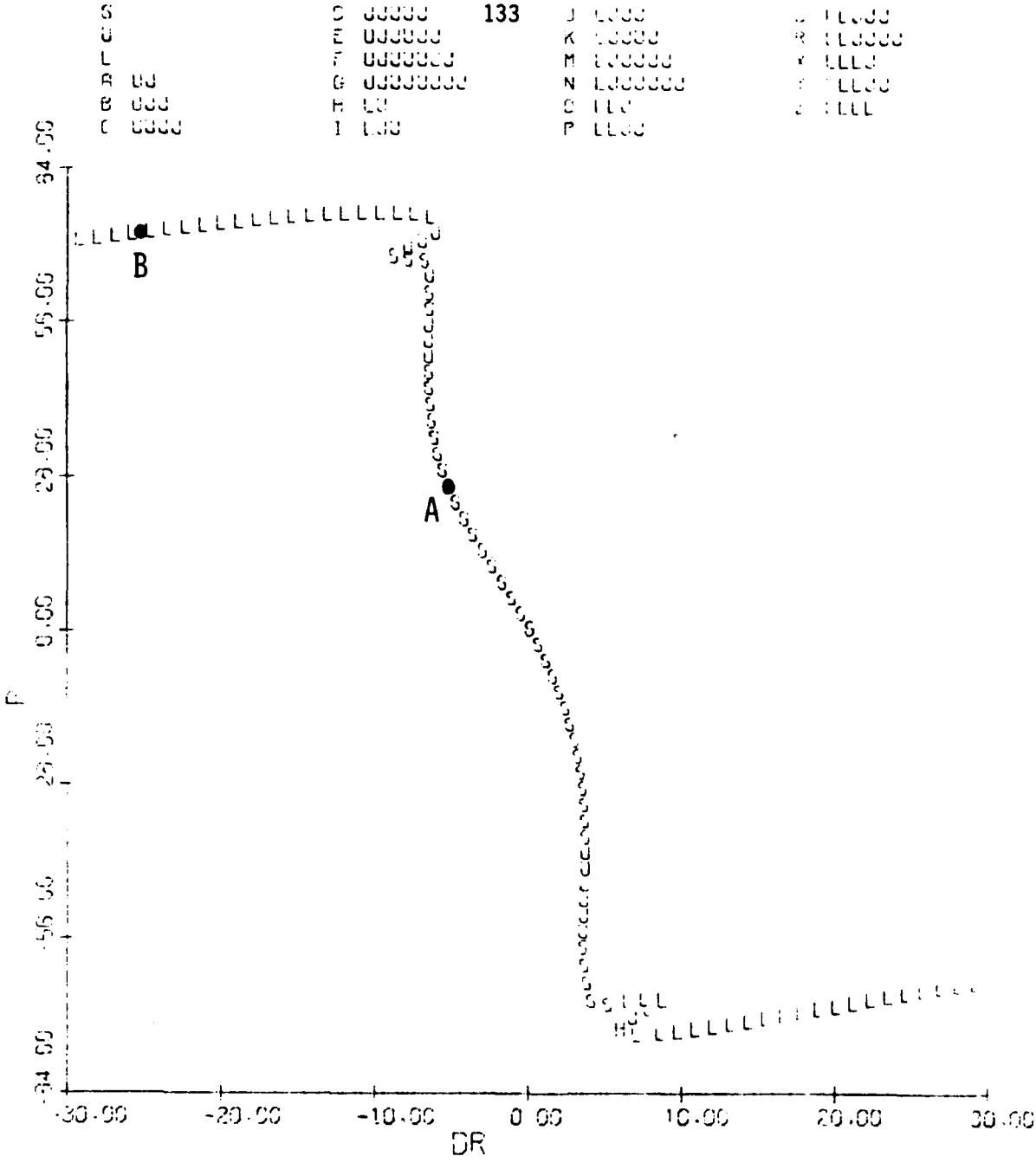

FIGURE 3.15(c) (concluded)

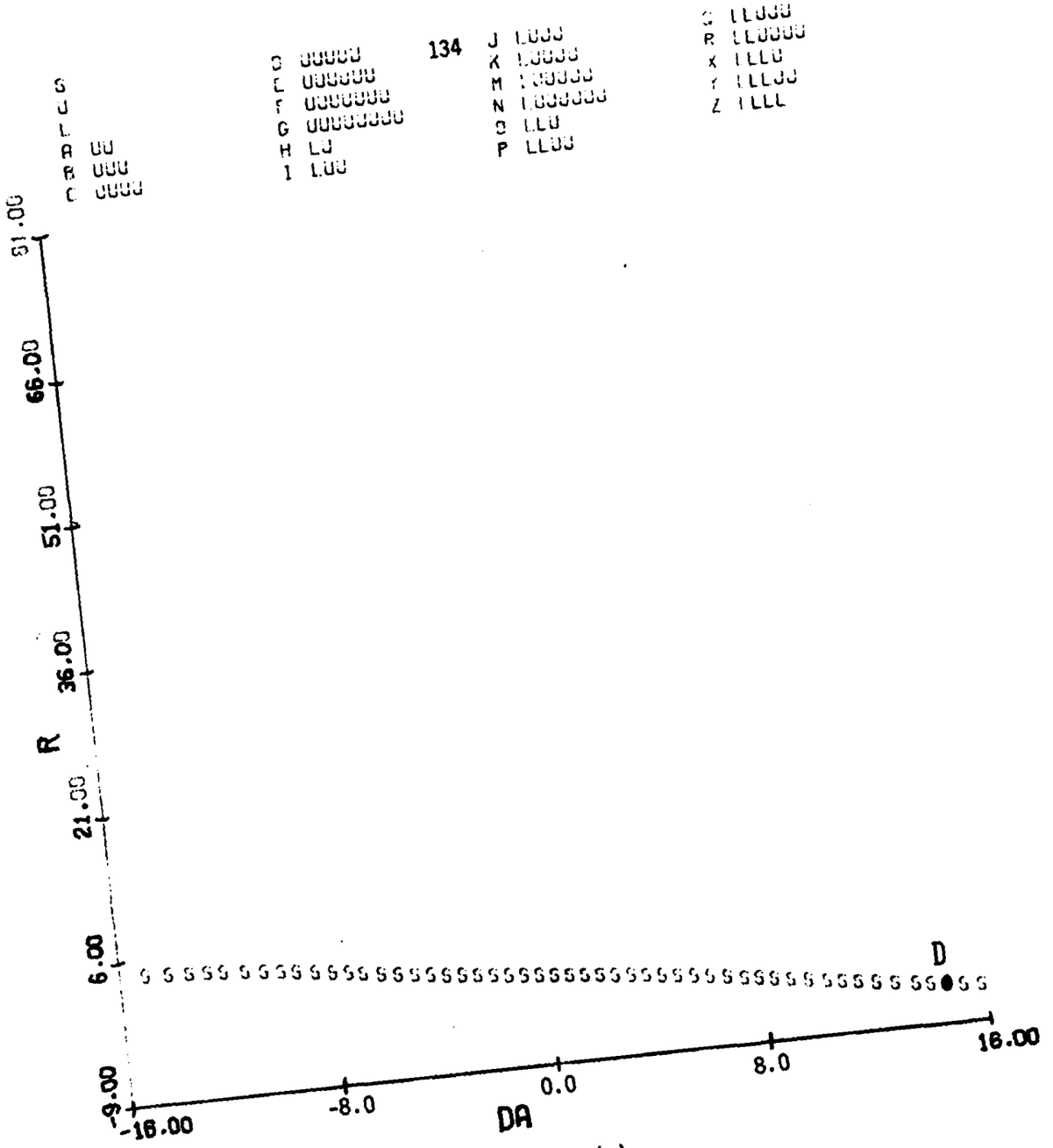

FIGURE 3.16(a)
Equilibrium Surface: r,α,p vs. δa
δe = 0°, δr = 0°, V = 600 fps, g = 0

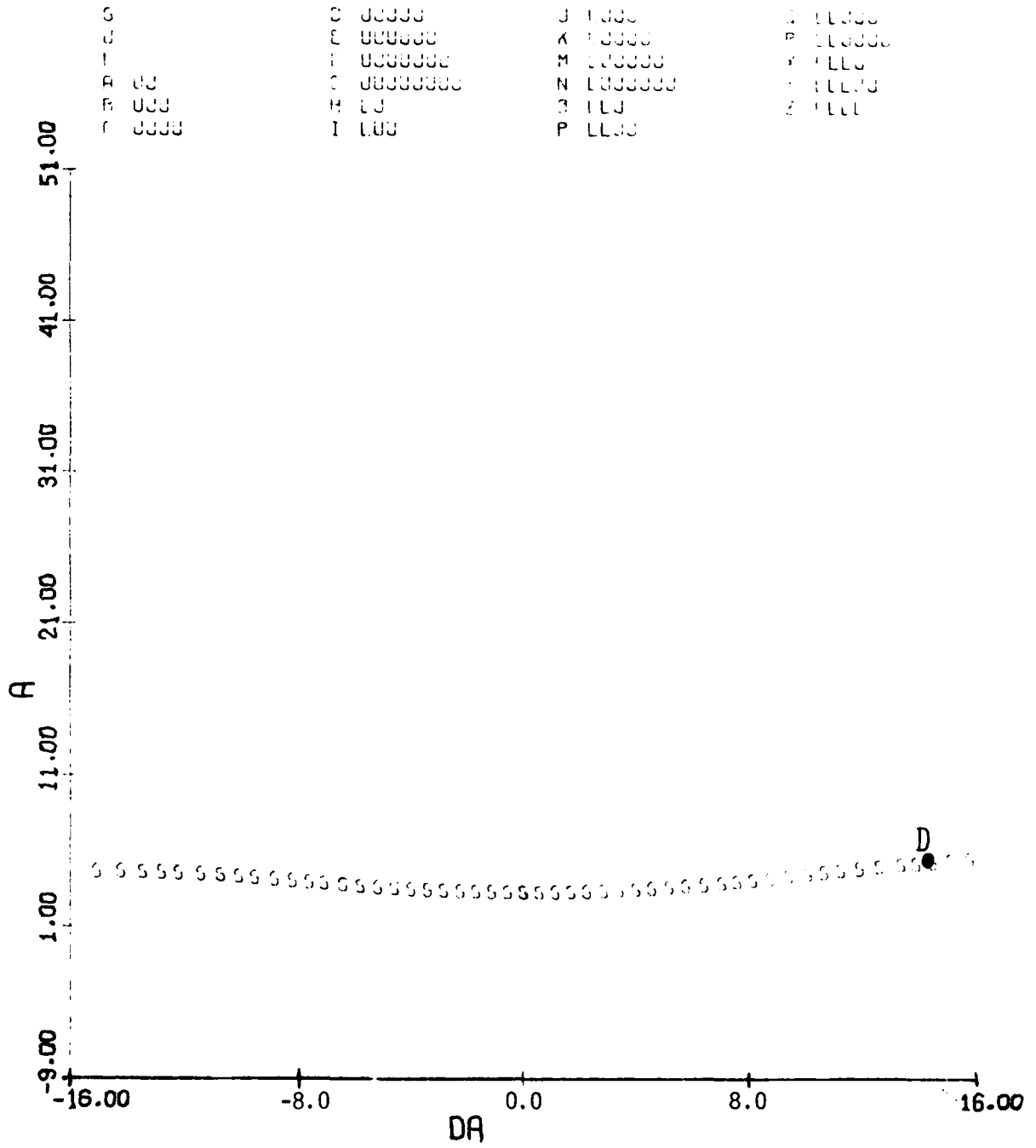

FIGURE 3.16(b) (cont.)

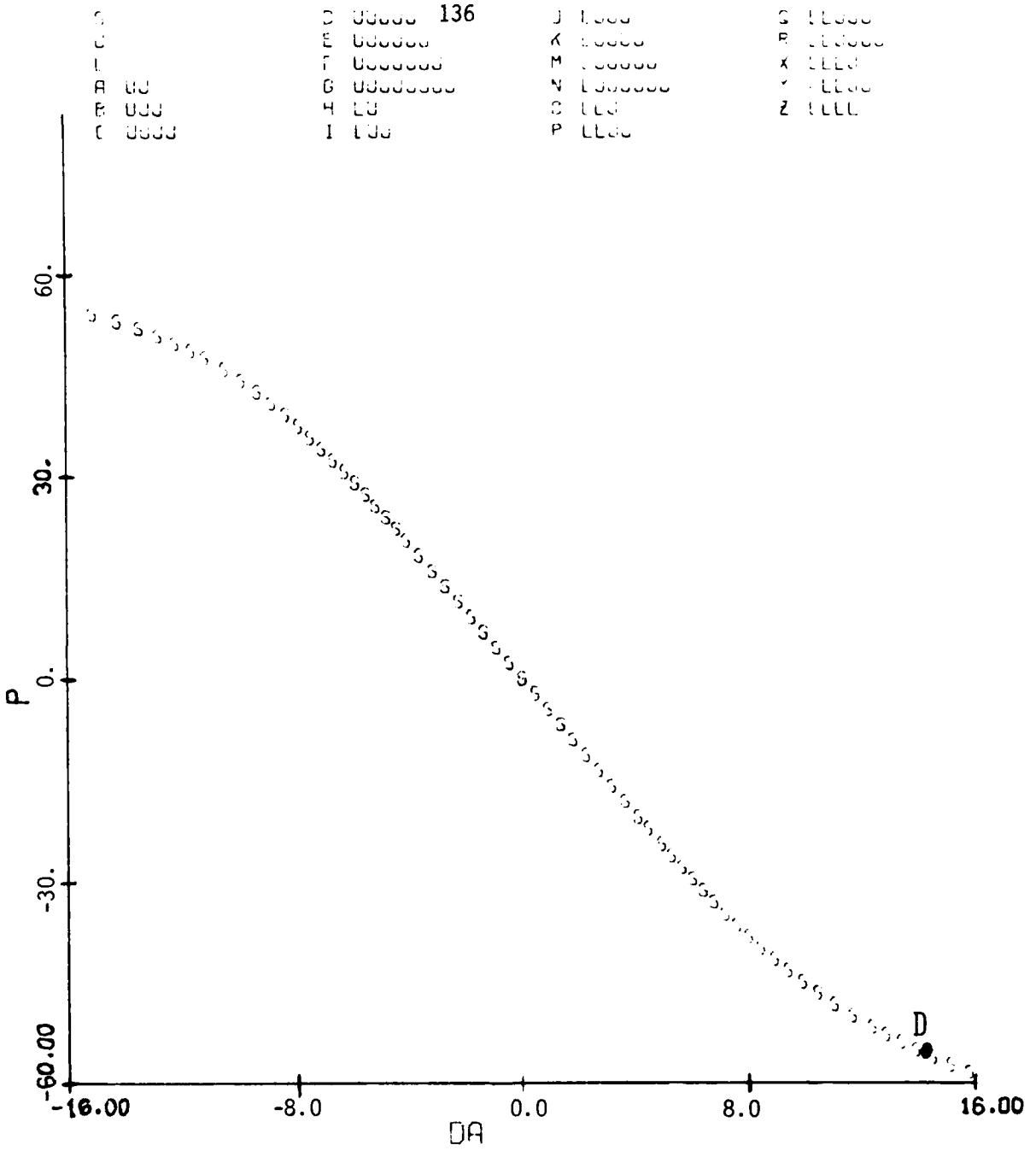

FIGURE 3.16(c) (concluded)

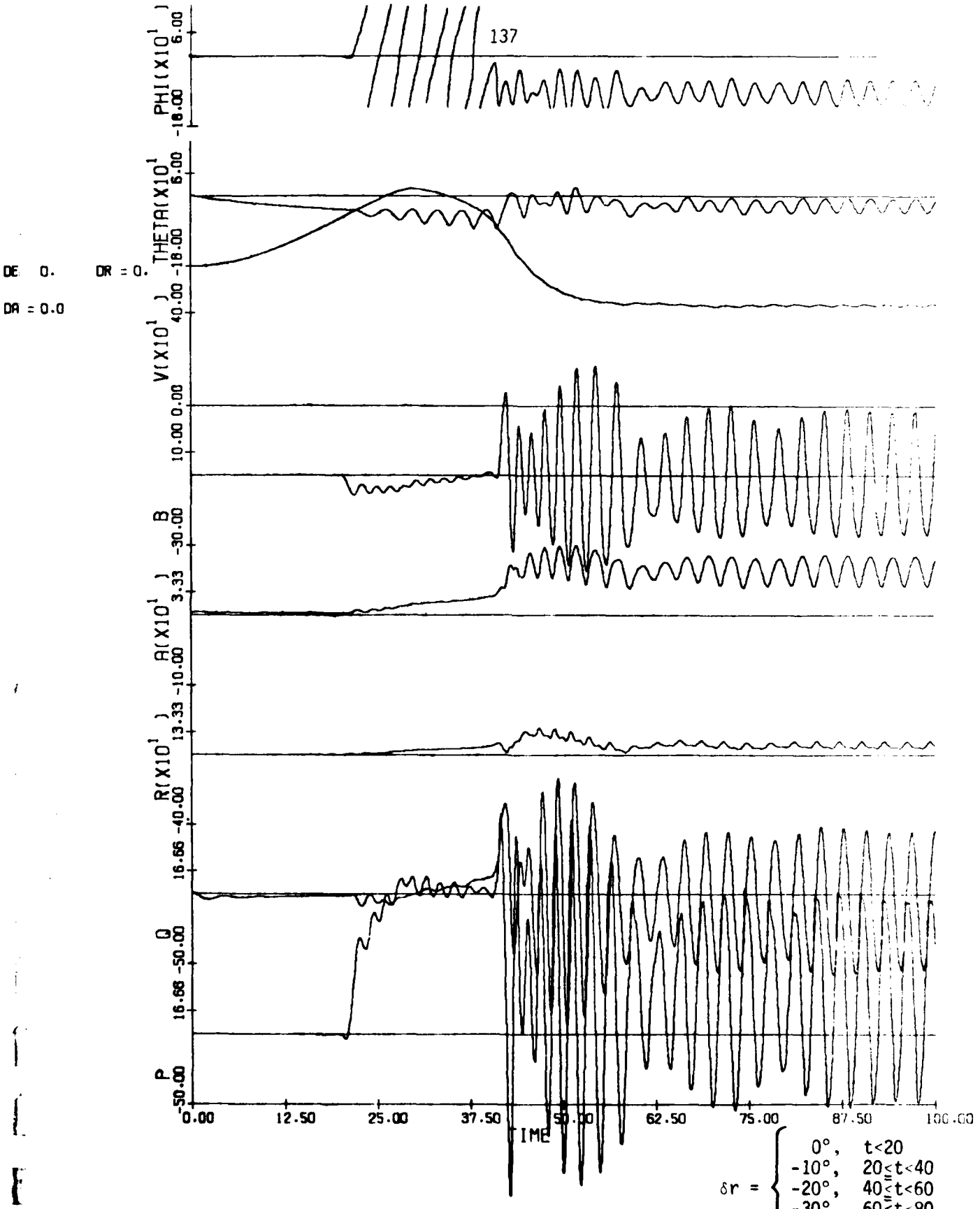

Figure 3.17
Time History: Rudder Coupling Effects; δa=δe=0°
Trim Initial Conditions

DA= 0.0
DR= -6.4

S	D UUUUU	J LUUU	Q LLUUU
U	E UUUUUU	K LUUUU	R LLUUUU
L	F UUUUUUU	M LUUUUU	X LLLU
A UU	G UUUUUUUU	N LUUUUUU	Y LLLUU
B UUU	H LU	O LLU	Z LLLL
C UUUU	I LUU	P LLUU	

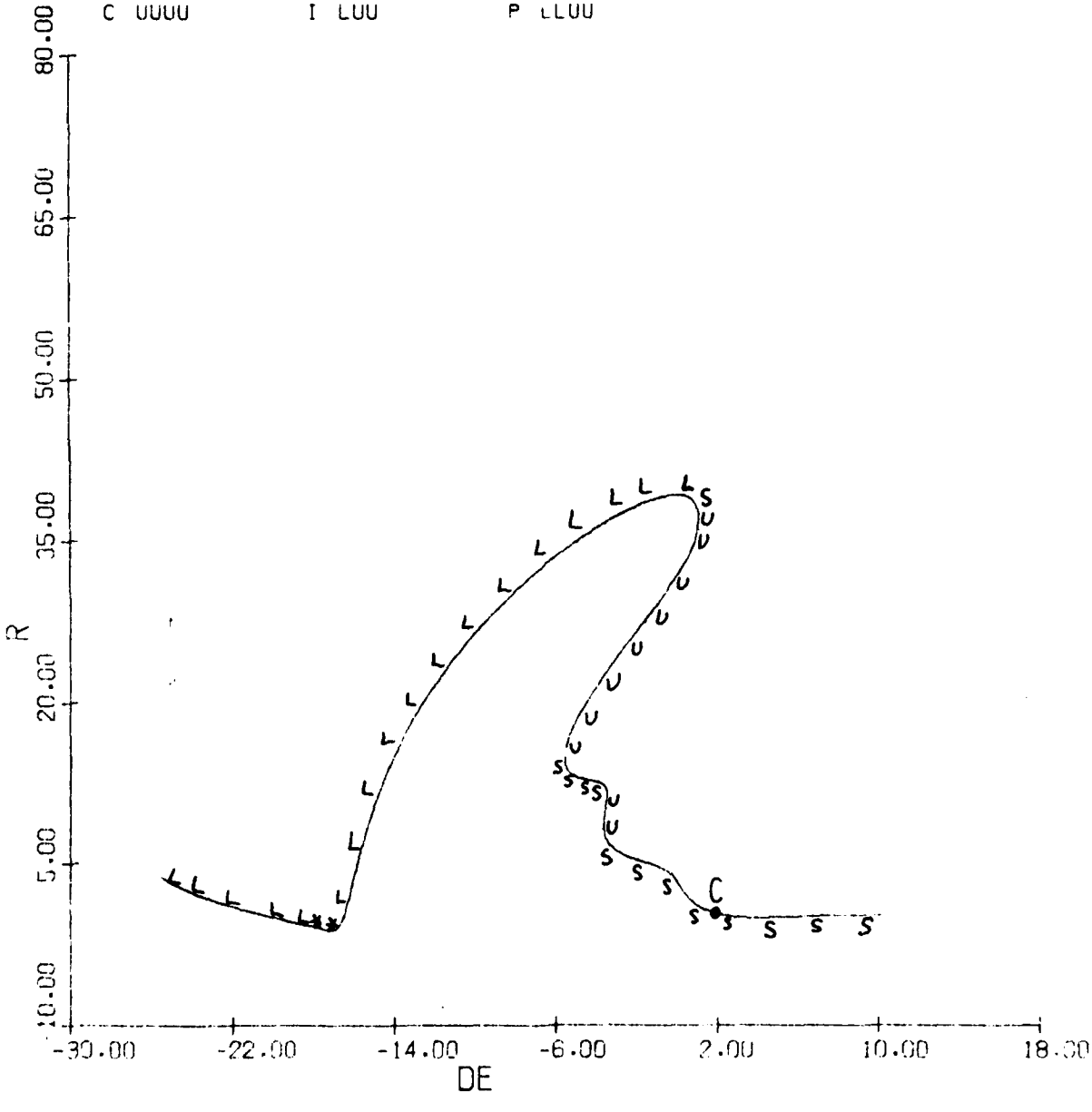

Figure 3.18(a)

Equilibrium Surface: r,α,p vs. δe
V = 600 fps, g = 0.
The symbol * refers to an LL-type instability (two unstable complex pairs)

DA= 0.0
DR= -6.4

S	D UUUUU	J LUUU	Q LLUUU
U	E UUUUUU	K LUUUU	R LLUUUU
L	F UUUUUUU	M LUUUUU	X LLLU
A UU	G UUUUUUUU	N LUUUUUU	Y LLLLU
B UUU	H LU	O LLU	Z LLLL
C UUUU	I LUU	P LLUU	

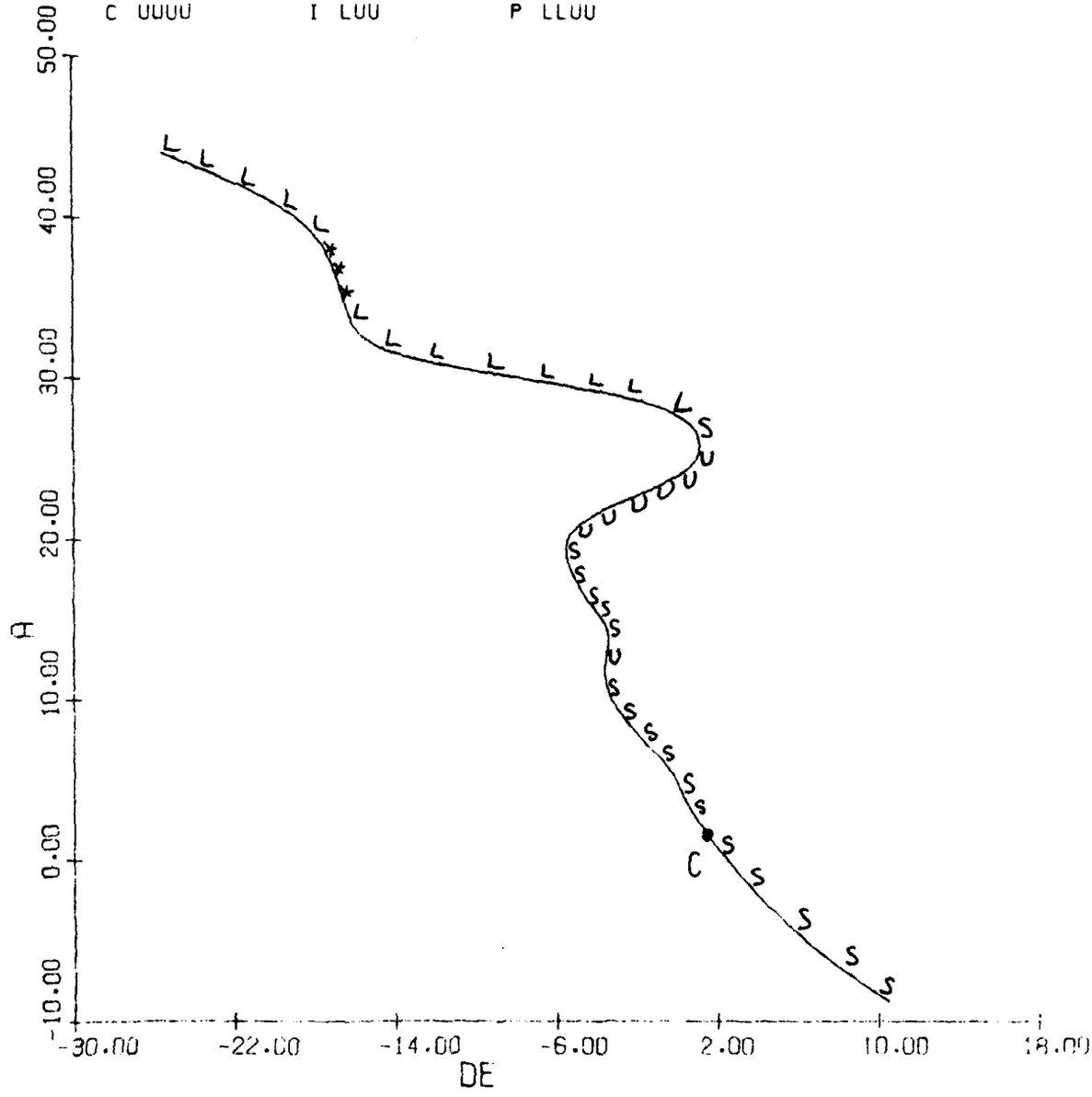

Figure 3.18(b) (cont.)

DA= 0.0
DR= -6.4

S	D UUUUU	J LUUU	Q LLUUU
U	E UUUUUU	K LUUUU	R LLUUUU
L	F UUUUUUU	M LUUUUU	X LLLU
A UU	G UUUUUUUU	N LUUUUUU	Y LLLUU
B UUU	H LU	O LLU	Z LLLL
C UUUU	I LUU	P LLUU	

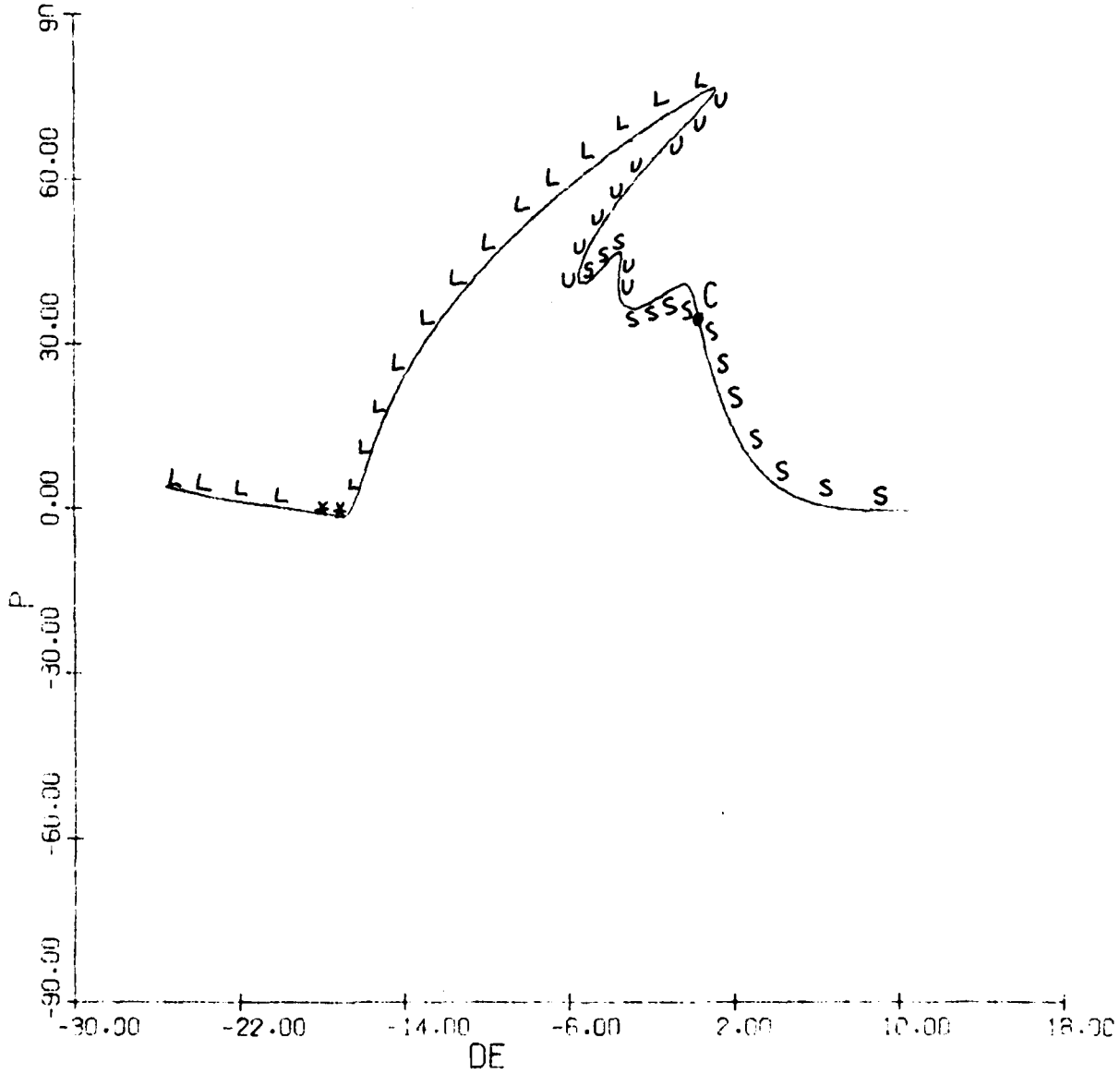

Figure 3.18(c) (concluded)

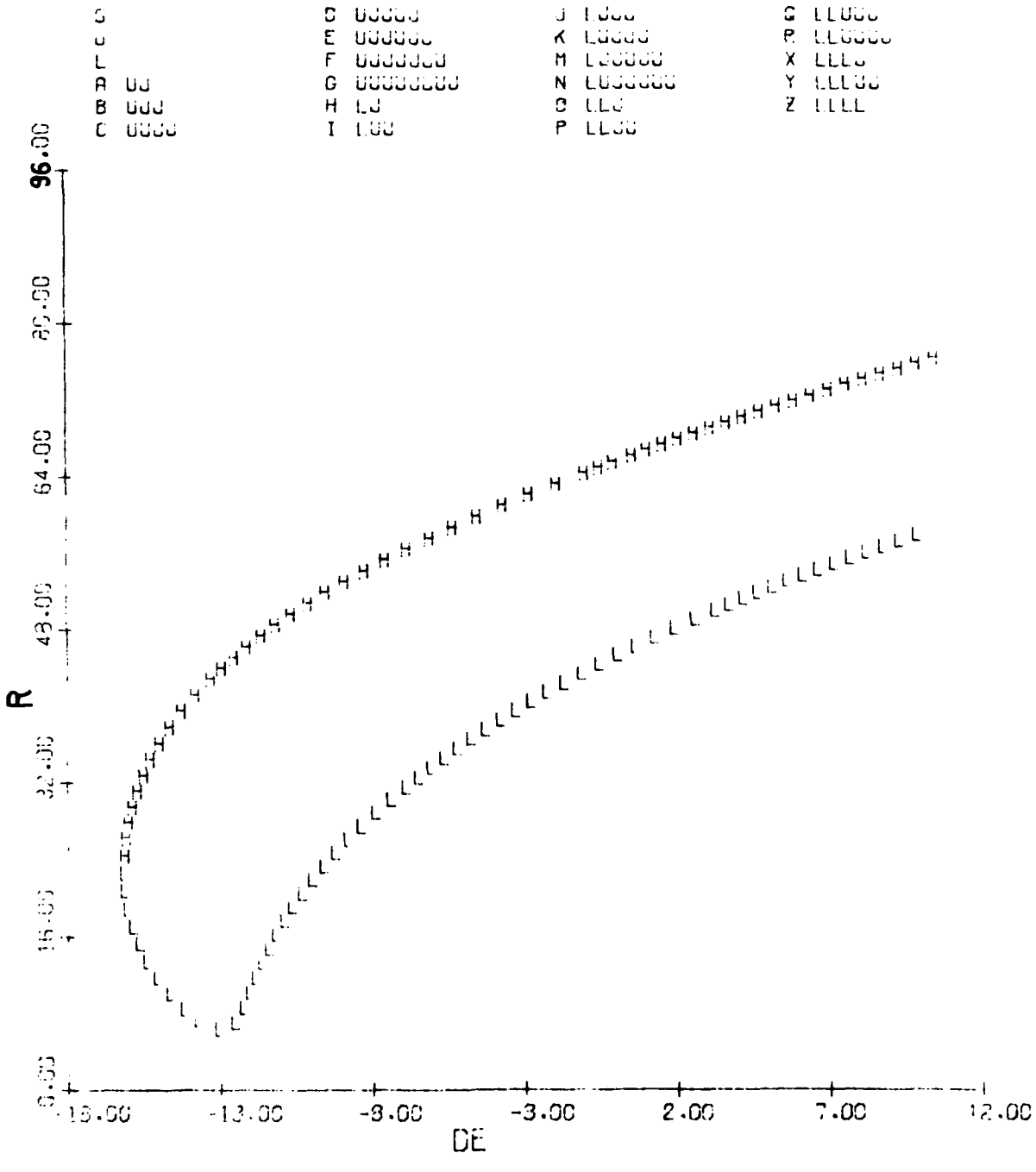

FIGURE 3.19(a)
Equilibrium Surface: r,α,p vs. δe
δa = 0°, δr = -25°, V = 600 fps, g = 0

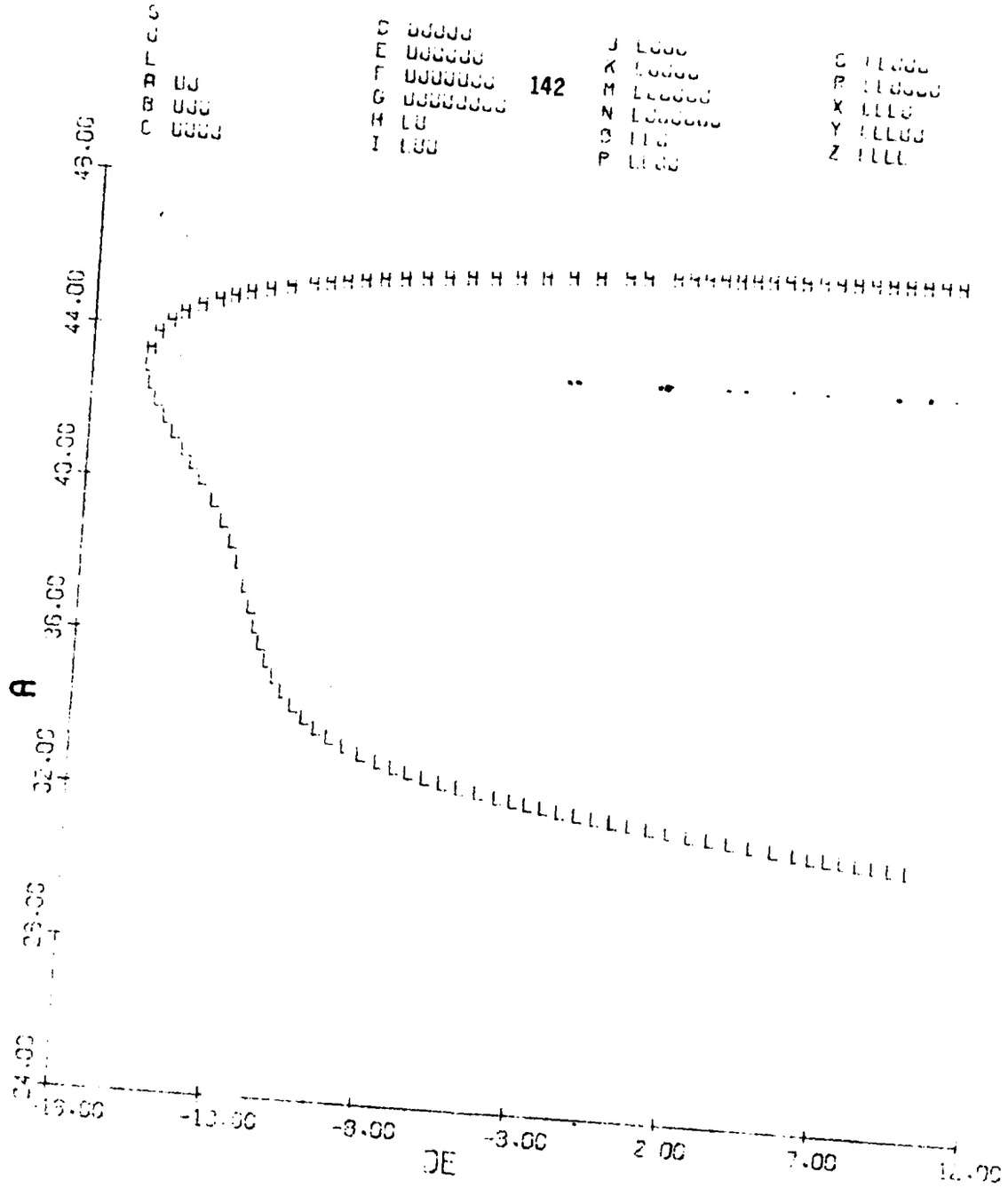

FIGURE 3.19(b) (cont.)

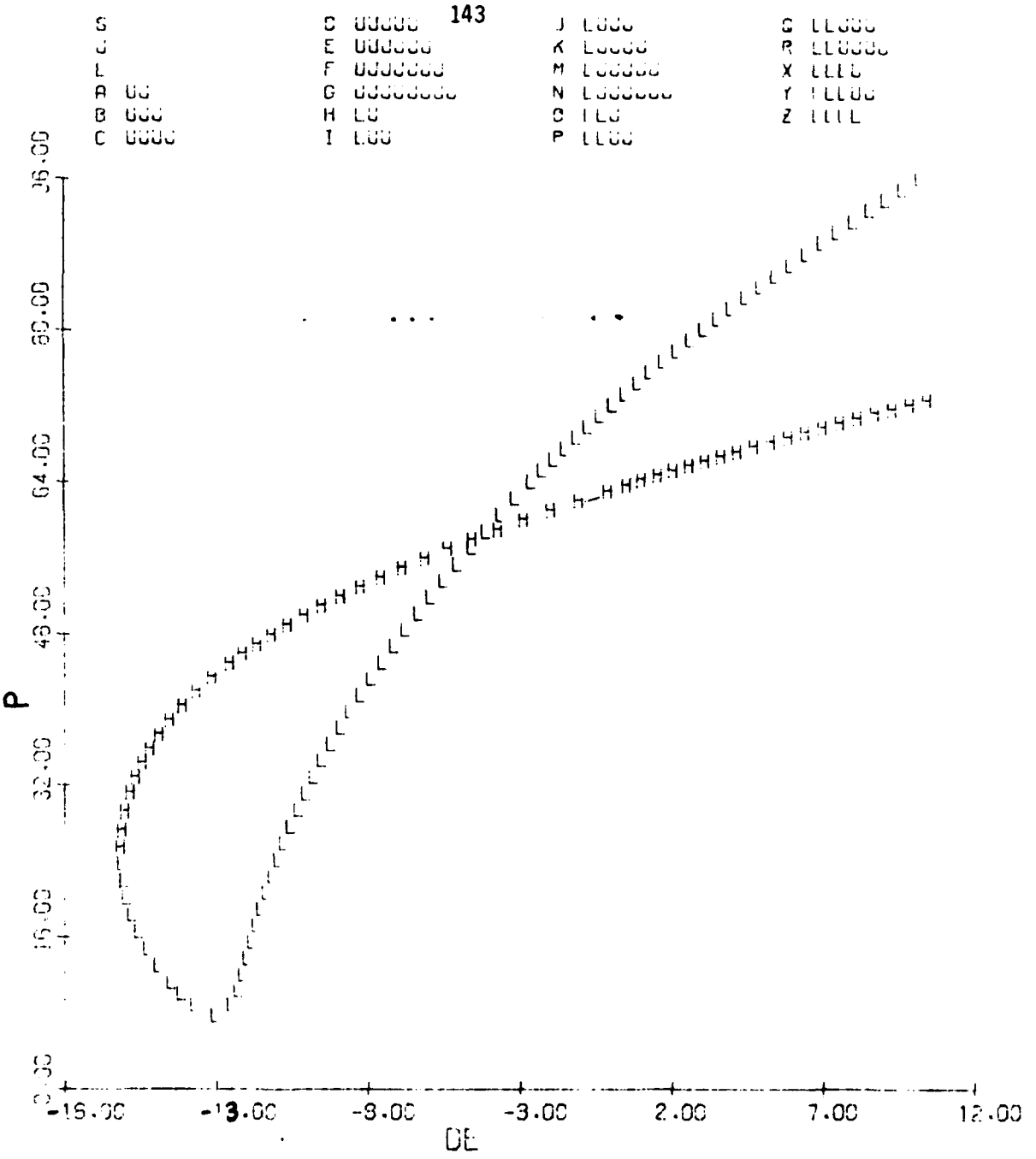

FIGURE 3.19(c) (concluded)

DE= 0.0
DR= -6.4

S
U
L
A UU
B UUU
C UUUU
D UUUUU
E UUUUUU
F UUUUUUU
G UUUUUUUU
H LU
I LUU
J LUUU
K LUUUU
M LUUUUU
N LUUUUUU
O LLU
P LLUU
Q LLUUU
R LLUUUU
X LLLU
Y LLLUU
Z LLLL

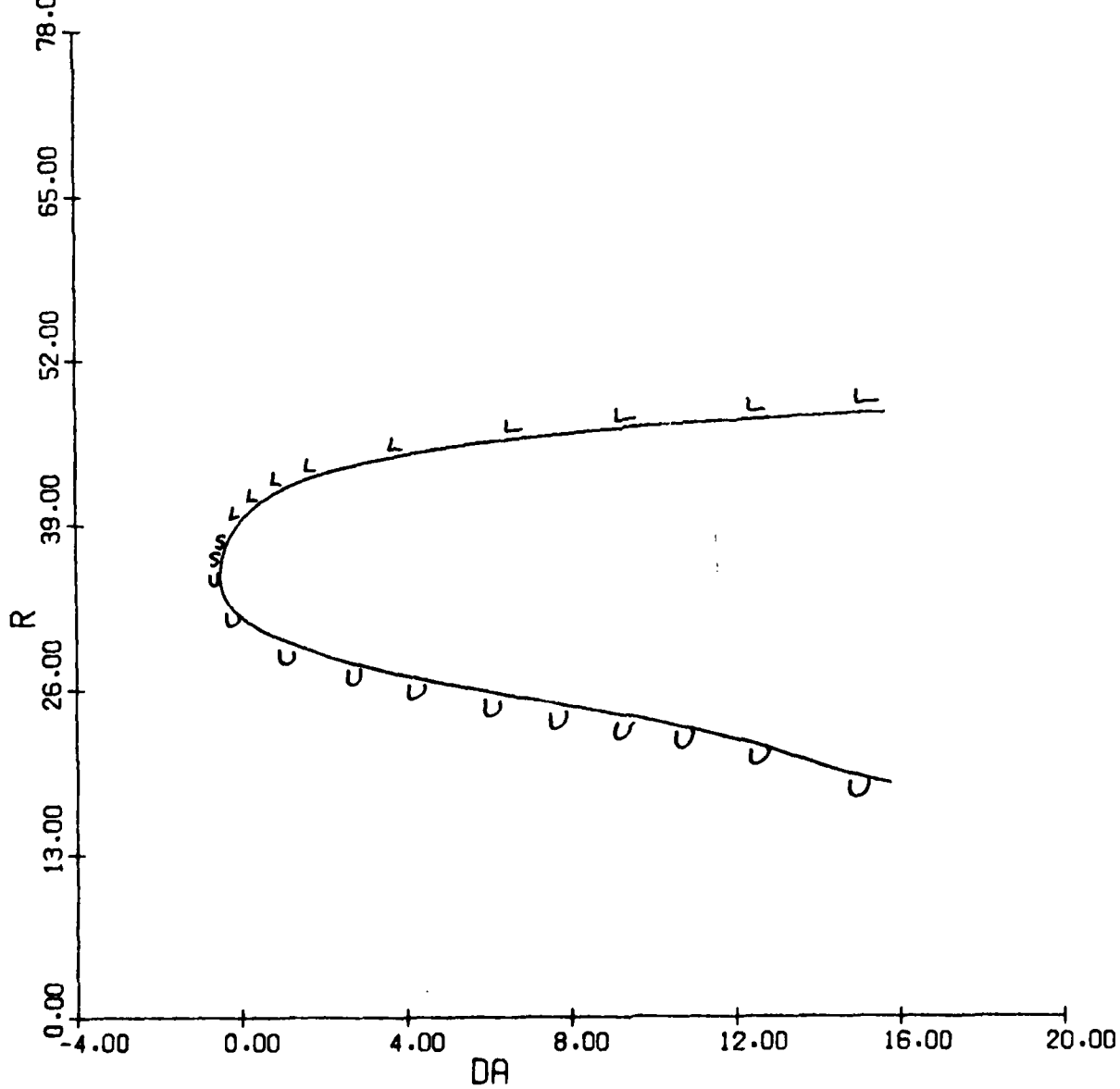

Figure 3.20(a)

Equilibrium Surface: r,α,p vs. δa
V = 600 fps; g = 0

DE= 0.0
DR= -6.4

S	D UUUUU	J LUUU	Q LLUUU
U	E UUUUUU	K LUUUU	R LLUUUU
L	F UUUUUUU	M LUUUUU	X LLLU
A UU	G UUUUUUUU	N LUUUUUU	Y LLLUU
B UUU	H LU	O LLU	Z LLLL
C UUUU	I LUU	P LLUU	

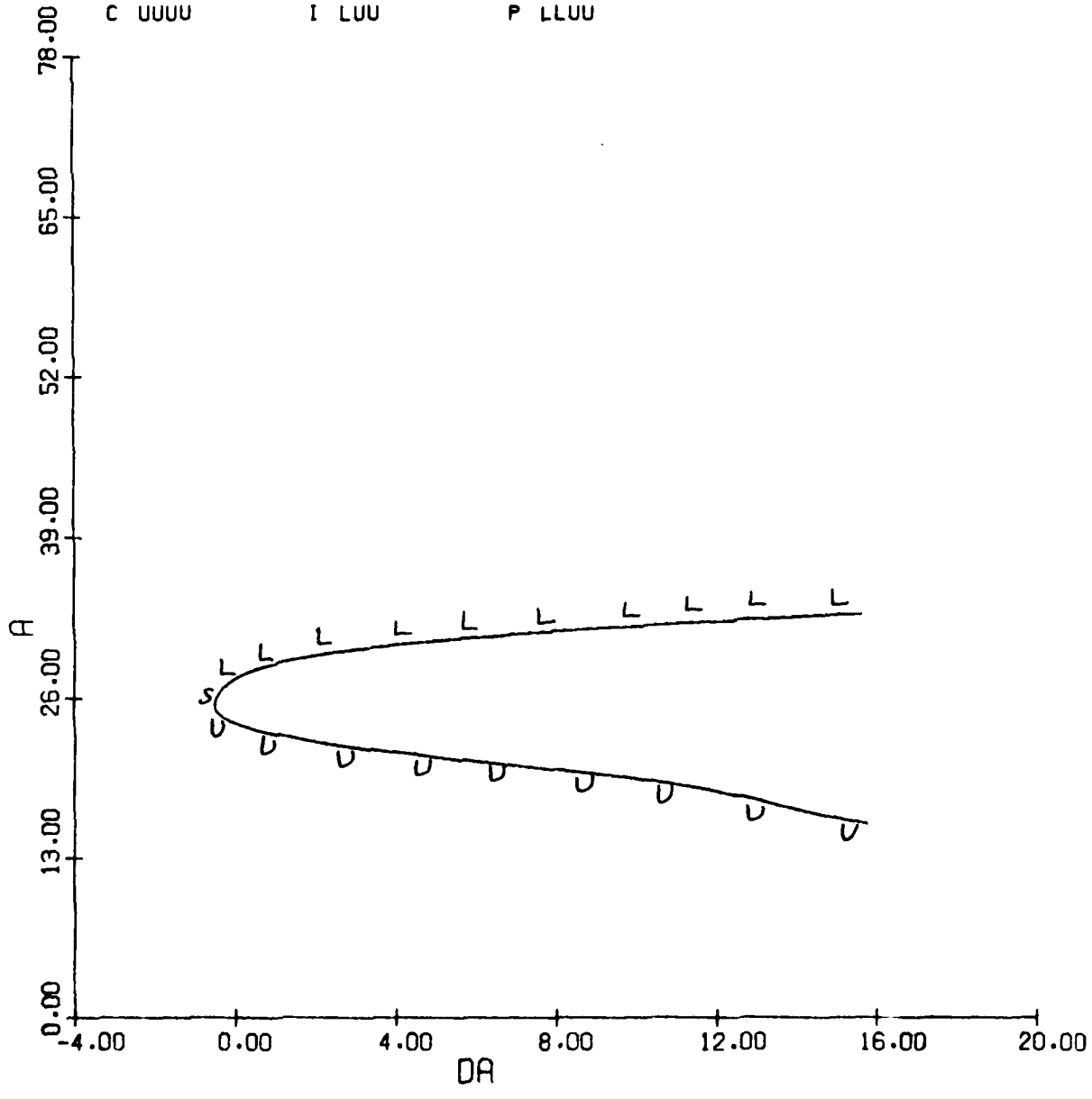

Figure 3.20(b) (cont.)

DE= 0.0
DR= -6.4

S	D UUUUU	J LUUU	Q LLUUU
U	E UUUUUU	K LUUUU	R LLUUUU
L	F UUUUUUU	M LUUUUU	X LLLU
A UU	G UUUUUUUU	N LUUUUUU	Y LLLUU
B UUU	H LU	O LLU	Z LLLL
C UUUU	I LUU	P LLUU	

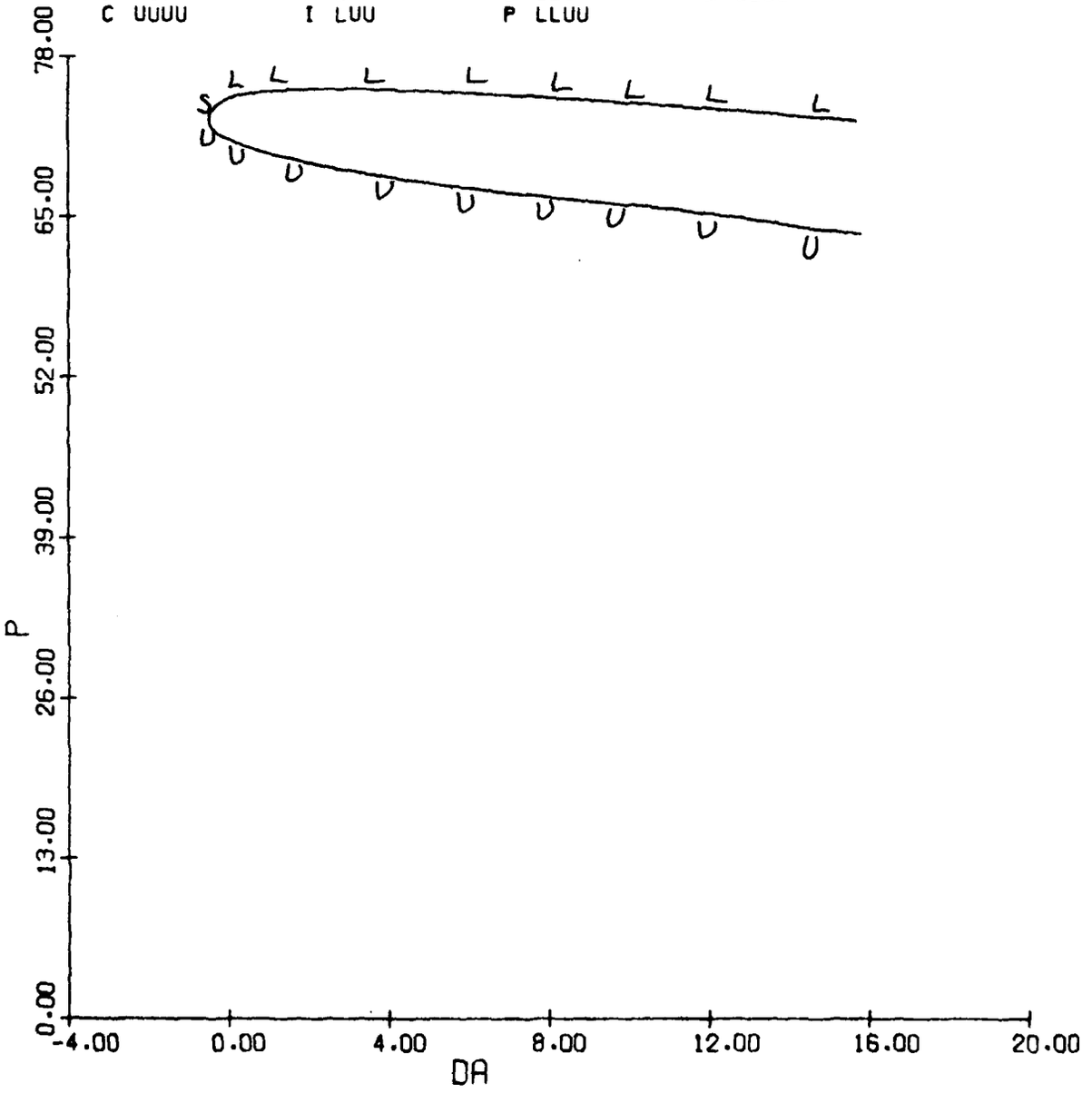

Figure 3.20 (concluded)

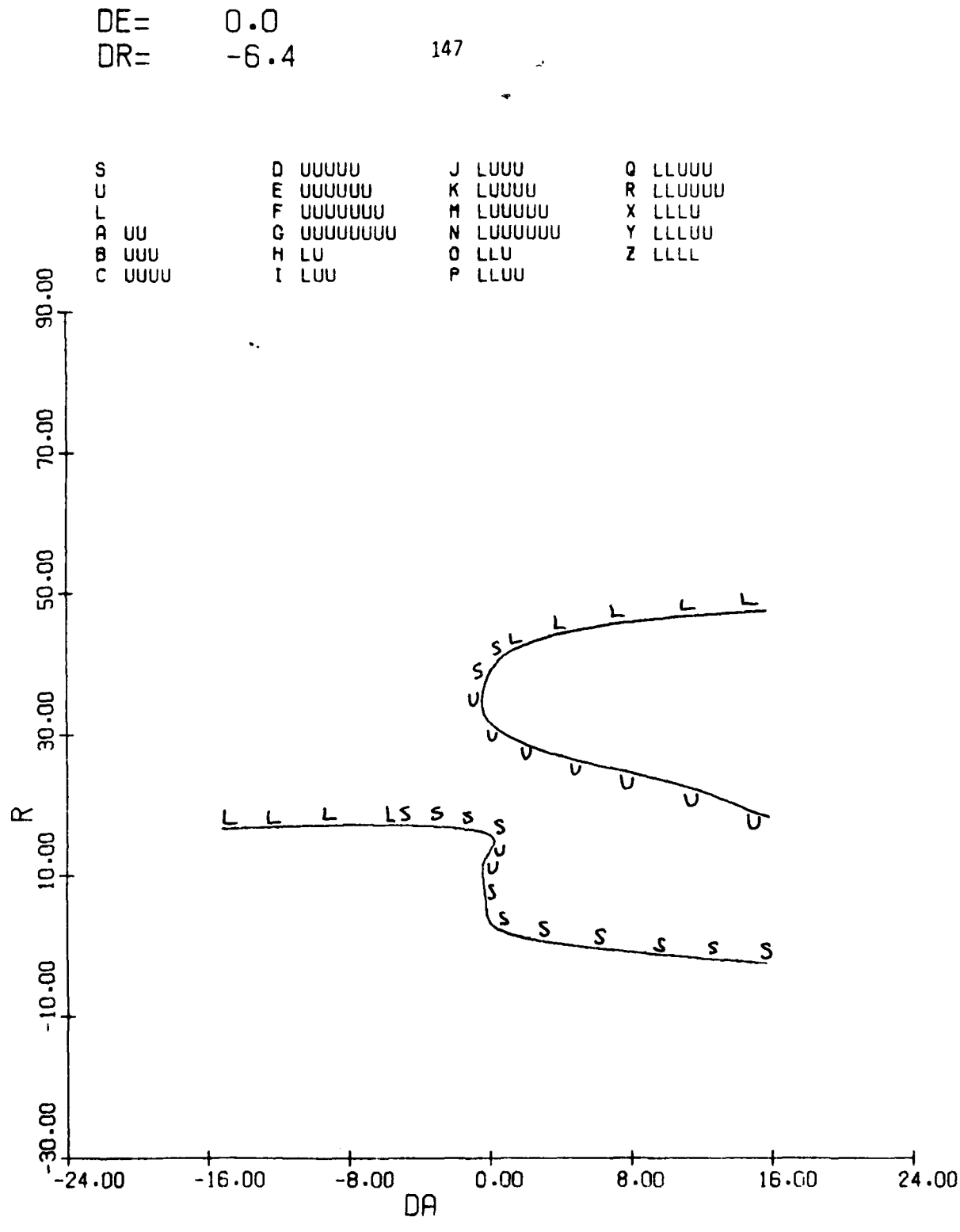

Figure 3.21(a)

Equilibrium Surface: r,α,p vs. δa
V = 600 fps, g = 0; Note that the
Fig. 3.20 branches are also in this figure.

DE= 0.0
DR= -6.4

S	D UUUUU	J LUUU	Q LLUUU
U	E UUUUUU	K LUUUU	R LLUUUU
L	F UUUUUUU	M LUUUUU	X LLLU
A UU	G UUUUUUUU	N LUUUUUU	Y LLLUU
B UUU	H LU	O LLU	Z LLLL
C UUUU	I LUU	P LLUU	

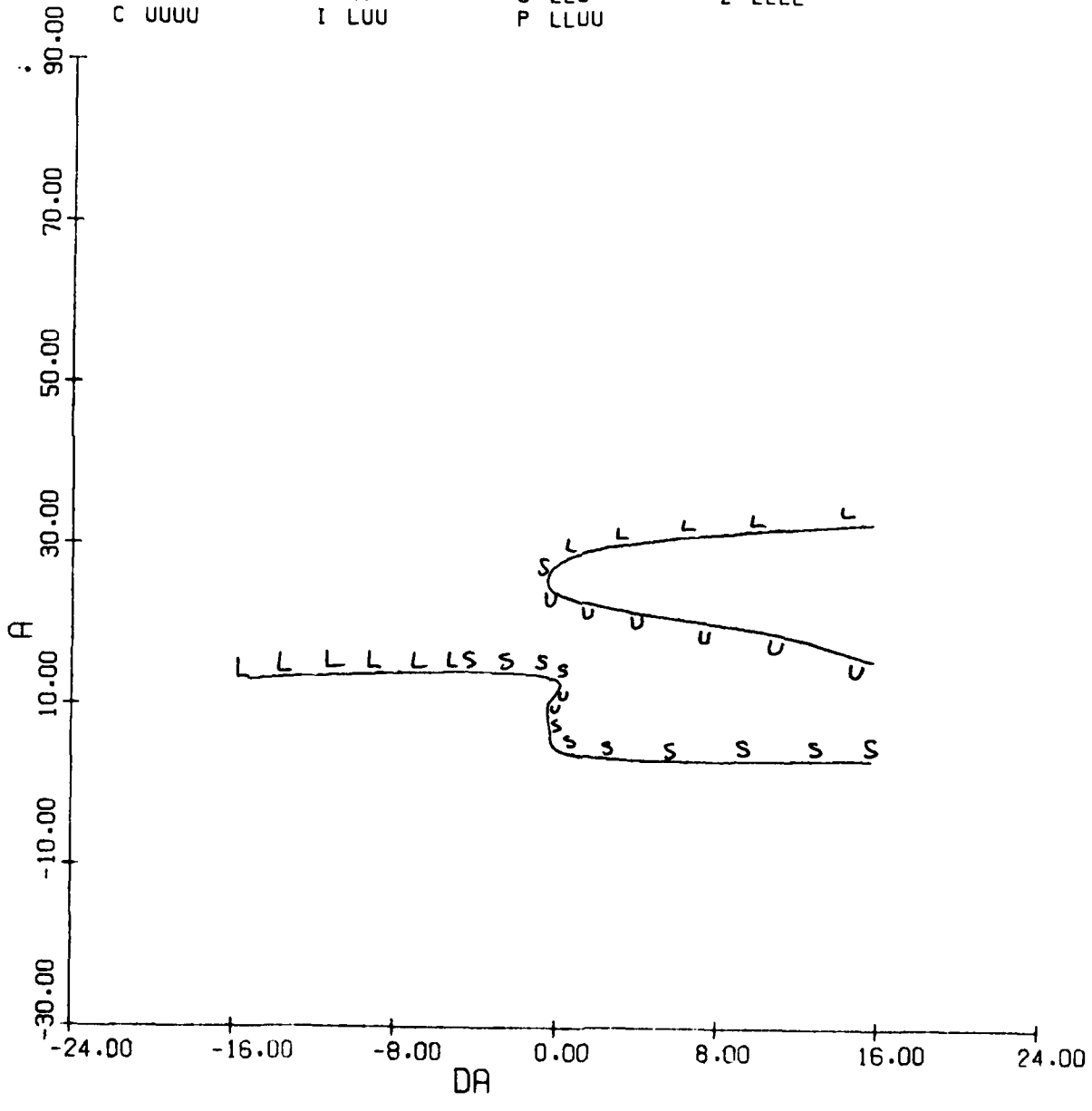

Figure 3.21(b) (cont.)

DE= 0.0
DR= -6.4

S	D UUUUU	J LUUU	Q LLUUU
U	E UUUUUU	K LUUUU	R LLUUUU
L	F UUUUUUU	M LUUUUU	X LLLU
A UU	G UUUUUUUU	N LUUUUUU	Y LLLUU
B UUU	H LU	O LLU	Z LLLL
C UUUU	I LUU	P LLUU	

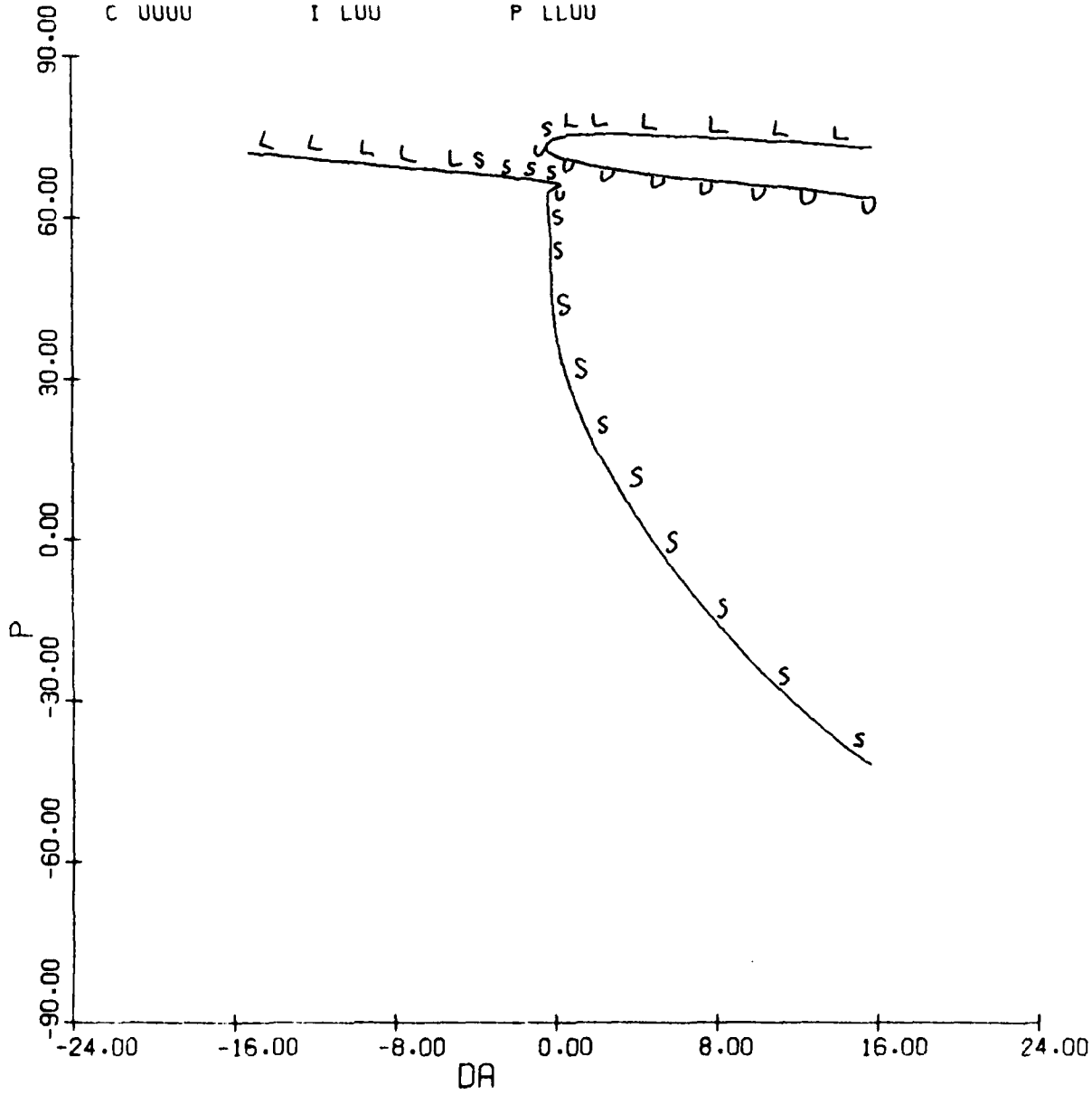

Figure 3.21(c) (concluded)

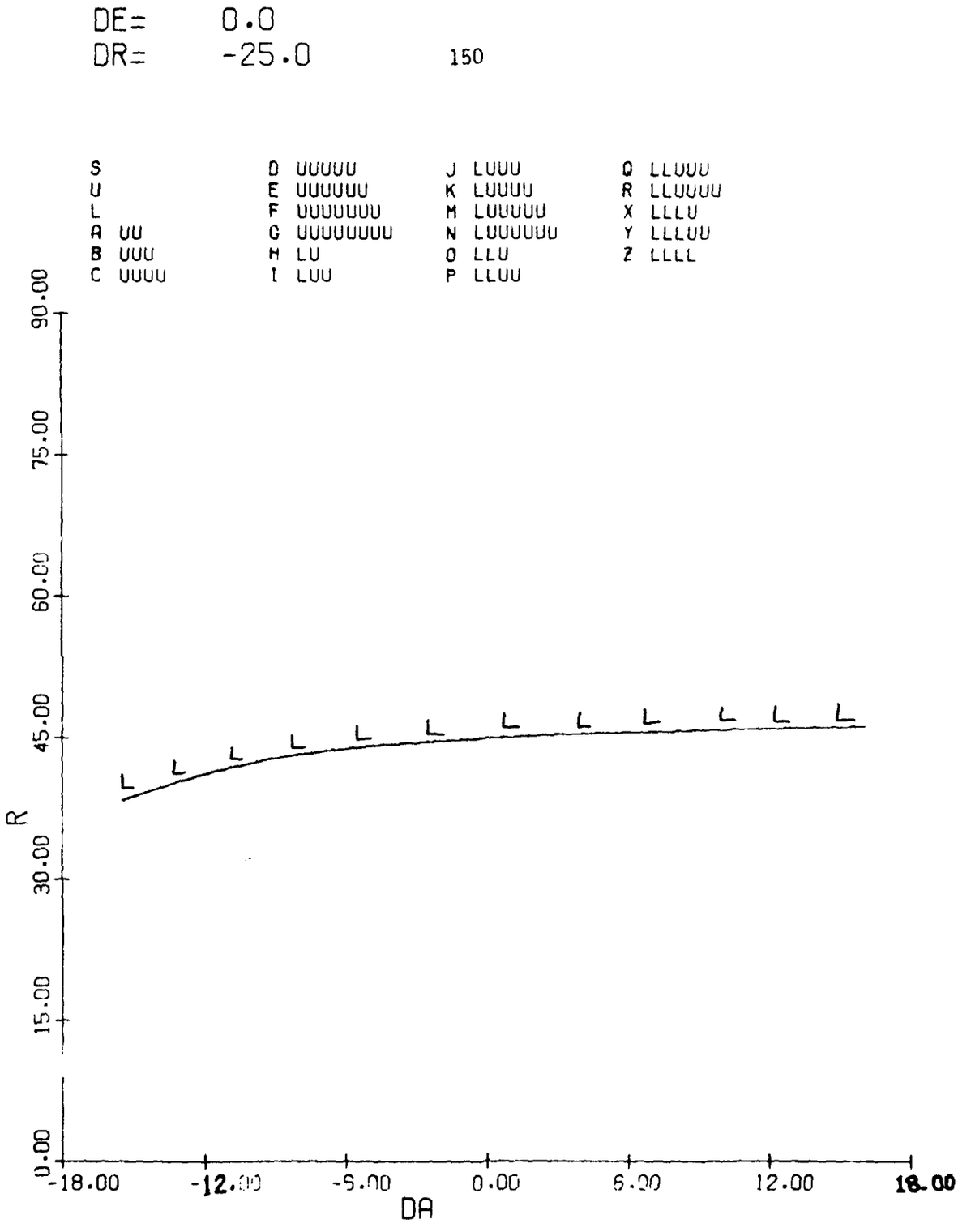

Figure 3.22(a)

Equilibrium Surface: r,α,p vs. δa
V = 600 fps, g = 0

DE= 0.0
DR= -25.0 151

S	D UUUUU	J LUUU	Q LLUUU
U	E UUUUUU	K LUUUU	R LLUUUU
L	F UUUUUUU	M LUUUUU	X LLLU
A UU	G UUUUUUUU	N LUUUUUU	Y LLLUU
B UUU	H LU	O LLU	Z LLLL
C UUUU	I LUU	P LLUU	

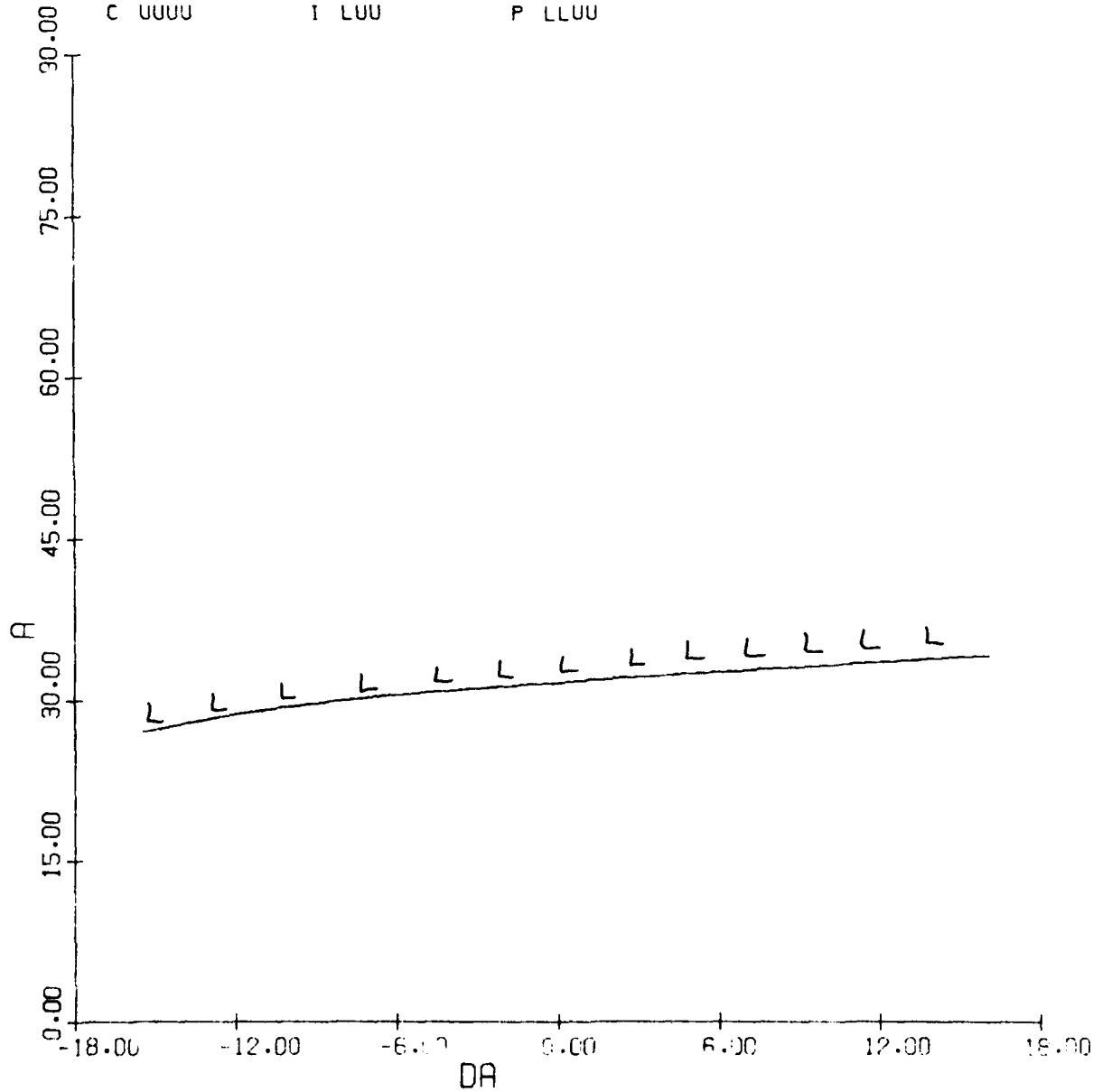

Figure 3.22(b) (cont.)

DE= 0.0
DR= -25.0

S	D UUUUU	J LUUU	Q LLUUU
U	E UUUUUU	K LUUUU	R LLUUUU
L	F UUUUUUU	M LUUUUU	X LLLU
A UU	G UUUUUUUU	N LUUUUUU	Y LLLUU
B UUU	H LU	O LLU	Z LLLL
C UUUU	I LUU	P LLUU	

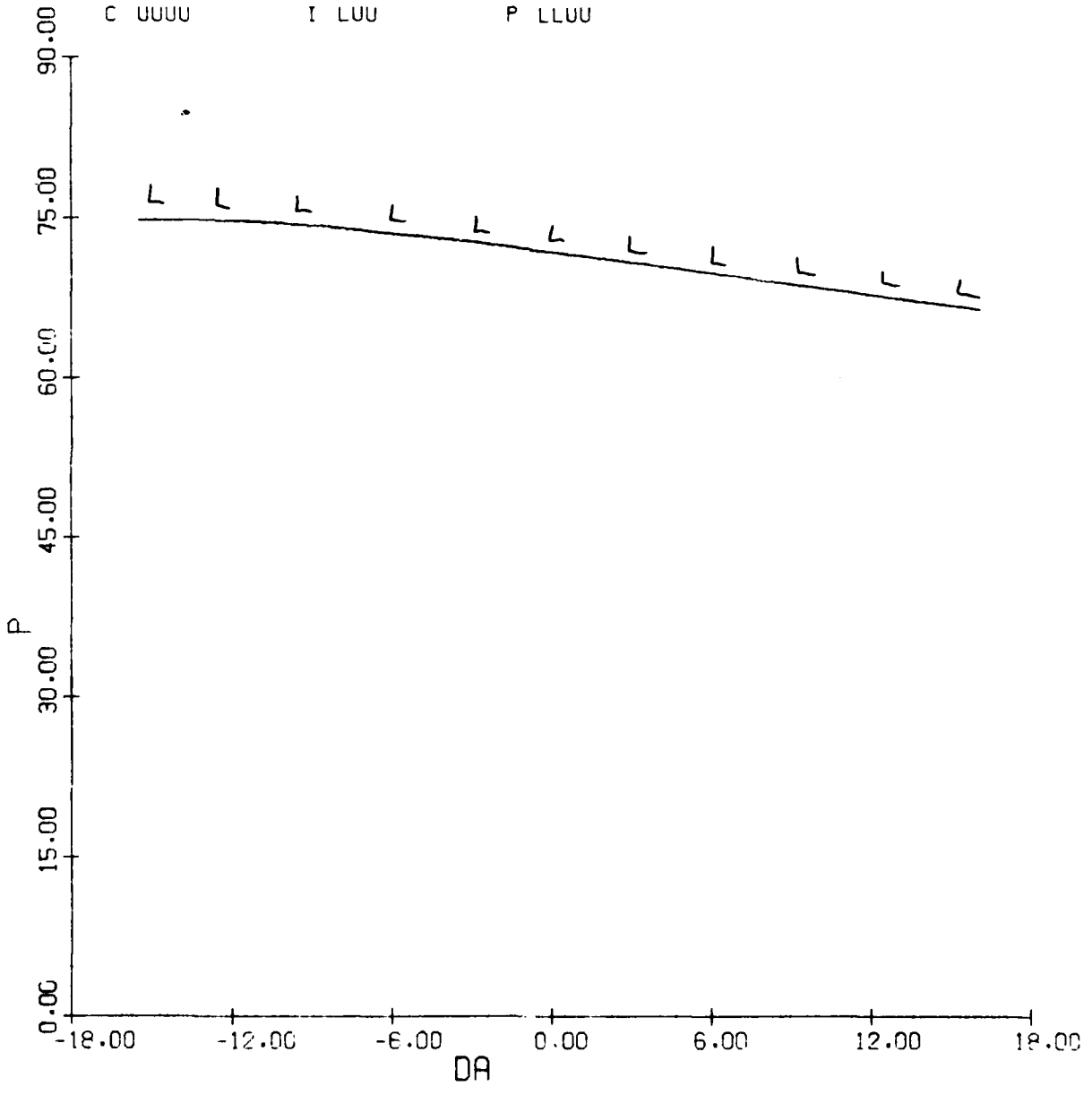

Figure 3.22(c) (concluded)

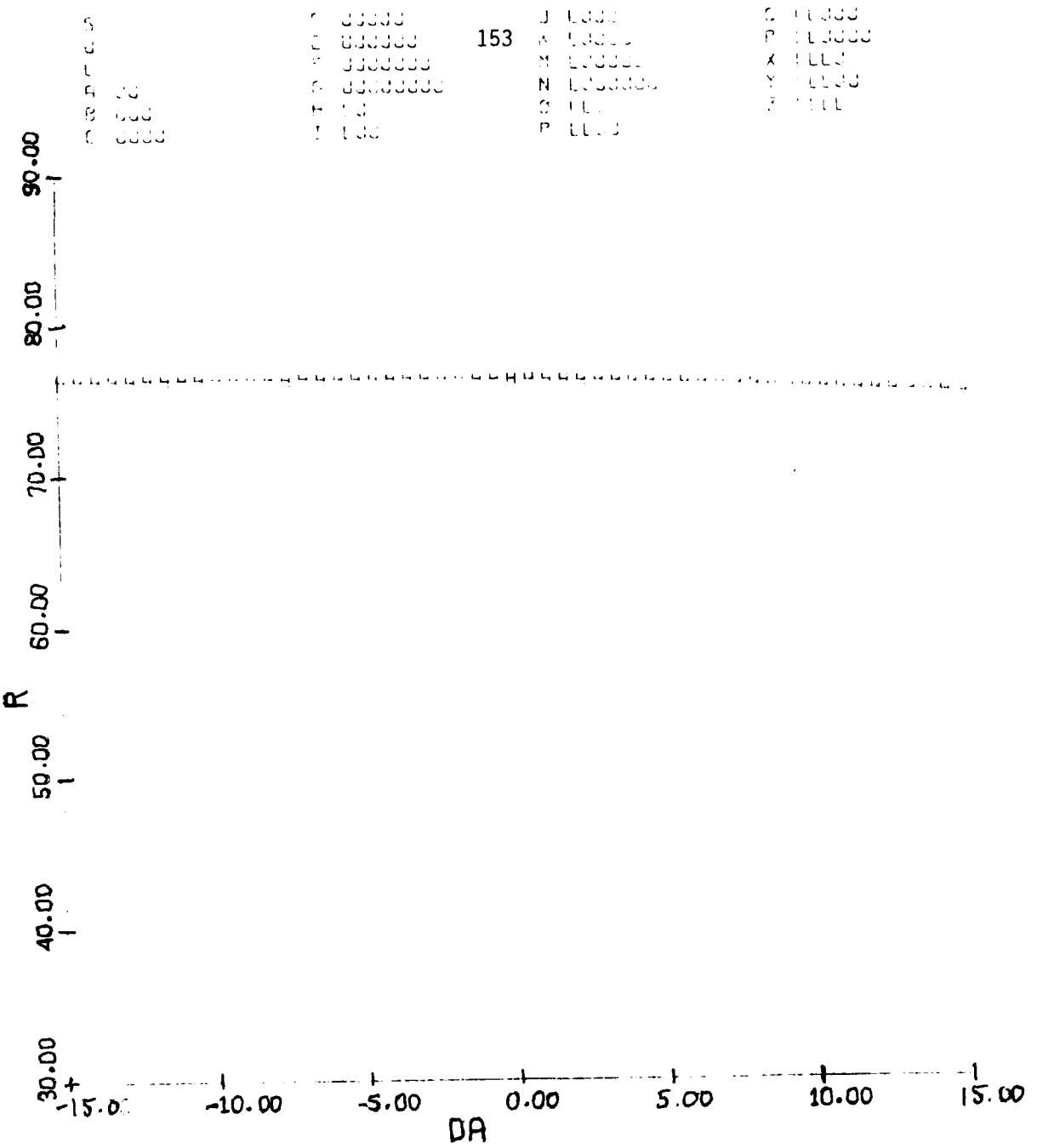

FIGURE 3.23
Equilibrium Surface: r vs. δa
δe = 10.3°, δr = -25°, V = 600 fps, g = 0

DE= -11.0
DR= 13.0

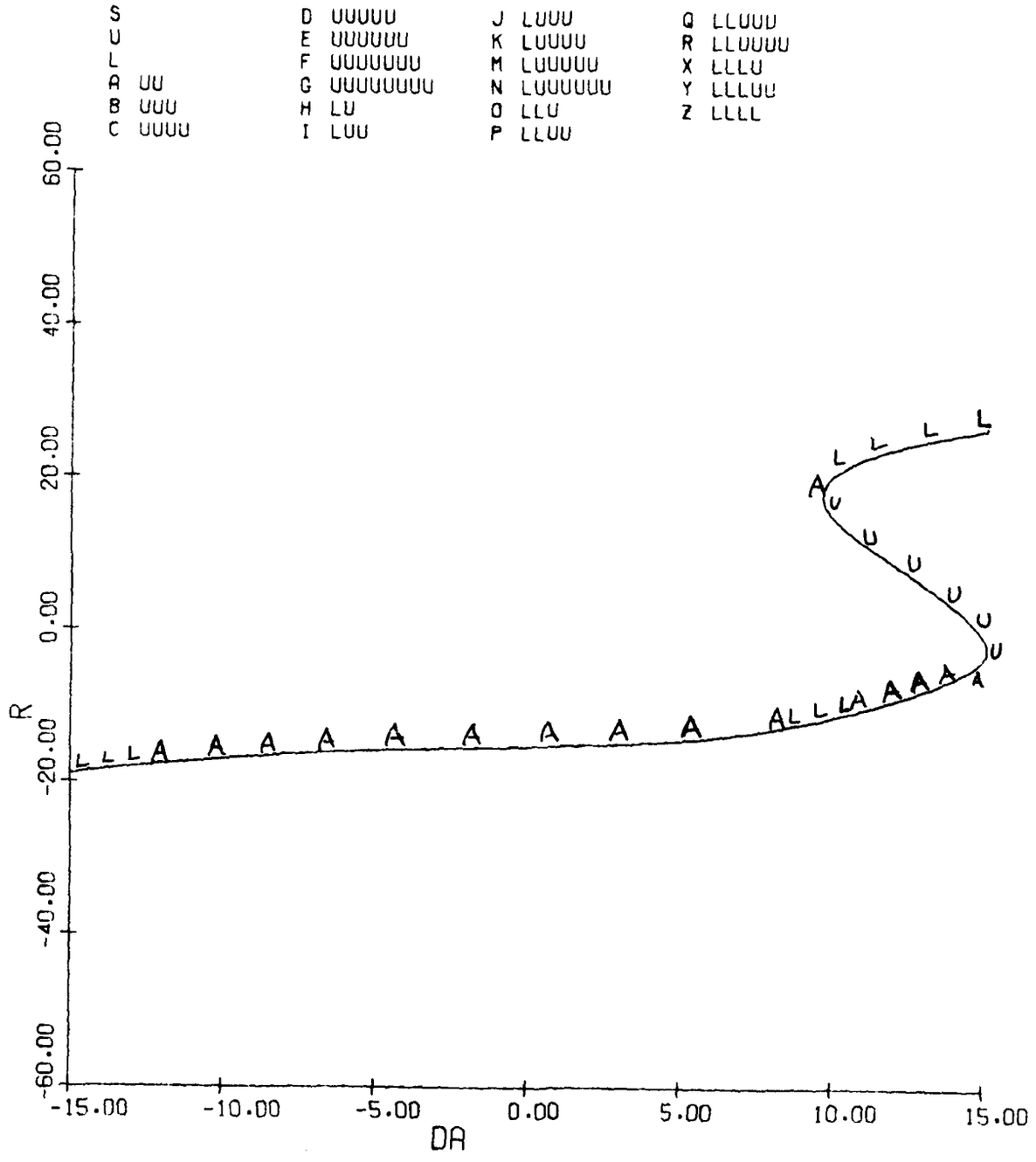

Figure 3.24(a)

Equilibrium Surface: r,α,p vs. δa
V = 600 fps, g = 0

DE= -11.0
DR= 13.0

S	D UUUUU	J LUUU	Q LLUUU
U	E UUUUUU	K LUUUU	R LLUUUU
L	F UUUUUUU	M LUUUUU	X LLLU
A UU	G UUUUUUUU	N LUUUUUU	Y LLLUU
B UUU	H LU	O LLU	Z LLLL
C UUUU	I LUU	P LLUU	

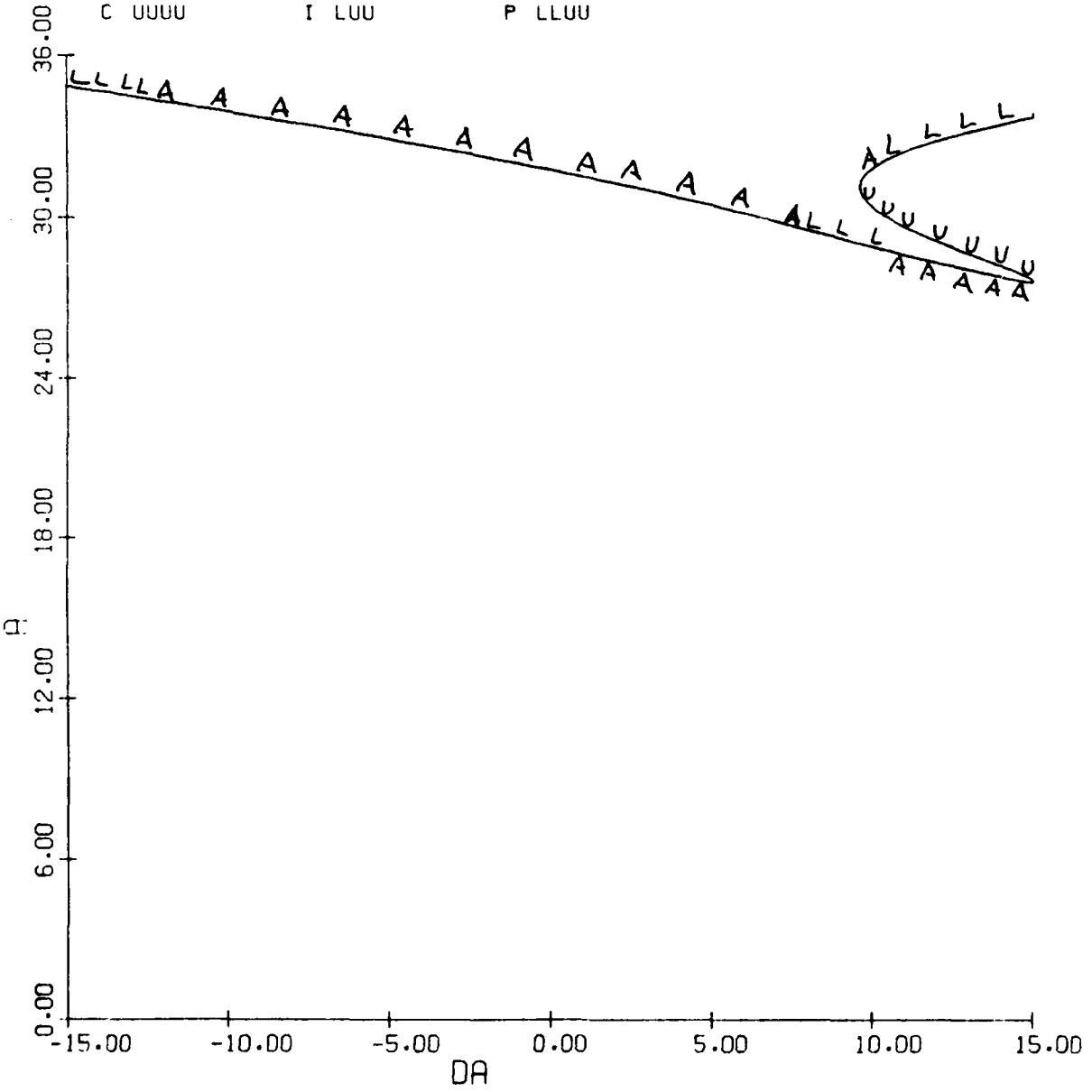

Figure 3.24(b) (cont.)

DE= −11.0
DR= 13.0

S	D UUUUU	J LUUU	Q LLUUU
U	E UUUUUU	K LUUUU	R LLUUUU
L	F UUUUUUU	M LUUUUU	X LLLU
A UU	G UUUUUUUU	N LUUUUUU	Y LLLUU
B UUU	H LU	O LLU	Z LLLL
C UUUU	I LUU	P LLUU	

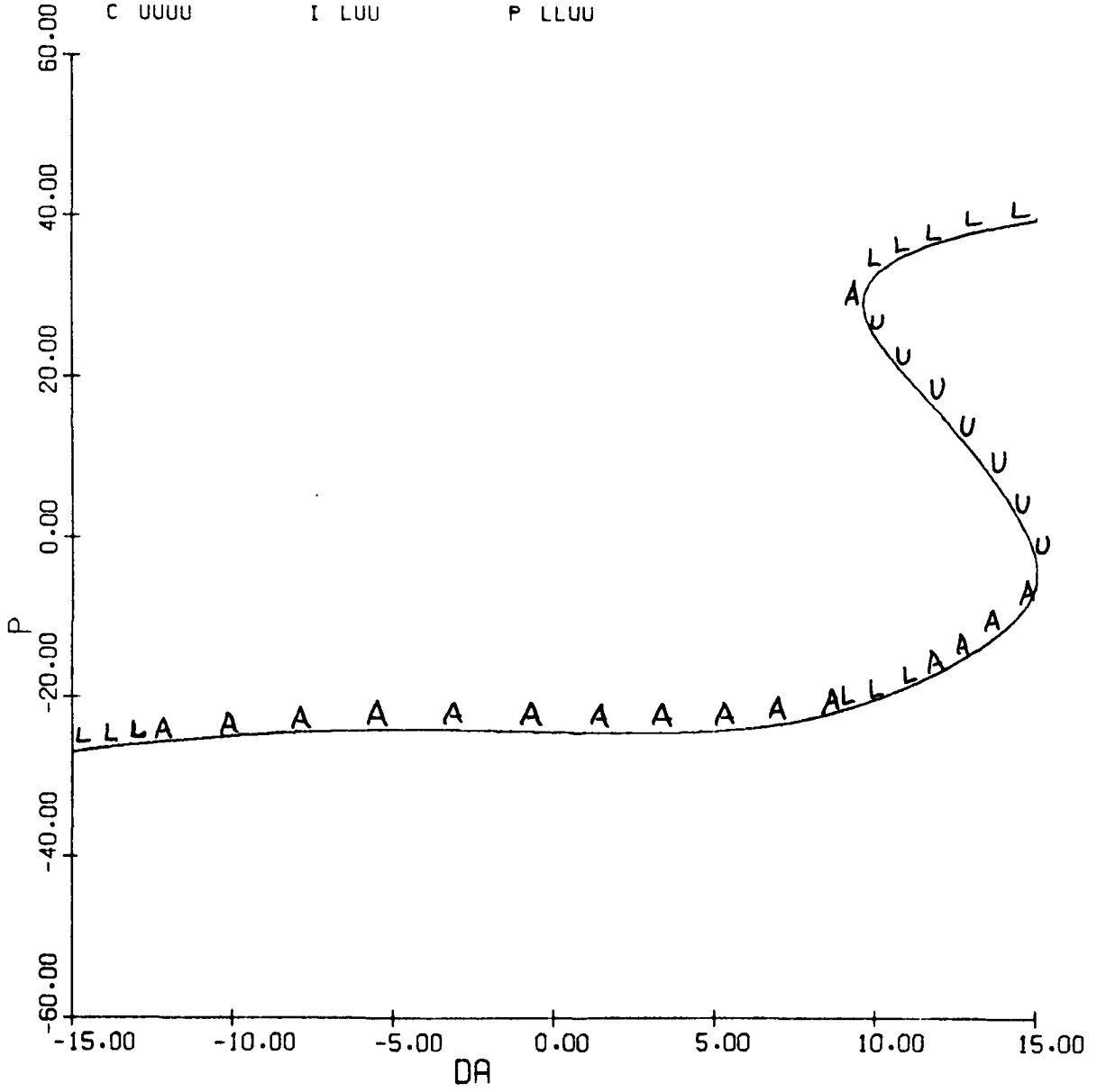

Figure 3.24(c) (concluded)

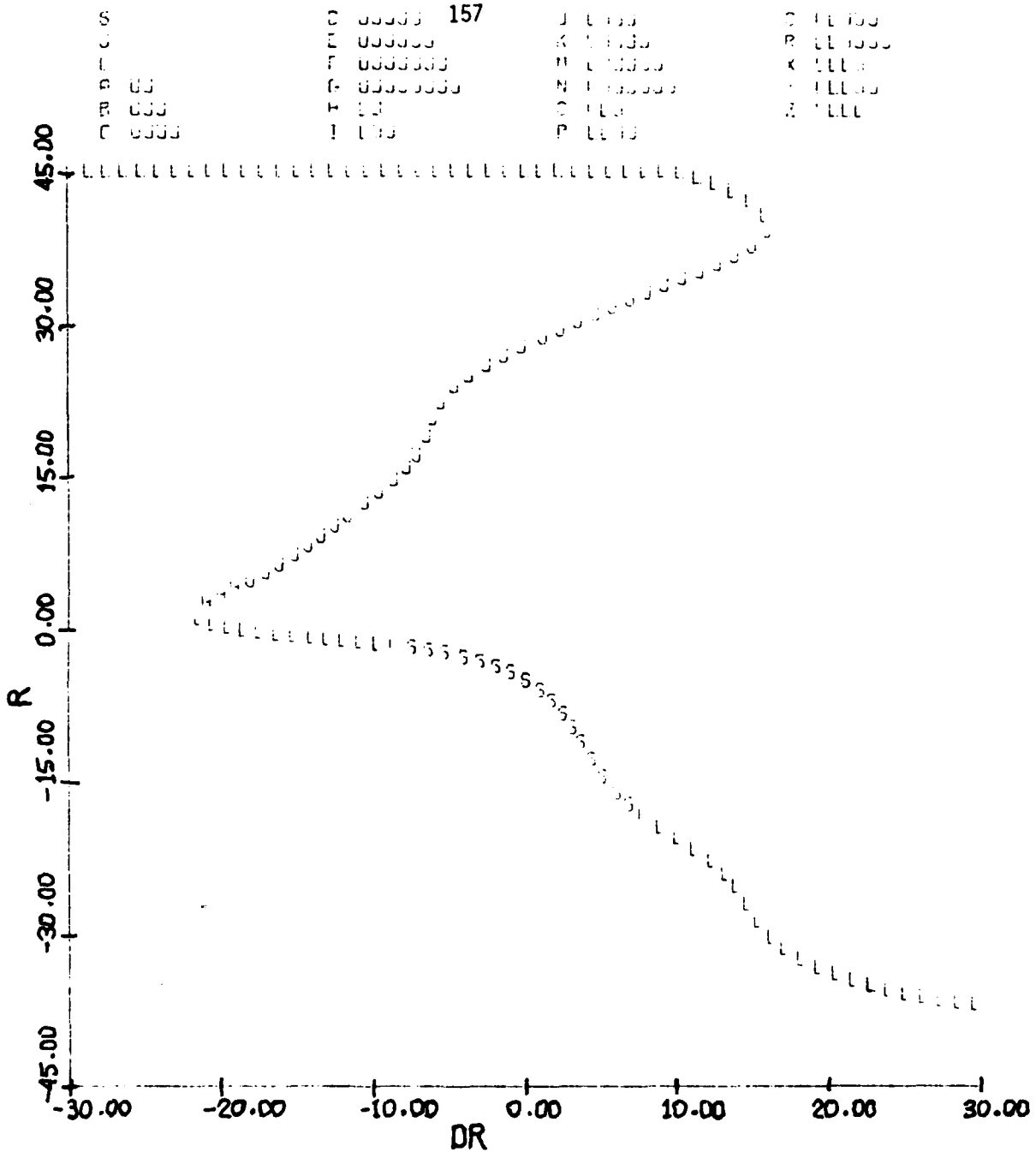

FIGURE 3.25(a)
Equilibrium Surface: r,α,p vs. δr
δa = 15°, δe = 0°, V = 600 fps, g = 0

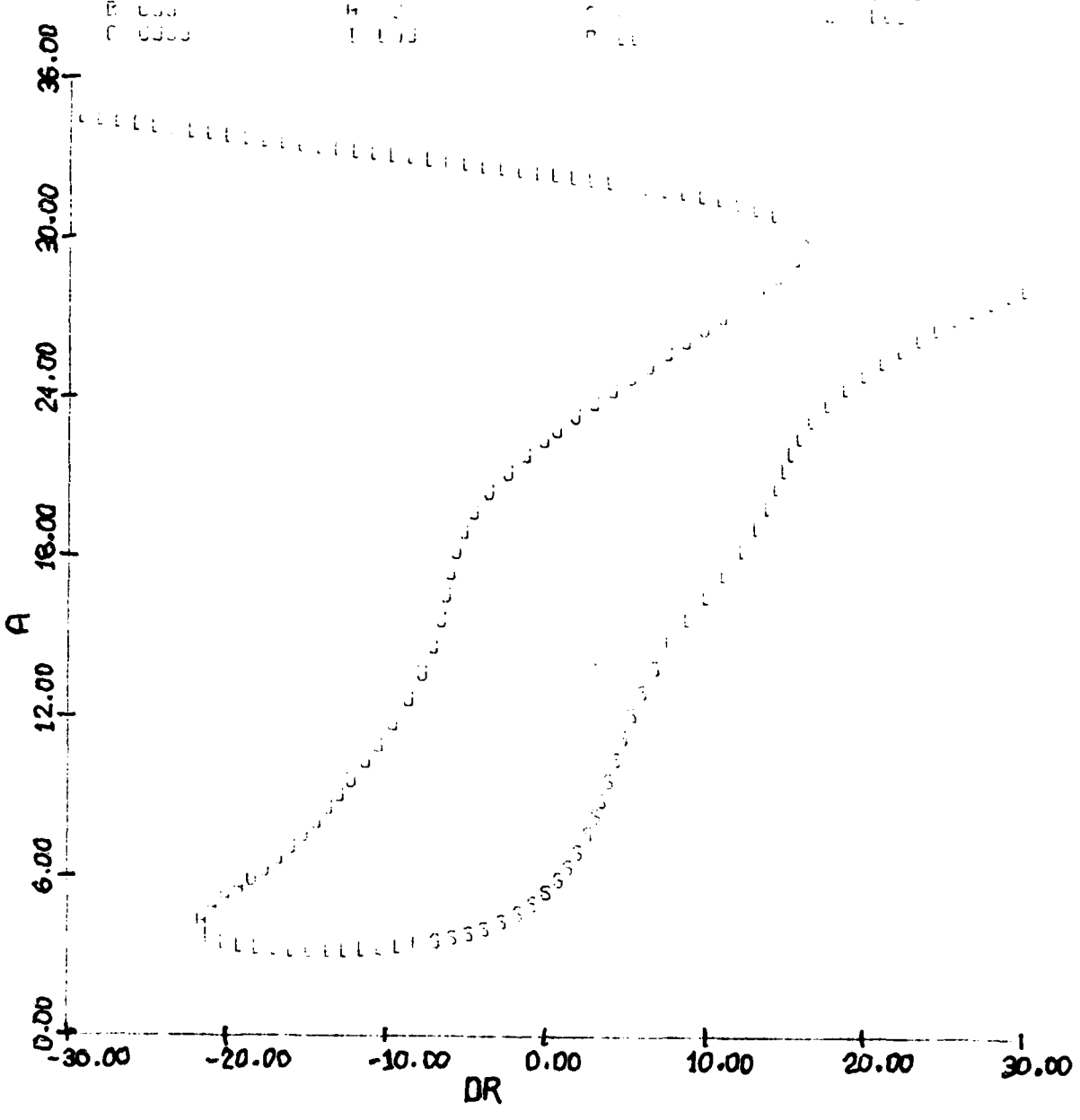

FIGURE 3.25(b) (cont.)

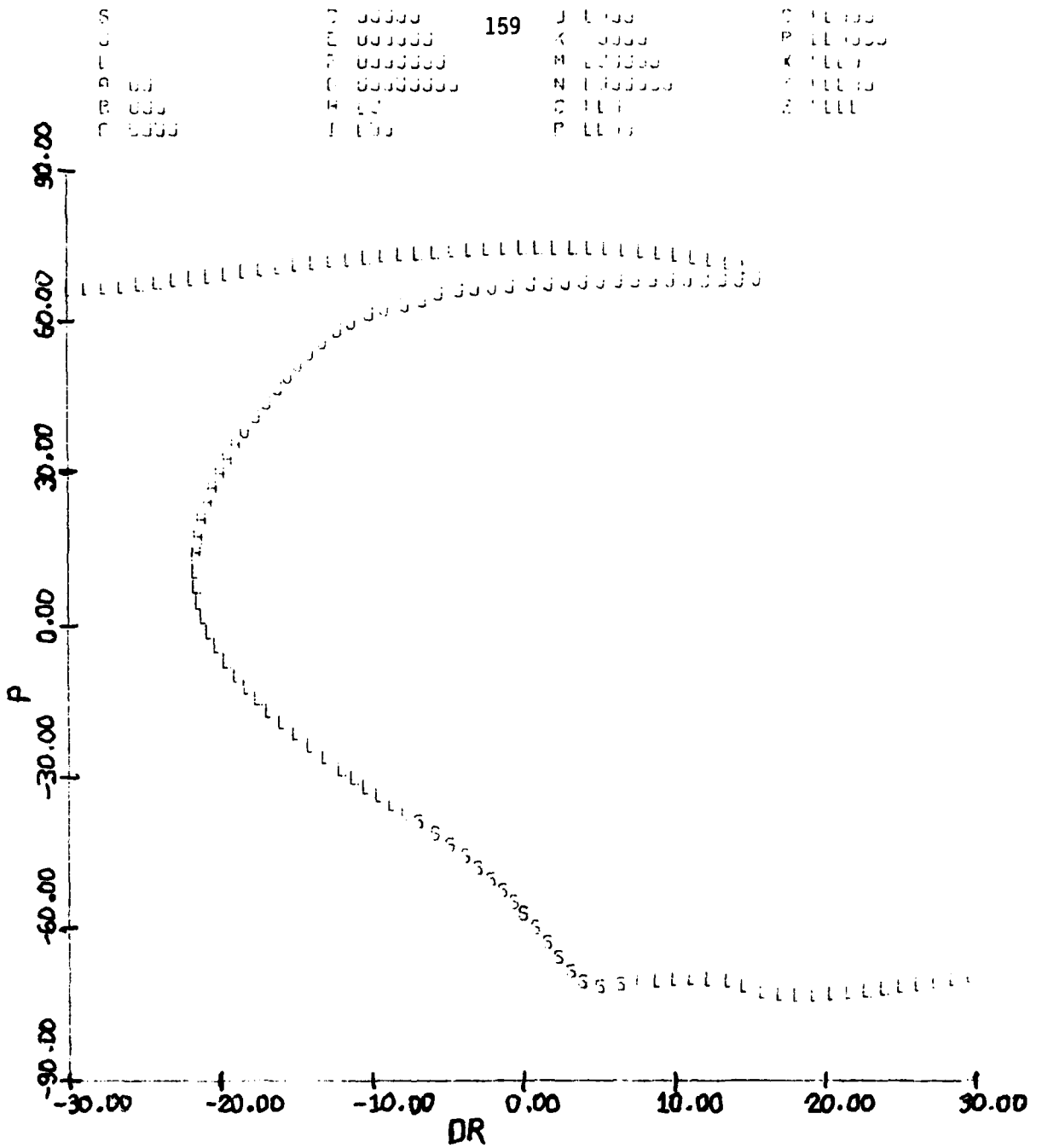

FIGURE 3.25(c) (concluded)

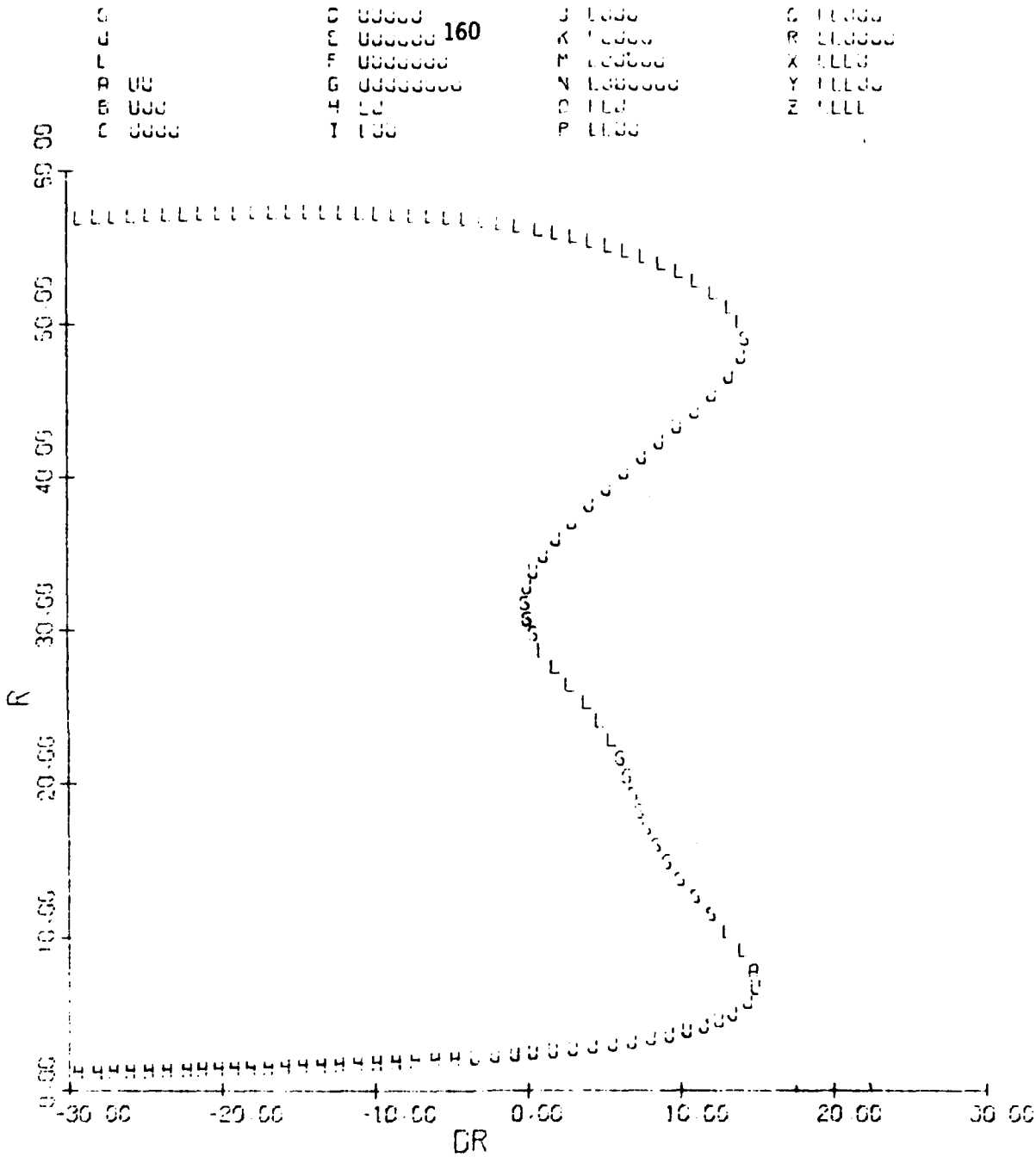

FIGURE 3.26(a)
Equilibrium Surface: r,α,p vs. δr
δa = 15°, δe = 7.3°, V = 600 fps, g = 0

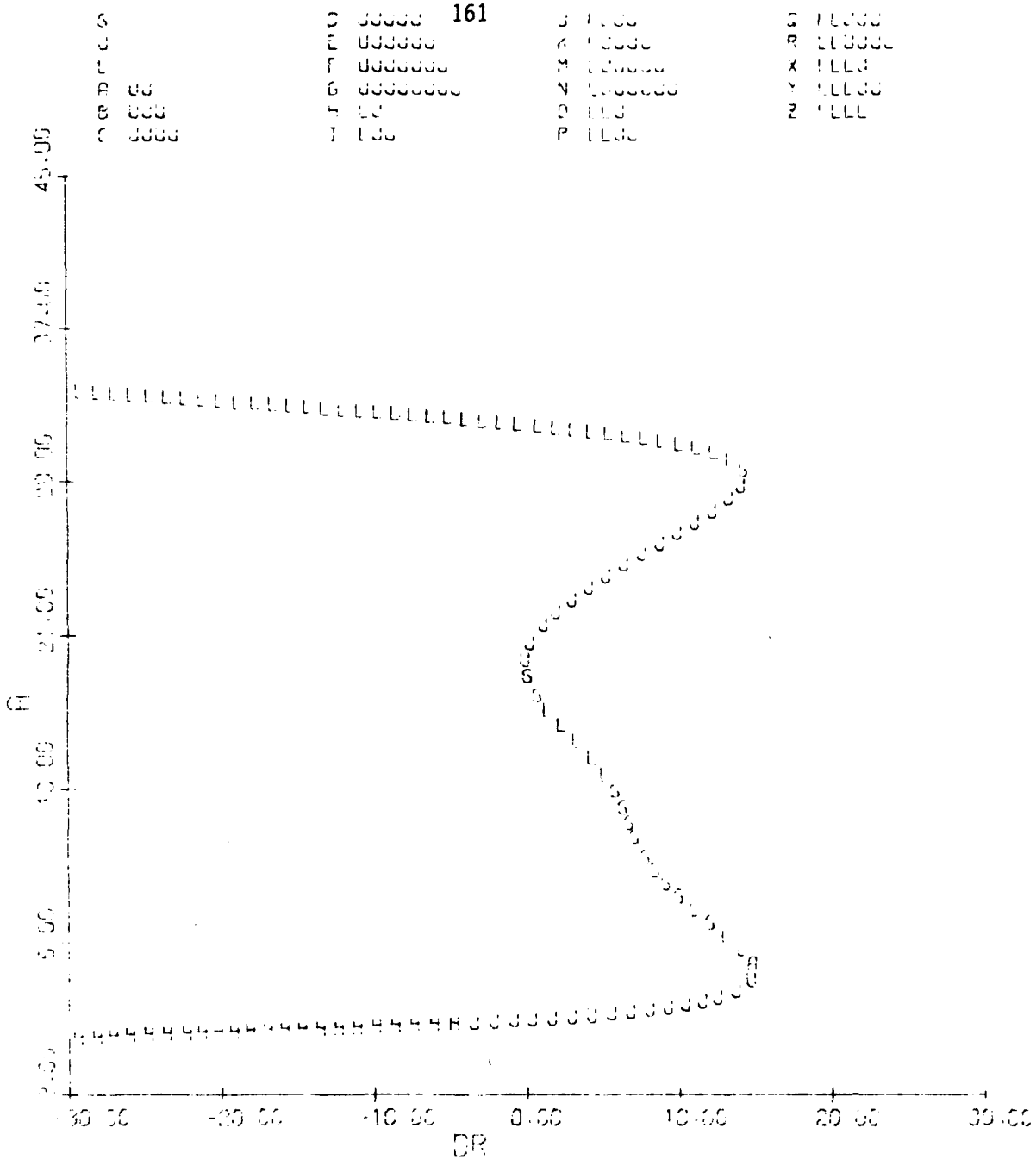

FIGURE 3.26(b) (cont.)

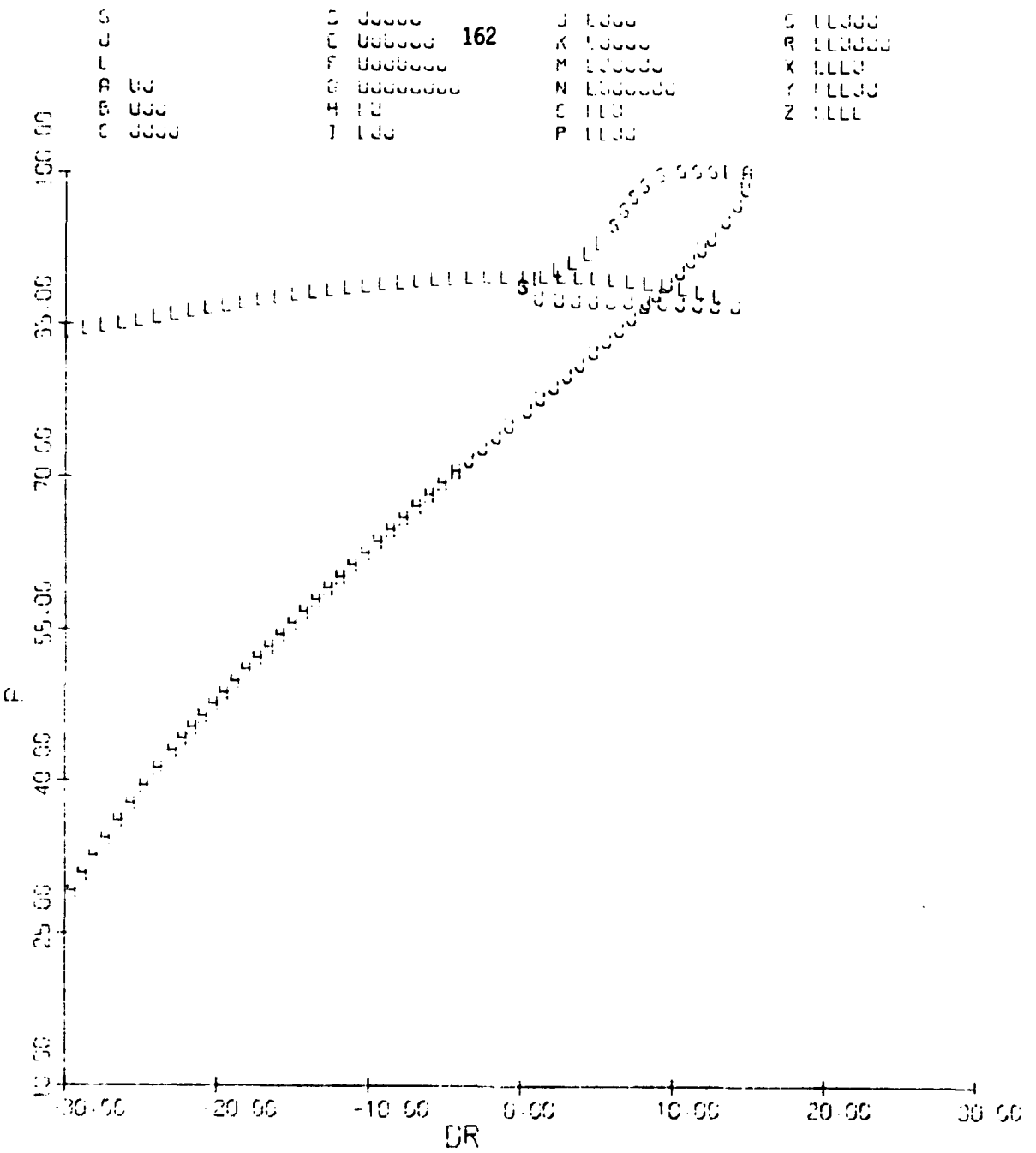

FIGURE 3.26(c) (concluded)

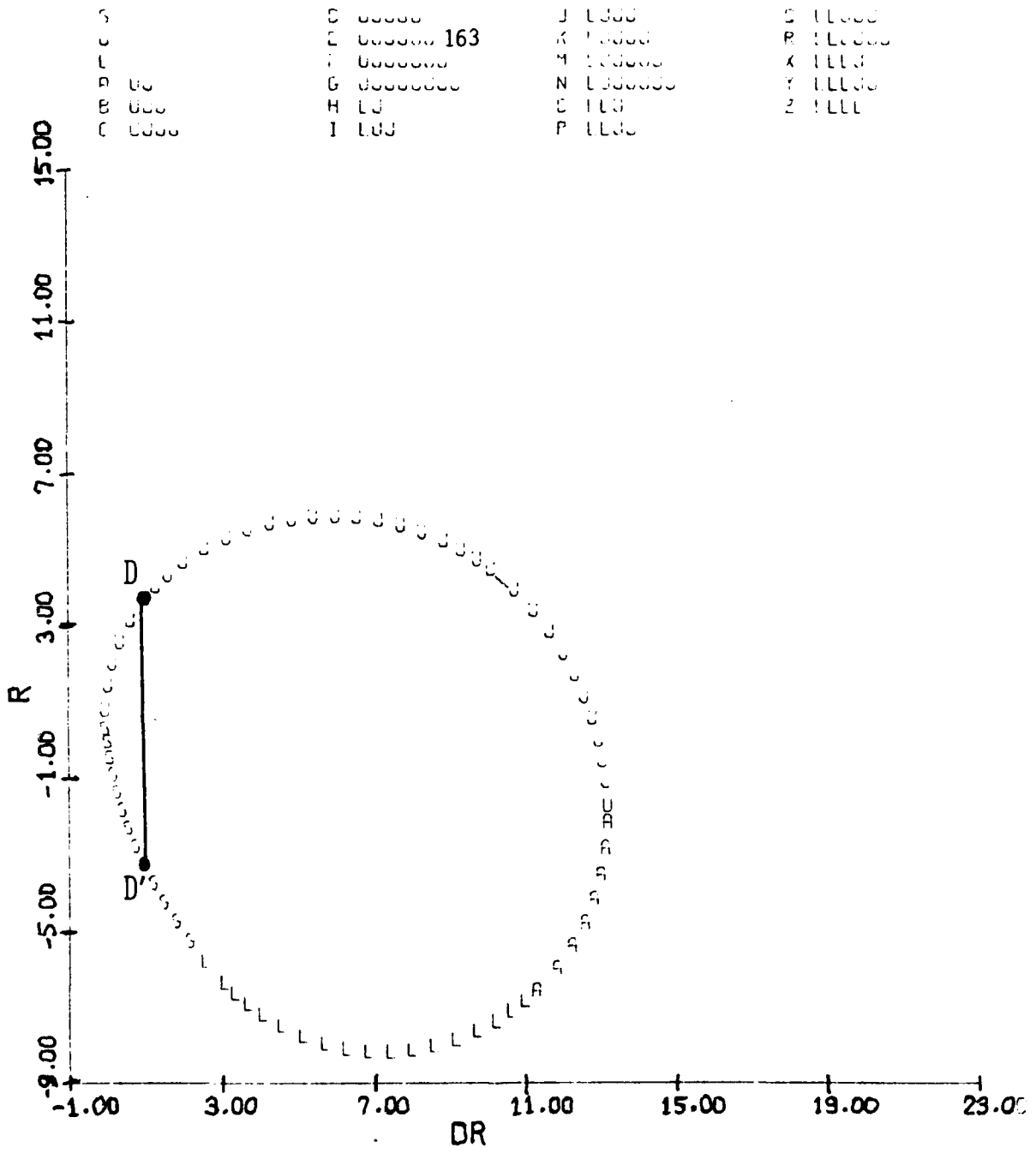

FIGURE 3.27(a)
Equilibrium Surface: r,α,p vs. δr
δa = 15°, δe = -11°, V = 600 fps, g = 0

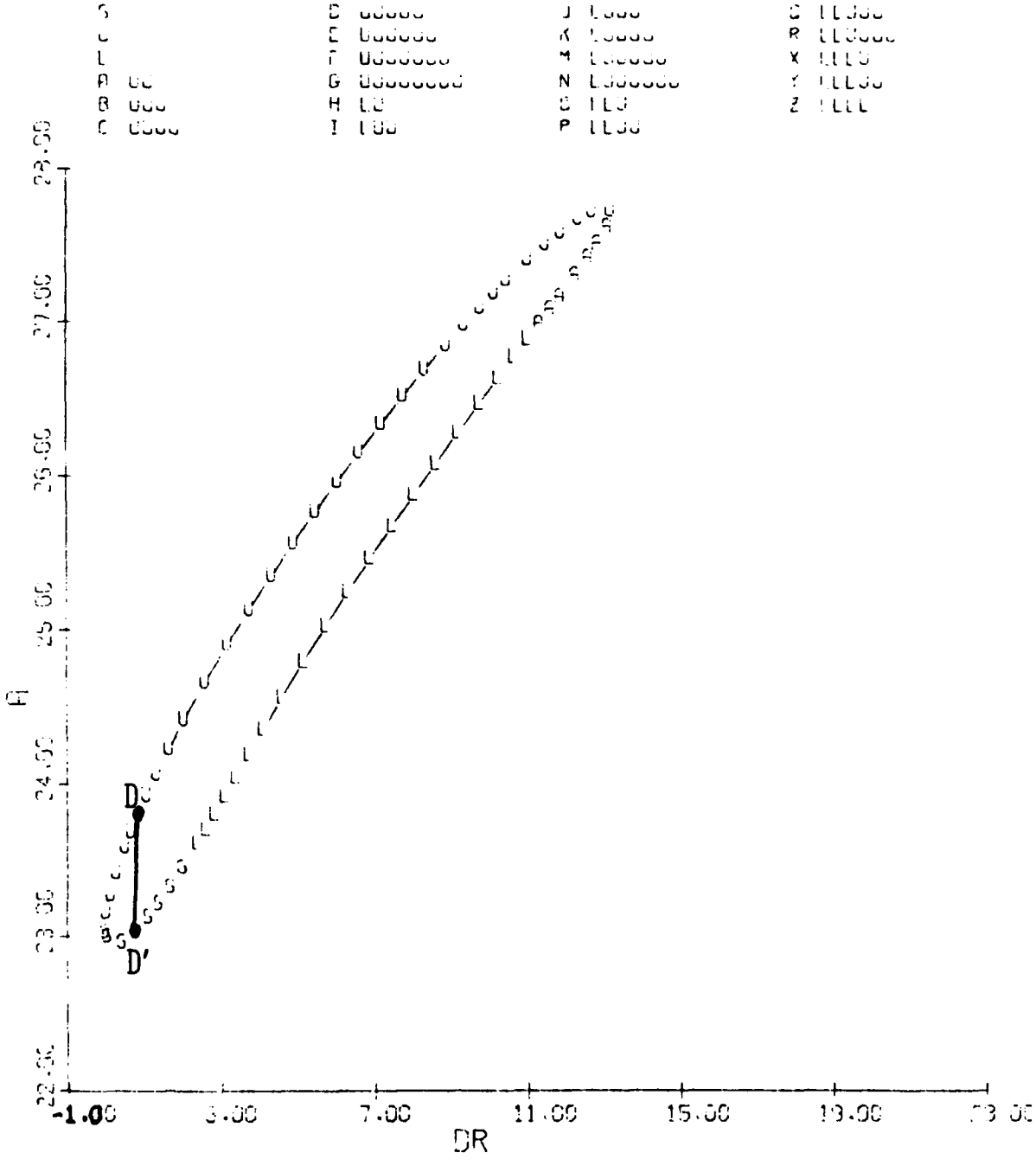

FIGURE 3.27(b) (cont.)

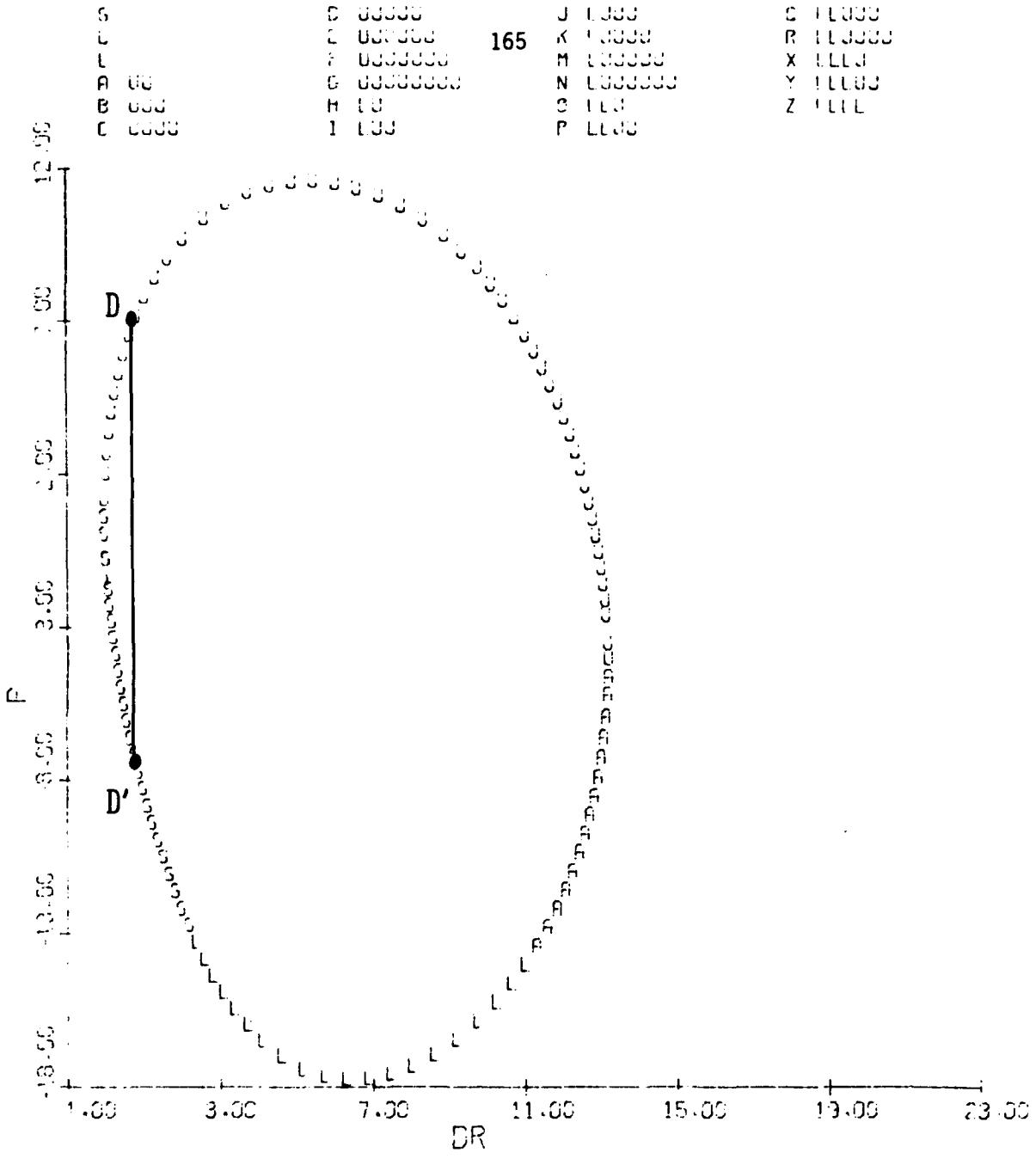

FIGURE 3.27(c) (concluded)

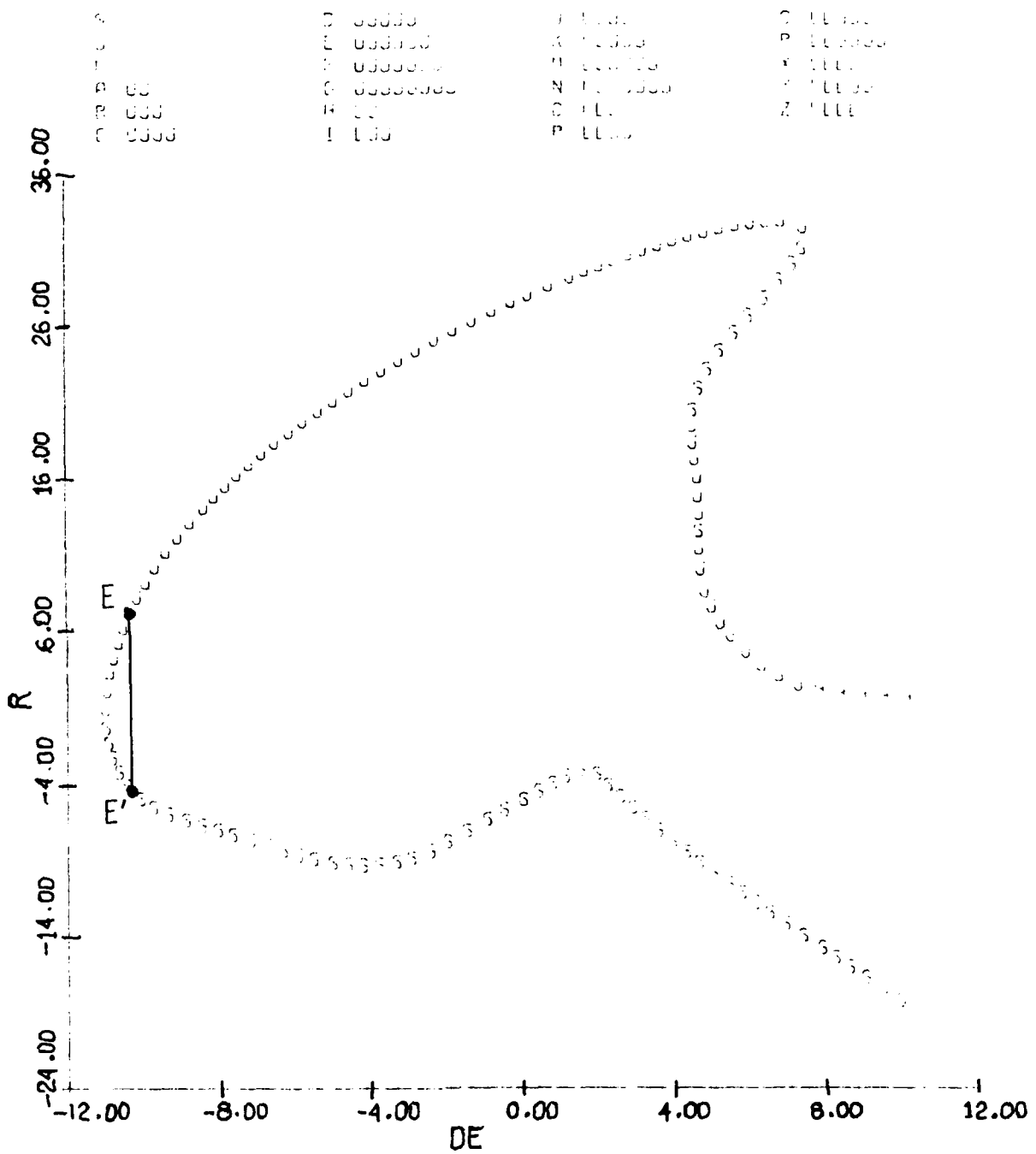

FIGURE 3.28(a)
Equilibrium Surface: r,α,p vs. δe
δa = 15°, δr = 0°, V = 600 fps, g = 0

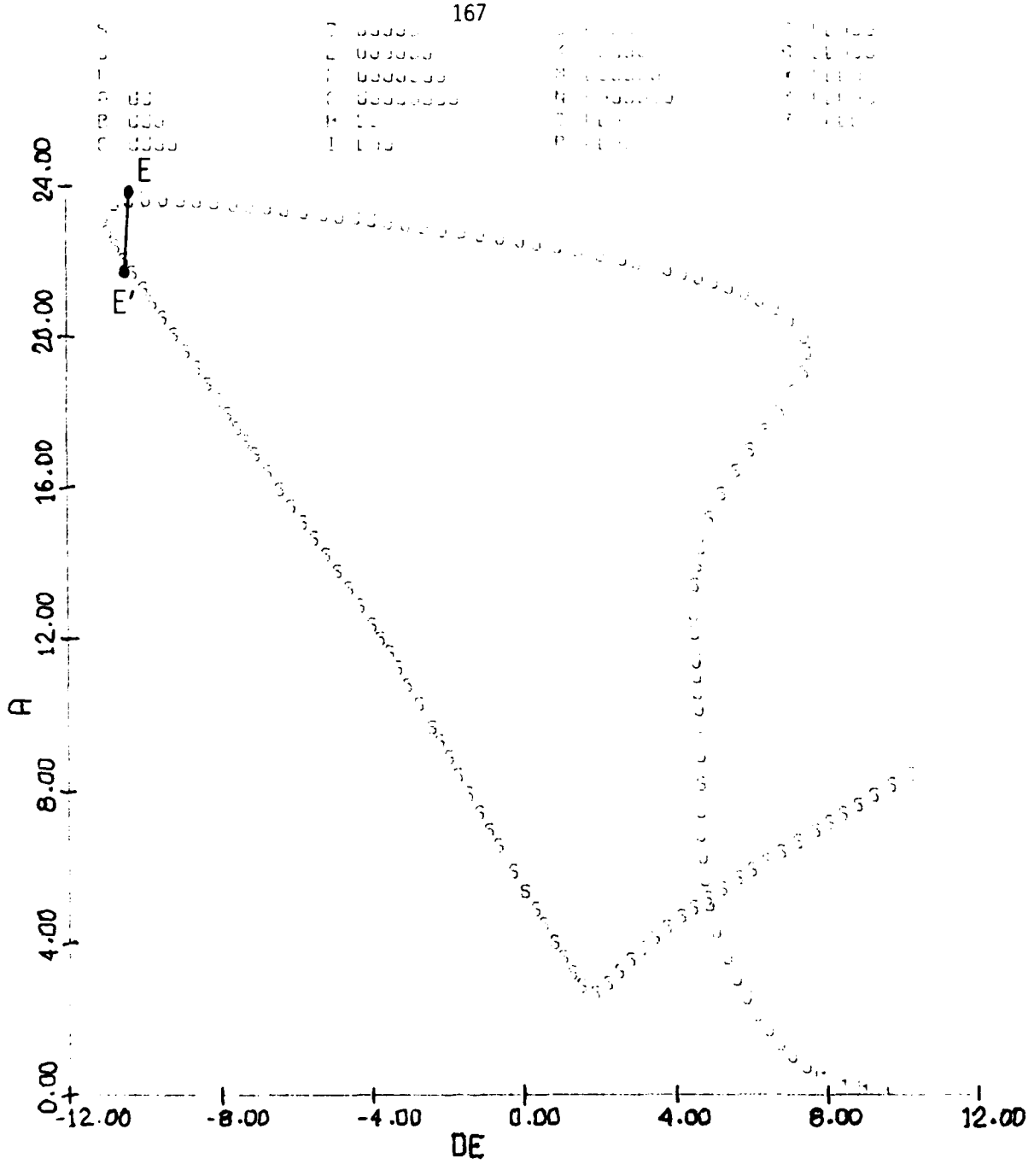

FIGURE 3.28(b) (cont.)

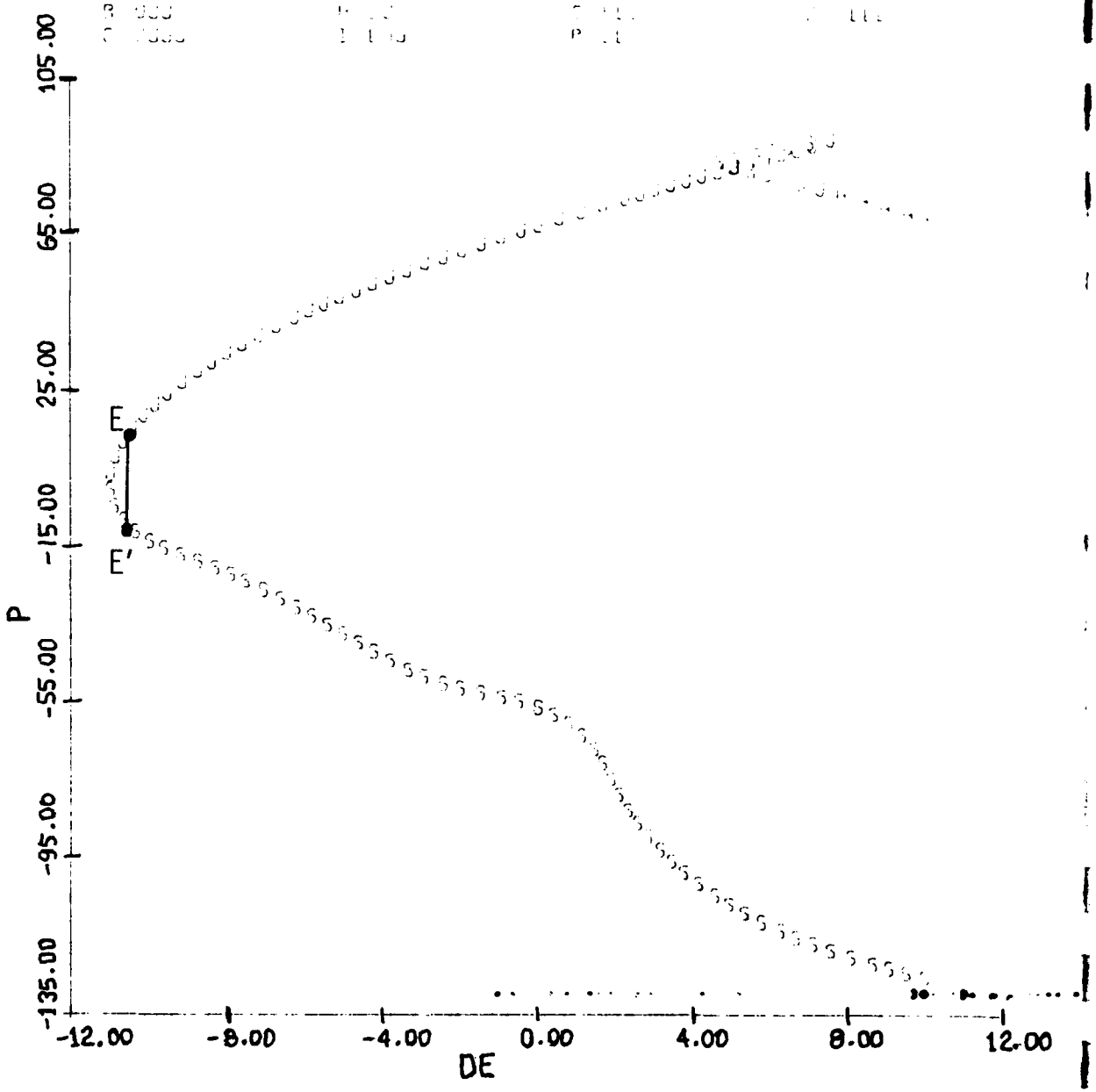

FIGURE 3.28(c) (concluded)

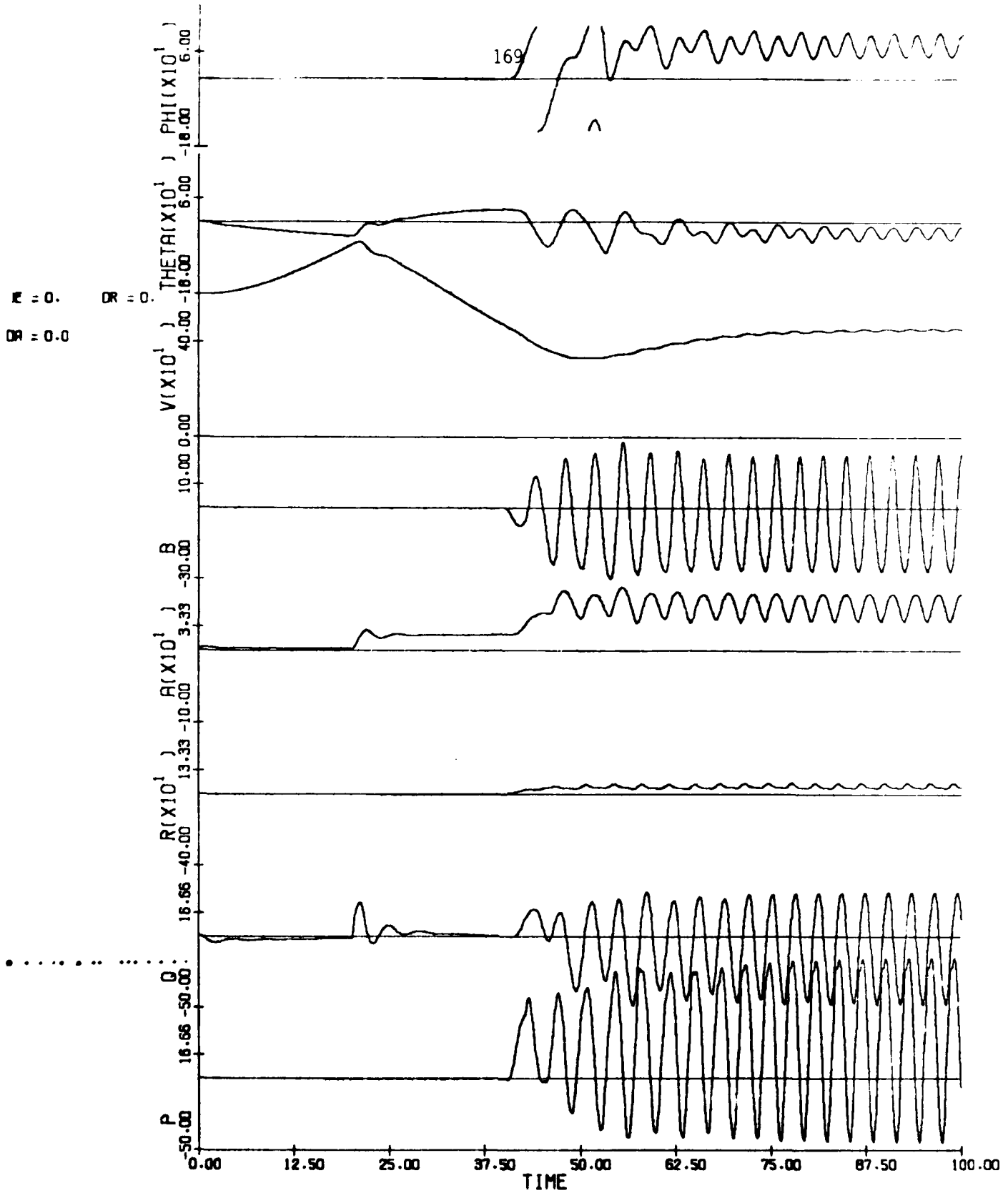

Figure 3.29
Time History: Spin Entry Study

$\delta a = \begin{cases} 0°, & t \leq 45 \\ 15°, & t > 45 \end{cases}$ $\delta e = \begin{cases} 0°, & t \leq 20 \\ -10°, & t > 20 \end{cases}$ $\delta r = \begin{cases} 0°, & t \leq 40 \\ -29°, & t > 40 \end{cases}$

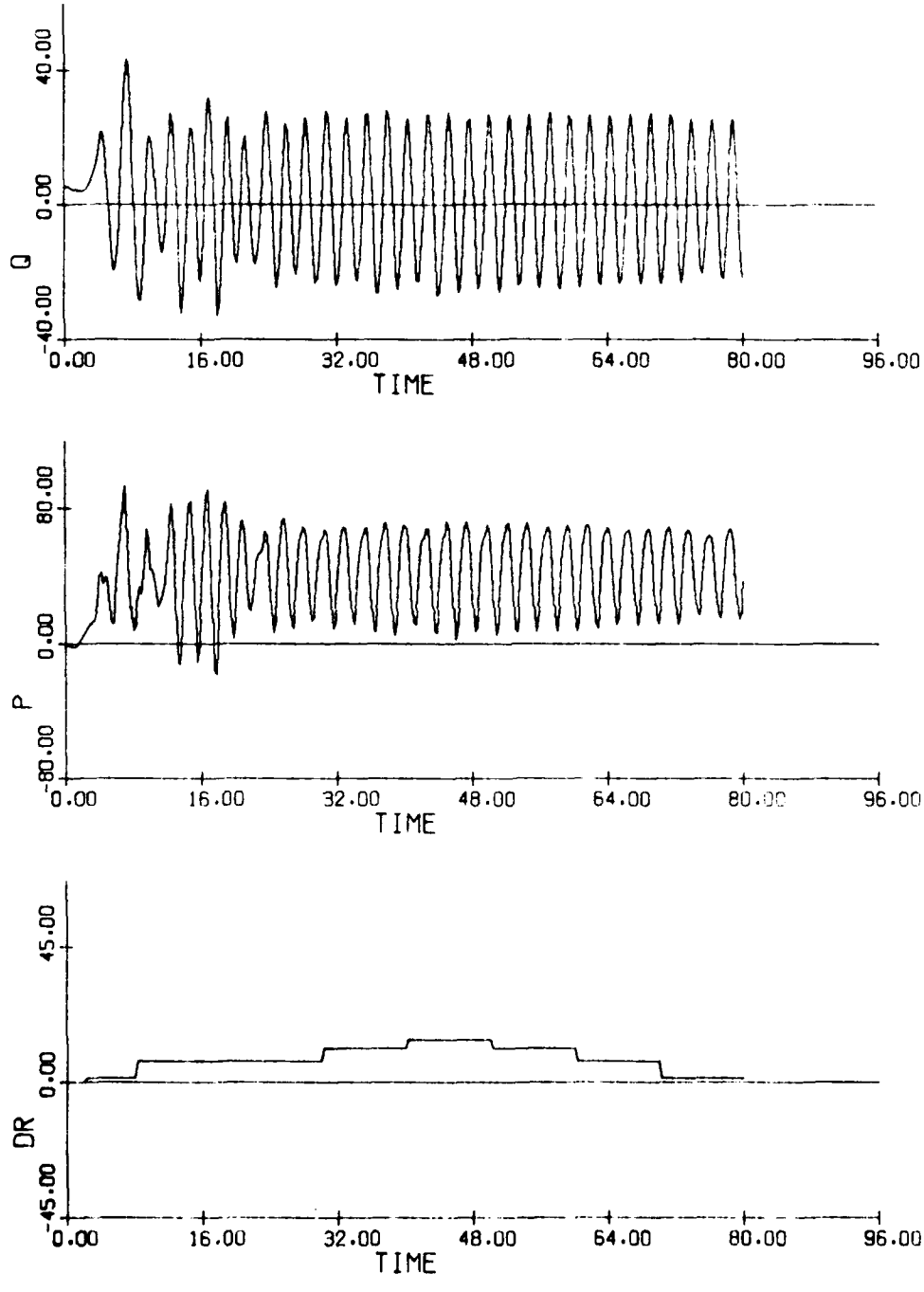

Figure 3.30(a)

Time History: Oscillatory Spin Entry
$\delta a = 15°$, $\delta e = -11°$

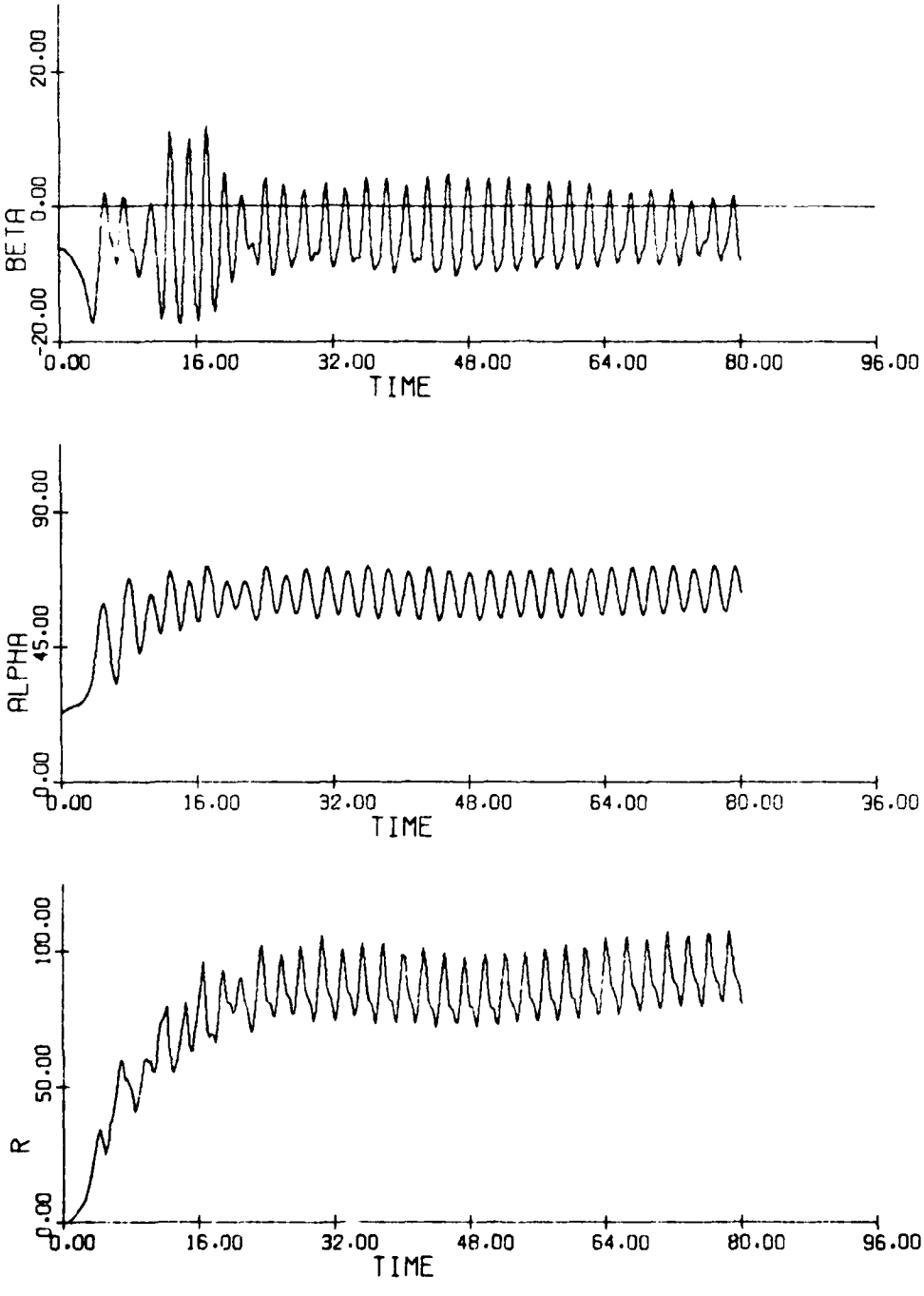

Figure 3.30(b) (cont.)

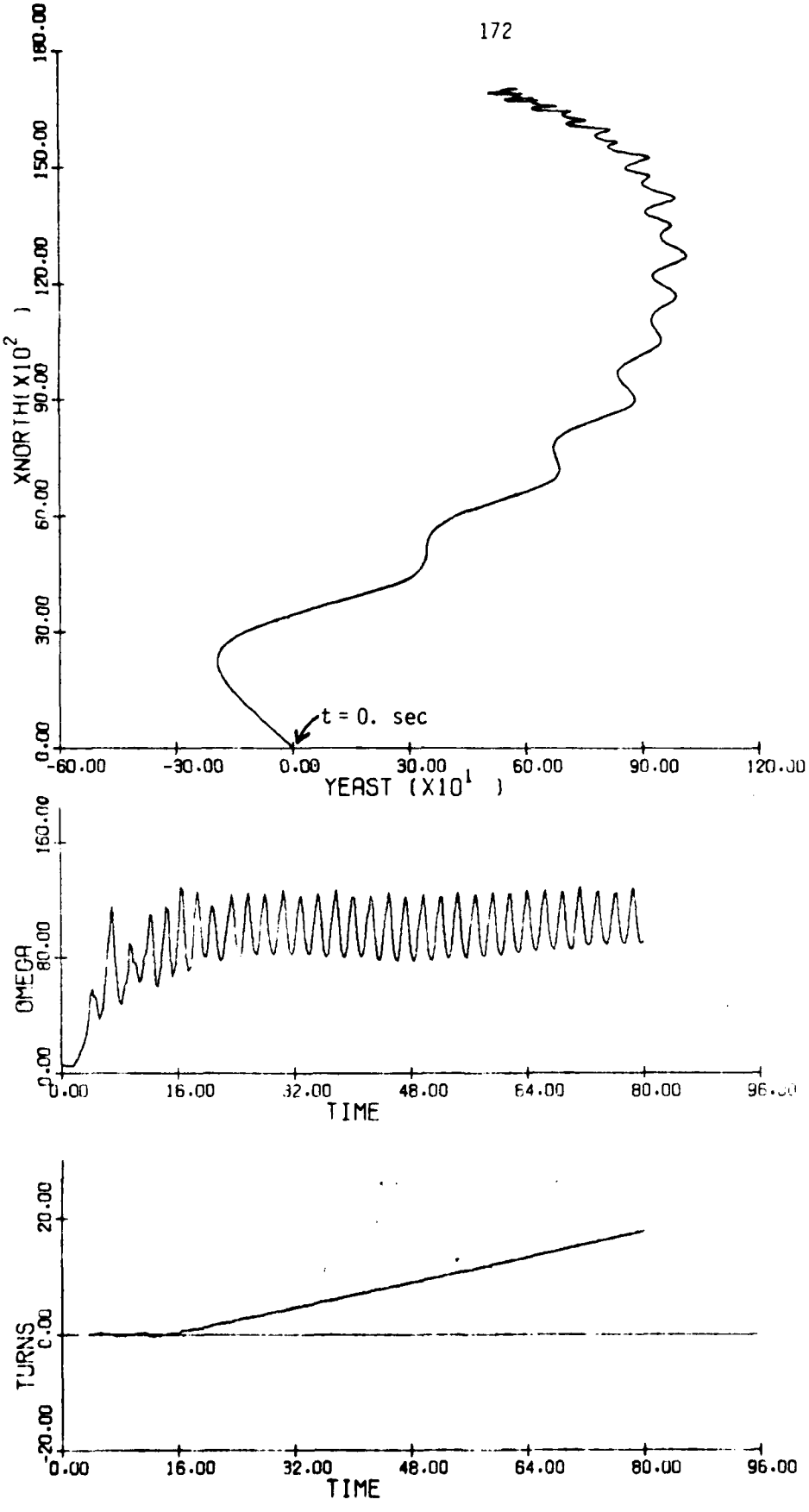

Figure 3.30(c) (concluded)

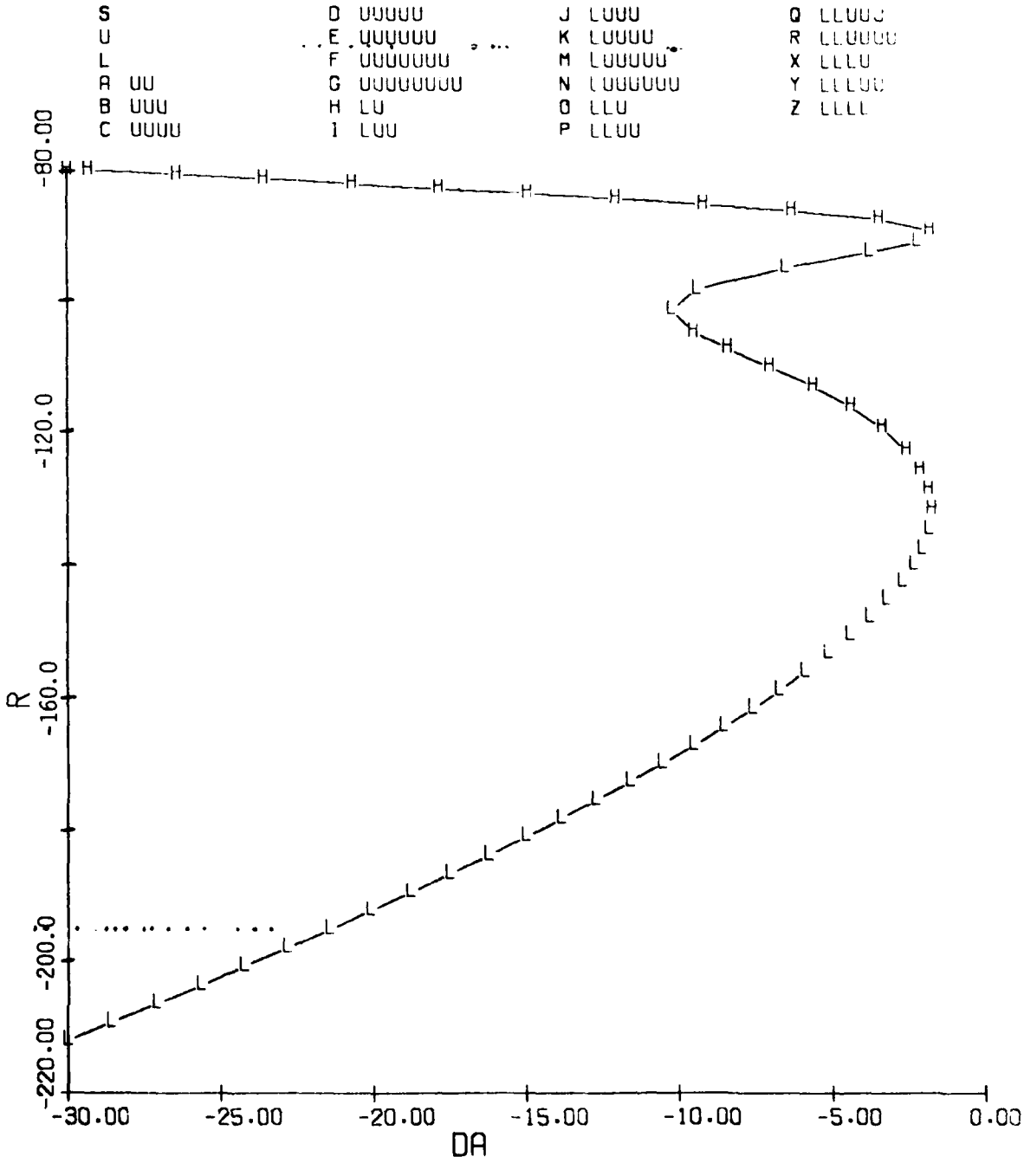

Figure 3.31(a)

Equilibrium Surface - Spin Regime: Yaw Rate vs. Aileron Deflection

$\delta e = 0°$ $\delta r = 28.3°$

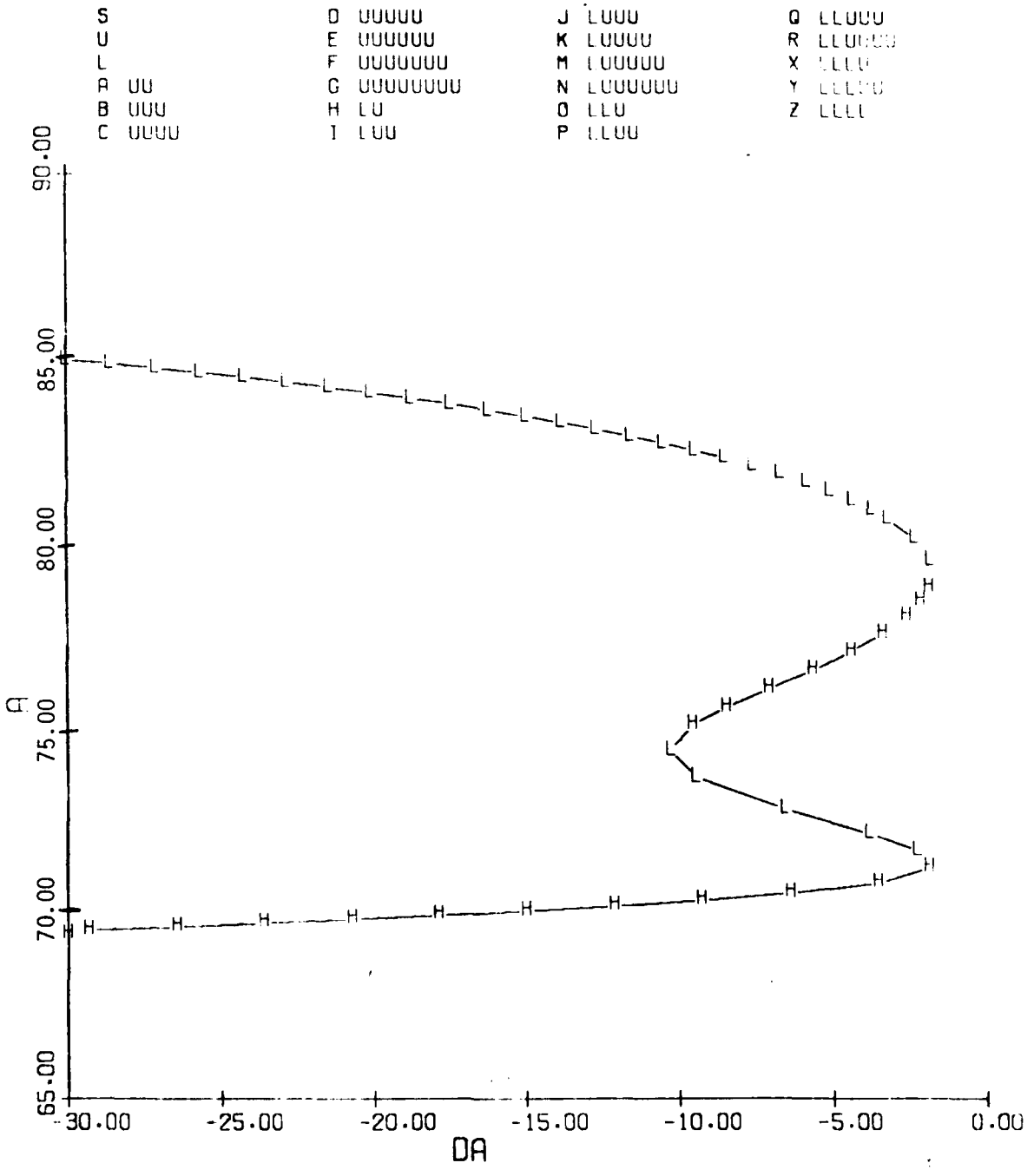

Figure 3.31(b) (concluded)
Equilibrium Surface - Spin Regime: Angle of Attack vs. Aileron Deflection
$\delta e = 0°$ $\delta r = 28.3°$

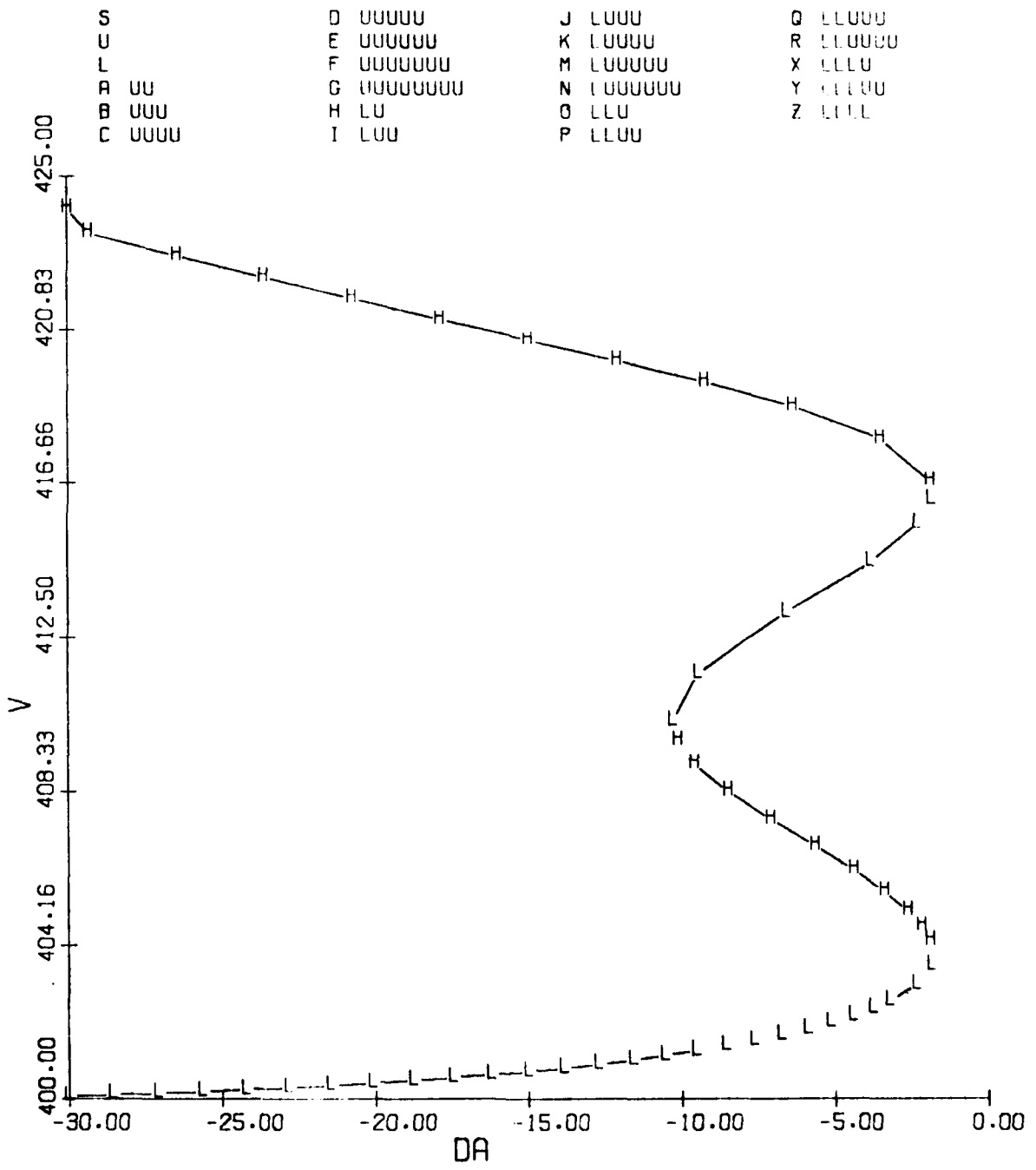

Figure 3.32

Equilibrium Surface - Spin Regime: Velocity vs. Aileron Deflection

$\delta e = 0°$ $\delta r = 28.3°$

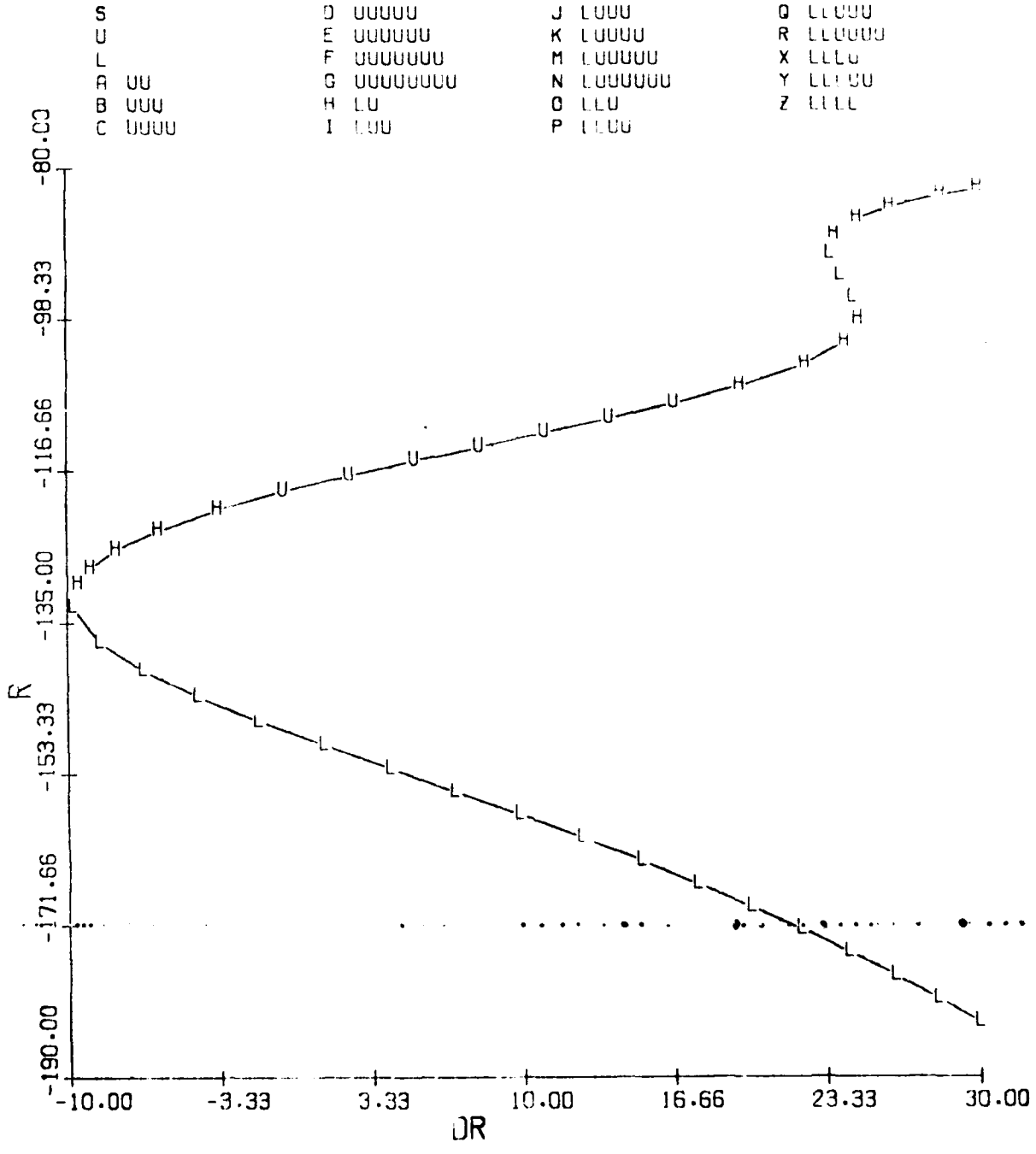

Figure 3.33

Equilibrium Surface - Spin Regime: Yaw Rate vs. Rudder Deflection

$\delta a = -15°$ $\delta e = 0°$

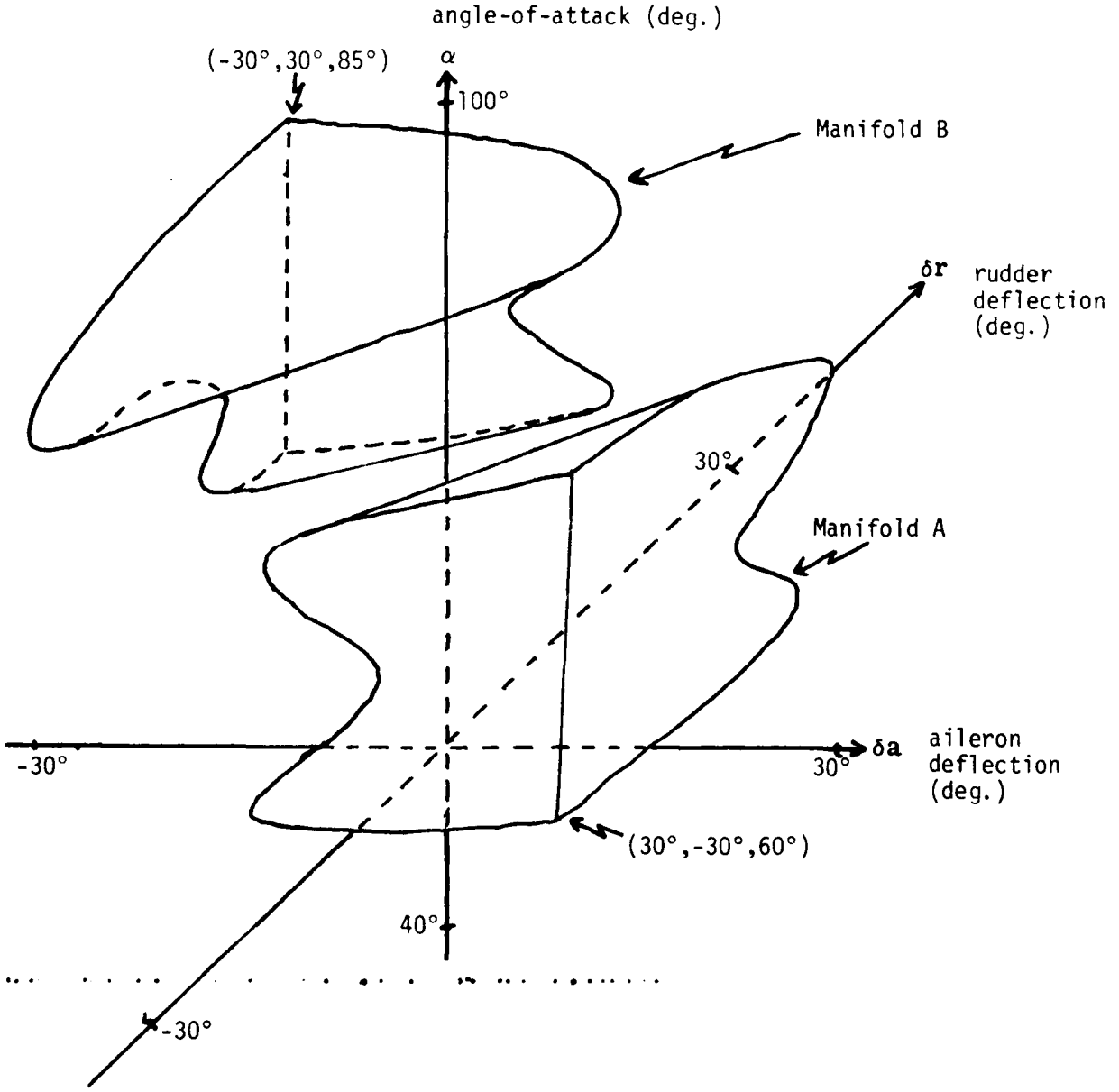

Figure 3.34

Equilibrium Manifolds - Spin Regime, Aircraft F

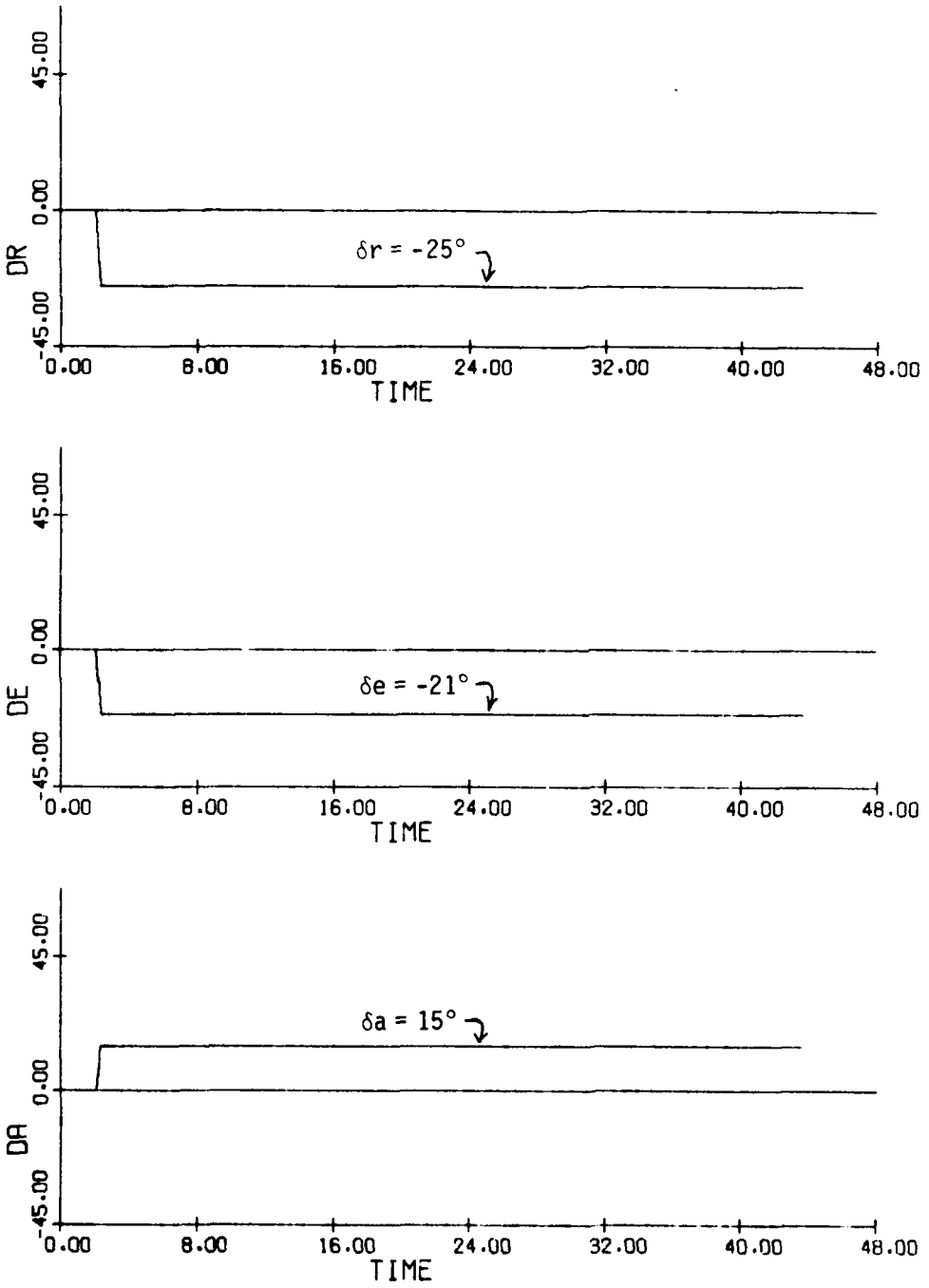

Figure 3.35(a)
Time History: Spin Entry

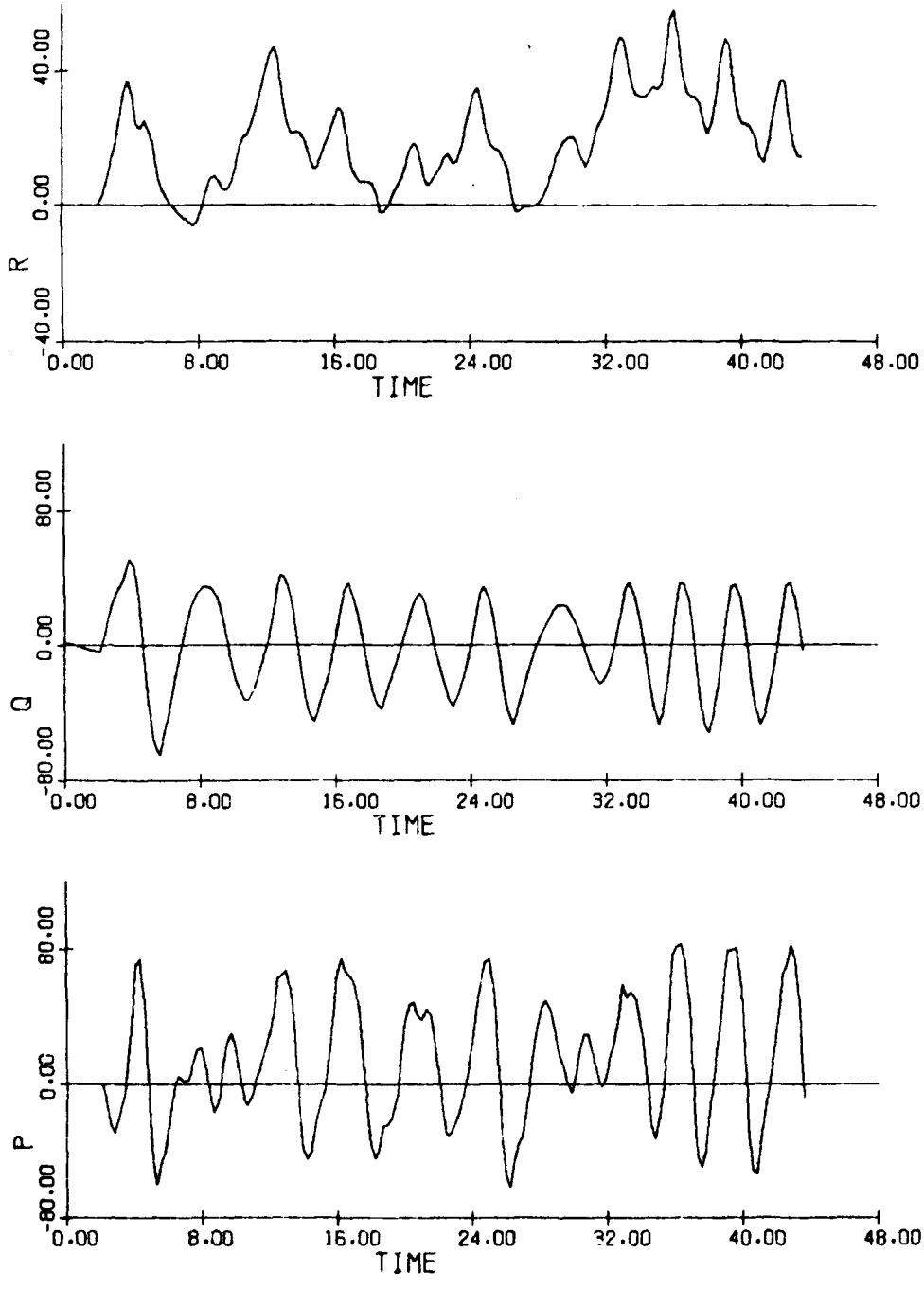

Figure 3.35(b) (cont.)

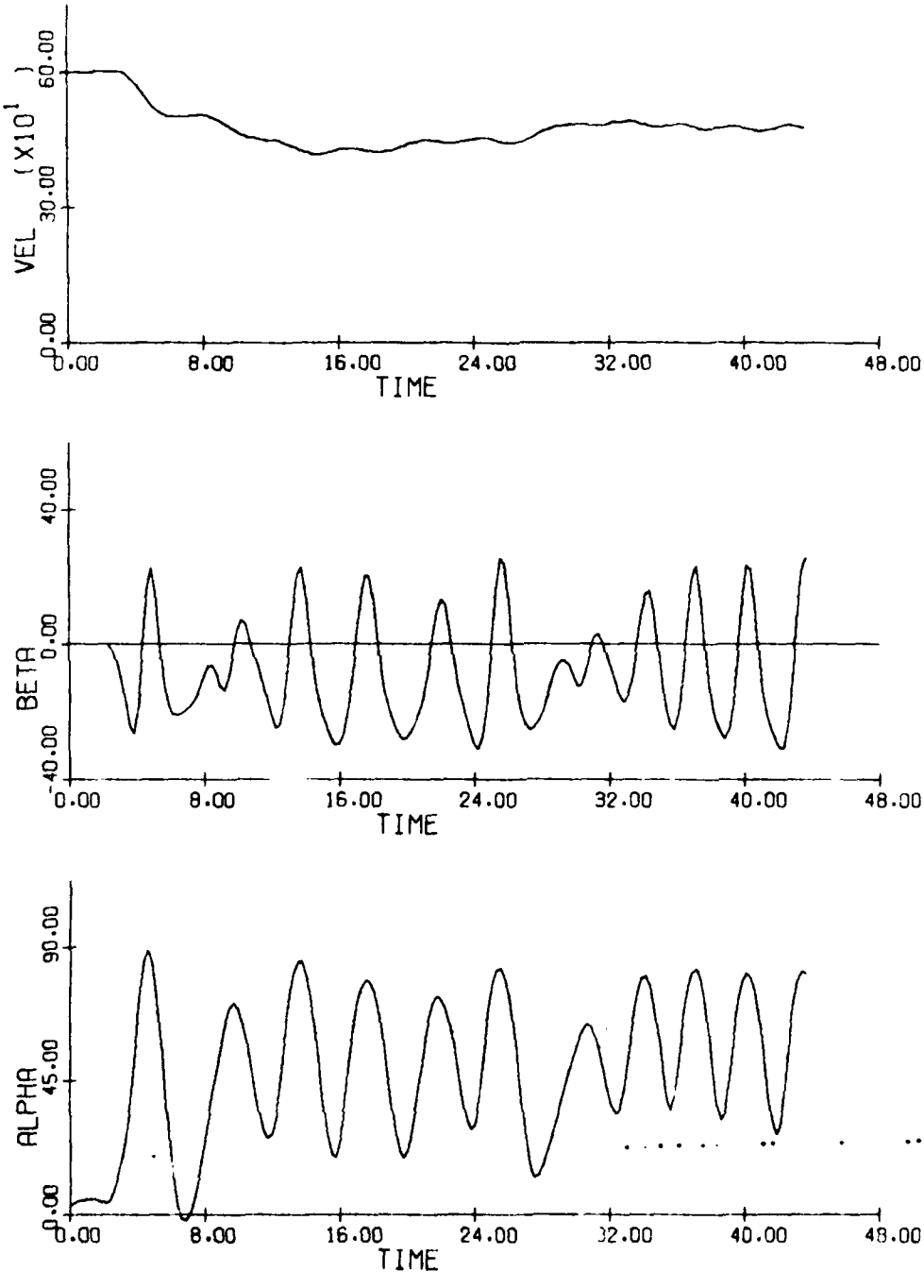

Figure 3.35(c) (cont.)

AD-A084 921 SCIENTIFIC SYSTEMS INC CAMBRIDGE MA F/G 20/4
GLOBAL STABILITY AND CONTROL ANALYSIS OF AIRCRAFT AT HIGH ANGLE--ETC(U)
JUN 78 R K MEHRA, J V CARROLL N00014-76-C-0780
UNCLASSIFIED ONR -CR215-248-2 NL

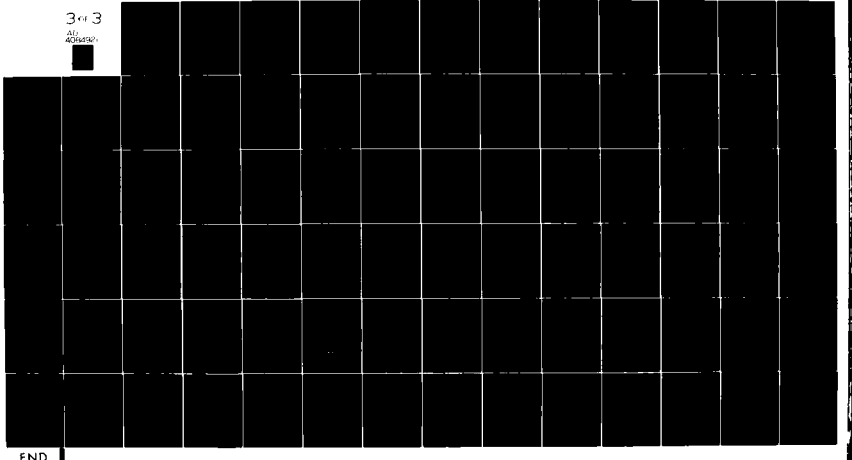

END
DATE FILMED
7-80
DTIC

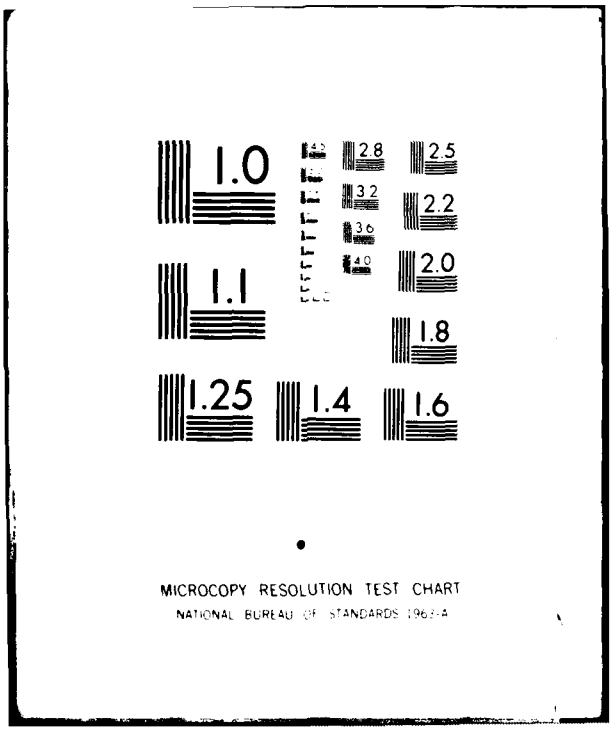
1.0
1.1
1.25
1.4
1.6
1.8
2.0
2.2
2.5
2.8
3.2
3.6
4.0
MICROCOPY RESOLUTION TEST CHART
NATIONAL BUREAU OF STANDARDS 1963-A

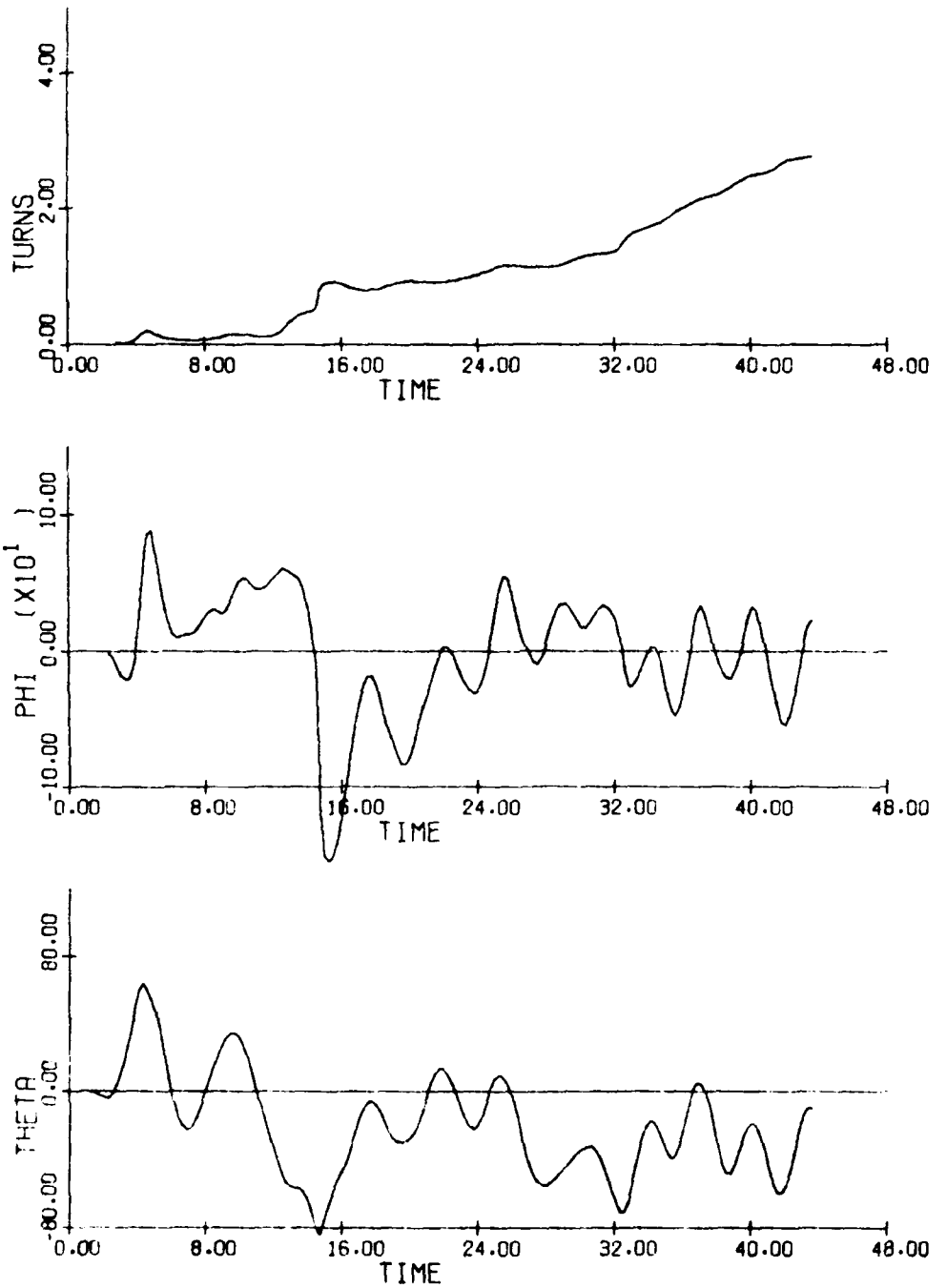

Figure 3.35(d) (cont.)

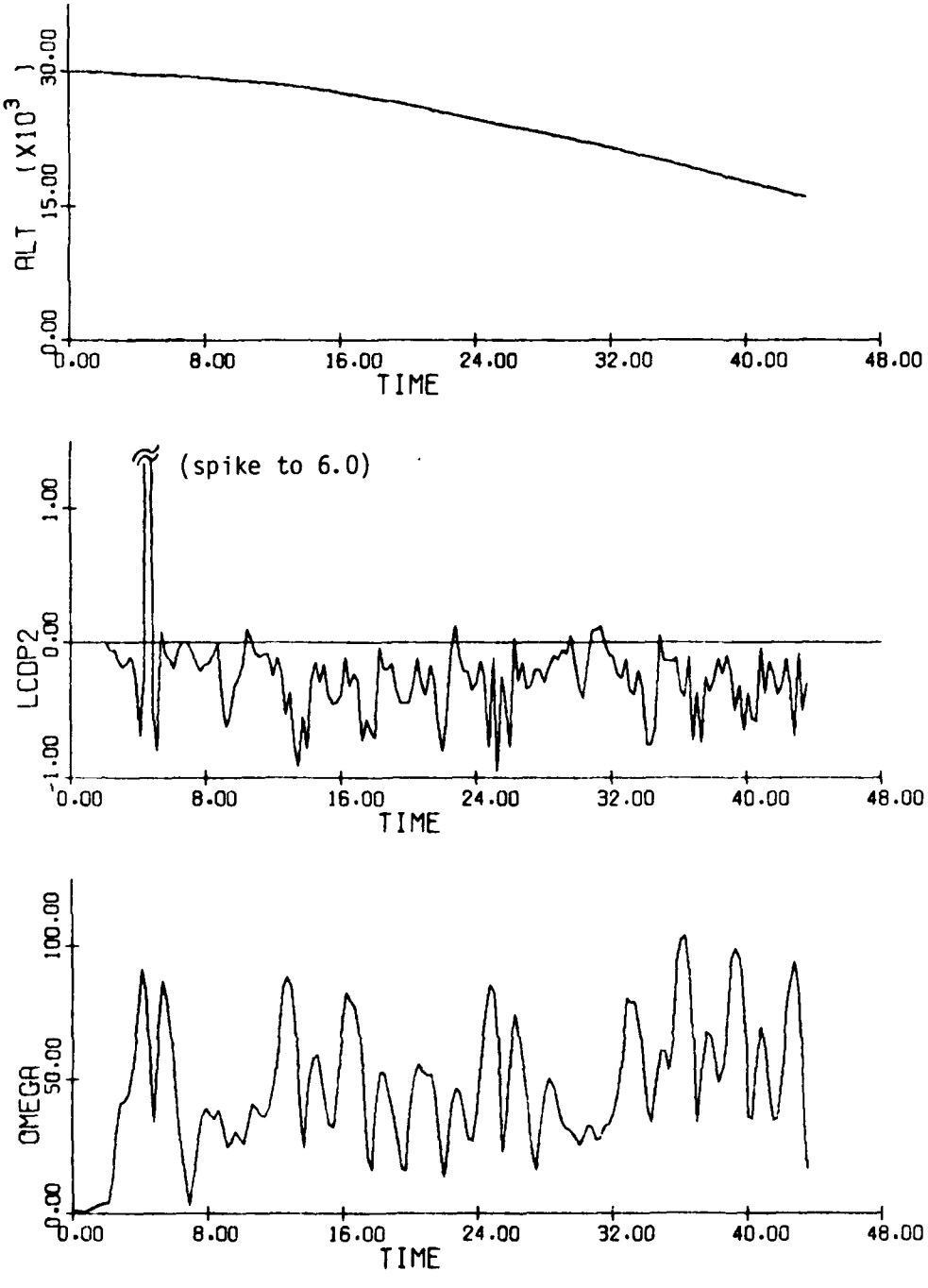

Figure 3.35(e) (cont.)

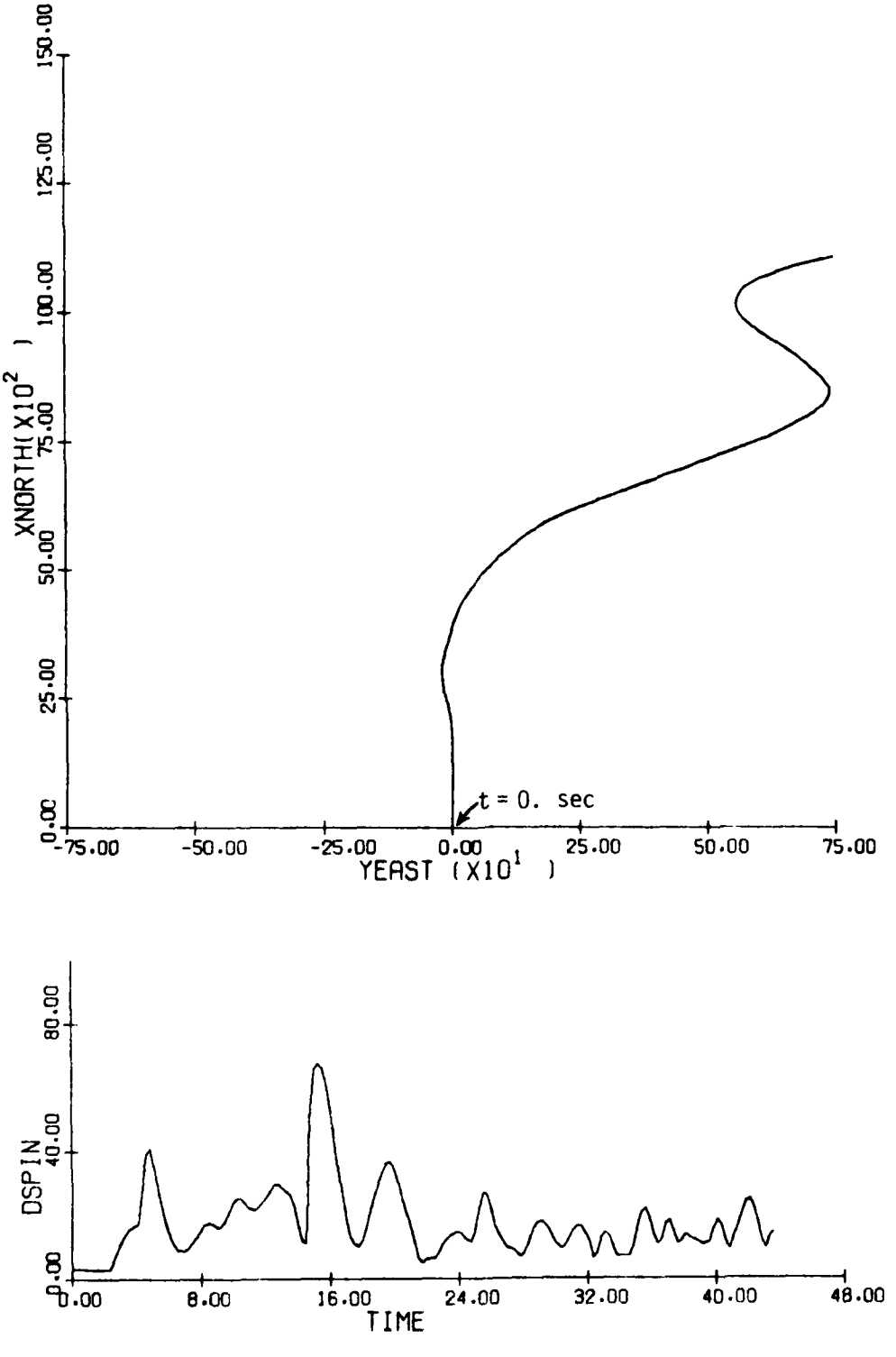

Figure 3.35(f) (concluded)

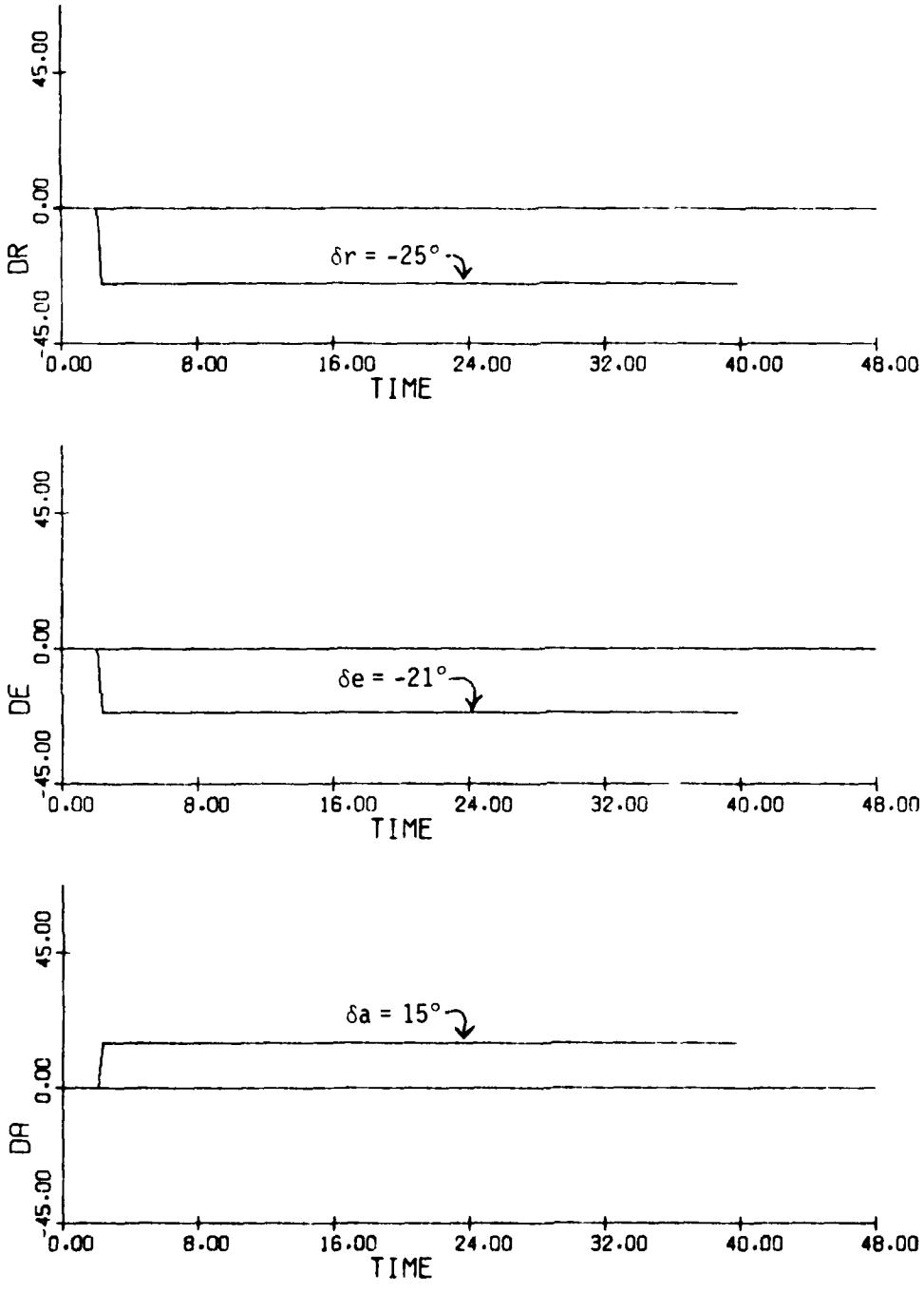

Figure 3.36(a)

Time History: Spin Entry
$\mathring{V} = 0$, $V = 443$ fps

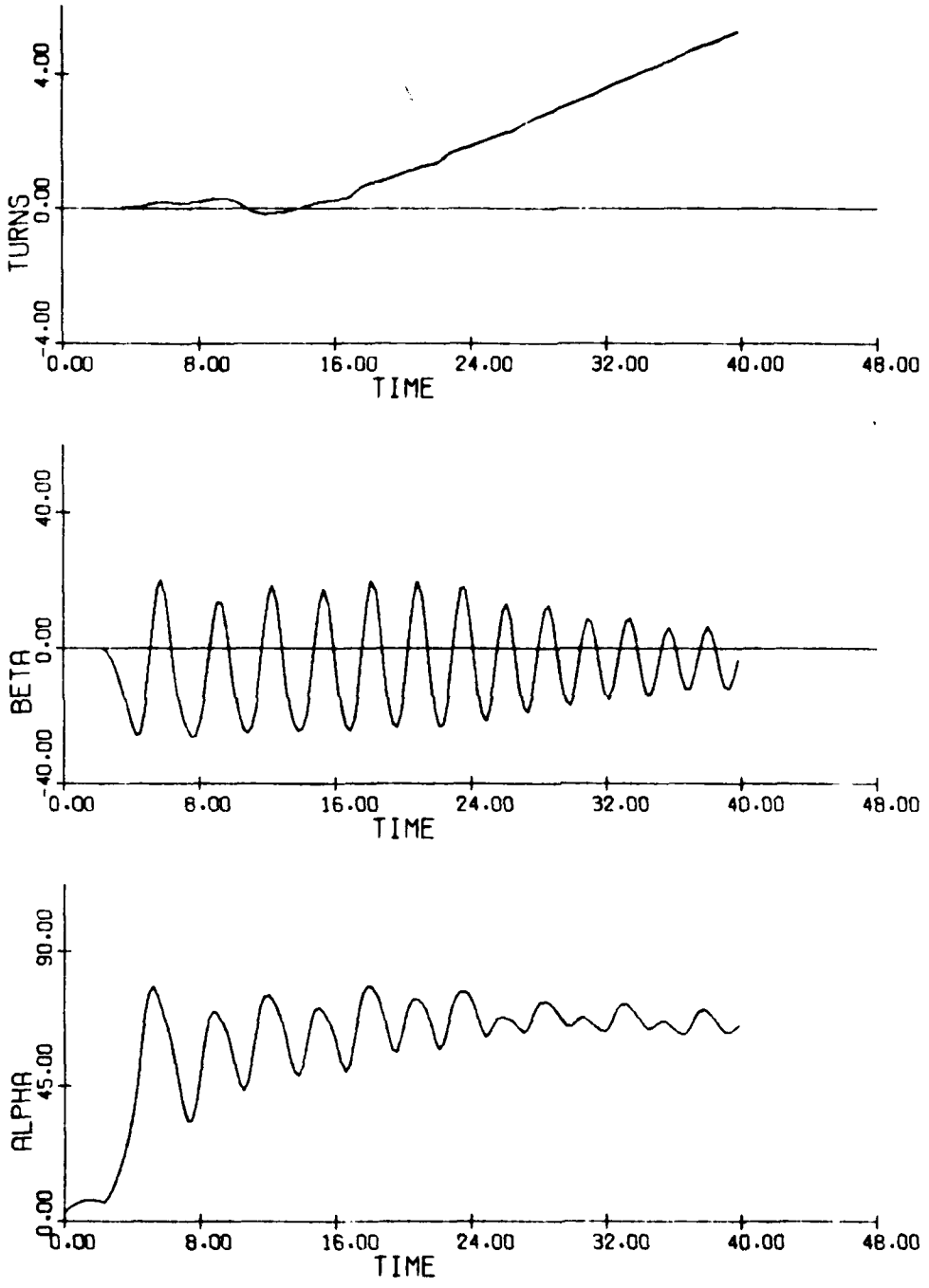

Figure 3.36(b) (cont.)

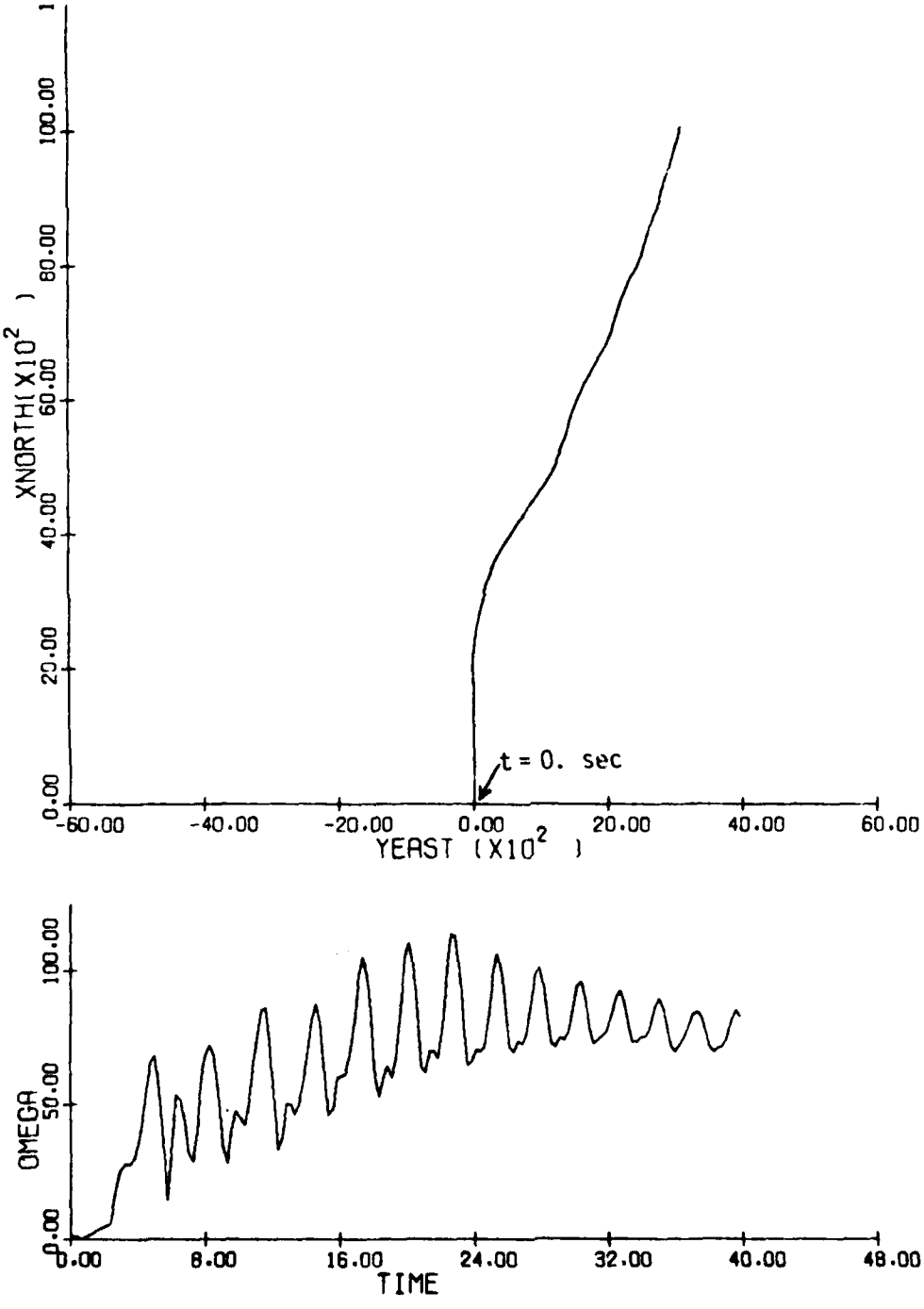

Figure 3.36(c) (concluded)

FIGURE 3.37
Time History: $\delta a = 0°$, $\delta r = 10°$
(δe stepped from 0° to -14°, 2° at a step, at 2 sec. intervals)

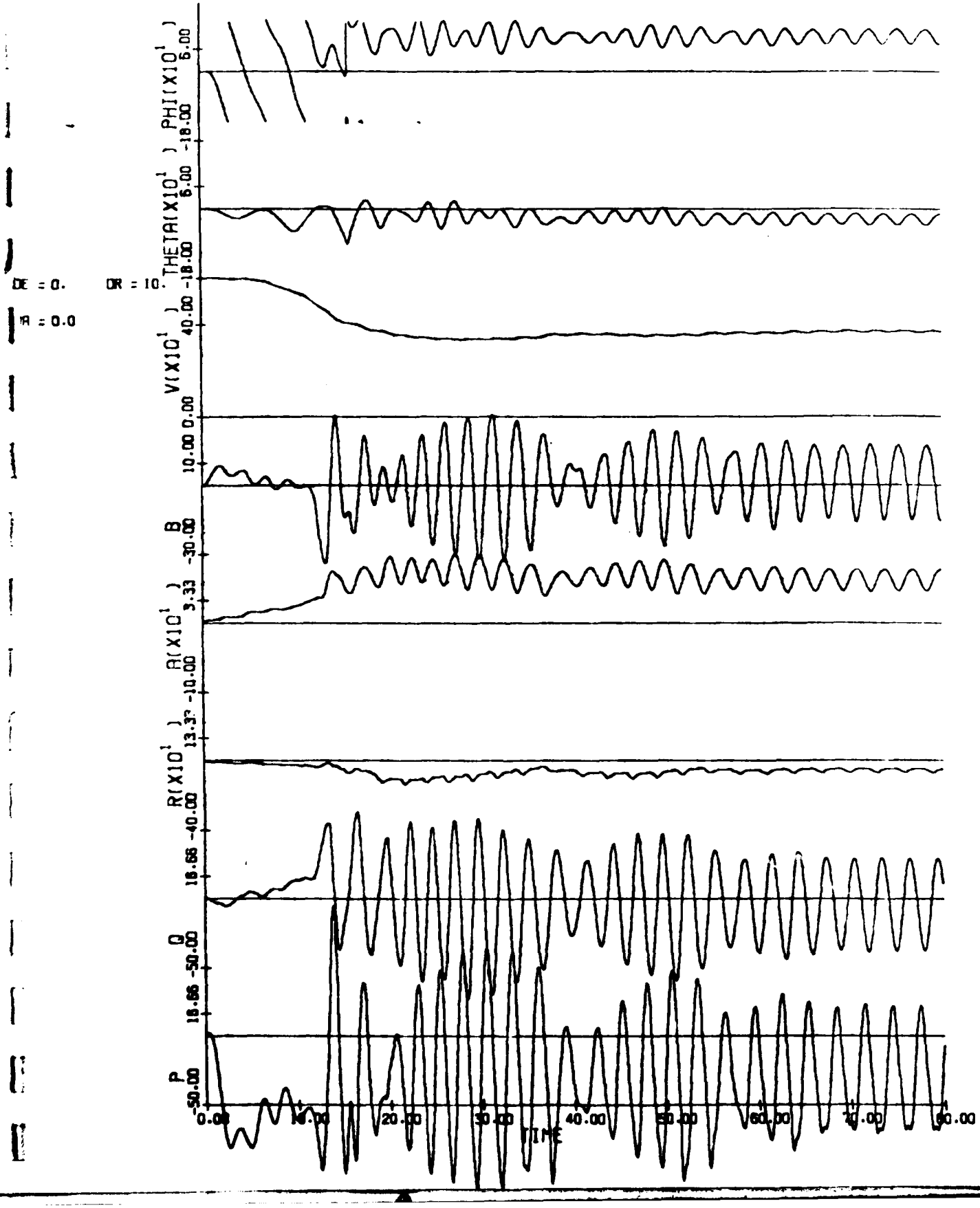

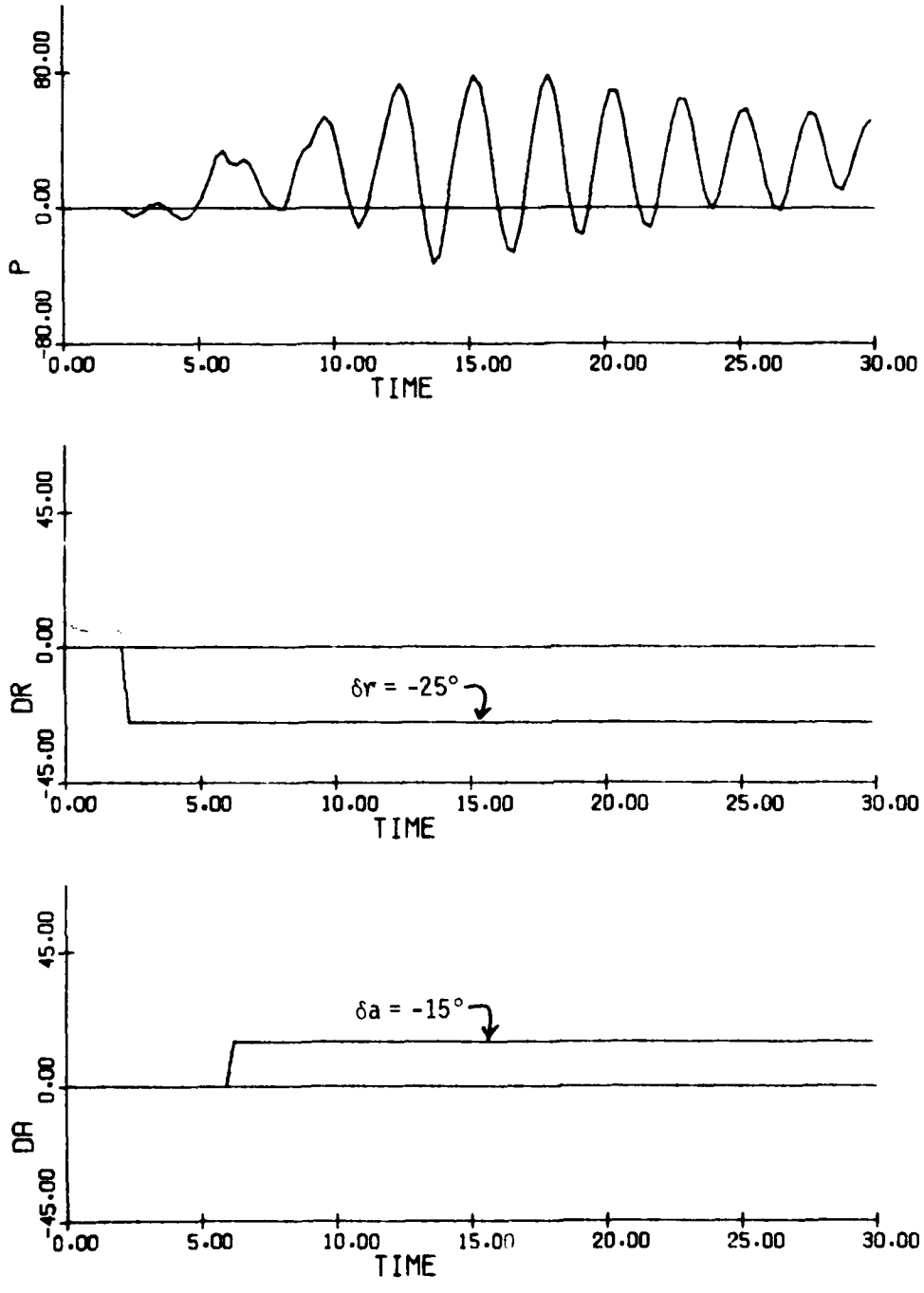

Figure 3.38(a)

Time History: Spin Entry; $\delta e = -21°$, $\dot{V} = 0$, $V = 443$ fps

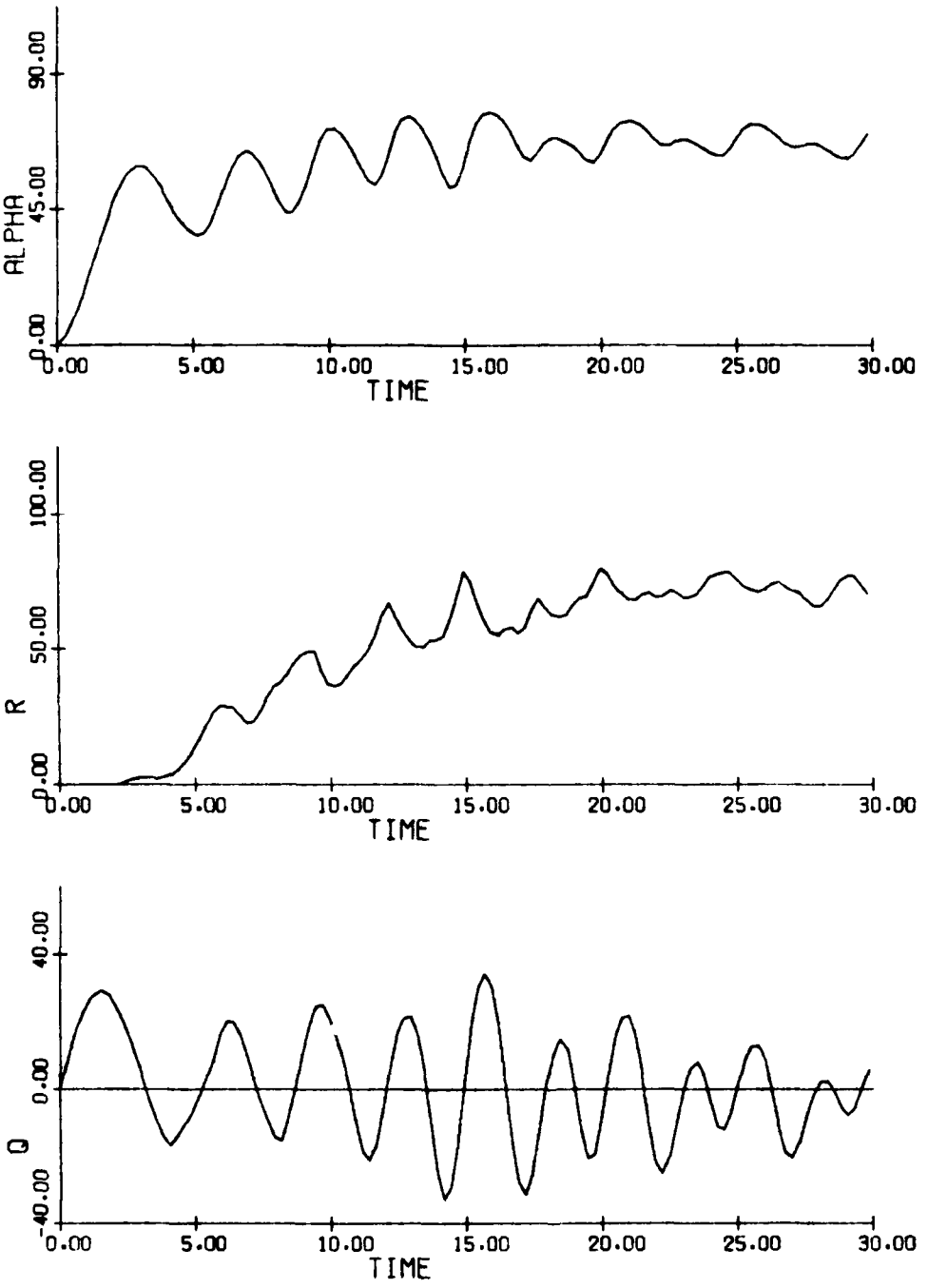

Figure 3.38(b) (cont.)

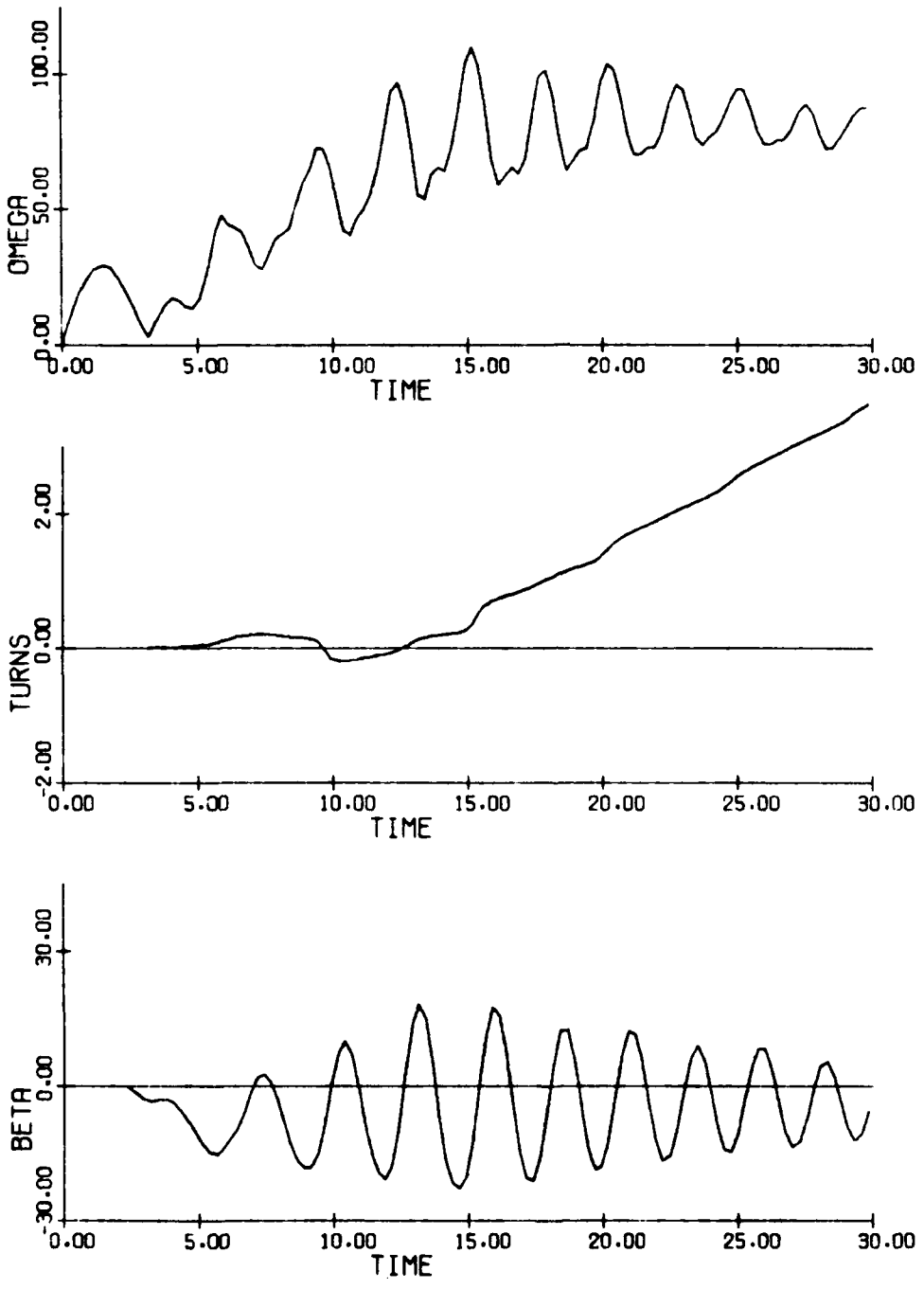

Figure 3.38(c) (cont.)

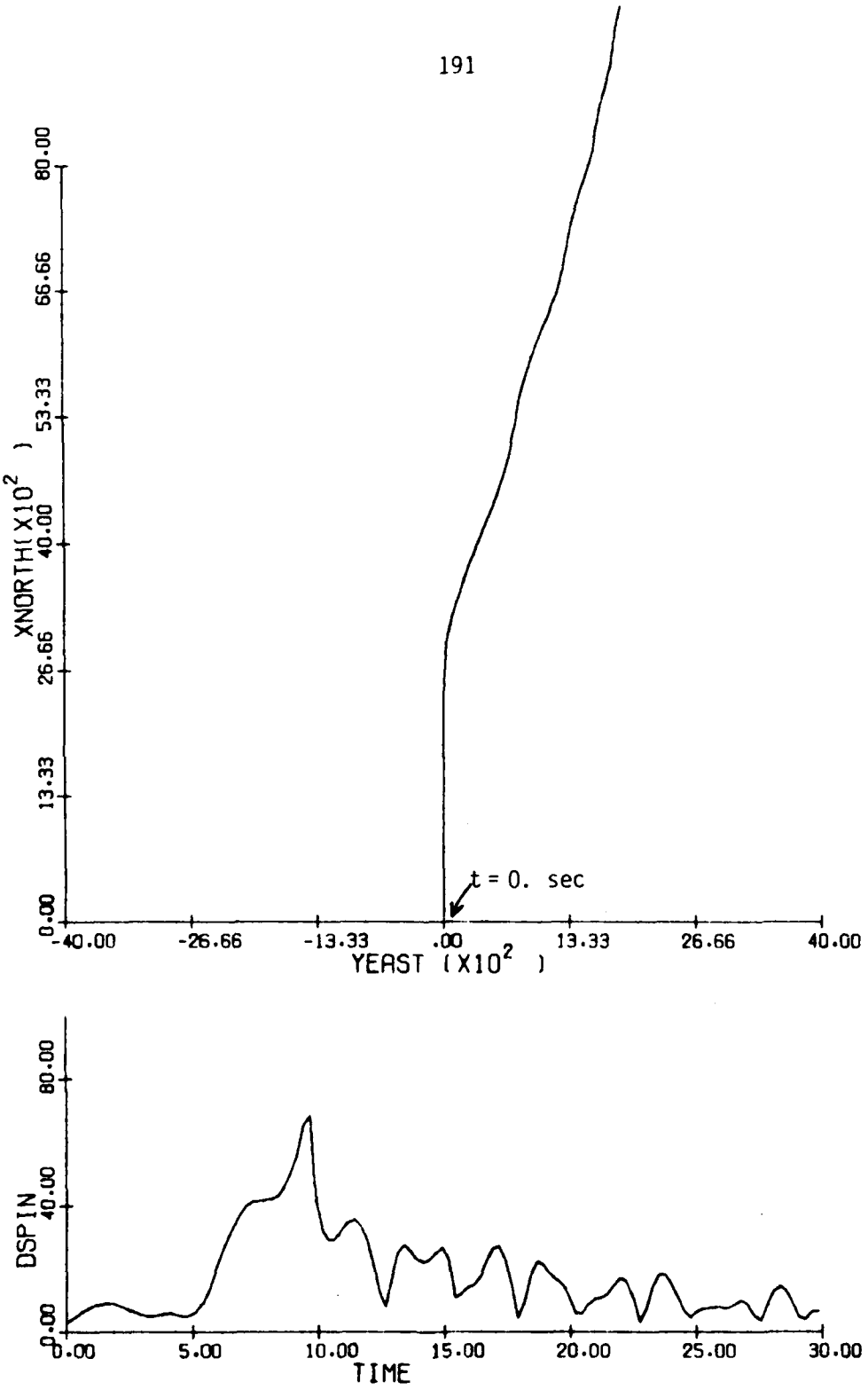

Figure 3.38(d) (concluded)

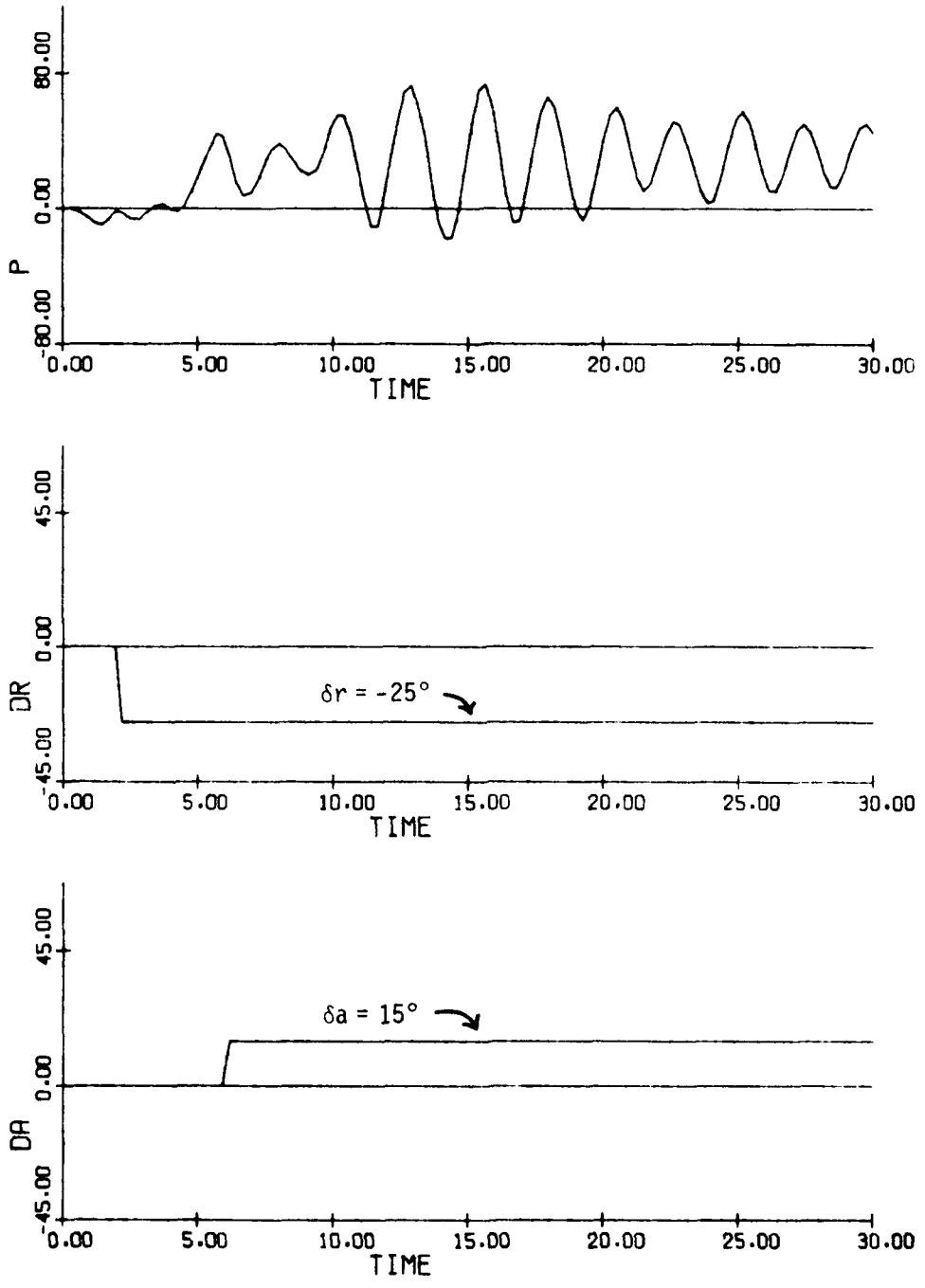

Figure 3.39(a)

Time History: Spin Entry;
$\delta e = -21°$, $\dot{V} = 0$, $V = 443$ fps, $\phi_0 = 60°$

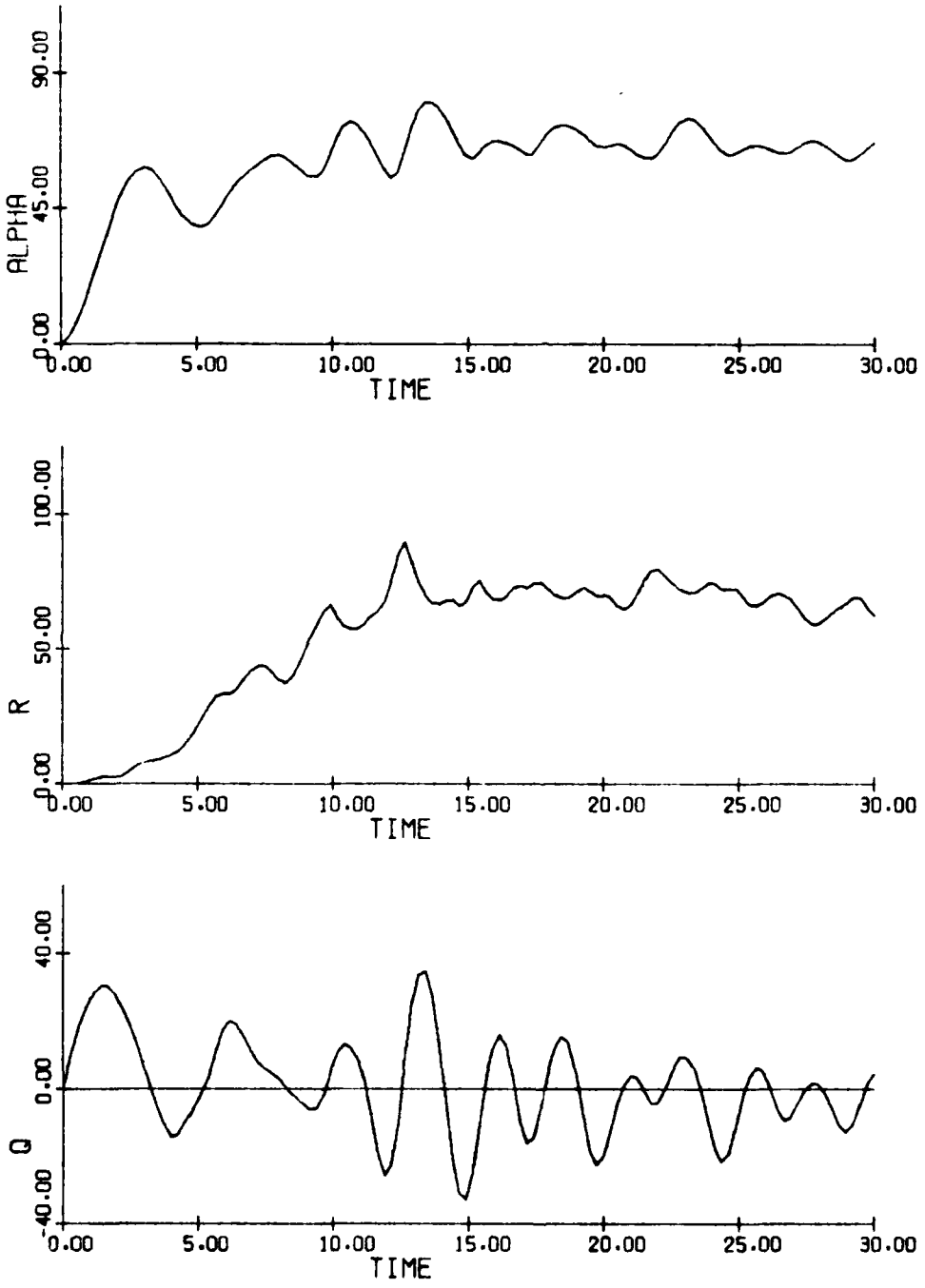

Figure 3.39(b) (cont.)

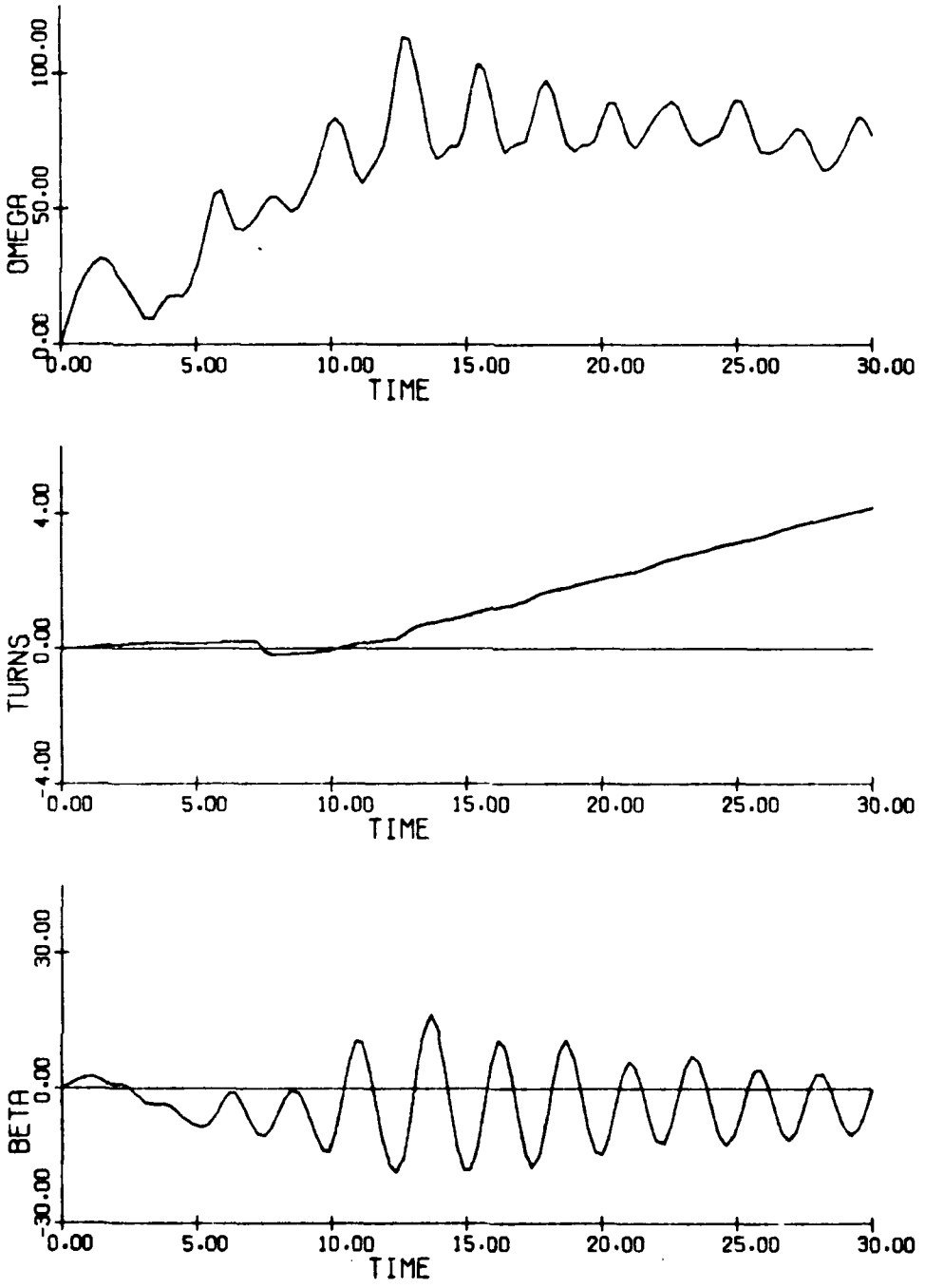

Figure 3.39(c) (cont.)

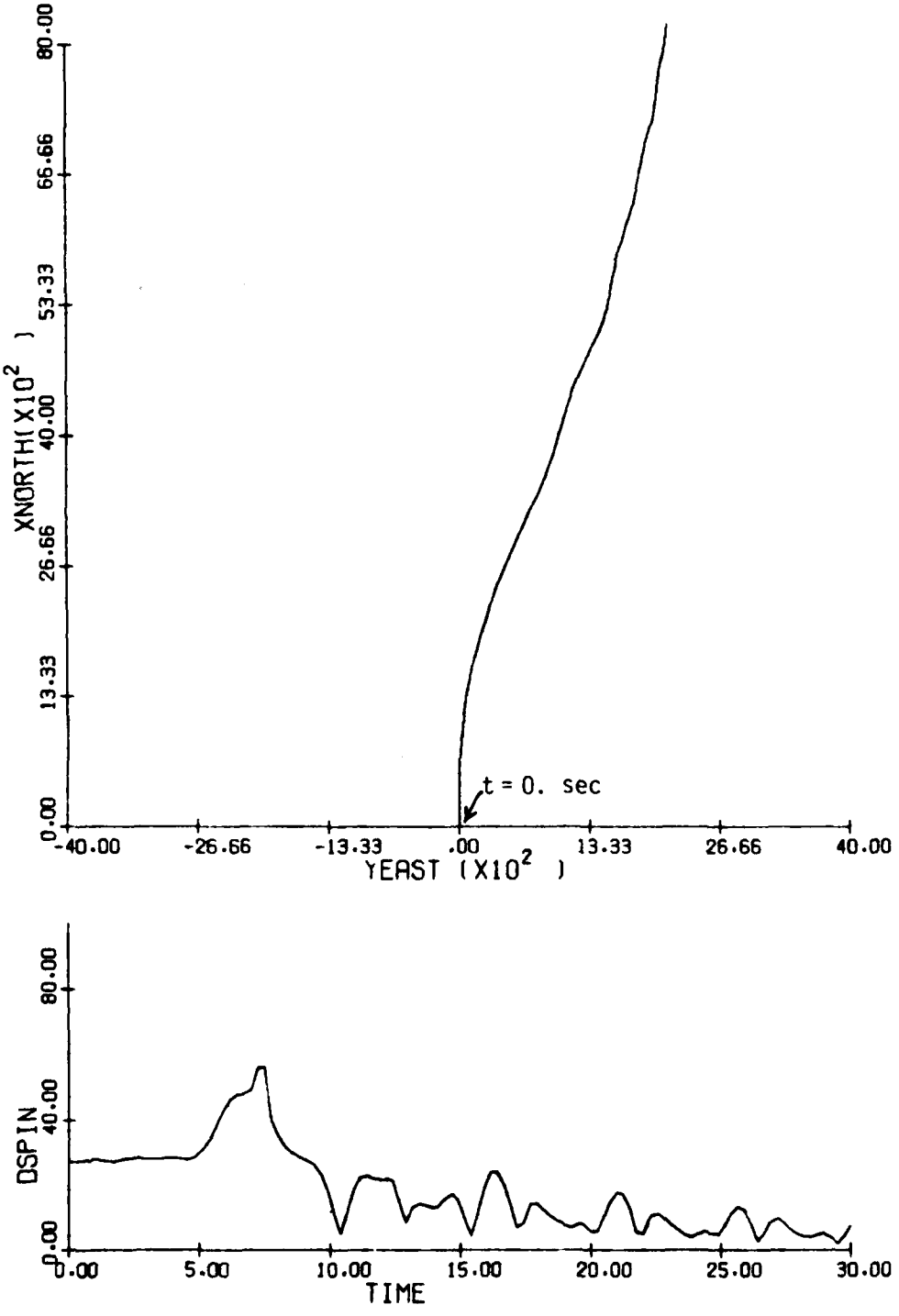

Figure 3.39(d) (concluded)

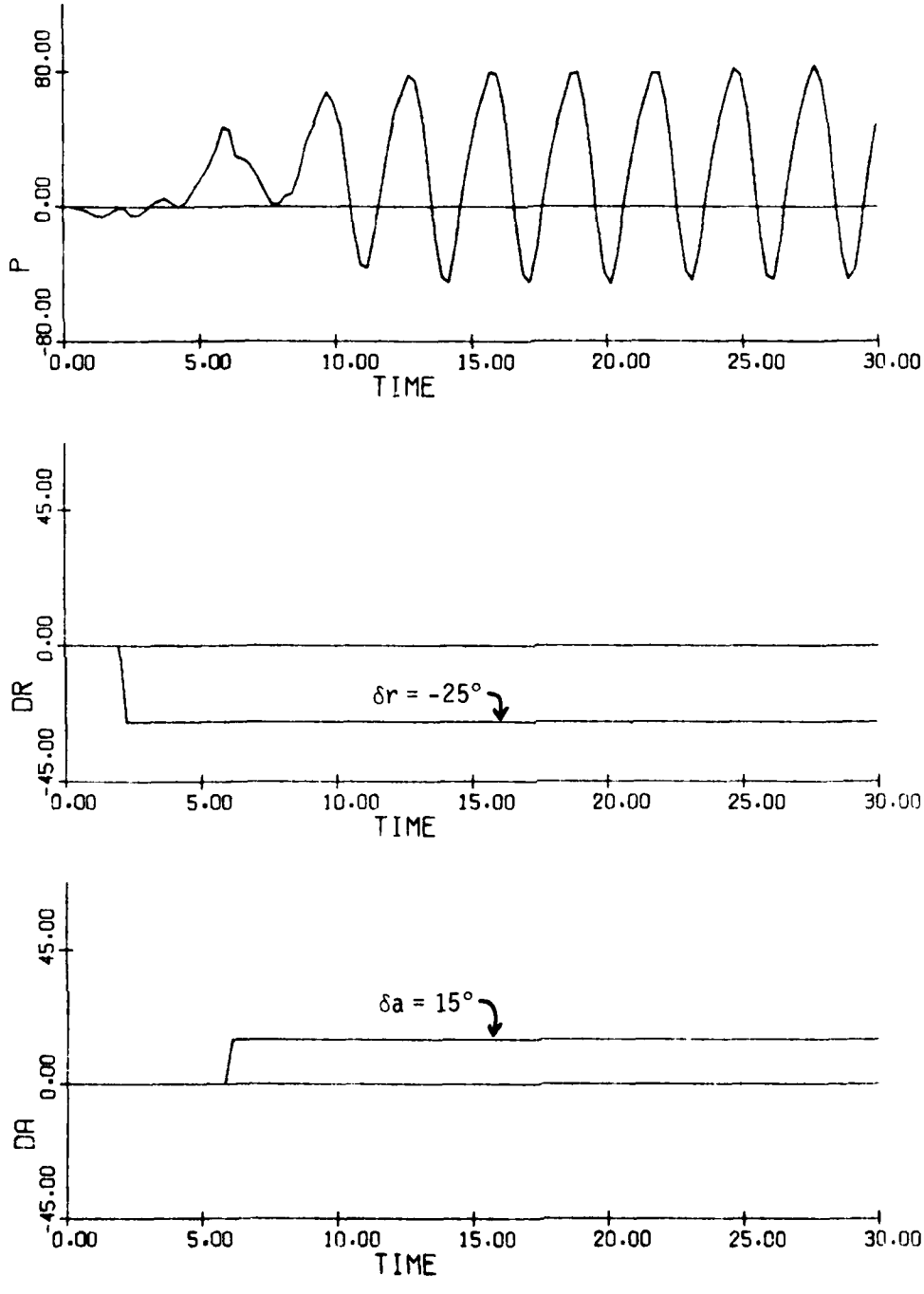

Figure 3.40(a)

Time History: Spin Entry;
$\delta e = -21°$, $\dot{V} = 0$, $V = 443$ fps, $\phi_0 = 60°$, $\theta_0 = -50°$

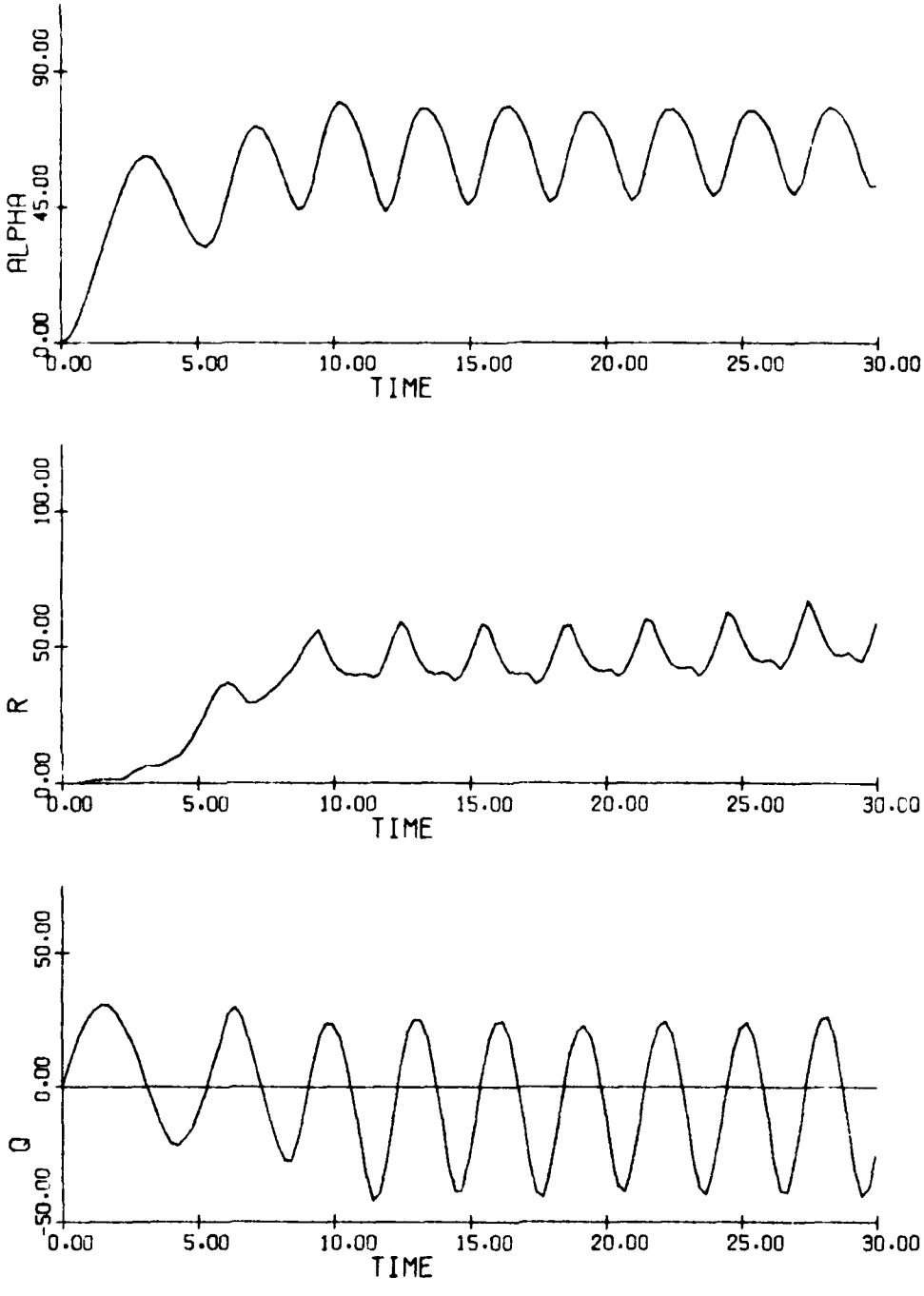

Figure 3.40(b) (cont.)

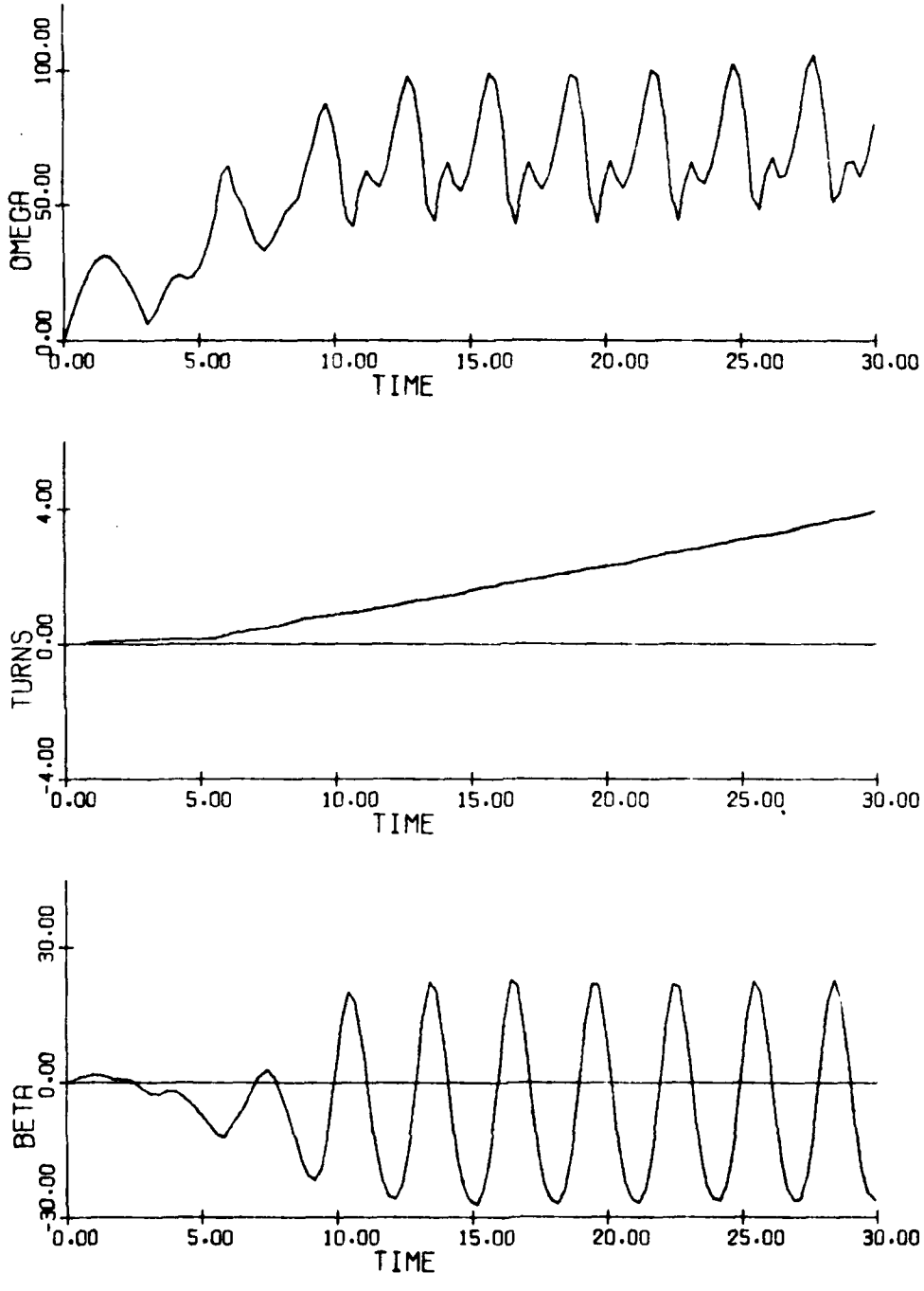

Figure 3.40(c) (cont.)

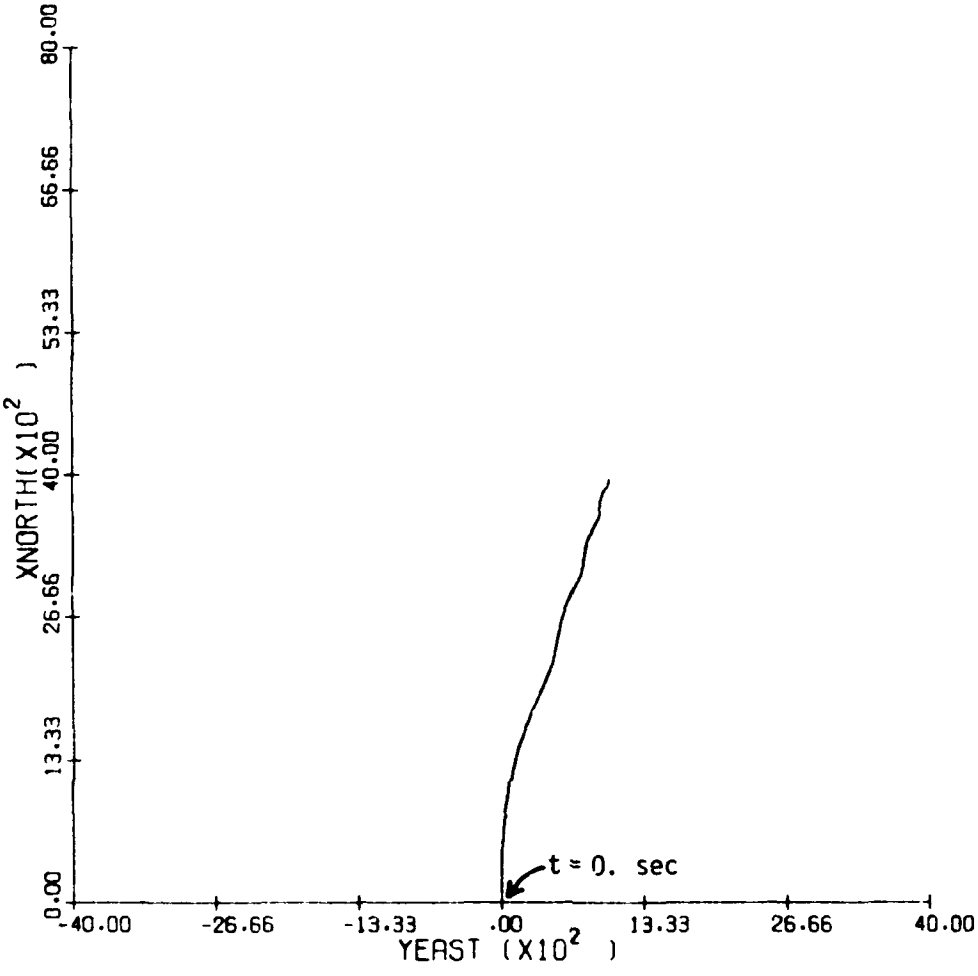

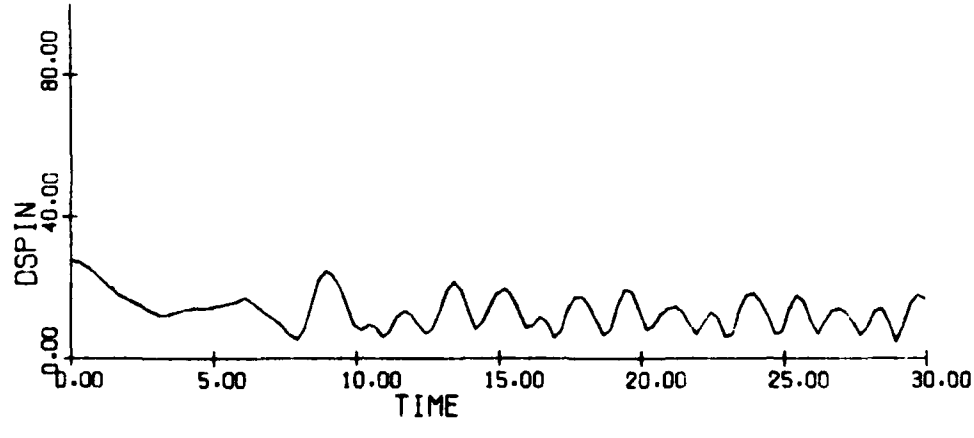

Figure 3.40(d) (concluded)

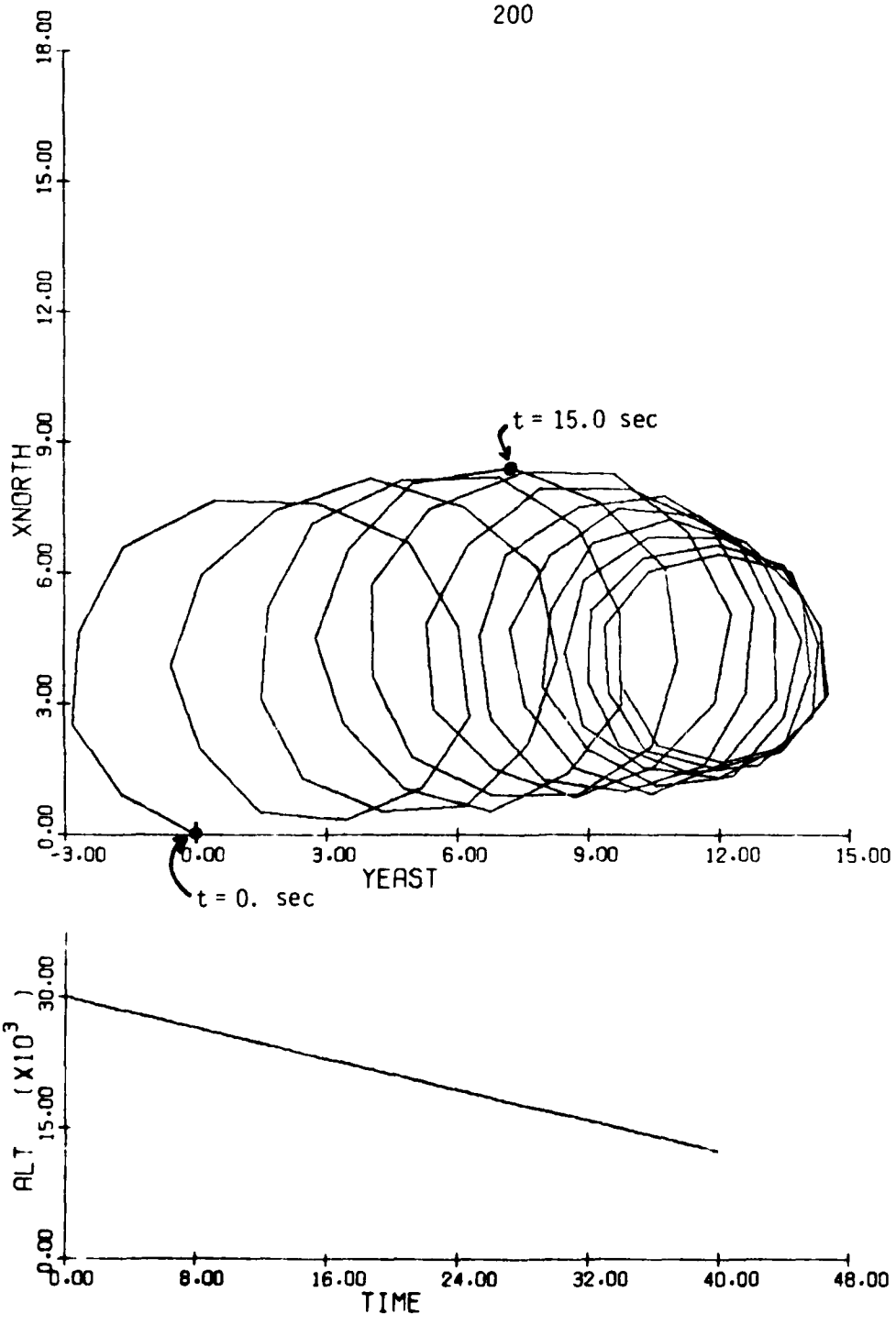

Figure 3.41

Time History: Flat Spin;
$\delta a = 15°$, $\delta e = -21°$, $\delta r = \begin{cases} -25°, & t \leq 15 \text{ sec} \\ -29.5°, & t \geq 15 \text{ sec} \end{cases}$

DA= 15.0
DE= -21.0

201

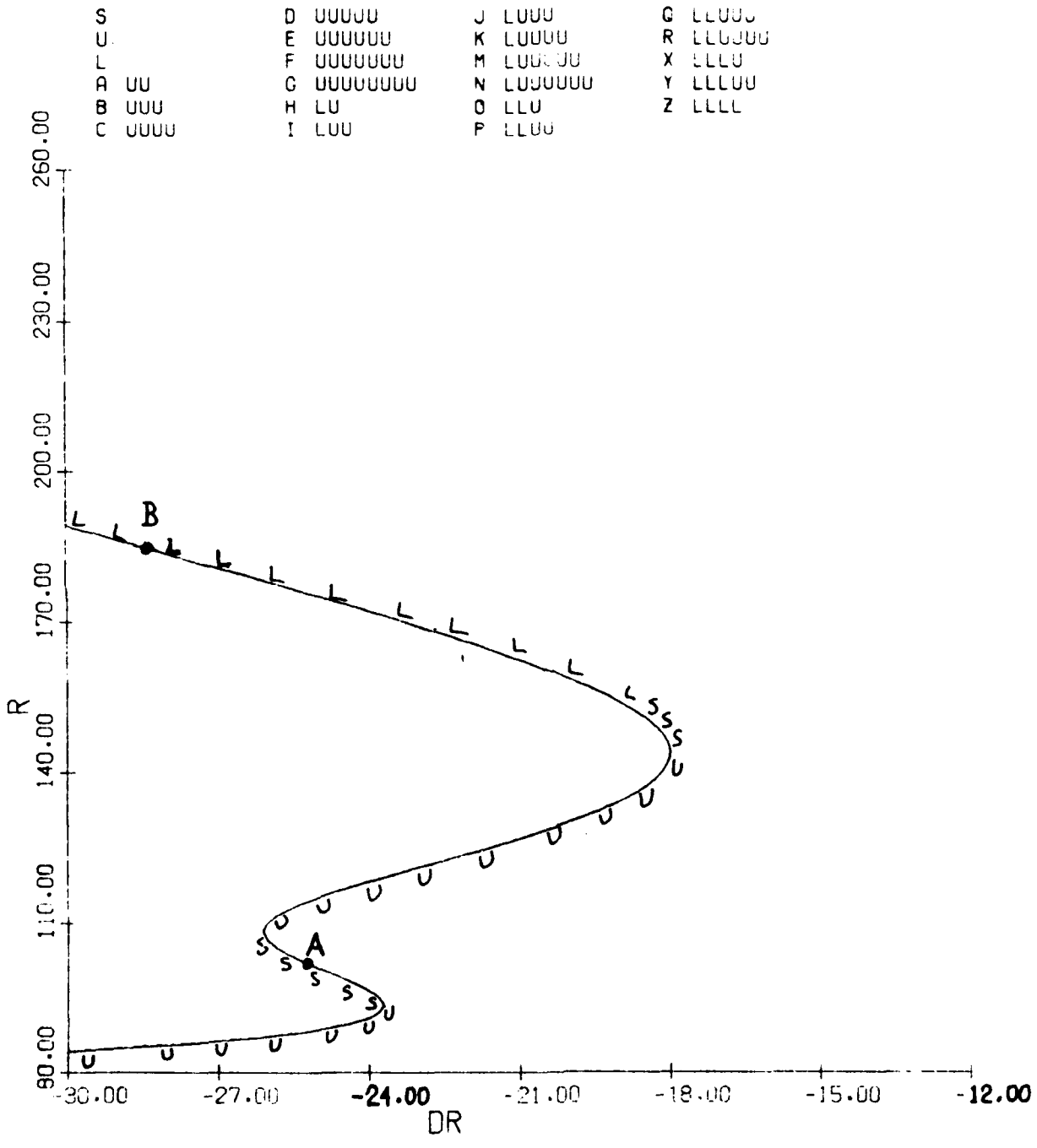

Figure 3.42

Equilibrium Surface: r vs. δr
V = 443 fps, g = 0

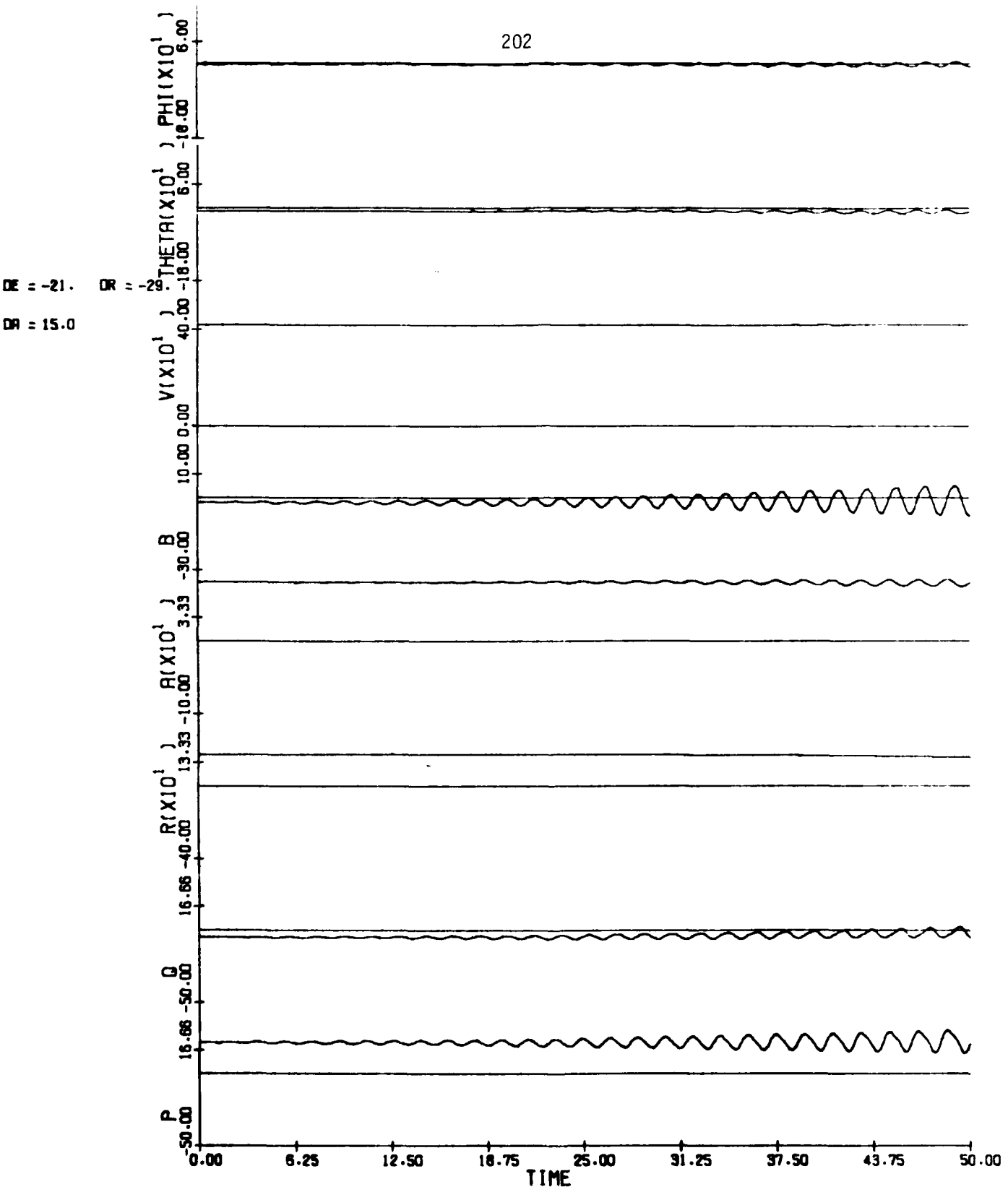

Figure 3.43

Time History: Flat Spin; $\delta a = 15°$, $\delta e = -21°$, $\delta r = -29°$

DA= 15.0
DE= 0.0

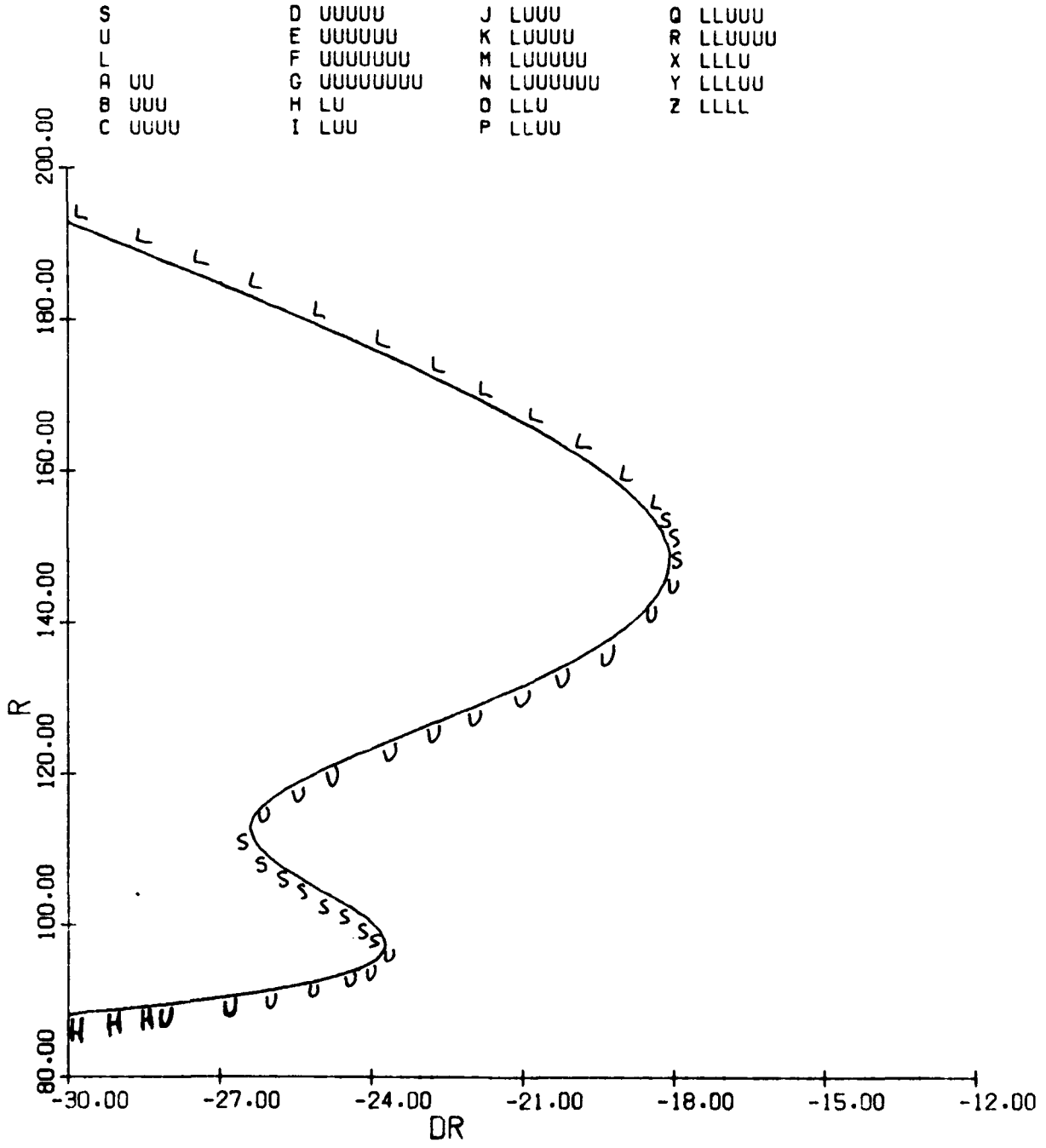

Figure 3.44(a)

Equilibrium Surface: r,α,p vs. δr
V = 443 fps, g = 0

DA= 15.0
DE= 0.0

S	D UUUUU	J LUUU	Q LLUUU
U	E UUUUUU	K LUUUU	R LLUUUU
L	F UUUUUUU	M LUUUUU	X LLLU
A UU	G UUUUUUUU	N LUUUUUU	Y LLLUU
B UUU	H LU	O LLU	Z LLLL
C UUUU	I LUU	P LLUU	

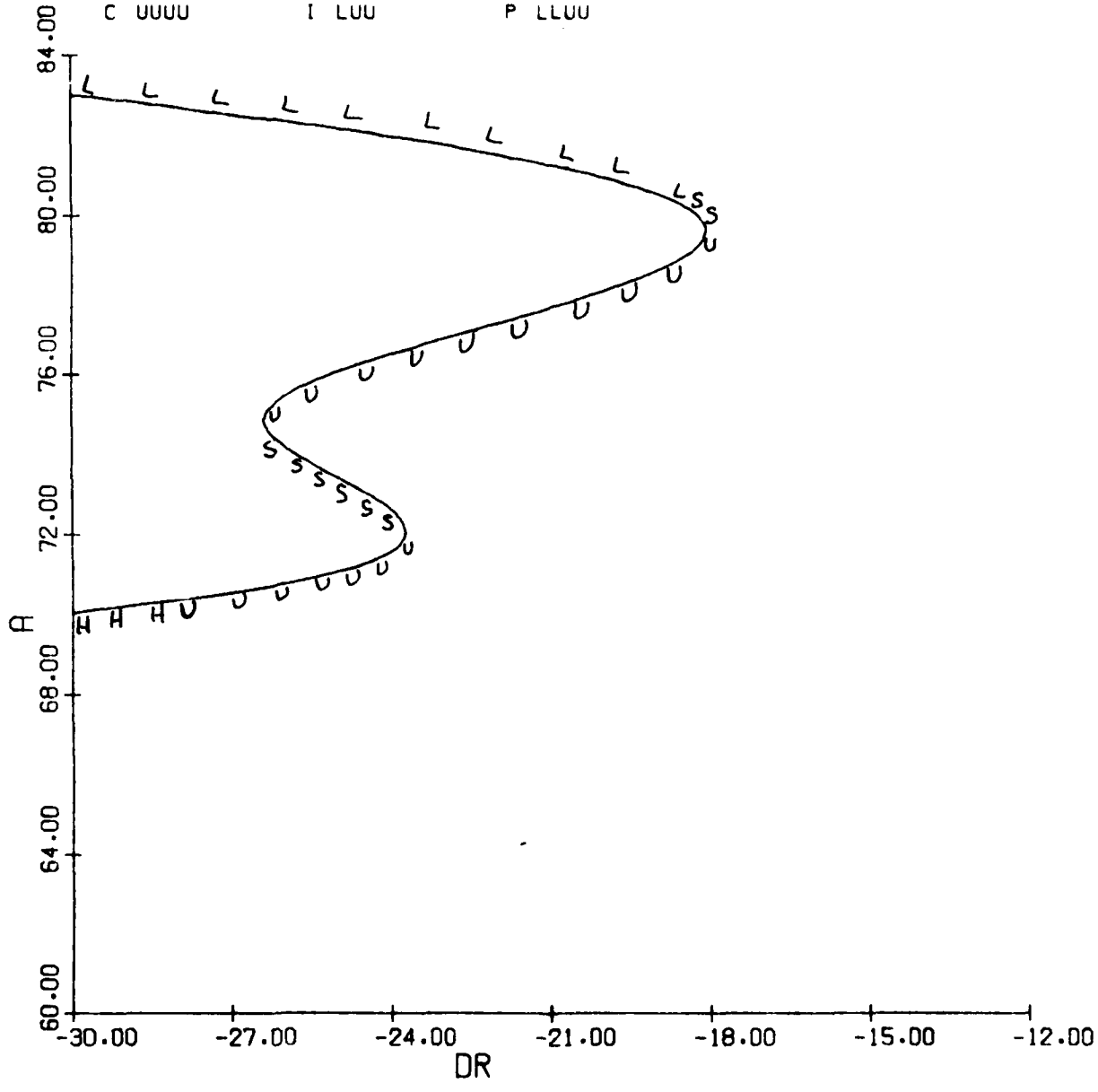

Figure 3.44(b) (cont.)

DA= 15.0
DE= 0.0

S	D UUUUU	J LUUU	Q LLUUU
U	E UUUUUU	K LUUUU	R LLUUUU
L	F UUUUUUU	M LUUUUU	X LLLU
A UU	G UUUUUUUU	N LUUUUUU	Y LLLUU
B UUU	H LU	O LLU	Z LLLL
C UUUU	I LUU	P LLUU	

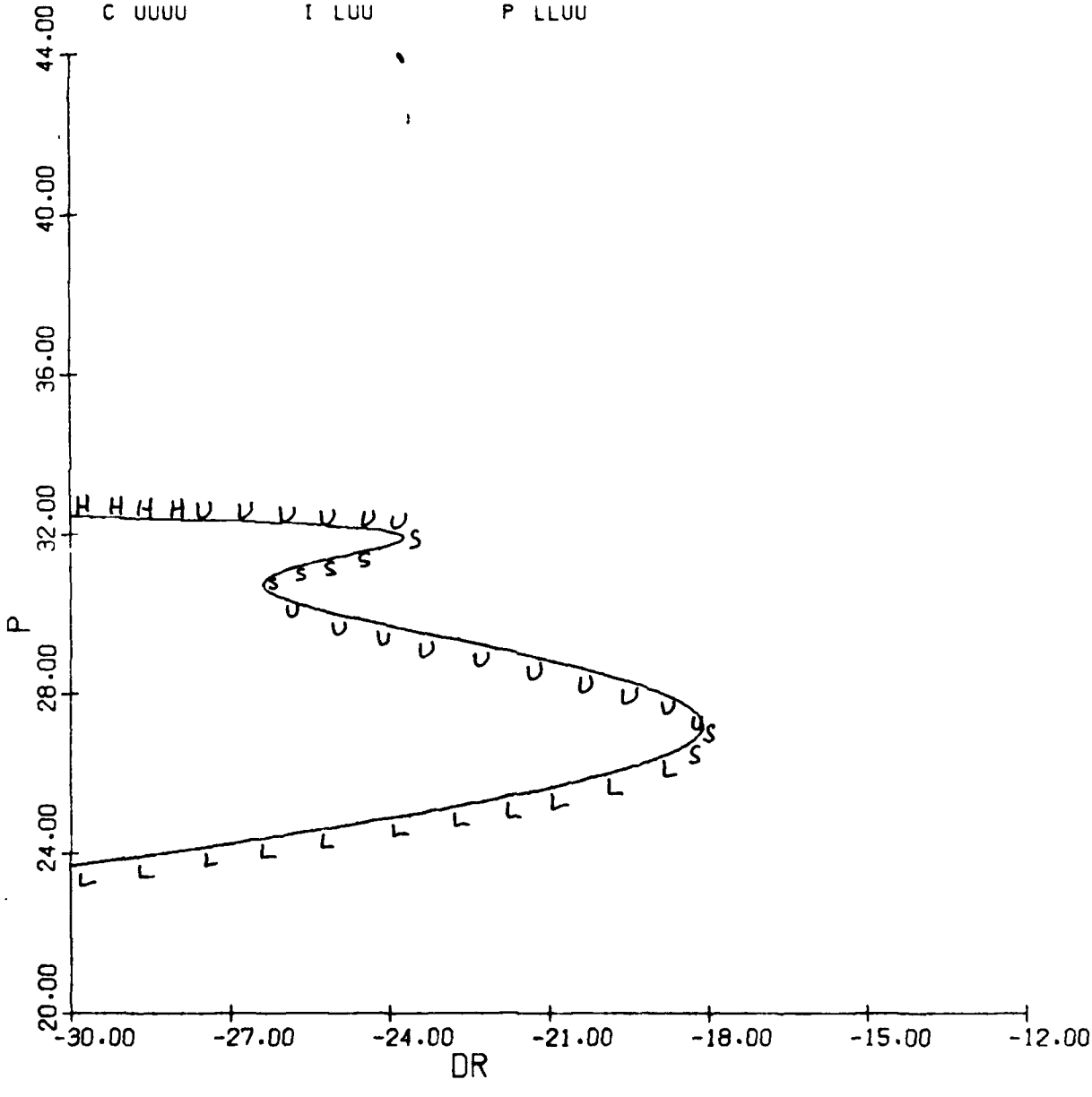

Figure 3.44(c) (concluded)

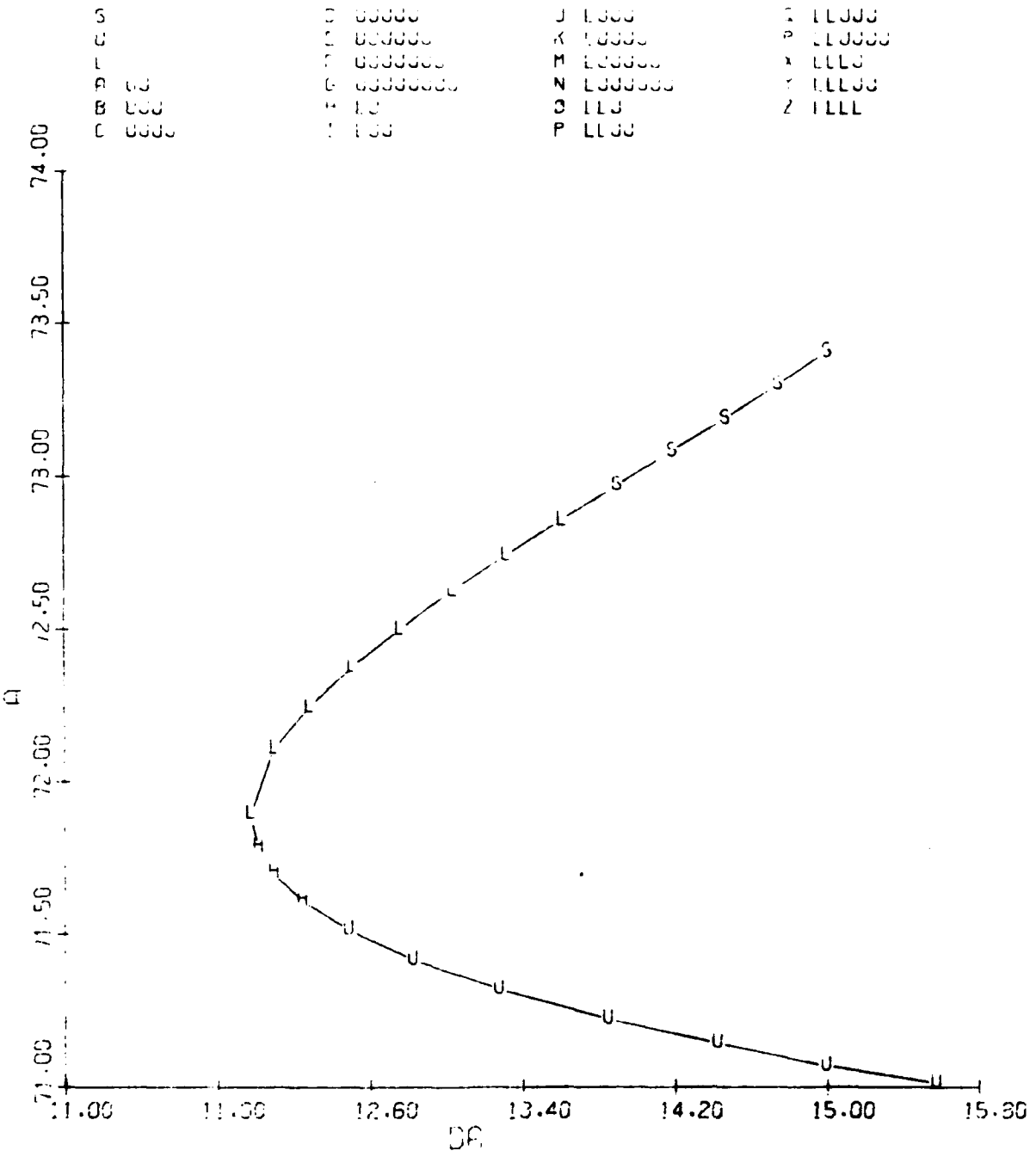

FIGURE 3.45
Equilibrium Surface: α vs. δa
$\delta e = 0°$, $\delta r = -25°$, V = 443 fps, g = 0

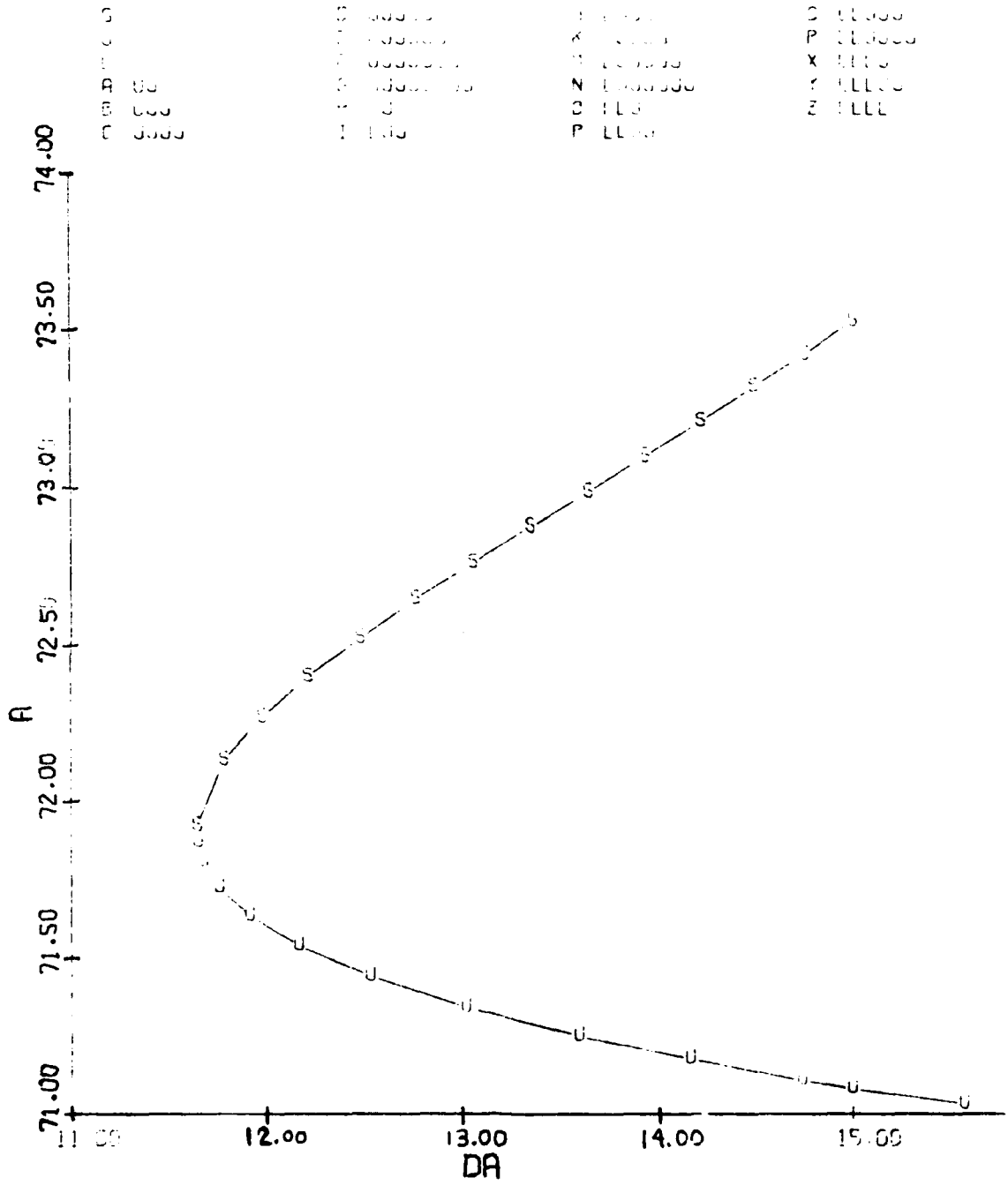

FIGURE 3.46
Equilibrium Surface: α vs. δa
$\delta e = -21°$, $\delta r = -25°$, V = 443 fps, g = 0

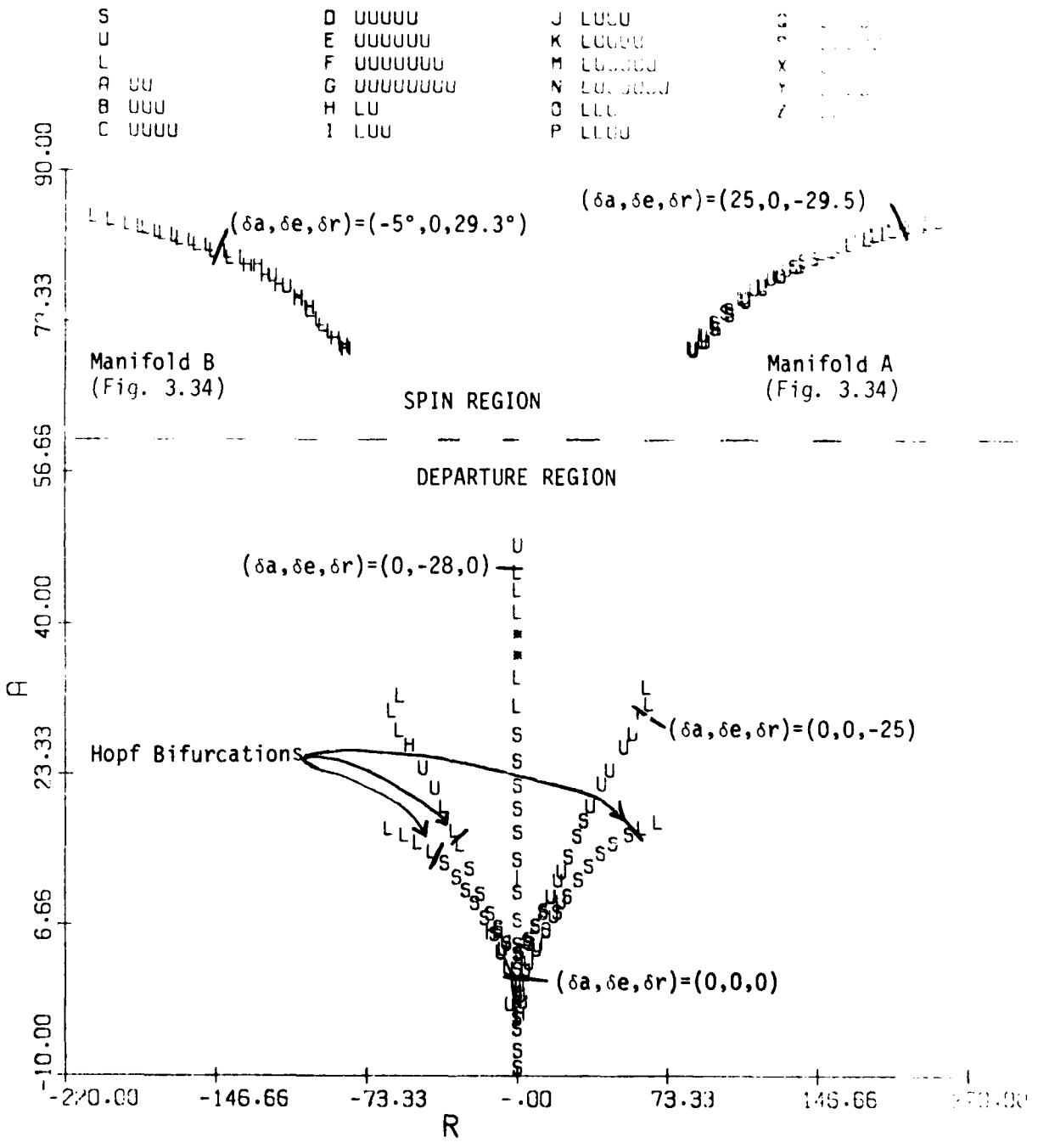

Figure 3.47

Equilibrium Surfaces - Composite Angle of Attack vs. Yaw Rate at Various Control Settings

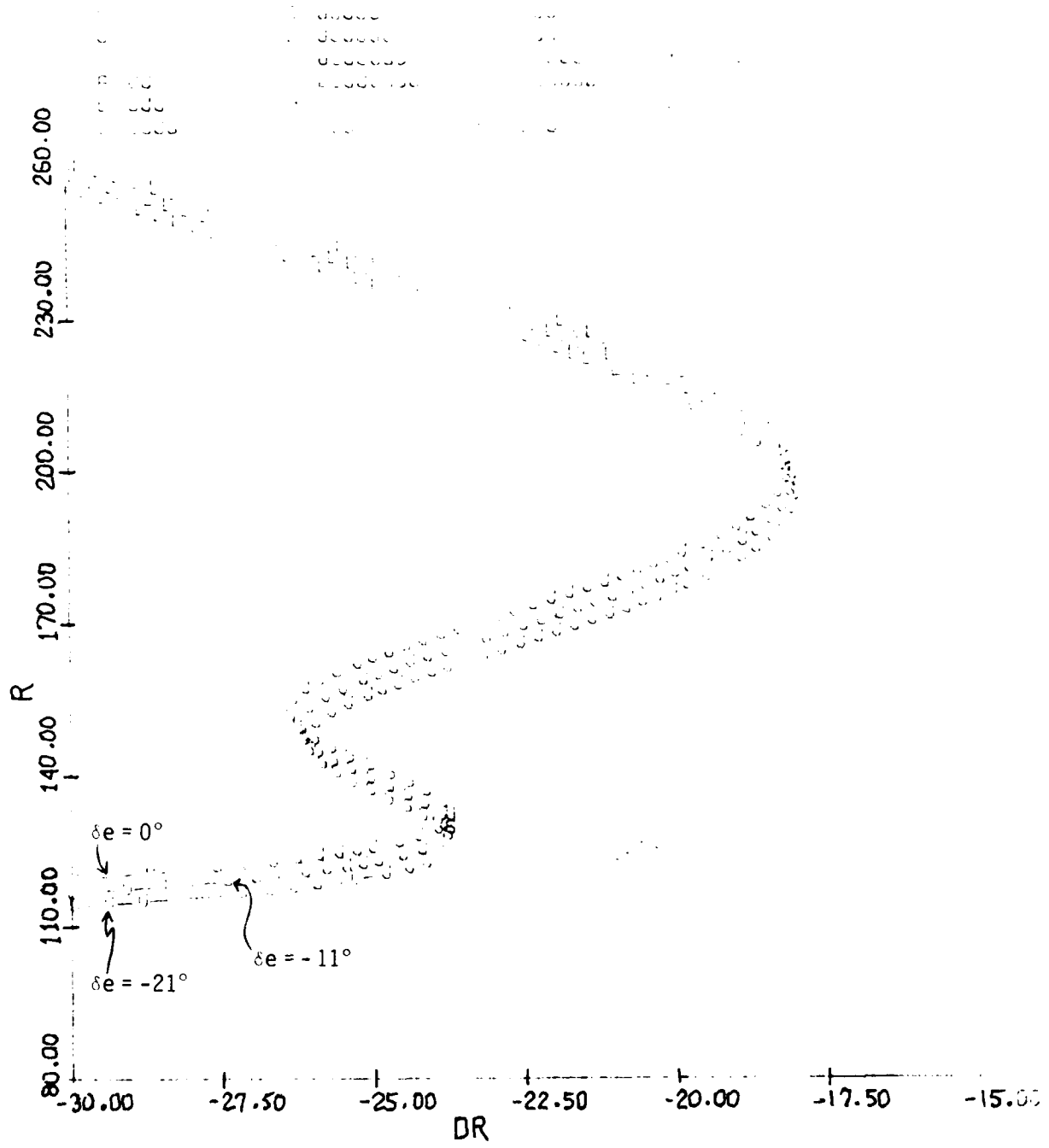

FIGURE 3.48(a)
Equilibrium Surface: Comparison of Elevator
r,α,p vs. δr; δa = 15°, V = 600 fps, g = 0

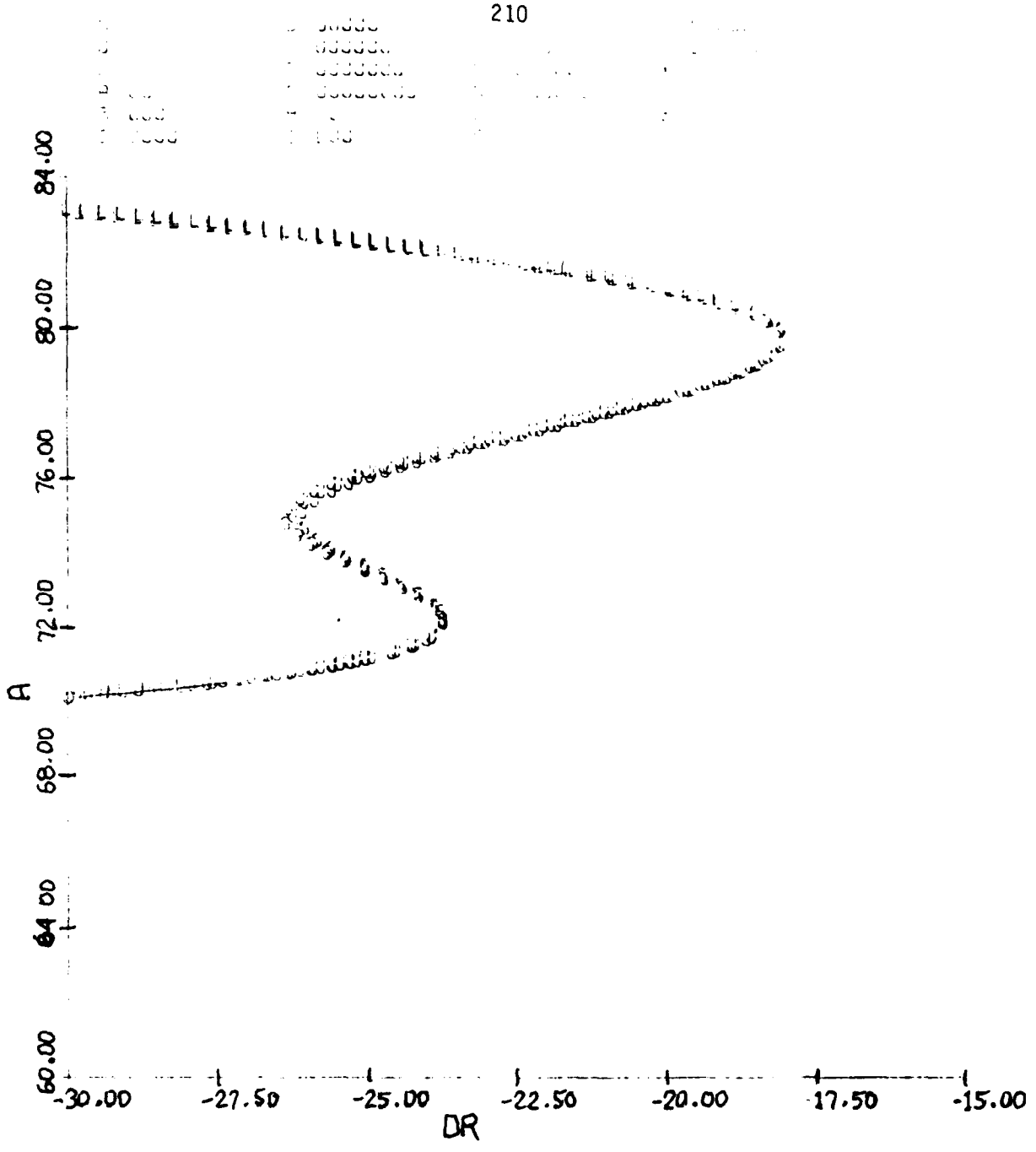

FIGURE 3.48(b) (cont.)

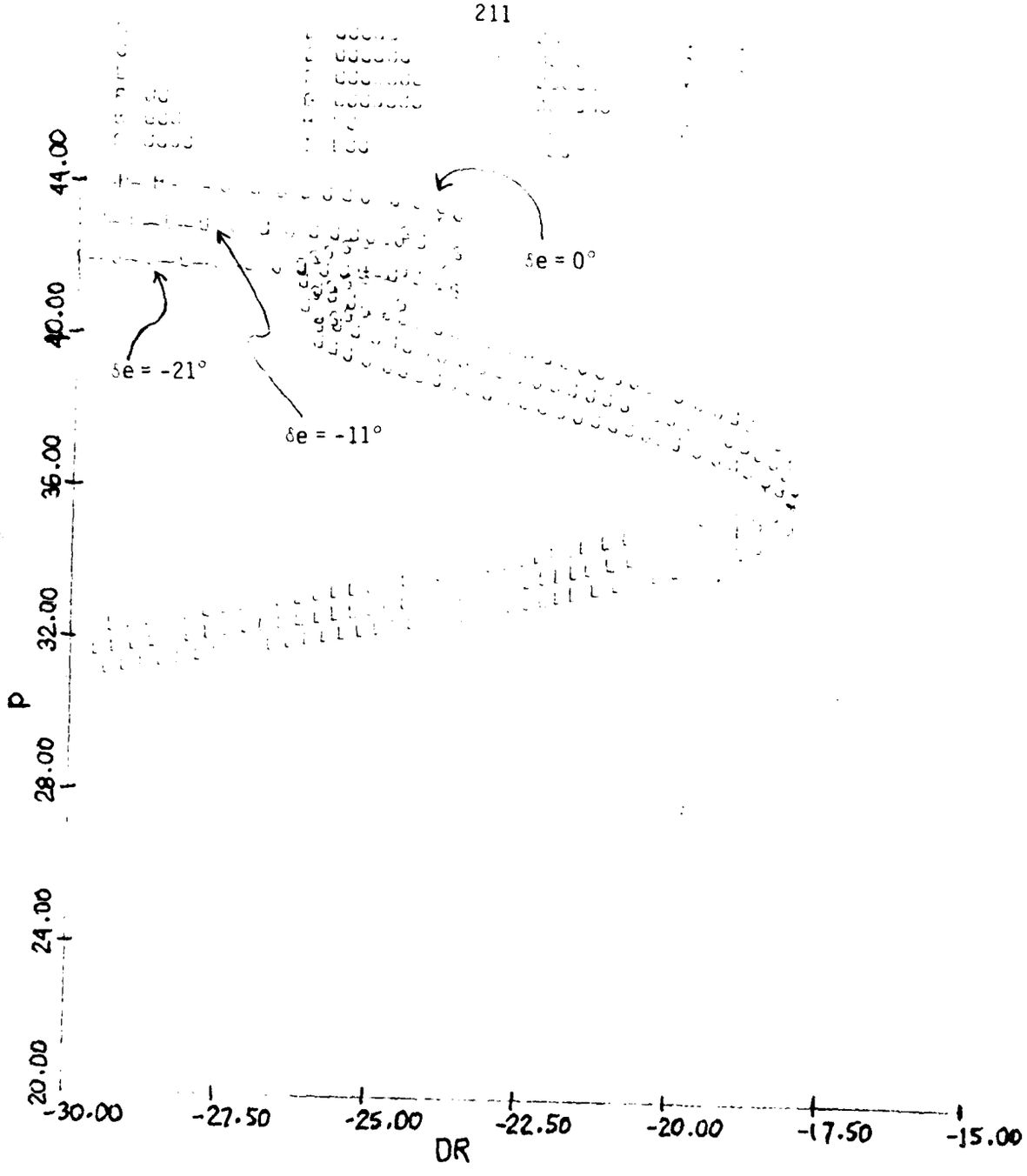

FIGURE 3.48(c) (concluded)

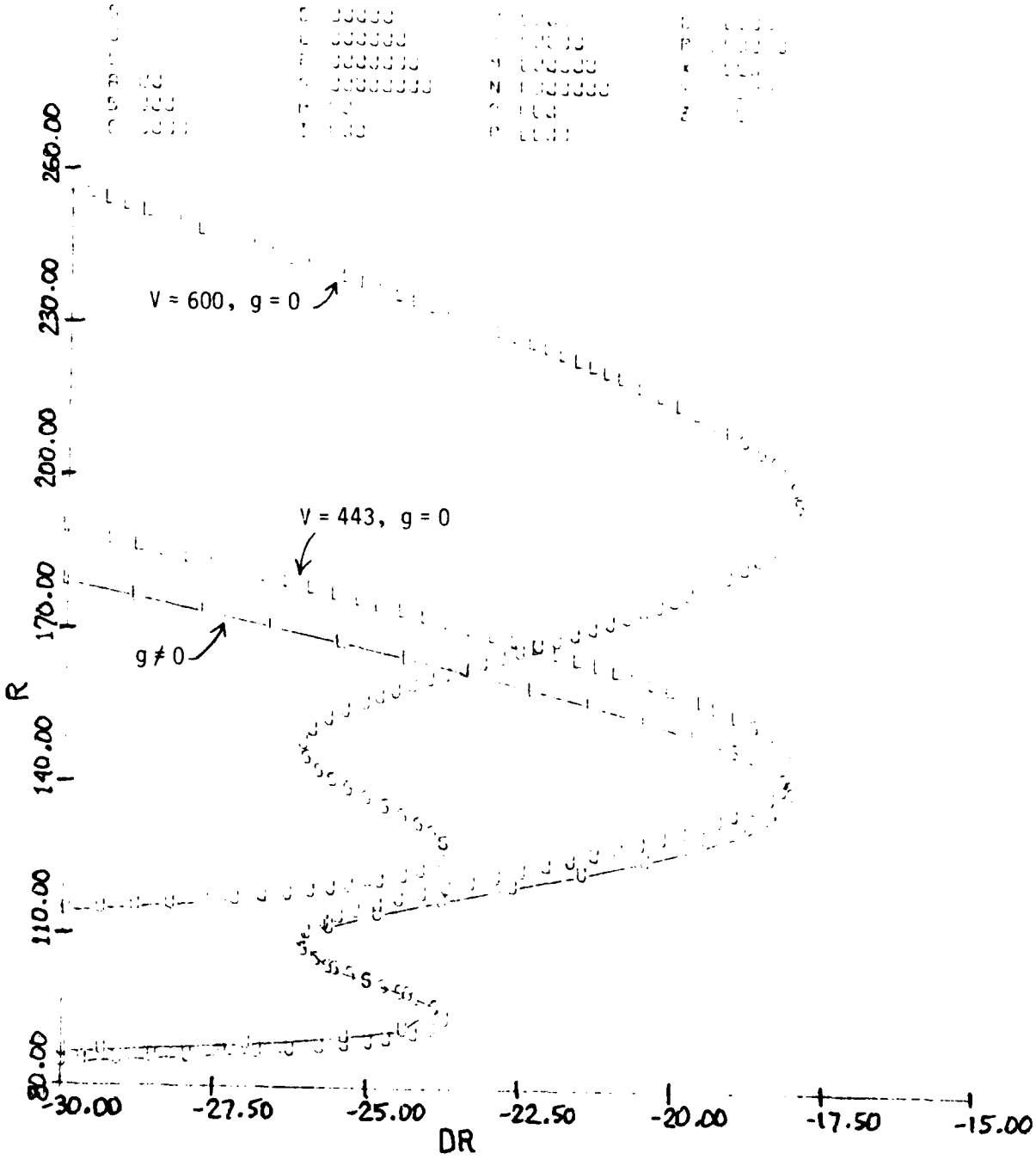

FIGURE 3.49(a)
Equilibrium Surfaces: Comparison of V, g Effects
r,α,p vs. δr; δa = 15°, δe = -21°

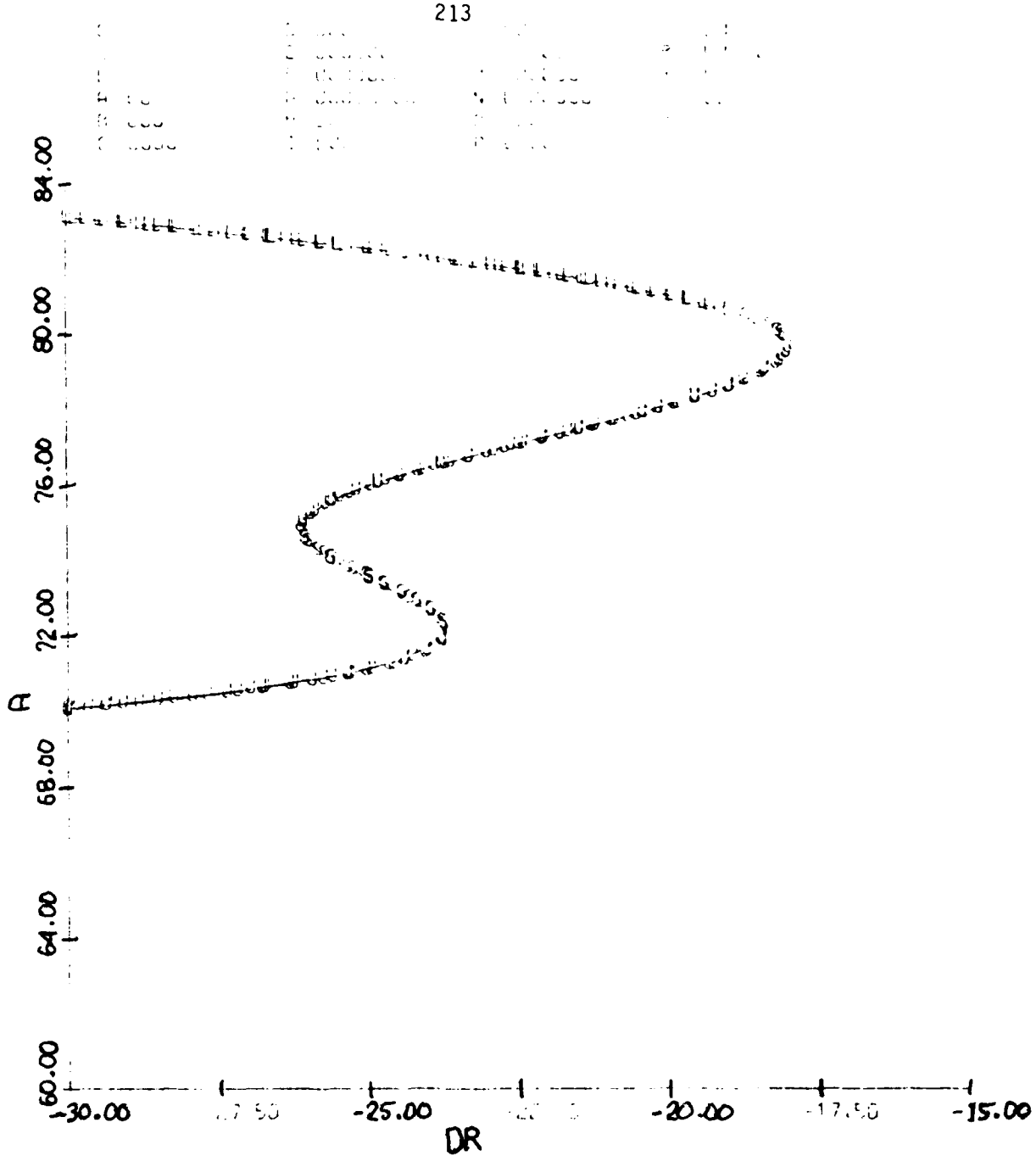

FIGURE 3.49(b) (cont.)

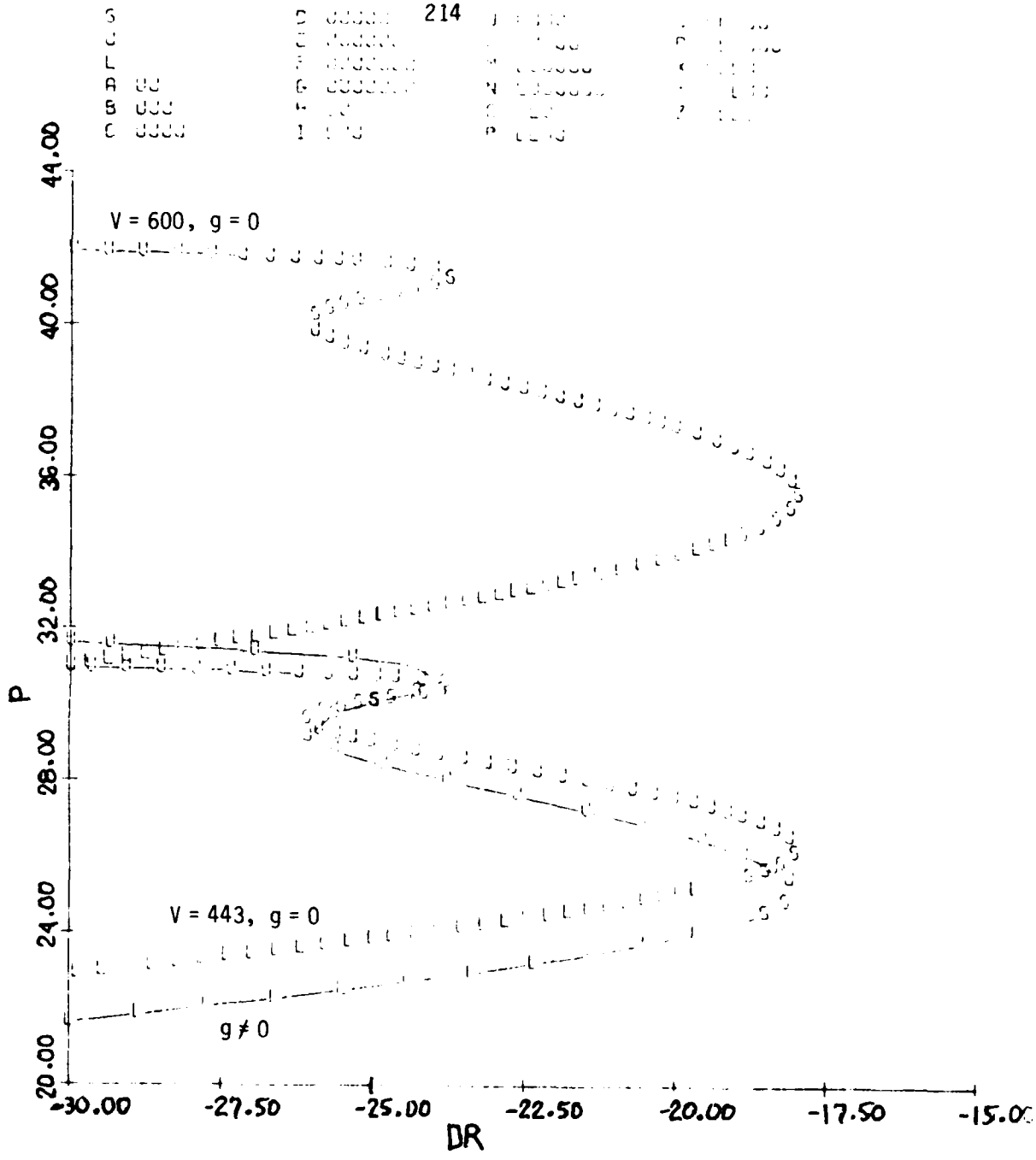

FIGURE 3.49(c) (concluded)

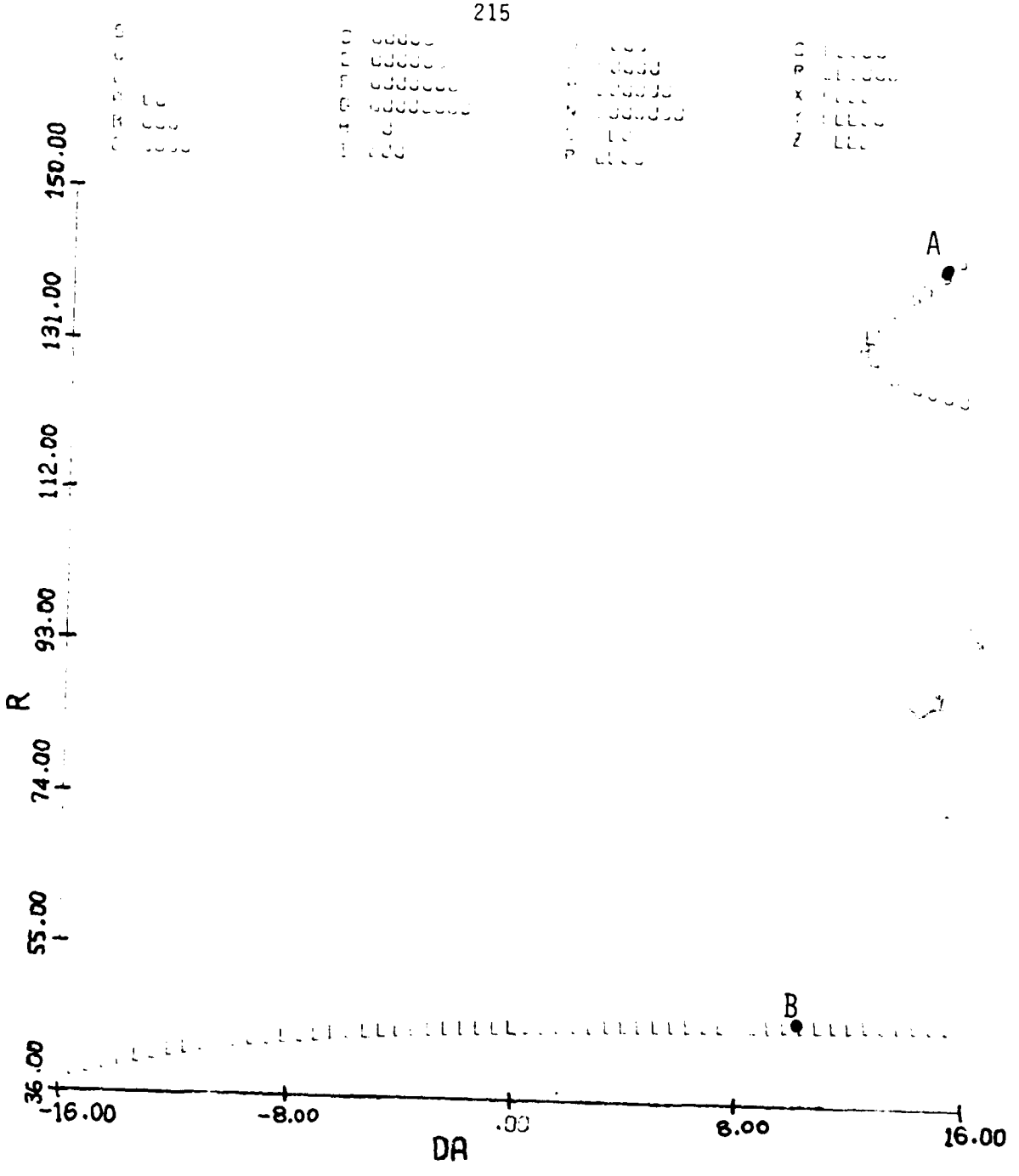

FIGURE 3.50(a)
Equilibrium Surface: r,α,p vs. δa
δe = 0°, δr = -25°, V = 600 fps, g = 0

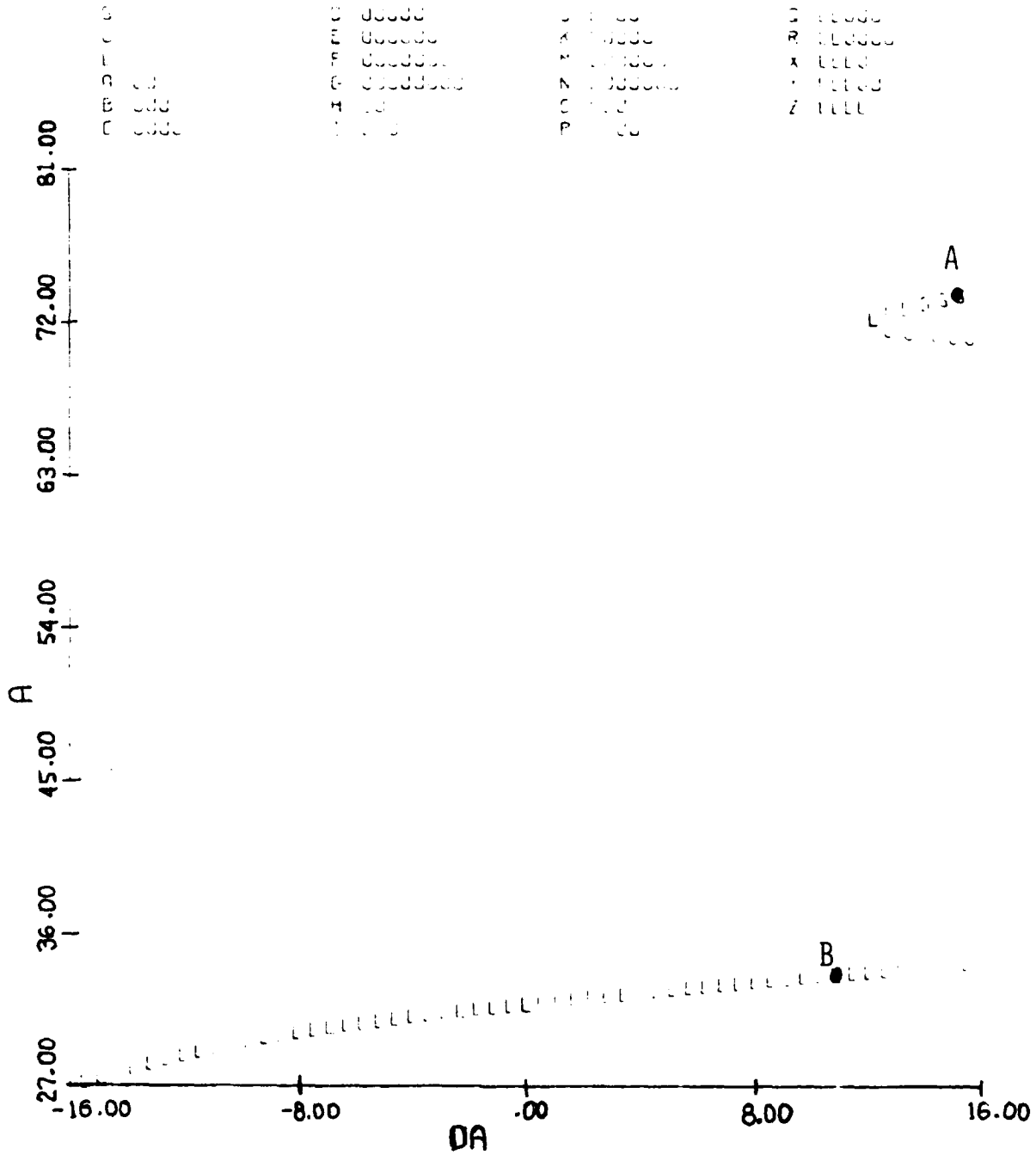

FIGURE 3.50(b) (cont.)

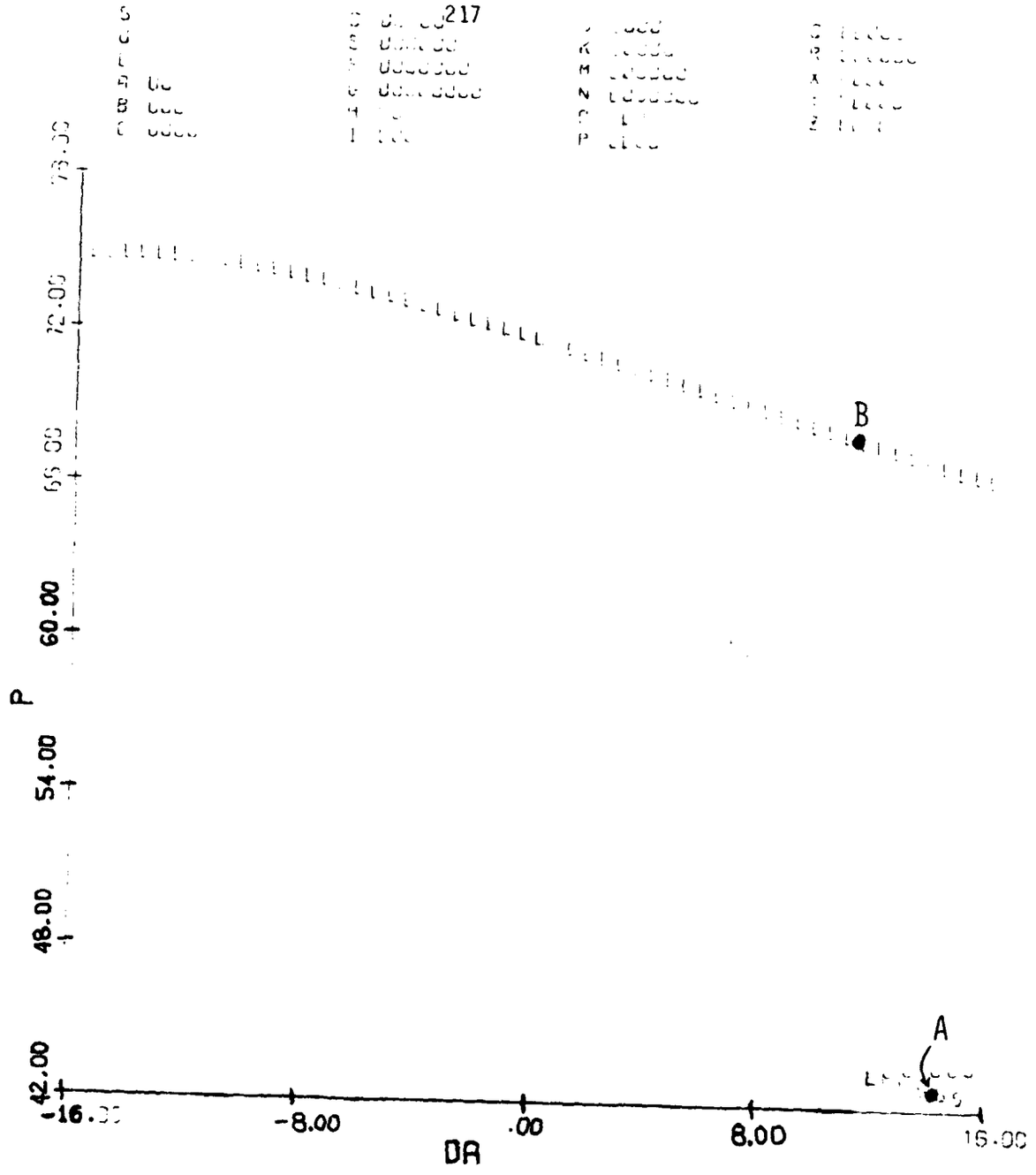

FIGURE 3.50(c) (concluded)

Time History: Spin Reversal

$$\delta a = \begin{cases} 0, & t \le 6 \\ 15, & 6 \le t \le 42 \\ -15, & t > 42 \end{cases} \qquad \delta e = \begin{cases} -21, & t < 60 \\ 0, & t \ge 60 \end{cases} \qquad \delta r = \begin{cases} 0, & t \le 2 \\ -30, & 2 < t \le 42 \\ 30, & t > 42 \end{cases}$$

DE = -21. DR = 0.

DA = 0.0

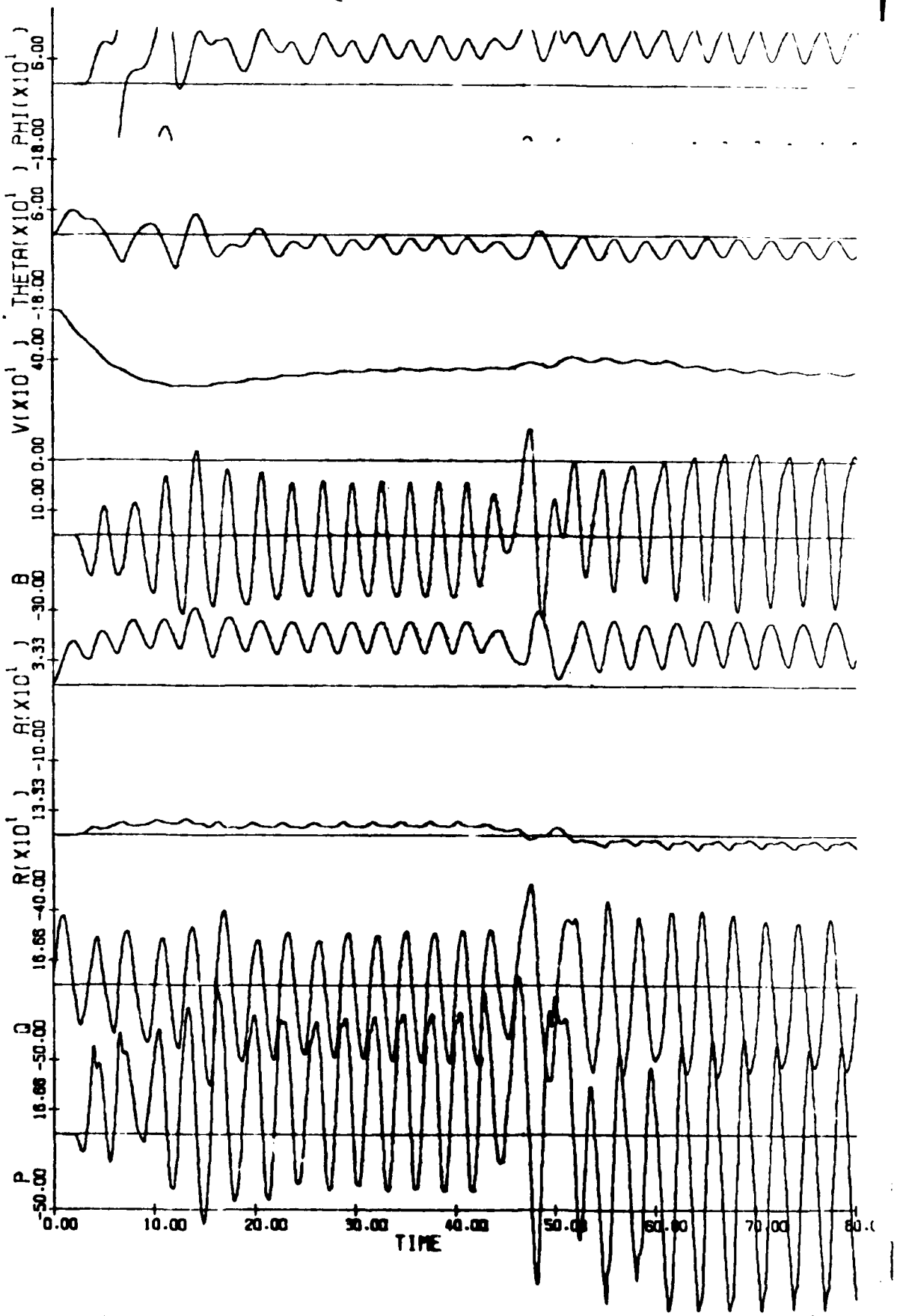

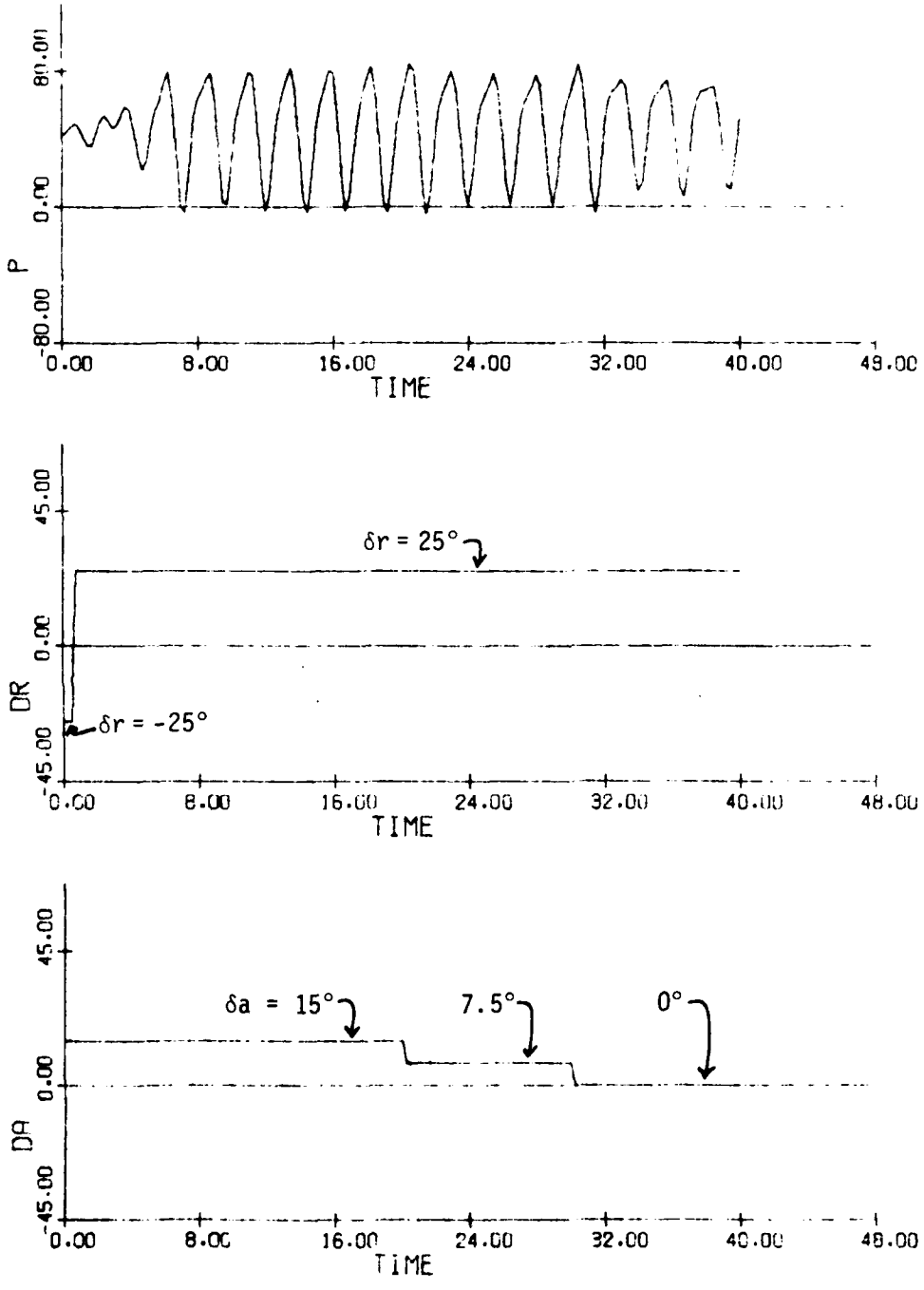

Figure 3.52(a)

Time History: Spin Recovery; $\delta e = 0°$

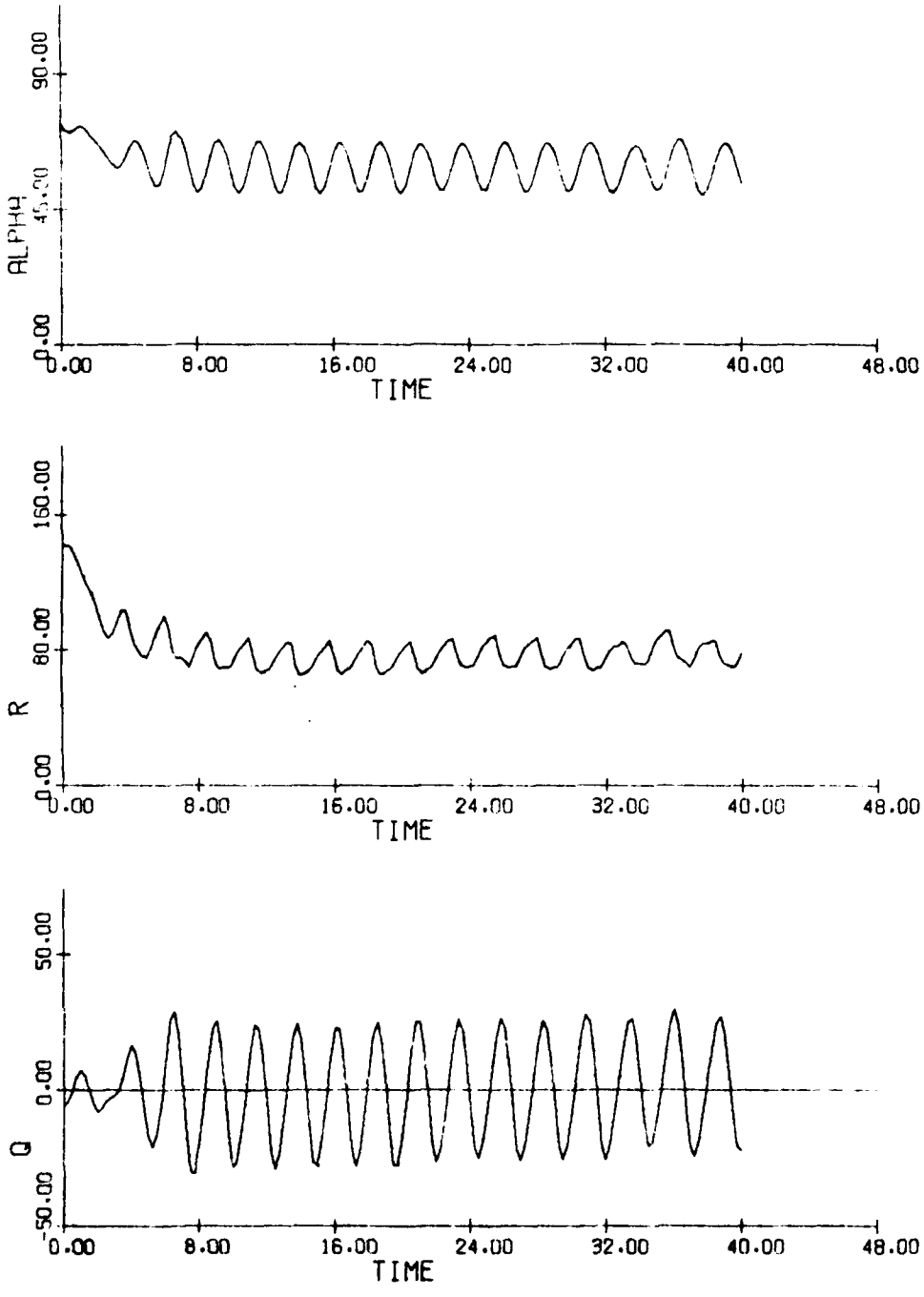

Figure 3.52(b) (cont.)

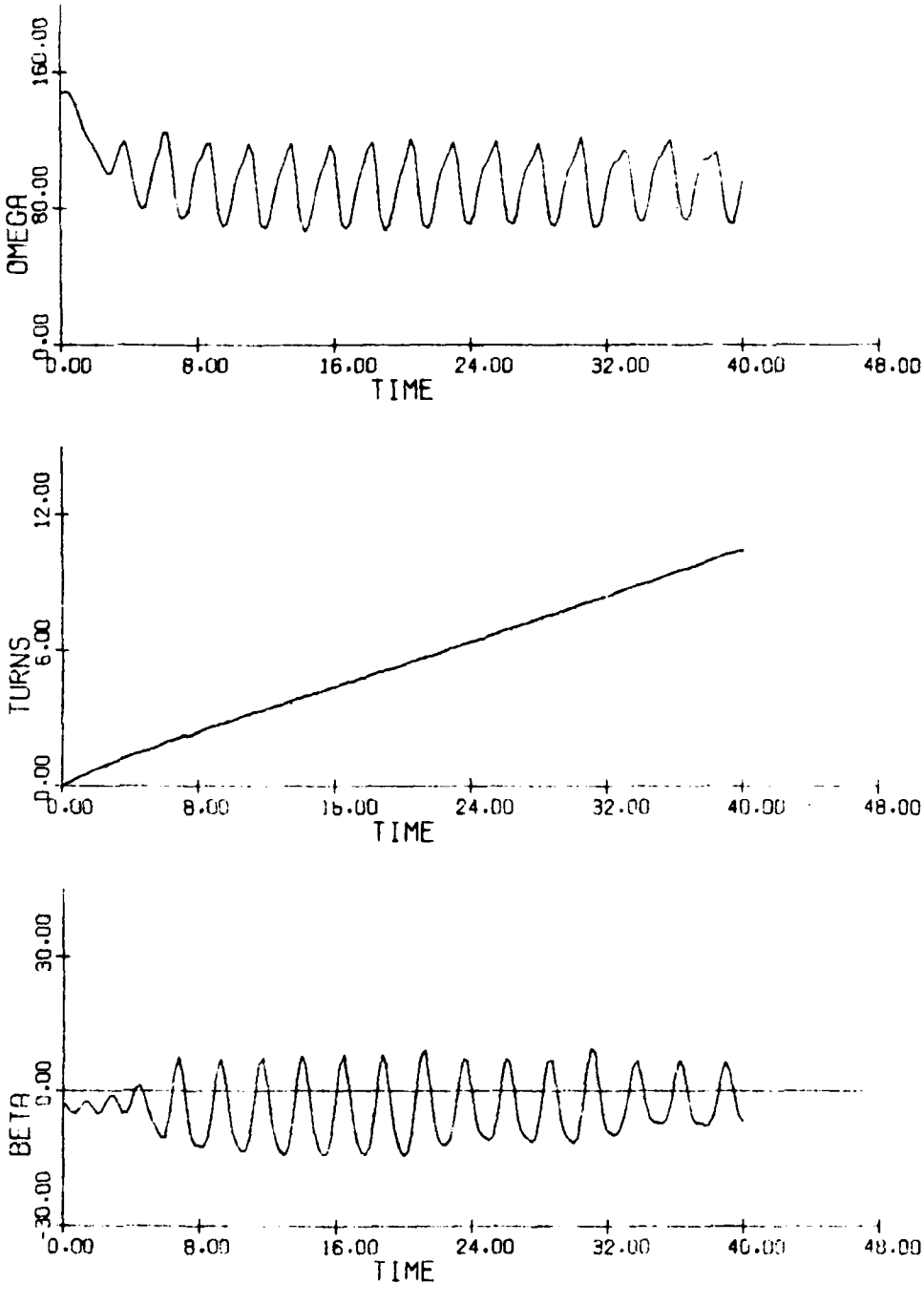

Figure 3.52(c) (cont.)

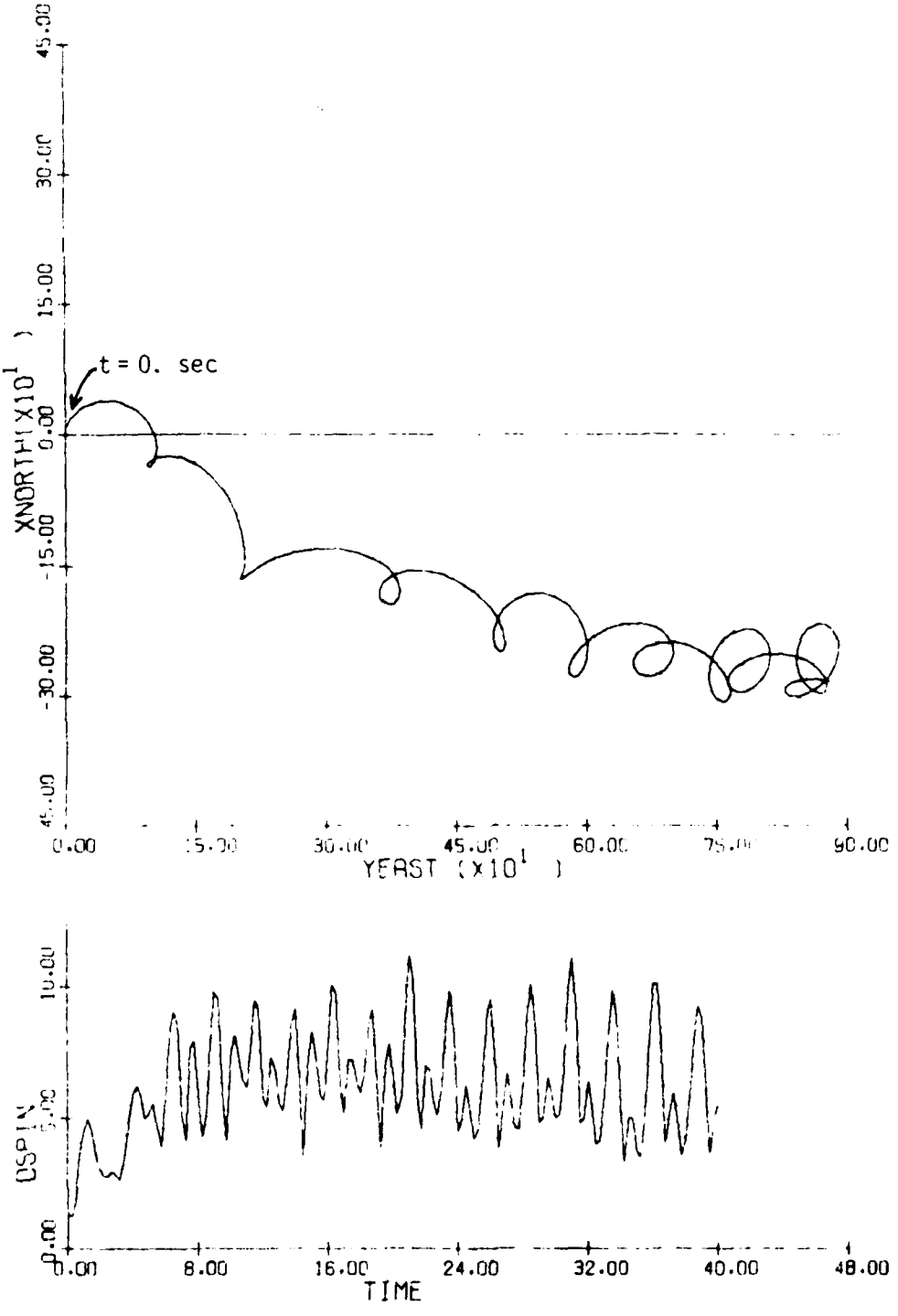

Figure 3.52(d) (concluded)

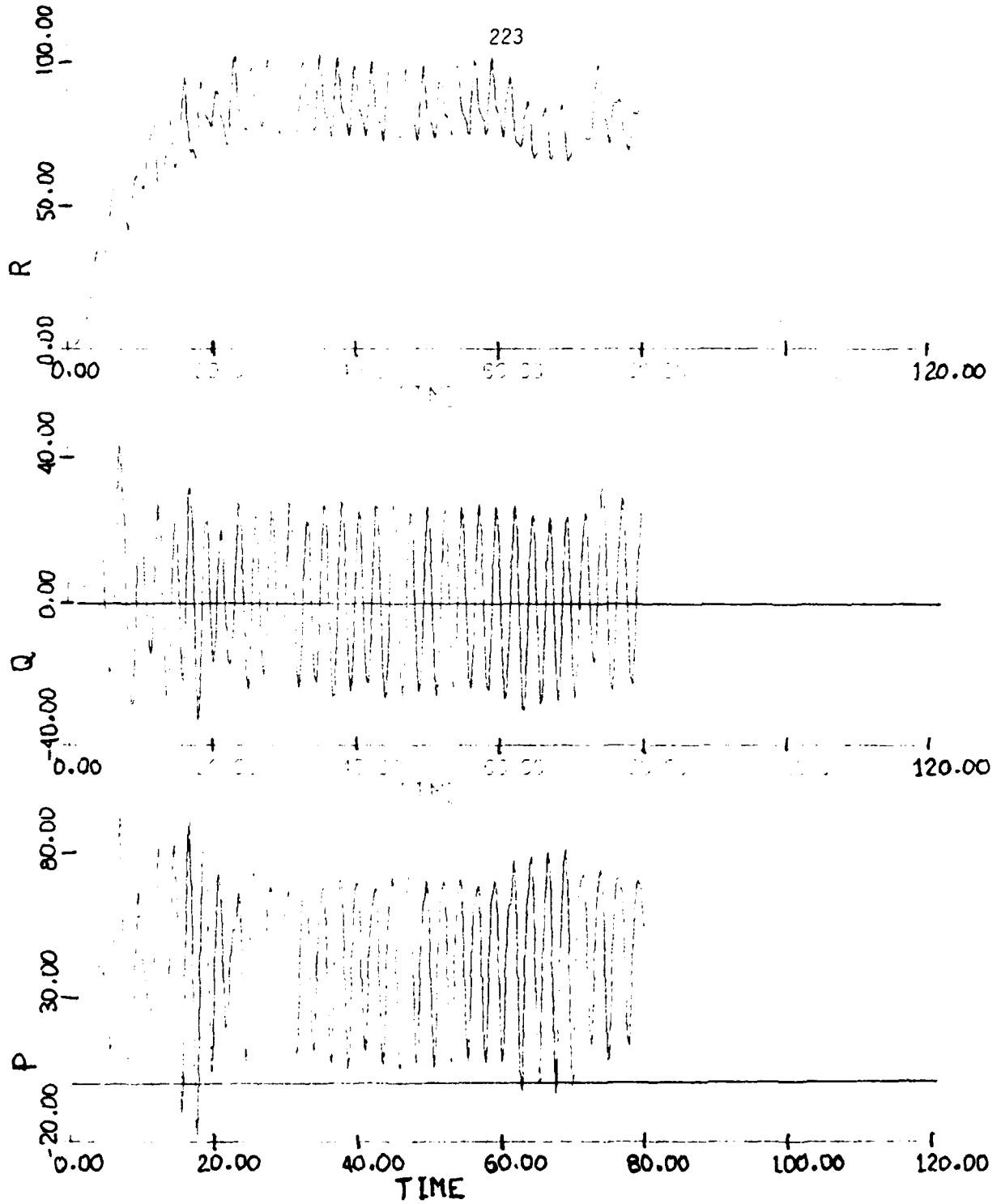

FIGURE 3.53(a)
Time History: Spin Entry

$$\delta a = \begin{cases} 15, & t \leq 70 \\ 0, & t > 70 \end{cases} \qquad \delta e = \begin{cases} -11, & t \leq 60 \\ 0, & t > 60 \end{cases}$$

$$\delta r = \begin{cases} 0, & t \leq 2 \\ 1.5, & 2 < t \leq 8 \\ 7, & 8 < t \leq 30 \\ 11.3, & 30 < t \leq 40 \\ 14, & 40 < t \leq 50 \\ 11.3, & 50 < t \leq 60 \\ 25, & t > 60 \end{cases}$$

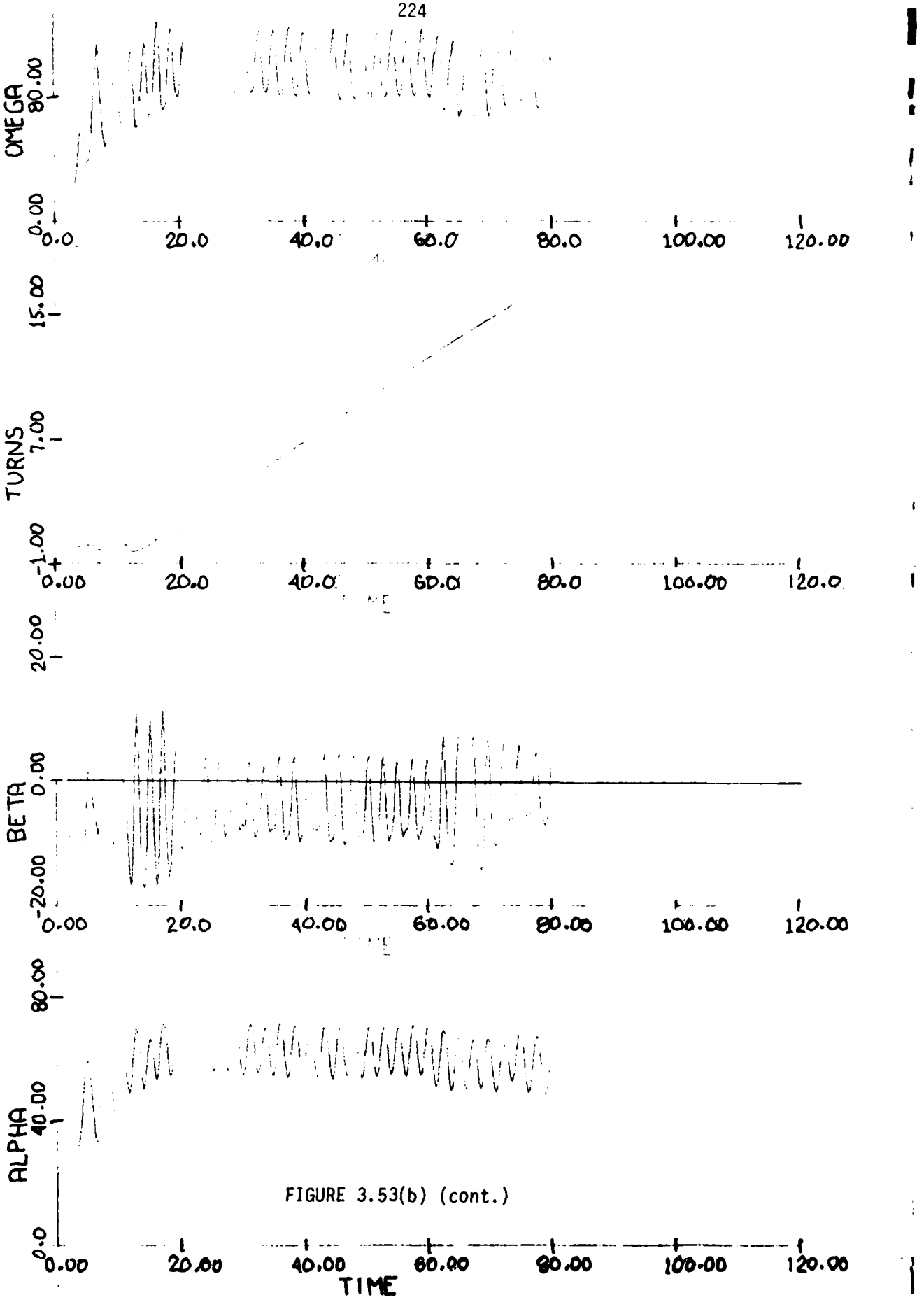

FIGURE 3.53(b) (cont.)

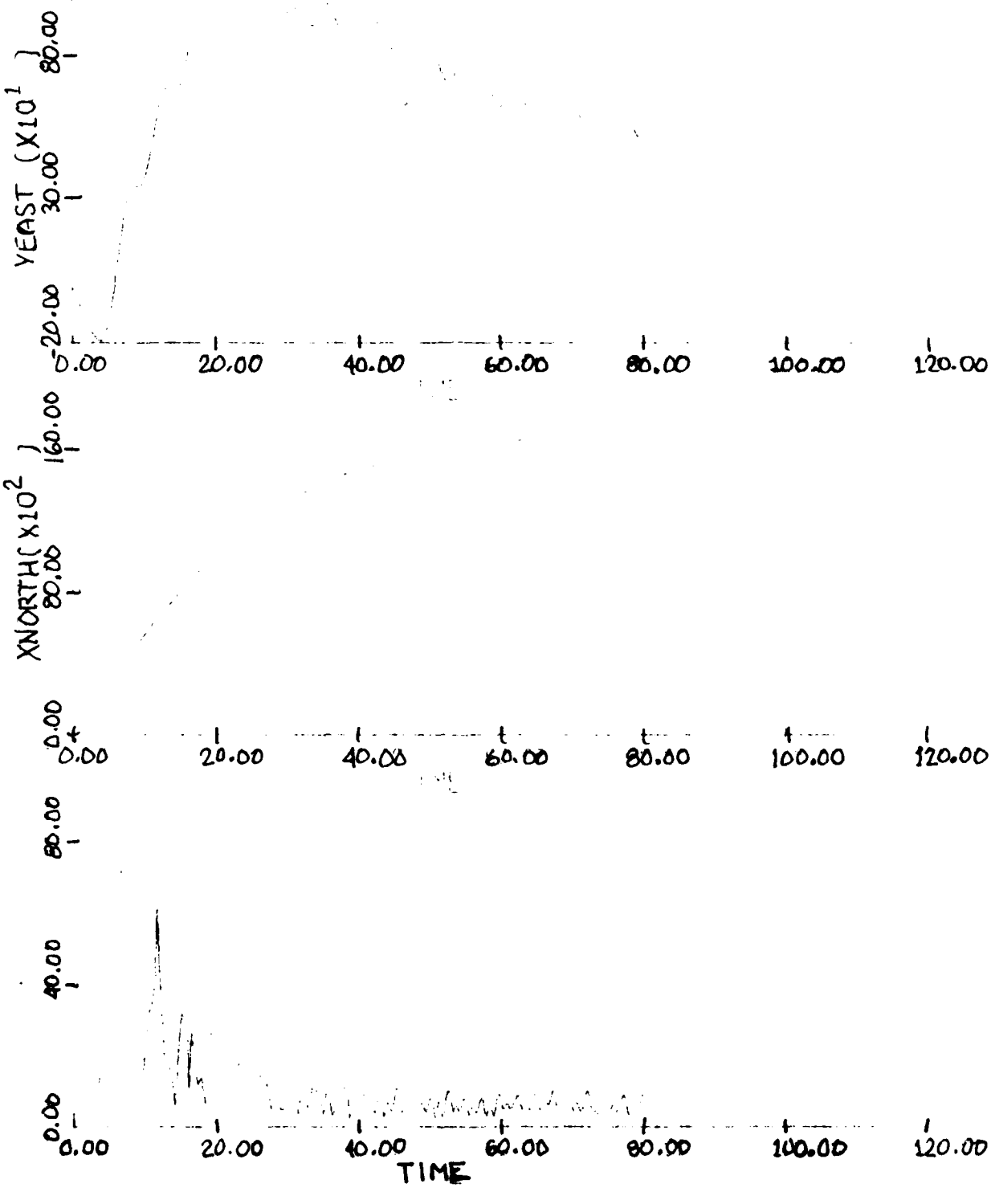

FIGURE 3.53(c) (concluded)

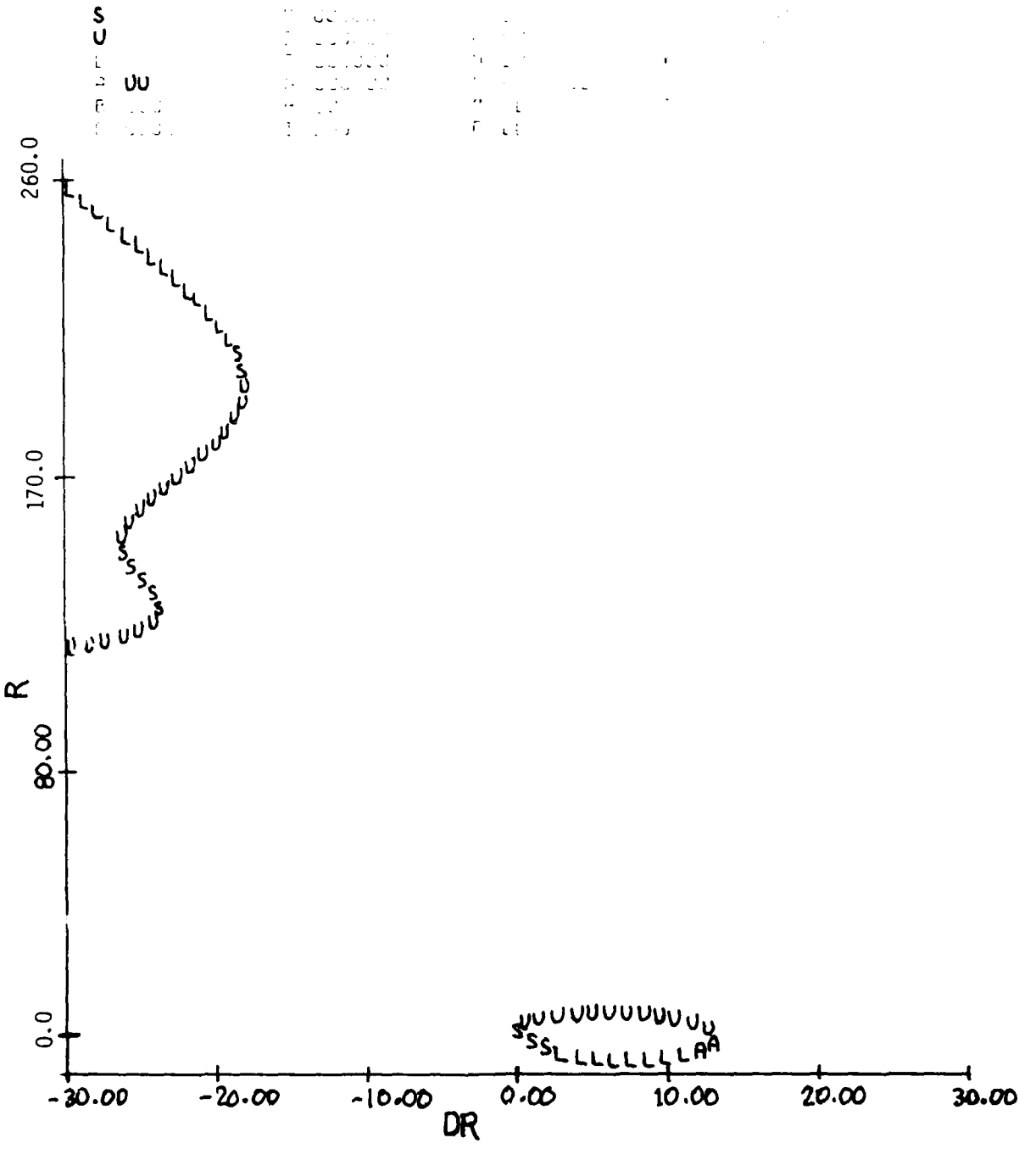

FIGURE 3.54(a)
Equilibrium Surface: r,α,p vs. δr
δa = 15°, δe = -11°, V = 600 fps, g = 0

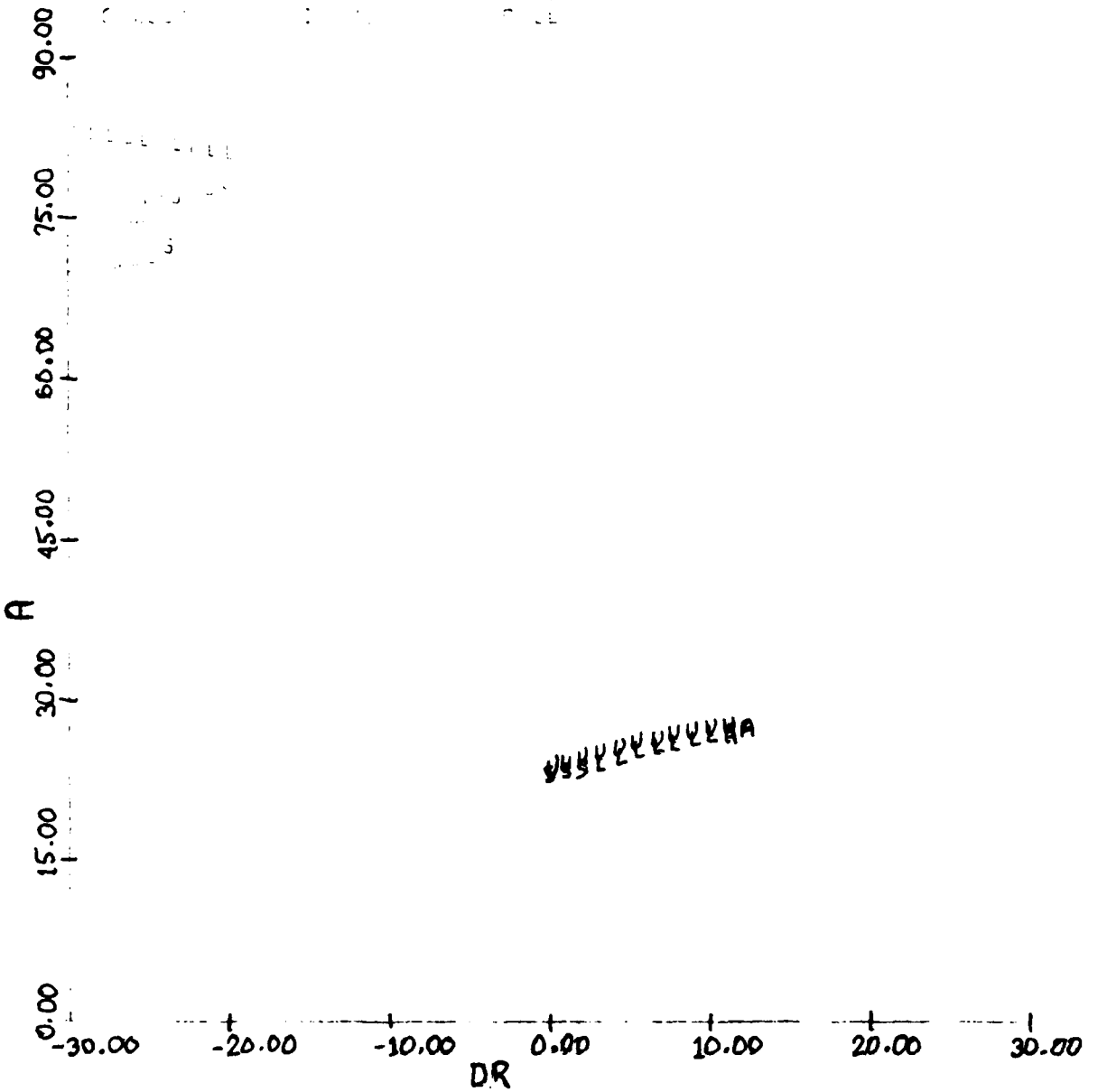

FIGURE 3.54(b) (cont.)

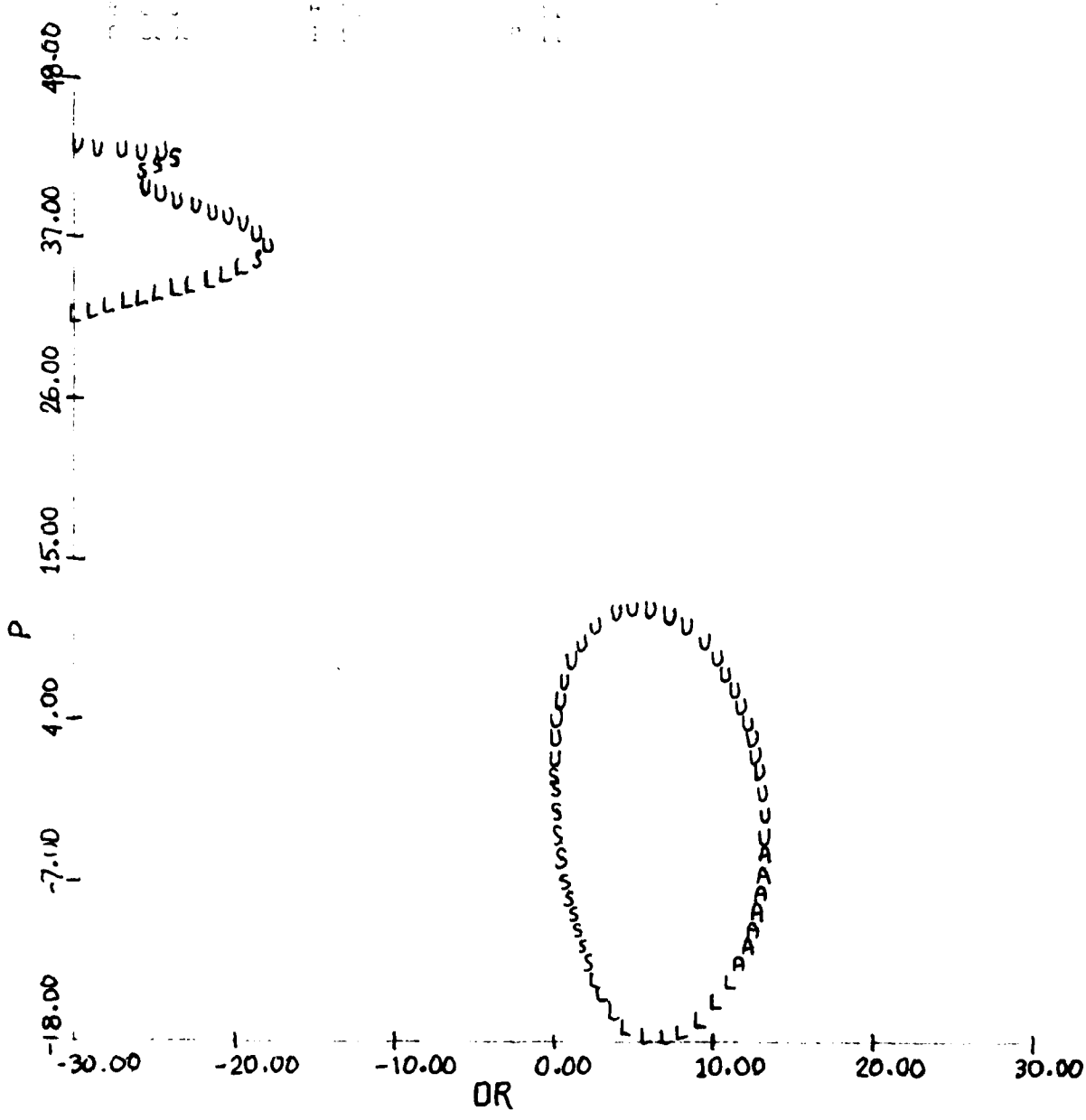

FIGURE 3.54(c) (concluded)

CHAPTER IV

Other Topics

During this reporting period, further work has been performed to understand the nature of the nonlinear high-α dynamic behavior of aircraft H (Mehra et al. (1977)). In this regard, there are two topics which merit discussion at this time. The first topic, exploring the power spectra of some motions, is part of an overall study which will be expanded on in the future with the F-4 aircraft model. The second topic deals with using our knowledge of the global (nonlinear) characteristics of the aricraft model of interest to synthesize a command/stability augmentation system.

4.1 Power Spectra of Time Histories for A/C H

As a means of gaining further insight into the nature of the Hopf Bifurcation and the limit cycle motions which subsequently arise, we have studied certain time history responses of aircraft H in order to see whether responses become multiperiodic and tend towards nonperiodicity or chaos (Ruelle (1977)). It was shown previously (Mehra et al. (1977)) that most of the aircraft H time histories exhibit one of the following two types of motions:

1) the state variables behave in a noticeably periodic manner, with an amplitude growth/decay time constant which is much greater than the interval of interest over which the motion is observed;
2) the motion decays to a steady-state equilibrium in which all of

the state variables arrive at a unique value, without oscillations.

However, there are initial conditions and control settings which produce a response that appears to be erratic and it is not possible to conclusively determine whether or not the motion possesses limit cycle behavior, based purely on an inspection of time histories. Ruelle (1977) states that when a motion contains at least three basic frequencies, it is possible for the periodic response to appear random in nature, due to certain nonlinear perturbations.

It is therefore worthwhile to look at the spectra of these responses. Aircraft H has been used in this study, because it models adequately the kind of nonlinear terms which generate periodic behavior. The spectra used here are merely the Fourier transforms of the autocorrelation functions of each of the state variables (p,q,r,α,β) computed from their time histories. A routine from the IMSL library package was used to generate the spectra.

The control values for which spectra of resulting time histories were computed are shown in Fig. 4.1. These figures are taken from the report by Mehra et al. (1977).

Fig. 4.2 shows a time history which is well-behaved. The small transient behavior at the beginning decays rapidly to steady state values for each of the states. The controls for this case are held at $\delta a = 0°$, $\delta e = 2°$, $\delta r = 5°$, and the initial conditions are $\alpha = \beta = p = q = r = 0$. The corresponding spectra are shown in Fig. 4.3. These are generated for a time interval from 2 to 100 seconds which includes the initial transient motions. Note that

there are 2 frequencies, a secondary one which has roughly twice the value of the fundamental frequency, the latter being about 0.40 cycles per second (cps). Note also that the secondary frequency appears only in the spectra of the longitudinal variables, α and q. The control settings for this case are in the linear region, so such decoupling is not a surprise. Averaging effects have reduced the amplitude of the spectra (i.e., for most of the time period over which the spectra are computed, the system is at equilibrium. The amplitude thus changes with the ratio of transient time interval to total time interval).

Fig. 4.4 shows the results of computing the spectra over the time period 22 to 85 sec. which effectively avoids all transient behavior. The magnitudes have been reduced several orders of magnitude, and the secondary frequency has vanished. Note, however, that the fundamental frequency is still detectable, and it still has the same value (about 0.40 cps).

Limit cycle motions were next studied by repeating the above run, except for δa which is set at -18°. Since the initial conditions are again at the origin, a Hopf Bifurcation (i.e., jump) to a limit cycle occurs for this value of δa, as seen in Fig. 4.5. The resulting spectra, shown in Fig. 4.6, indicate that the fundamental frequency is about 1.3 cps, with a secondary frequency at about 2.3 cps and hints of a third frequency (see the p spectrum) at 1.05 cps. The major difference from the $\delta a = 0°$ case, however, lies in the amplitudes of the spikes, which are at least three orders of magnitude greater. The spikes are sharper, indicating a "clean" oscillation (the spectrum of a pure sinusoid is an impulse located at the frequency of the sinusoid; the

spectrum of white noise is a constant over all frequencies and is proportional to the power of the signal).

A run was next made with $\delta a = -6°$, $\delta e = 2°$, $\delta r = 0°$, and initial conditions $p = -46.3$, $q = 23.4$, $r = 59.2$ deg/sec, $\alpha = -2.39°$, $\beta = -31.5°$. The time history, Fig. 4.7, indicates evidence of at least 2 frequencies. The corresponding spectra, Fig. 4.8, show a dominant frequency at 1.2 cps, and three subharmonics at about 0.15, 0.3 and 0.45 cps. As in all cases except Fig. 4.4, the time interval for the spectrum computation in 2 to 100 sec. The somewhat irregular spacing of the high peaks in Fig. 4.7 gives rise to the cluster of 3 secondary peaks in the spectra. The absence of rudder in this case may explain the lack of secondary frequencies in the spectra for β and r, the two variables most directly dependent on δr.

Fig. 4.9 shows a more erratic motion, and its spectrum is in Fig. 4.10. The initial values for the state variables are again zero, and $\delta a = 0°$, $\delta e = 2°$, and δr is moved to 10°. Again the roll motion (p) is dominant with a primary frequency of 0.375 cps. The pitch rate (q) motion is less periodic and has several frequencies. It is not clear, however, whether any chaotic regimes exist for aircraft H. McLaughlin and Martin (1974, 1975) show that in fluid flow, chaotic motions can result either via a phenomenon known as an inverted Hopf bifurcation (i.e., existence of unstable limit cycles at control values below the control values for which a pair of complex conjugate eigenvalues crosses the imaginary axis) or via normal Hopf bifurcation exceeding three in number. (Ruelle (1977) has shown, however, that chaotic motions or "strange attractors" are possible even after three Hopf-type bifurcations.) Since the order of the aircraft H model is five and at most two pairs of complex conjugate eigenvalues can

cross the imaginary axis, "strange attractors" cannot be present if only normal bifurcations are considered. At this time, it does not seem that inverted bifurcations are present in the aircraft H model, though this does require further study.

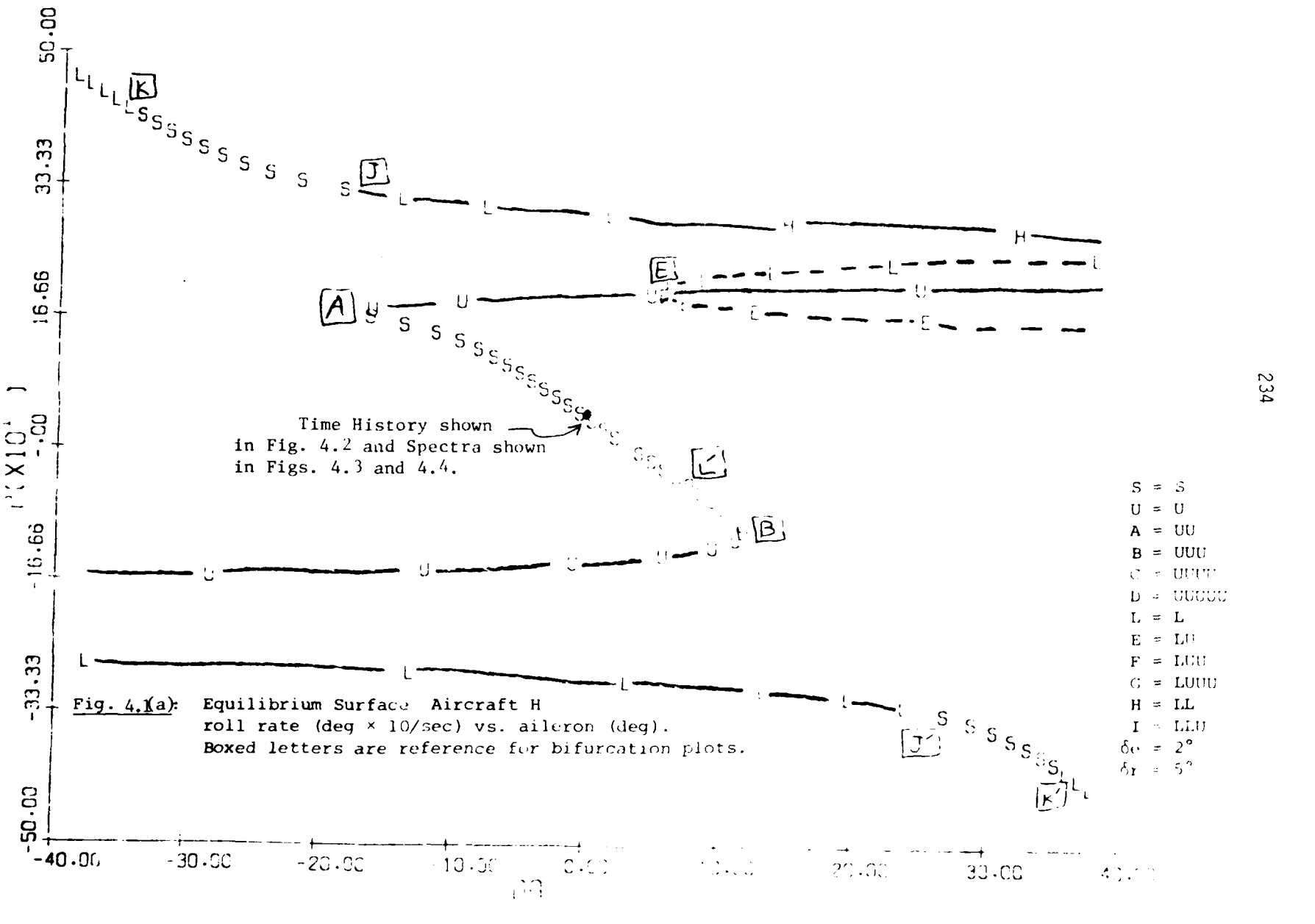

Fig. 4.1(a): Equilibrium Surface Aircraft H
roll rate (deg × 10/sec) vs. aileron (deg).
Boxed letters are reference for bifurcation plots.

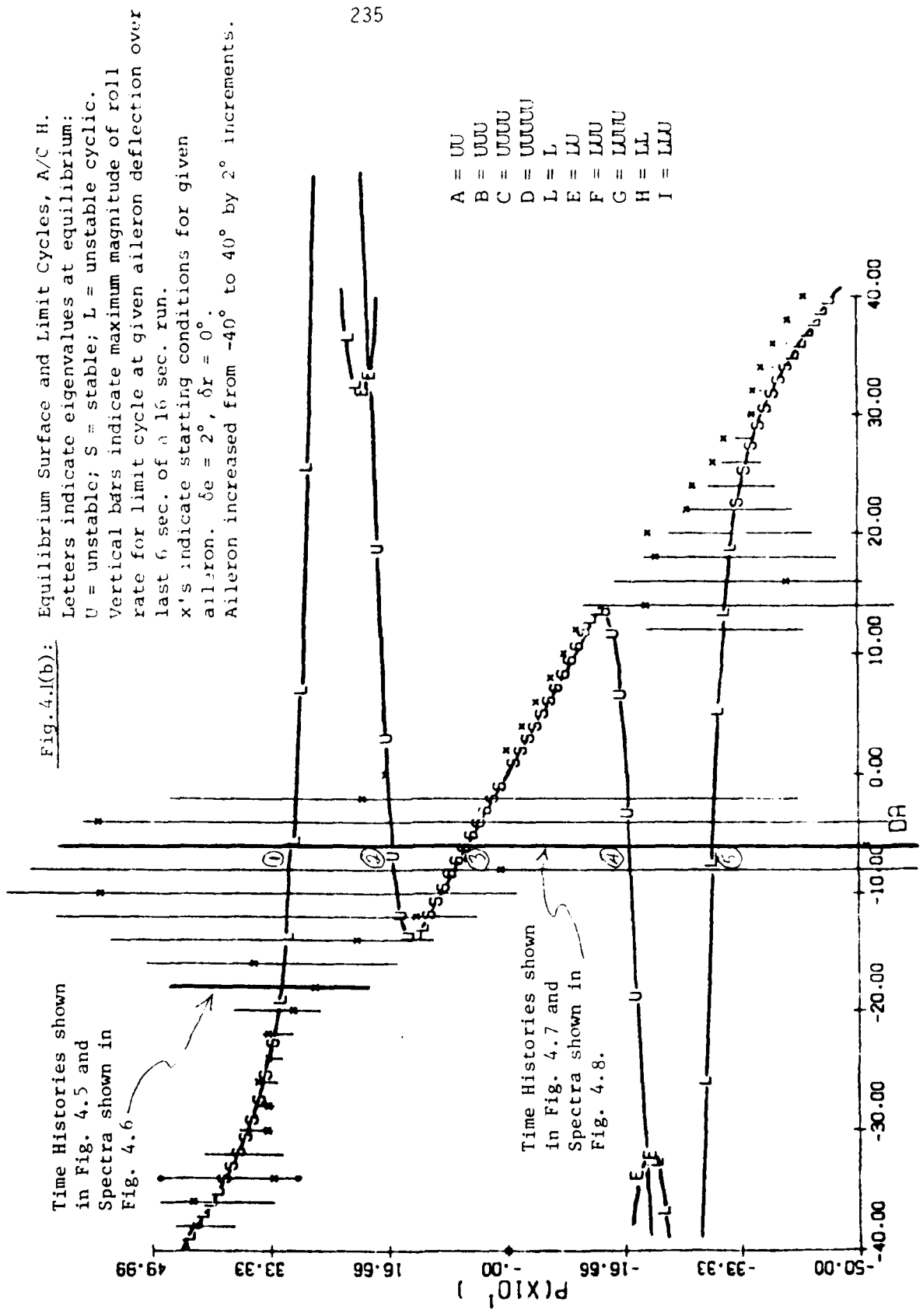

Fig. 4.4(b): Equilibrium Surface and Limit Cycles, A/C H.
Letters indicate eigenvalues at equilibrium:
U = unstable; S = stable; L = unstable cyclic.
Vertical bars indicate maximum magnitude of roll rate for limit cycle at given aileron deflection over last 6 sec. of a 16 sec. run.
x's indicate starting conditions for given aileron. $\delta e = 2°$, $\delta r = 0°$.
Aileron increased from -40° to 40° by 2° increments.

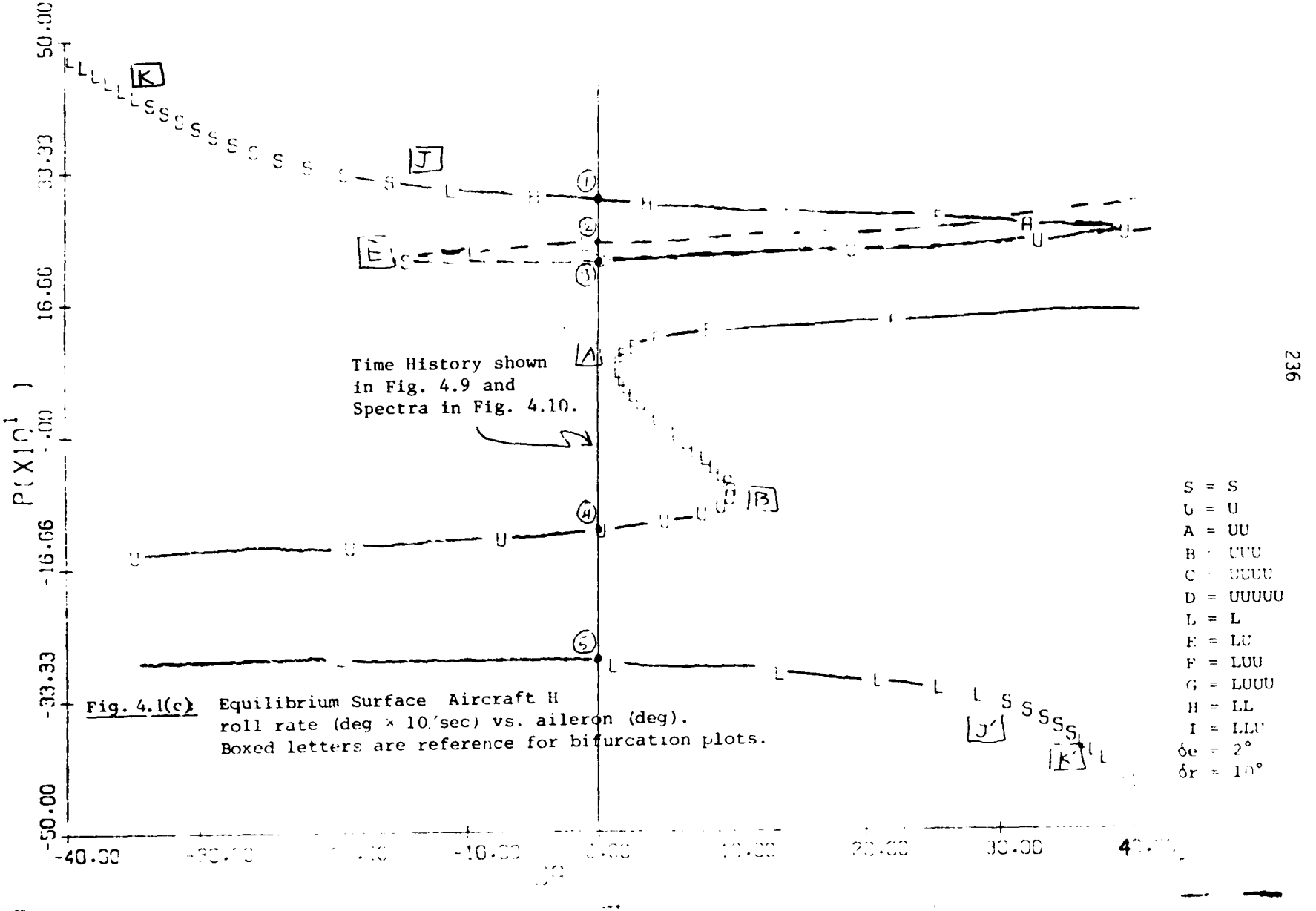

Fig. 4.1(c) Equilibrium Surface Aircraft H
roll rate (deg × 10/sec) vs. aileron (deg).
Boxed letters are reference for bifurcation plots.

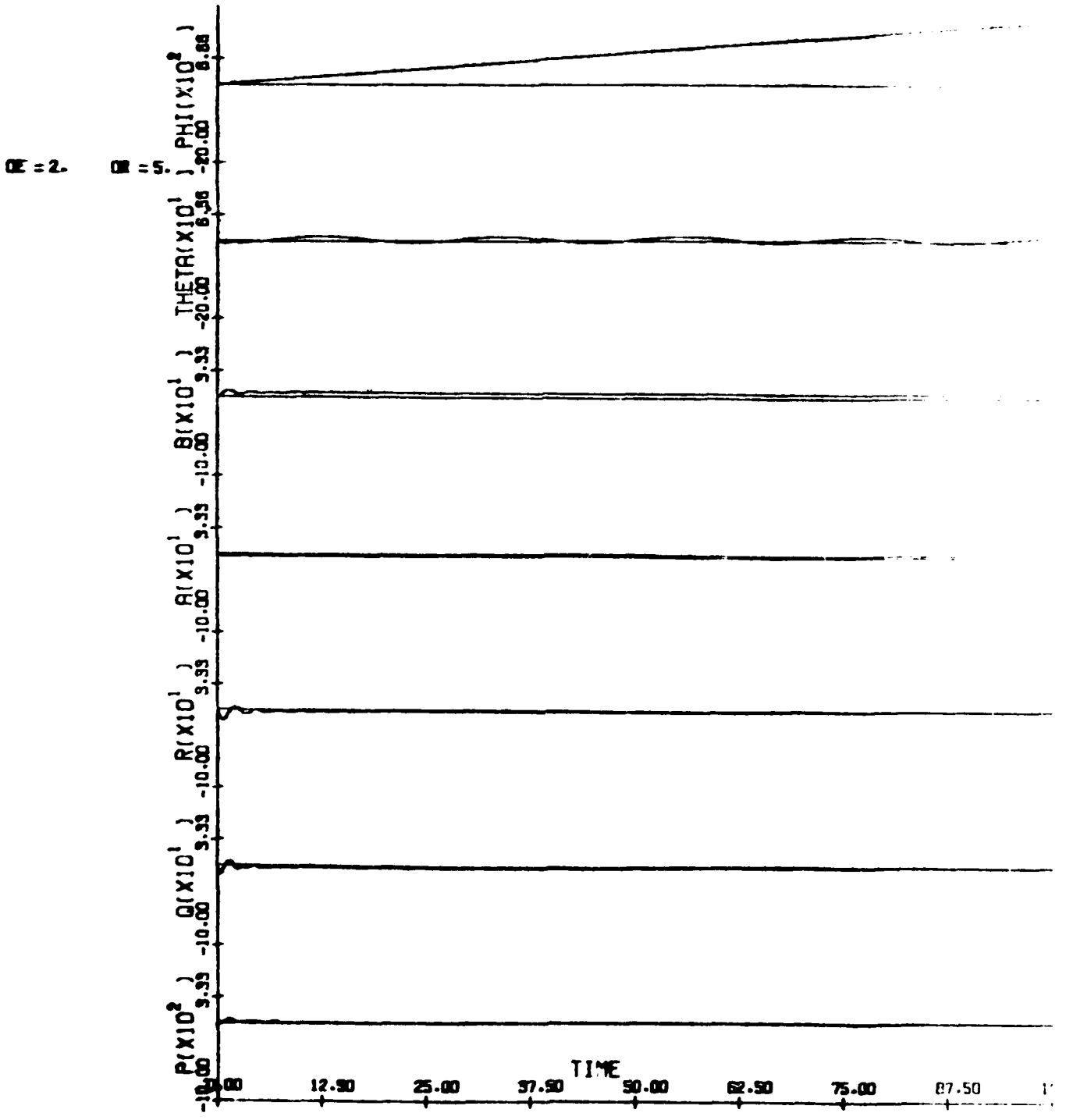

Fig. 4.2: A/C II Time History; $\delta a = 0°$, $\delta e = 2°$, $\delta r = 5°$; initial conditions at origin.

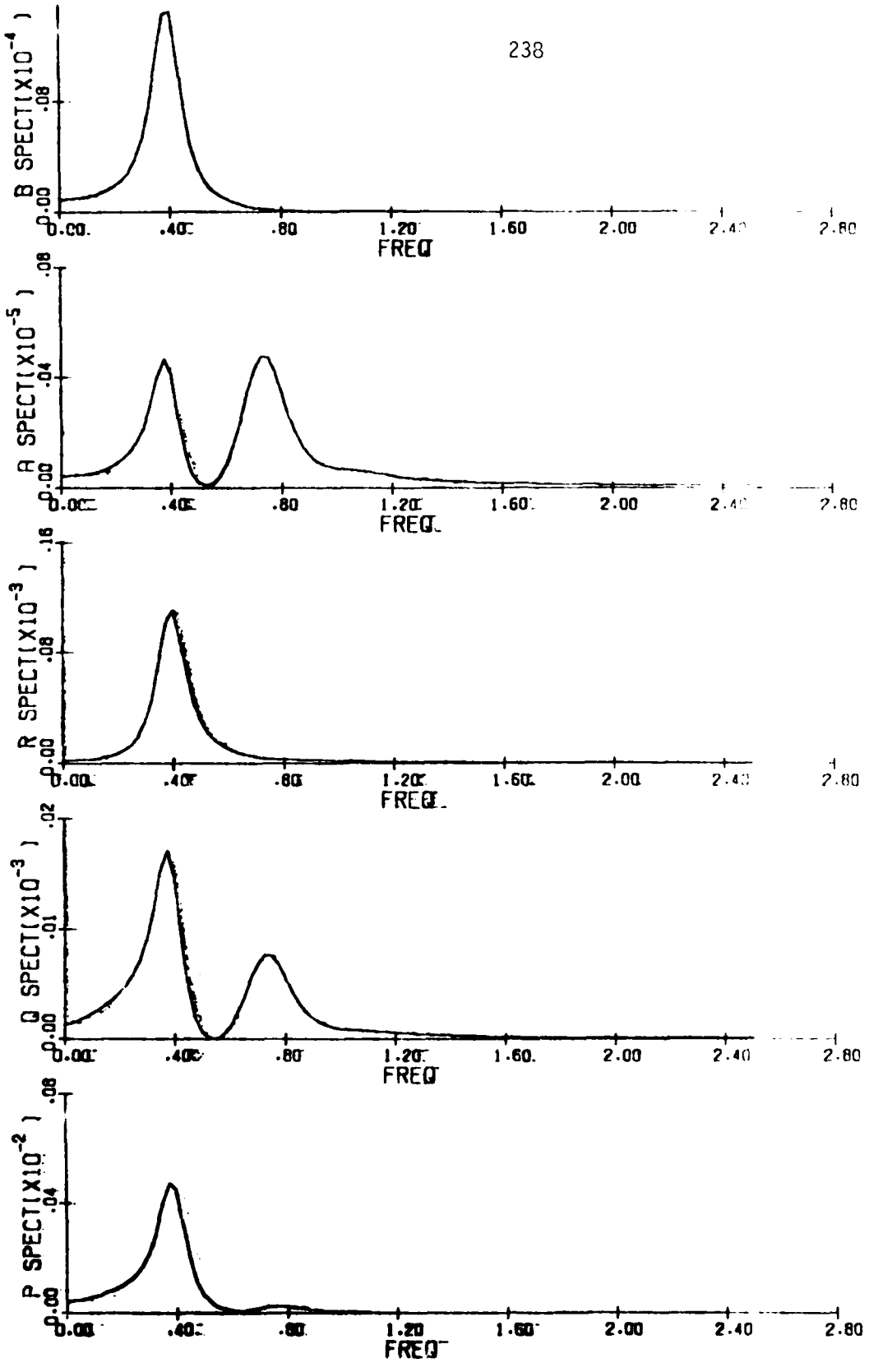

Fig. 4.3: A/C H Autocorrelation Spectra, for Control Settings of Fig. 4.2; transient response included.

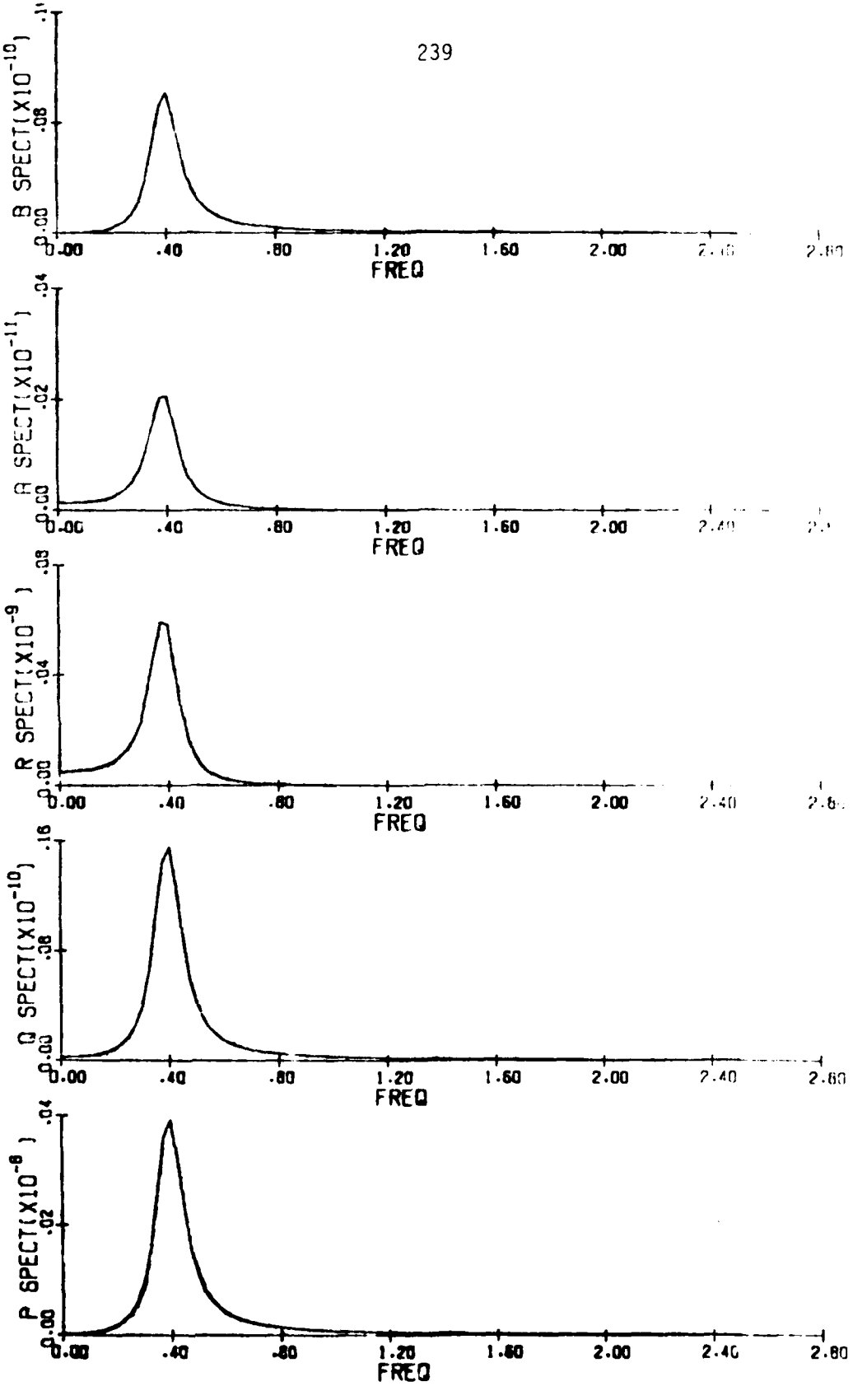

Fig. 4.4: A/C H Autocorrelation Spectra, for Control Settings of Fig. 4.2; no transient motion.

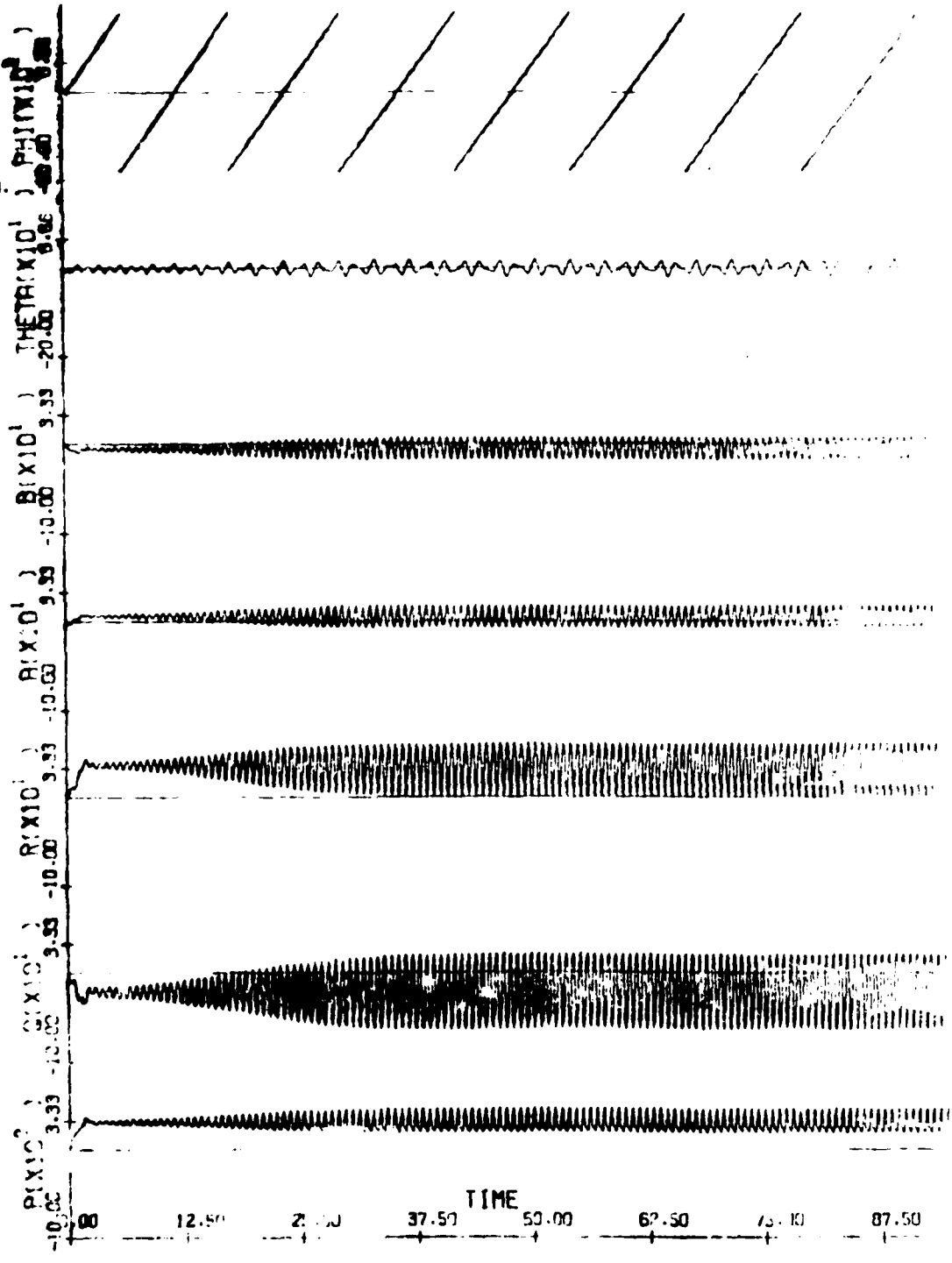

Fig. 4.5: A/C H Time History; $\delta a = -18°$, $\delta e = 2°$, $\delta r = 0°$; initial conditions at origin.

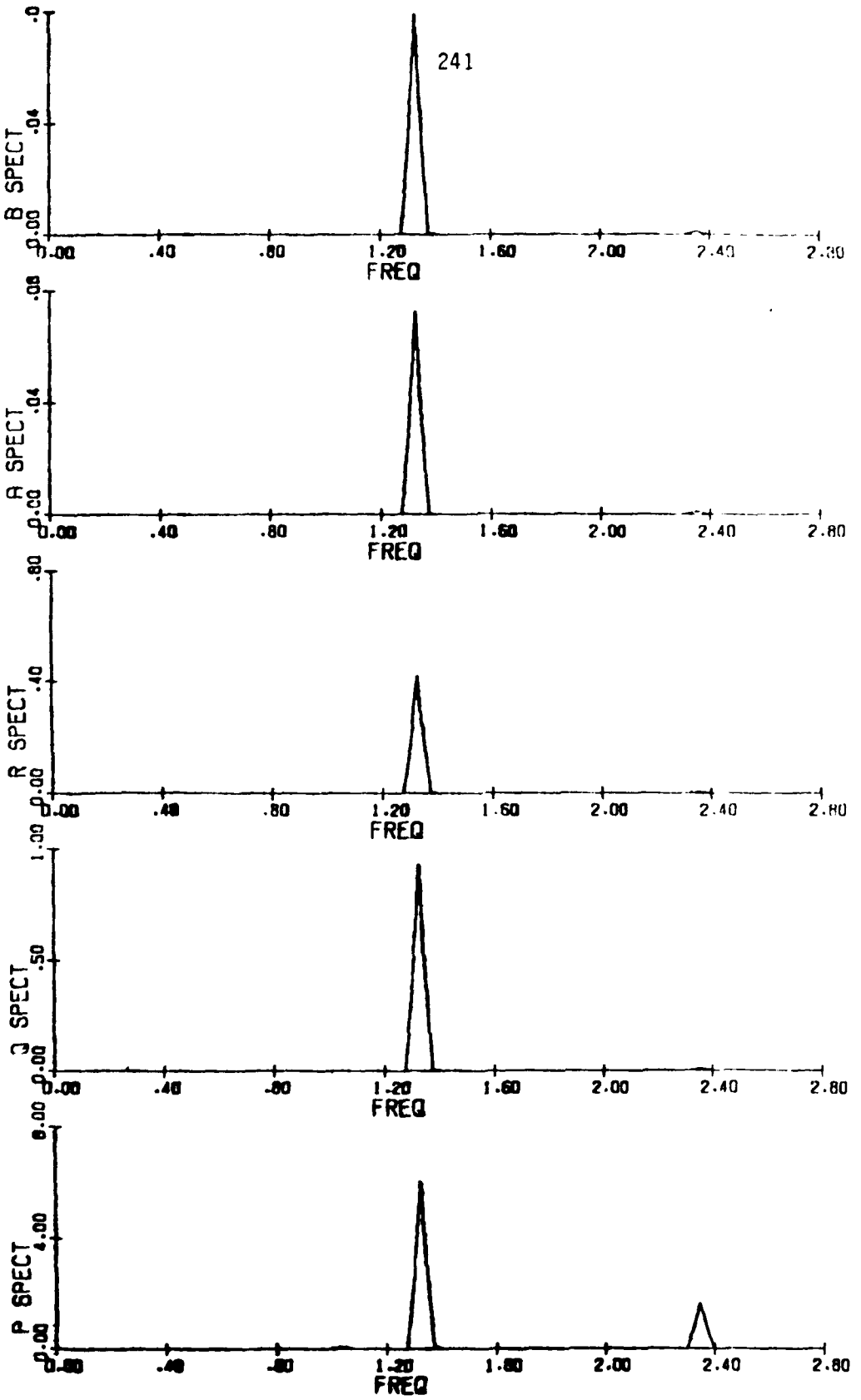

Fig. 4.6: A/C H Autocorrelation Spectra, for Control Settings of Fig. 4.4.

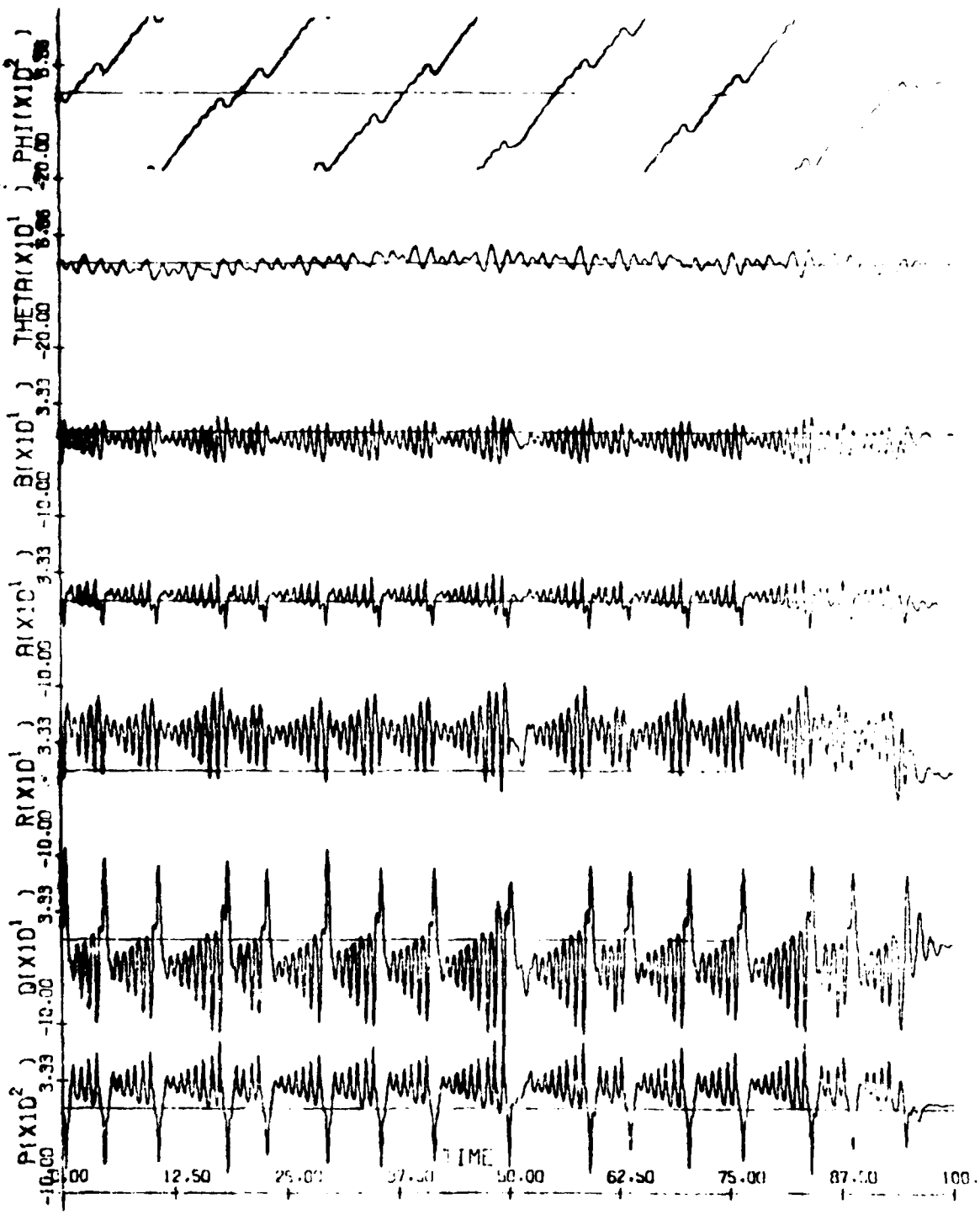

Fig. 4.7: A/C H Time History; $\delta a = -6°$, $\delta e = 2°$, $\delta r = 0°$;
$p_o = -46.3$, $q_o = 23.4$, $r_o = 59.2$ deg/sec; $\alpha_o = -2.39°$, $\beta_o = -31.5°$.

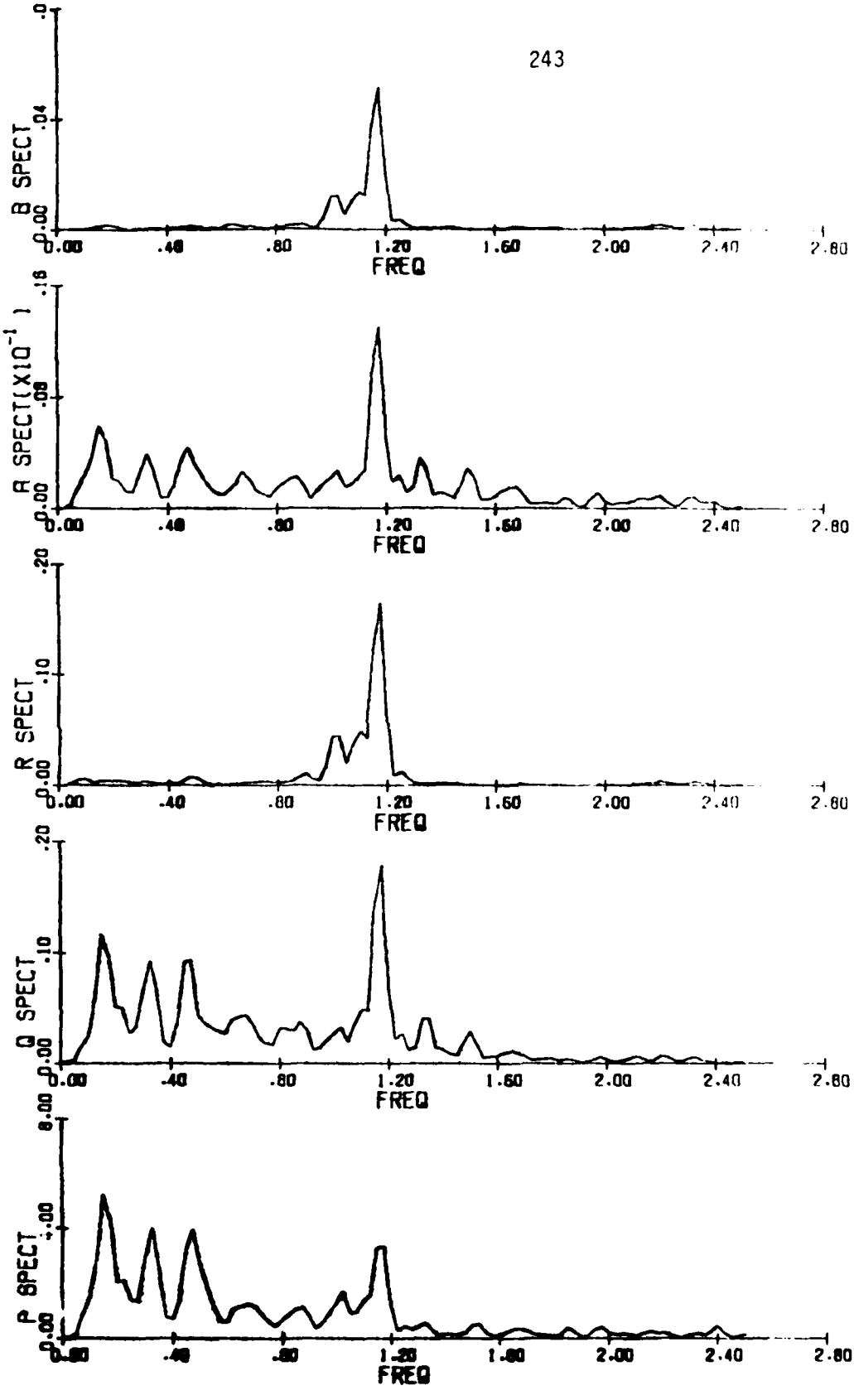

Fig. 4.8: A/C H Autocorrelation Spectra, for Control Settings of Fig. 4.7.

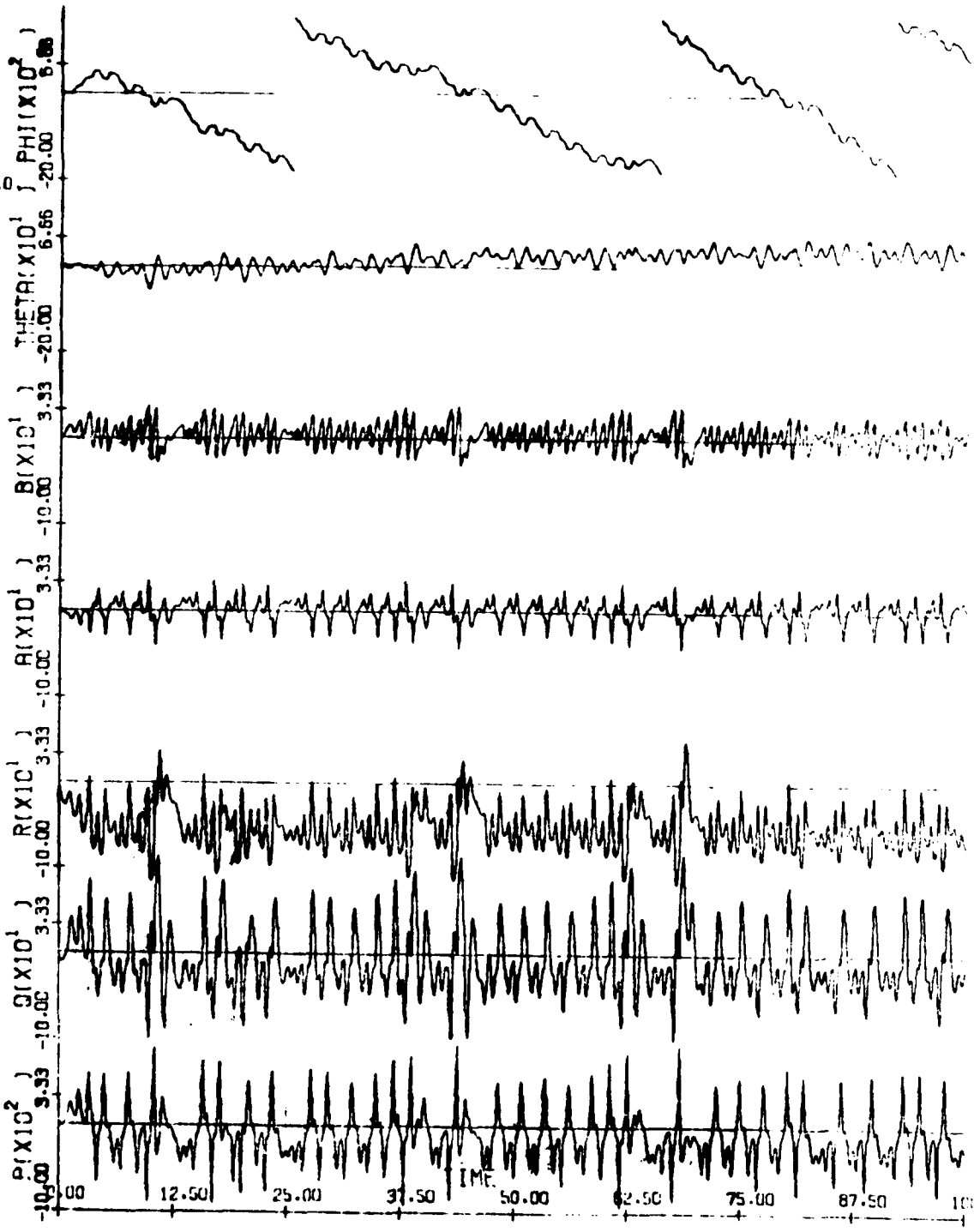

Fig. 4.9: A/C H Time History; $\delta a = 0°$, $\delta e = 2°$, $\delta r = 10°$; initial conditions at origin.

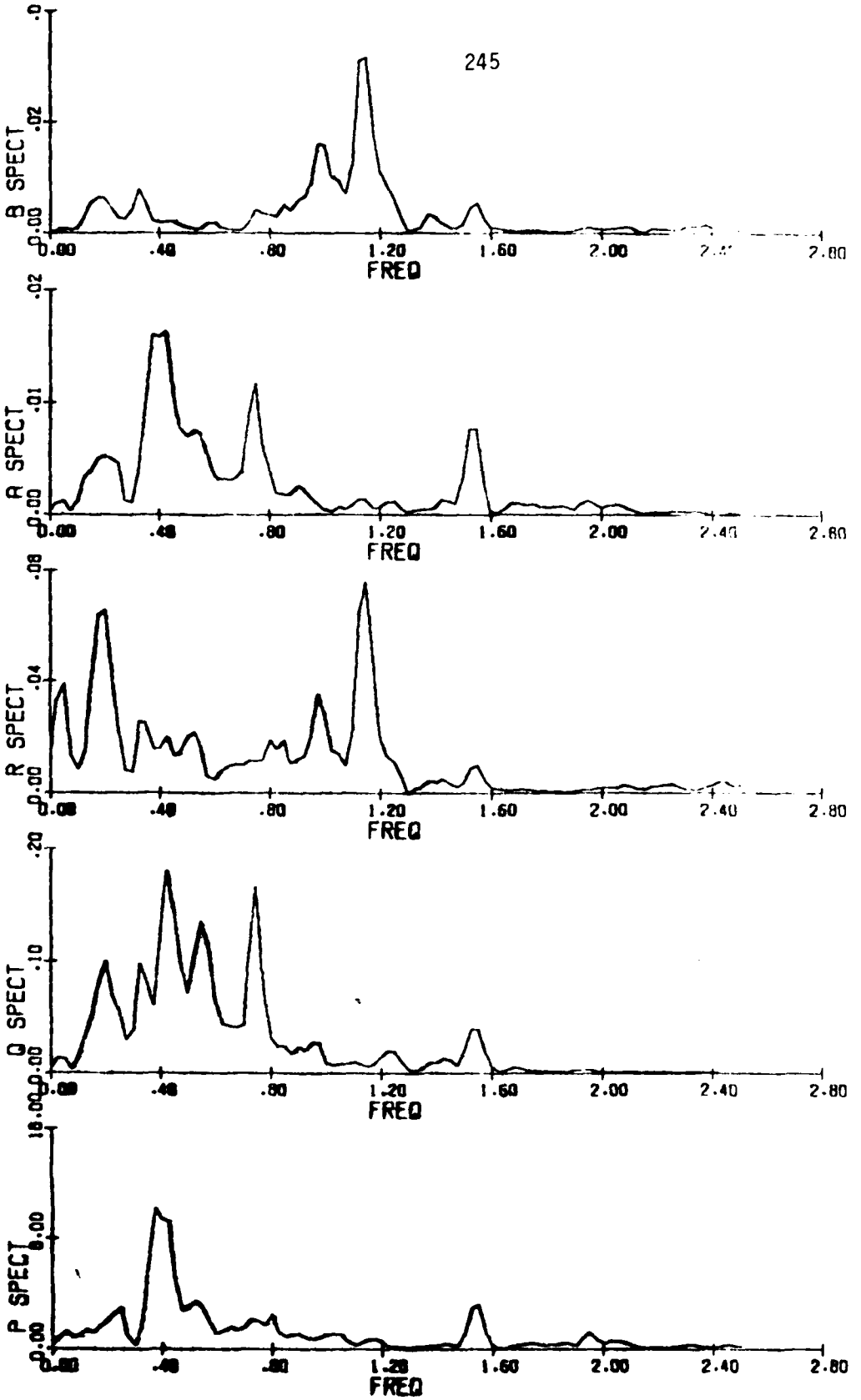

Fig. 4.10: A/C H Autocorrelation Spectra, for Control Settings of Fig.4.9.

4.2 Command and Stability Augmentation

Progress of a significant nature in this area awaits the development of the spin bifurcation algorithm, discussed in Sec. 2.1. Using the current algorithm several computer runs are required in order to generate adequately all of the branches of the bifurcation surfaces in the two-dimensional control space. When the third control is varied, an entirely new surface must be generated.

However, the results developed so far for two-dimensional command augmentation systems using the aircraft H model of Mehra, Kessel and Carroll (1977) have been very promising. The (two-dimensional) bifurcation surfaces are used to define relationships between the two control variables which serve to expand as much as possible the region in the equilibrium-state space for which bifurcations are avoided. Work has been centered to date on the control pair (δa, δr). Command augmentation gains relating δr to δa are generally called aileron-rudder interconnect (ARI) systems. ARI gains cause the rudder to deflect in conjunction with aileron movement. The purpose is to compensate in some manner for the effect of changing flight conditions on control response of the aircraft. The standard method of defining the ARI gains is to set them as linear functions of angle-of-attack. By using BACTM, in particular the bifurcation surface plots, it is possible to generate directly ARI, or any other type of command augmentation, functions. This is a more general, or global, procedure than those which reduce to a gain linear in α. It does not rely on localized analyses throughout the control-state space, but incorporates the global aircraft behavior information inherent in the BACTM results.

Work done to date has used aircraft H bifurcation surfaces. For each value of δe, a surface was generated, and a linear relationship between rudder and aileron was derived.* The criterion was to expand as much as possible the "non-catastrophic, non-limit-cycle" region in the control space. Since each setting of δe corresponds to an equilibrium value of angle-of-attack, $\bar{\alpha}$, the BACTM ARI gains can similarly be plotted versus $\bar{\alpha}$. Fig. 4.11 shows this plot compared to the linear ARI gains selected by Gilbert, Nguyen and VanGrunst (1976). The main point to be made here is that the general sense of the two plots is similar. (In Fig. 4.11, the values at the break points refer to the elevator deflection, in degrees). The gain values are of comparable magnitude, and a "mean slope" for the BACTM points would not be very different. It is felt that the BACTM method would result in better overall performance because of the global stability information inherent in it. Work will be continued in this area with the F-4 model.

*BACTM does not require that this relationship be linear. Later results may show better response for gains nonlinear in (δa,δr).

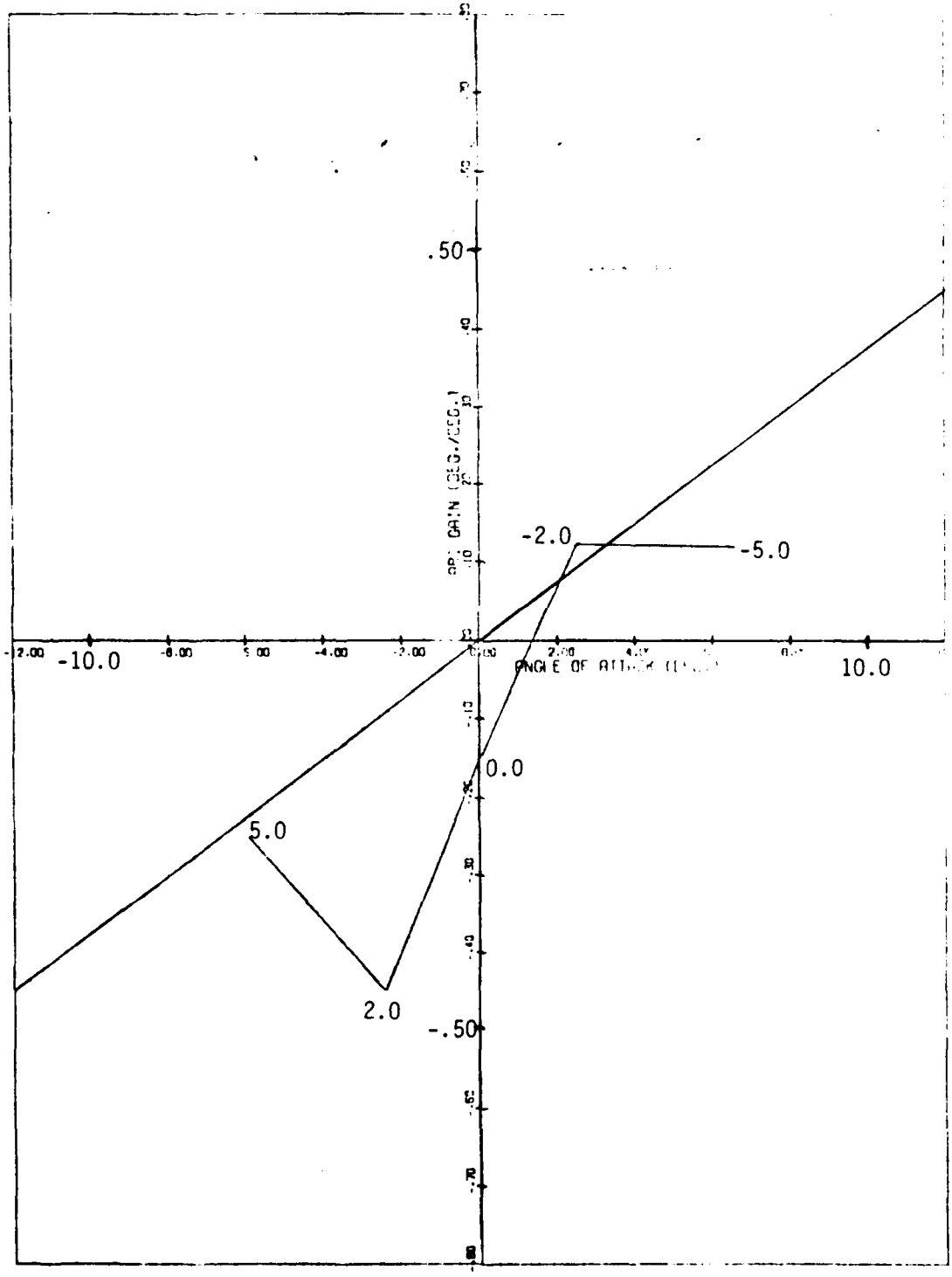

Fig. 4.11: BACTM ARI Gain and Gilbert et al. (1976) ARI Gain, vs. α
The numbers of the break points of the BACTM gain curve refer to elevon settings (deg.)

CHAPTER V

Conclusions and Recommendations for Further Research

5.1 Conclusions

Based on analysis using BACTM of the aircraft F model defined in this report, we can conclude that

(i) BACTM has been succesfully expanded and modified so that it now has the capability to perform analysis of aircraft in the highly complex post-stall and spin regimes. This was achieved by introducing more powerful continuation methods for solving equilibrium and bifurcation surfaces, and by utilizing an aircraft model with sufficient aerodynamic data to simulate motions over extreme ranges of angle-of-attack and sideslip.

(ii) The aircraft F model was very useful for its role in the development of the BACTM spin analysis program. Also, it was useful for studying developed spin motion. However, the aerodynamic data as given cannot with uniform accuracy deal with the wide variation in flight conditions which results from maneuvers proceeding from trim to spin conditions. It is necessary to begin using a more complete model, with the aerodynamics divided into static, forced oscillation and rotary balance data. In this way, combinations of the three sets may be varied from one flight regime to another, to more accurately simulate actual flight test results.

(iii) Spin study via BACTM can be made easier by assuming, on a

first-trial basis, that gravity effects are negligible. This assumption must be applied with care, however, because gravity plays an important role in post-stall dynamics as well as most spin motions. Nonetheless, it appears to be reasonable to apply this assumption to aircraft F studied here.

(iv) The transition between the non-spin and spin stable equilibria for aircraft F is difficult to achieve due to the strongly attracting nature of the intermediate, high-α equilibrium region. The BACTM analysis shows a high degree of nonlinear, oscillatory, limit cycle behavior associated with a large domain of attraction and a large region of structural stability for the limit cycle family.

(v) Aircraft F in flat developed spin follows a tight vertical helical path, which is characterized by constant speed, sink rate, and a high, autorotational, steady yaw rate. In this condition, the elevator is ineffective as a control, and recovery is possible only by using the rudder and aileron.

(vi) Entry into spin for aircraft F is strongly affected by assumptions about velocity. A spin of smaller amplitude oscillations and higher angle-of-attack (i.e., a more flat, developed spin) results when velocity is fixed, as opposed to when it is allowed to vary. The fixed velocity case, for small α and β angles, corresponds to a nonzero thrust situation, with the thrust neutralizing drag effects. When velocity is allowed to vary in this report, zero thrust is assumed.

(vii) The stall departure region is preceded by a wing rock type of limit cycle motion which is typical of modern high performance aircraft.

5.2 Recommendations

Based on our experience during this reporting period, it is suggested that the following areas be investigated in the future:

(i) The F-4 data should be analyzed using BACTM since it contains more realistic aerodynamics, is well documented and well supported by flight tests.

(ii) Computational development of BACTM should be continued, as more accurate and efficient algorithms are needed, particularly for the generation of a full set of bifurcation surfaces.

(iii) More analysis should be made of the assumptions regarding equilibrium motion in spin, particularly the assumption that gravity can be neglected in certain cases.

(iv) More time history runs and analyses should be done with initial conditions in selected regions of the state-control space; the purpose being to more clearly define persistence of limit cycle behavior and to establish boundaries for the domains of attraction. Analytical and computational procedures need to be developed for generating Hopf bifurcation surfaces.

(v) Using aircraft F-4 data to generate bifurcation surfaces, perform preliminary synthesis of a command augmentation system using BACTM. This system should then be compared to other systems in the literature.

(vi) Using the F-4 model, study the role of thrust in post-stall, departure, spin entry and developed spin flight conditions.

(vii) Determine the parameter values under which structurally stable limit cycles such as high-α oscillatory spins exist for a given aircraft model and design dynamic control strategies for recovery from such limit cycles.

APPENDIX A

Notation

b	wing span
$\bar{c}$	mean aerodynamic chord
$C_\ell = \frac{M_x}{\bar{q}Sb}$	rolling moment coefficient
$C_m = \frac{M_y}{\bar{q}S\bar{c}}$	pitching moment coefficient
$C_n = \frac{M_z}{\bar{q}Sb}$	yawing moment coefficient
$C_x = \frac{(\underline{F}-m\underline{g})\cdot\hat{\underline{x}}}{\bar{q}S}$	longitudinal force coefficient
$C_y = \frac{(\underline{F}-m\underline{g})\cdot\hat{\underline{y}}}{\bar{q}S}$	side force coefficient
$C_z = \frac{(\underline{F}-m\underline{g})\cdot\hat{\underline{z}}}{\bar{q}S}$	normal force coefficient
E	vehicle total kinetic energy
$\underline{f}$	force-moment terms in the aircraft
F	Jacobian matrix of partial derivatives, $\left[\frac{\partial f_i}{\partial x_j}\right]$
$\underline{F}$	aerodynamic force
g	(constant) acceleration due to gravity, 9.8067 m/sec^2 (32.174 ft/sec^2)
$\underline{g}$	algebraic system of terms for generating bifurcation surfaces (Chapter II)
G	augmented Jacobian matrix of partial derivatives, $\left[\frac{\partial g_i}{\partial y_j}\right]$, for bifurcation surfaces

h	altitude above earth's surface
I_x, I_y, I_z, I_{xz}	body axis moments and product of inertia, taken about the center of mass
$\underline{I}$	moment of inertia tensor (Eq. 3.2.38)
M_x, M_y, M_z	rolling, pitching, yawing moments acting about body axes
m	aircraft mass
$\underline{M}$	special vector, Sec. 2.1.2
$N(\cdot)$	null space
p,q,r	angular rates about body axes (roll, pitch, yaw, respectively)
$\bar{q}$	dynamic pressure, $\frac{1}{2}\rho V^2$
R	radius of helical path of airplane
$R(\cdot)$	range space
R^n	n-dimensional space of real numbers
$\hat{\underline{R}}, \hat{\underline{T}}, \hat{\underline{z}}^I$	unit vectors in cylindrical coordinates; $\hat{\underline{z}}^I$ is vertical, directed toward center of earth
S	wing area
t	time
t^*	time at which equilibrium solution is made
u,v,w	body axis components of $\underline{V}$
V	airspeed, = $\lvert\underline{V}\rvert$
V_H	horizontal component of velocity
$\underline{V}$	aircraft center of mass velocity, inertial with respect to local horizontal
W	aircraft weight
$\underline{x}$	vector of state variables; e.g., for n = 5 equilibrium system, $\underline{x} = (p,q,r,\alpha,\beta)$

$\underline{y}$	augmented vector of dependent variables, for bifurcation surfaces; e.g., for n = 5 equilibrium system, $\underline{y} = (\underline{x}, \delta_j)$, where $\delta_j \in (\delta a, \delta e, \delta r)$
$\hat{\underline{x}}, \hat{\underline{y}}, \hat{\underline{z}}$	aircraft body axis unit vectors ($\hat{\underline{x}}$ positive through nose, $\hat{\underline{y}}$ positive through right wing, $\hat{\underline{z}}$ positive down)
α	angle of attack, or incidence angle (Chapter III); also continuation variable (Chapter II)
β	angle of sideslip
δ	control parameter; either δa, δe, or δr (Chapter II)
Δ	determinant of F, the Jacobian matrix
$\underline{\delta}$	control vector, $(\delta a, \delta e, \delta r)$
$\delta a, \delta e, \delta r$	aileron, elevator, and rudder control deflections (positive δe is trailing edge down, positive δa is right trailing edge down, positive δr is trailing edge left)
ρ	atmospheric density
ψ, θ, ϕ	Euler angles defining orientation of body axes in the inertial reference axes (yaw, pitch, roll, in that sequence)
ω	angular rate about center of mass, $\sqrt{p^2 + q^2 + r^2}$
η	polar angle in cylindrical coordinate system defining aircraft position
$\alpha \in [-1,1]$	α such that $-1 \leq \alpha \leq 1$
$\alpha \in (-1,1)$	α such that $-1 < \alpha < 1$

the combinations $[\cdot)$ and $(\cdot]$ are similar; i.e., $\alpha \in [-1,1)$ means $-1 \leq \alpha < 1$

$\alpha \in A$	α is an element of the set A
$\alpha \notin A$	α is not an element of the set A
$[a_{ij}]$	a matrix array whose elements are designated by a_{ij}, the element at row i, column j

(a_i)	a vector array whose elements are designated by a_i, the i th location element
$\underline{v}^I$	indicates vector $\underline{v}$ is in inertial coordinates
$(\ )^T$	matrix transpose
$(\ )^*$	i) complex conjugate, as in Eq. (2.1.41) ii) equilibrium solution, as in Sec. 2.1.4.1
$\|\| \underline{x} \|\|$	the Euclidean norm of the vector x, i.e., $\|\| \underline{x} \|\| = \sqrt{\sum_{i=1}^{n} x_i^2}$ if $\underline{x} \in R^n$
$\det(\cdot)$	the determinant of the argument (which must be a square matrix)
$(\dot{\ })$	d( )/dt; also d( )/ds in Sec. 2.1.1
$\triangleq$	equal by definition

Stability Derivatives

$$C_{i_\xi} \triangleq \frac{\partial C_i}{\partial \xi}, \text{ for } i = \ell,m,n,x,y,z \text{ and } \xi = \delta a, \delta e, \delta r$$

$$C_{i_\eta} \triangleq \frac{\partial C_i}{\partial (\frac{b}{2V}\eta)}, \text{ for } \eta = p,r,\dot{\beta}$$

$$C_{i_\zeta} \triangleq \frac{\partial C_i}{\partial (\frac{\bar{c}}{2V}\zeta)}, \text{ for } \zeta = q$$

In addition, the coefficients C_i and the derivatives $\partial C_i/\partial\{\xi,\eta,\zeta\}$ are functions of α and β, and are usually determined via tabular or graphical look-up.

REFERENCES

Adams, W. M. (1972), "Analytic Prediction of Airplane Equilibrium Spin Characteristics," NASA TN D-6926.

Ahlberg, J., E. Nilson and J. Walsh (1967), "The Theory of Splines and Their Applications," New York: Academic Press.

Anglin, E. and S. Scher (1964), "Analytical Study of Aircraft--Developed Spins and Determination of Moments Required for Satisfactory Spin Recovery," NASA TN D-2181.

Anglin, E. (1977), "Recent Research on Aerodynamic Characteristics of Fighter Configuration During Spins," AIAA Atmospheric Flight Mechanics Conf., Hollywood, FL.

Bihrle, W. (1976), "Correlation Study of Theoretical and Experimental Results for Spin Tests of a 1/10-Scale Radio Controlled Model," NASA CR-144995.

Brady, C. C. et al. (1969), "Model F-4 Spin Evaluation Program," McDonnell-Douglas Report No. MDC A0005, Vol. II.

Carlson, J. (1971), "Status of Problem Area Including Historical Review," Stall/Post-Stall/Spin Symp., Wright-Patterson AFB, OH.

Davidenko, D. F. (1953), "On a New Method of Numerical Solution of Systems of Nonlinear Equations," Dokl. Akad. Nauk. SSSR, Vol. 88 (in Russian).

Deist, F. H. and L. Sefor (1967), "Solutions of Systems of Nonlinear Equations by Parameter Variation," Computer J., Vol. 10.

Etkin, B. (1972), Dynamics of Atmospheric Flight, New York: Wiley.

Ficken, F. A. (1951), "The Continuation Method for Functional Equations," Comm. Pure Appl. Math., Vol. 4.

Gilbert, W. P., L. T. Nguyen and R. W. VanGunst (1976), "Simulator Study of the Effectiveness of an Automobile Control System Designed to Improve the High Angle-of-Attack Characteristics of a Fighter Airplane," NASA TN D-8176.

Glenzer, H. (1971), "Navy Flying Safety," Stall/Post-Stall/Spin Symp., Wright-Patterson AFB, OH.

Goldstein, H. (1950), Classical Mechanics, Reading, Mass.: Addison-Wesley.

Grafton, S. B. (1966), "A Study to Determine the Effects of Applying Thrust on Recovery from Incipient and Developed Spins for Four Airplane Configurations," NASA TN D-3416.

Hacker, T. and C. Oprisiu (1974), "A Discussion of the Roll Coupling Problem," Progress in Aerospace Sciences, Vol. 15, Oxford: Pergamon Press.

Keller, H. B. (1977), "Numerical Solution of Bifurcation and Nonlinear Eigenvalue Problems," in Applications of Bifurcation Theory (ed. Rabinowitz), NY: Academic Press.

Kerr, T. H. (1956), "General Principles of Spinning," AGARD Flight Test Manual, Vol. II, Ch. 8, Part I.

Klinar, W. and W. Grantham (1959), "Investigation of the Stability of Very Flat Spins and Analysis of Effects of Applying Various Moments Using the Three Moment Equations of Motion," NASA Memo 5-25-59L.

Klopfenstein, R. W. (1961), "Zeroes of Nonlinear Functions," J. ACM, Vol. 8.

Krings, J. and W. Weber (1971), "McDonnell Aircraft Company's Experience and Viewpoint on the Stall/Post-Stall Region of Flight," Stall/Post-Stall/Spin Symp., Wright-Patterson AFB, OH.

Kubicek, M. (1976), "Algorithm 502. Dependence of Solution of Nonlinear Systems on a Parameter," ACM Trans. Math. Software, Vol. 2, No. 1.

Lahaye, E. (1934), "Une Méthode de Résolution d'une Catégorie d'Équations Transcendentes," C. R. Acad. Sci. Paris 198.

Lahaye, E. (1948), "Solution of Systems of Transcendental Equations," Acad. Roy. Belg. Bull. Cl. Sci. 5.

Lusby, W. A. et al. (1961), "T-38 Spin Evaluation," AFFTC-TR-61-31, USAF.

McLaughlin, J. B. and P. C. Martin (1975), "Transition to Turbulence in a Statically Stressed Fluid System," Physical Rev. A, Vol. 12.

Mehra, R. K., W. C. Kessel and J. V. Carroll (1977), "Global Stability and Control Analysis of Aircraft at High Angles-of-Attack," Scientific Systems, Inc. report ONR-CR215-248-1 for contract N00014-76-C-0780.

Moore, F. L., E. L. Anglin, et al. (1971), "Utilization of a Fixed-Base Simulator to Study the Stall and Spin Characteristics of Fighter Planes," NASA TN D-6117.

Neihouse, A., W. Klinar and S. Seber (1960), "Status of Spin Research for Recent Airplane Designs," NASA TR R-57 (supersedes NASA RM L57F12).

Rall, L. B. (1968), "Davidenko's Method for the Solution of Nonlinear Operator Equations," U. of Wisc., Math. Research Center, MRC Tech. Summary Rpt. 948.

Ralston, M. L. (1975), "DUD, a Derivative-Free Algorithm for Nonlinear Regression," PhD thesis, Dept. of Biostatistics, UCLA.

Ralston, M. L. and R. I. Jennrich (1978), "DUD, a Derivative-Free Algorithm for Nonlinear Least Squares," Technometrics, Vol. 20, pp. 7-14.

Rheinboldt, W. C. (1977), "Numerical Continuation Methods for Finite Element Applications," Ch. 20 in Proc. of U.S.-German Symp. on Formulation and Computational Algorithms in Finite Element Analysis," (ed. K. J. Bathe), MIT Press.

Ruelle, D. (1975), "The Lorenz Attractor and the Problem of Turbulence," presented at the Conf. on Quantum Dynamics Models and Mathematics, Bielefeld, Germany.

Ruelle, D. (1977), "Dynamical Systems with Turbulent Behavior," Int. Mathematical Physics Conf., Rome.

Rutan, et al. (1970), "Stall-Near Stall Investigation of the F-4E Aircraft," AFFTC, FTC-TR-70-20.

Sallada, R., G. Wheatley, and R. vonHusen (1967), "Evaluation of the Spin Characteristics of the T-2B Airplane," NAVAIR Test Ctr. Rpt. No. FT-73R-67.

Savidge, W. (1971), "USAF Out-of-Control Experience," Stall/Post-Stall/Spin Symp., Wright-Patterson AFB, OH.

Scher, S., E. Anglin and G. Lawrence (1959), "Analytical Investigation of Effect of Spin Entry Technique on Spin and Recovery Characteristics for a 60° Delta-Wing Airplane," NASA TN D-156.

Shaw, A. and M. Shields (1971), "VAC Experience in the Stall/Post-Stall and Spin Flight Regimes," Stall/Post-Stall/Spin Symp., Wright-Patterson AFB, OH.

Young, J. W. (1974), "Optimal and Suboptimal Technique for Aircraft Spin Recovery," NASA TN D-7714.

DISTRIBUTION LIST

Office of Naval Research
800 N. Quincy Street
Arlington, VA 22217
- R. von Husen, Code 211 — 4
- S. L. Brodsky, Code 432 — 1
- David Siegel — 1

Office of Naval Research
Eastern/Central Regional Office
495 Summer Street
Boston, MA 02210 — 1

Office of Naval Research
Western Regional Office
1030 E. Green Street
Pasadena, CA 91106 — 1

Naval Research Laboratory
Washington, DC 20375
- Code 2627 — 3

Naval Air Systems Command
Washington, DC 20361
- D. Kirkpatrick, AIR 320D — 1
- R. C. A'Harrah, AIR 50311 — 1

Naval Air Development Center
Warminster, PA 19874
- C. J. Mazza, Code 6153 — 1
- C. R. Abrams, Code 6072 — 1

Naval Material Command
Washington, DC 20360
- Code 08T23

Naval Weapons Center
China Lake, CA 93555
- B. Hardy, Code 3914 — 1
- R. Hewer — 1

Naval Surface Weapons Center
Silver Spring, MD 20910
- J. Wingate, Code R44 — 1

Naval Air Test Center
Patuxent River, MD 20670
- W. M. Branch, Code SA — 1
- R. E. Detrick, Code AT — 1
- J. McCue, Code TPS — 1

Naval Coastal Systems Center
Hydromechanics Division
Panama City, FL 32407
- D. Humphreys, Code 794 — 1

David Taylor Naval Ship R&D Center
Bethesda, MD 20084
- J. P. Feldman, Code 1564 — 1
- W. E. Smith, Code 1576 — 1

Naval Post Graduate School
Monterey, CA 93940
- Technical Reports Library — 1
- L. Schmidt — 1

Defense Technical Information Center
Building 5
Cameron Station
Alexandria, VA 22314 — 12

Air Force Office of Scientific Research
Building 410
Bolling Air Force Base
Washington, DC 20332
- G. W. McKemie — 1
- R. Buchal — 1

Air Force Flight Dynamics Laboratory
Wright-Patterson Air Force Base
Dayton, OH 45433
- R. Anderson, Control Dyn. Br. — 1
- D. Bowser, Control Dyn. Br. — 1

Air Force Institute of Technology
Wright-Patterson Air Force Base
Dayton, OH 45433
- P. Maybeck — 1
- J. G. Reid — 1

Army Armament R&D Command
Building #18
Dover, NJ 07801
- N. Coleman, DRDAR-SCFCC — 1

NASA Langley Research Center
Hampton, VA 23665
- J. R. Chambers — 1
- E. Anglin — 1
- V. Klein — 1
- A. Schy — 1
- G. Elliot — 1
- R. Dunning — 1

NASA Dryden Research Center
PO Box 273
Edwards, CA 93523
K. Iliff 1

Systems Technology, Inc.
13766 South Hawthorne Blvd.
Hawthorne, CA 90250
R. Whitbeck 1

The Analytic Sciences Corp.
6 Jacob Way
Reading, MA 01867
C. Price 1

Massachusetts Institute of Technology
Lab. for Information and Decision Systems
Cambridge, MA 02139
M. Athans 1

University of Michigan
Dept. of Naval Architecture and Marine Engineering
Ann Arbor, MI 48109
M. G. Parsons 1

Nielsen Engineering and Research, Inc.
510 Clyde Avenue
Mountain View, CA 94043
J. N. Nielsen 1

University of Notre Dame
Dept. of Electrical Engineering
Notre Dame, IN 46556
M. K. Sain 1

The C. S. Draper Laboratory, Inc.
555 Technology Square
Cambridge, MA 02139
R. V. Ramnath 1

Honeywell, Inc.
Systems and Research Center
2600 Ridgway Parkway
Minneapolis, MN 55413
C. A. Harvey 1

Alphatech, Inc.
3 New England Executive Park
Burlington, MA 01803
N. R. Sandell 1

Calspan Corp.
PO Box 400
Buffalo, NY 14225
E. G. Rynaski 1
K. S. Govindaraj 1

Systems Control Inc.
1801 Page Mill Road
Palo Alto, CA 94306
E. Hall 1

Flight Research Laboratory
Dept. of Mechanical and Aerospace Engineering
Princeton University
Princeton, NJ 08544
R. F. Stengel 1

Dynamics Research Corp.
60 Concord Street
Wilmington, MA 01887
H. L. Stalford 1

Oklahoma State University
Dept. of Mechanical and Aerospace Engr.
Stillwater, OK 74074
J. H. Taylor 1

Northrop Corporation
3901 West Broadway
Hawthorne, CA 90250
J. L. Lockenour 1
J. Kalviste 1

NASA Headquarters
Washington, DC 20546
H. Rediess 1

NASA Ames Research Center
Moffet Field, CA 94035
W. Johnson 1
D. Denery 1

Princeton University
Dept. of Mechanical and Aerospace Engr.
Princeton, NJ 08540
E. Dowell 1

University of Texas
Dept. of Aerospace Engineering
Austin, TX 78712
J. Speyer 1

SUNY at Buffalo
Dept. of Mathematics
106 Diefendorf Hall
Buffalo, NY 14216
B. Hassard 1

Stanford University
Dept. of Mechanical Engineering
Stanford, CA 94305
A. E. Bryson 1

University of California
Dept. of Electrical Engineering and
Computer Science
Berkeley, CA 94720
J. Marsden 1
P. Varaiya 1

Stanford University
Dept. of Aeronautics and Astronautics
Stanford, CA 94305
J. V. Breakwell 1

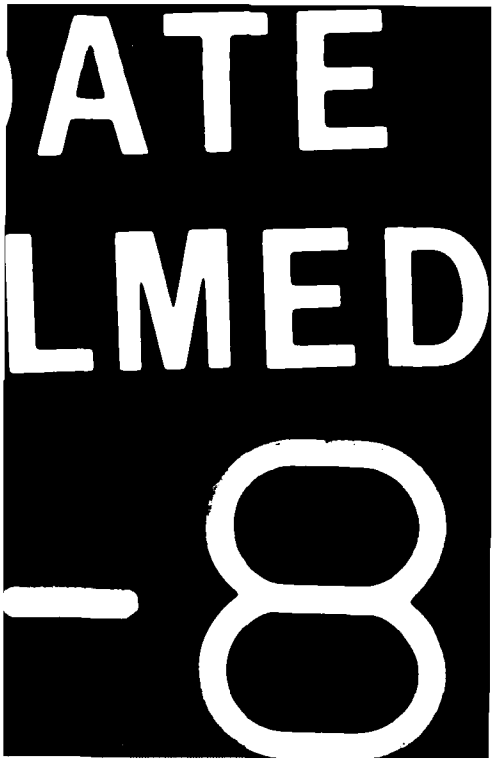
ATE
LMED
-8